

Development and investigation of protonic ceramic cells for hydrogen production at intermediate temperatures

Von der Fakultät Energie-, Verfahrens- und Biotechnik der Universität Stuttgart
zur Erlangung der Würde eines Doktors der
Ingenieurwissenschaften (Dr.-Ing.) genehmigte Abhandlung

Vorgelegt von

Haoyu Zheng

aus Hubei, China

Hauptberichter: Prof. Dr. André Thess
Mitberichter: Prof. Dr. Truls Norby
Prüfungsvorsitzender: Prof. Dr. K. Andreas Friedrich
Tag der mündlichen Prüfung: 08.05.2024

Institut für Gebäudeenergetik, Thermotechnik und Energiespeicherung
der Universität Stuttgart

2024

“博学之，审问之，慎思之，明辨之，笃行之。”

“Study extensively, enquire accurately, reflect carefully, discriminate clearly, practice earnestly.”

——《礼记·中庸》

Acknowledgments

I would like to express my gratitude to Prof. André Thess for giving me the opportunity to pursue my Ph.D. research at the Institute of Engineering Thermodynamics, German Aerospace Center (DLR). I appreciated a lot his encouragement and support during the whole work. Furthermore, I would also like to thank Dr. Rémi Costa for his daily supervision through the years, especially during the very challenging and fruitful last year. I was given the freedom to pursue my interests in electrochemical technologies, and in the meantime, he has always guided me to be on the right path towards the destination. I appreciated his valuable criticisms and enthusiastic encouragement during my daily work. He is always there ready to provide his support, knowledge, and insight.

I wish to thank Prof. K. Andreas Friedrich for his support and the discussions in the Ph.D. seminar. Let me broaden my knowledge to different electrochemical techniques. I would like to thank my colleagues at DLR. Special thanks go to my officemate Dr. Matthias Riegraf and Dr. Diana Amaya. I thank Diana for her daily help and encouragement during our PhD studies. Many thanks to Matthias for teaching me electrochemical knowledge, impedance analysis and numerous discussions. I also thank Dr. Feng Han and Dr. Noriko Sata for their support and sharing of their wide experience in process engineering and material science aspects. Many thanks to Ina Plock, Dr. Robert Ruckdäschel, Günter Roth and Szabo Patric for their technical support. I would like to thank Dr. Wang Li for all his help and encouragement.

I would like to express my gratitude to Prof. Truls Norby, I have greatly benefited from working with his group at the University of Oslo on thin film technology and solid-state electrochemistry, and many thanks for being the external advisor of my Ph.D. thesis. I would like to extend this also to Dr. Amir Masoud Dayaghi, Dr. Xin Liu and Yabing Wen from Prof. Norby's group for valuable discussions on protonic ceramics.

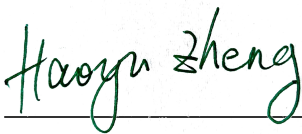
Last but not the least, I want to express my heartfelt gratitude to my parents for their endless love, encouragement, patience, and support.

Author's declaration

I hereby declare that I have written the submitted dissertation independently and have used no other sources or materials than those indicated.

Hiermit erkläre ich, dass ich die beigefügte Dissertation selbstständig verfasst und keine anderen als die angegebenen Hilfsmittel genutzt habe.

Stuttgart, May 09, 2024

A handwritten signature in green ink that reads "Haoyu Zheng". The signature is written in a cursive style and is positioned above a horizontal line.

Haoyu Zheng

Abstract

In a context of energy transition, high-temperature electrochemical energy convertors based on solid oxide cells are especially attractive due to fast kinetics and unrivalled efficiency. Yet, the high operating temperature, typically around 800 °C, implies numerous challenges in terms of materials stability to achieve adequate durability for industrial application. Reducing the operating temperature to the intermediate range, that is, between 500 °C and 700 °C, can be a strategy to increase the lifetime. Protonic ceramic cells (PCCs) are particularly suitable for operation within this temperature range. They can run in fuel cell mode with different fuel gases and in electrolysis mode for electrochemical synthesis (e.g., hydrogen, ammonia, ethylene, benzene, etc.). The technology is still at an early stage and challenges are still numerous for developing a scalable cell technology for practical and industrial application: i) the electrocatalyst for the oxygen and steam electrode (positrode) is still an issue due to the reduced activity at lower temperatures; ii) there is a lack of references about endurance and reliability of the materials in the long term, especially in electrolysis operation; iii) the refractory nature of state-of-the-art protonic ceramics (i.e., Y-doped BaZrO₃-BaCeO₃ solid solution materials) makes it challenging to manufacture cells in a planar configuration. To date, the most advanced cell design is based on tubular geometry, and it is desirable to develop planar cell designs that can enable higher current density.

In this work, double perovskite structure materials based on Ba_{1-x}Gd_{0.8}La_{0.2+x}Co₂O_{6-δ} (BGLC) were systematically investigated in button cells for both fuel cell and electrolysis modes. The electrochemical behavior was investigated and the influence of the operating parameters such as the atmosphere and the current density was elucidated. An equivalent circuit model for the electrode was developed to analyze the effect of the current leakage through the electrolyte that occurs due to the electron holes injected at the positrode. This yielded the conclusion that the water splitting process occurs preferably at the triple-phase boundary of BGLC, BZCY, and the gas phase. At the thermoneutral voltage for hydrogen production at 600 °C, the faradaic efficiency reached approximately 60%. Moreover, it was found that a reduced operating temperature, a high steam partial pressure, together with a low oxygen partial pressure can reduce the intensity of this current leakage.

Regarding the durability issue, the high reliability of the PCC with a BGLC-BZCY electrode operated in steam electrolysis mode was demonstrated for 1680 hours at a current density as

high as -0.8 A cm^{-2} close to the thermoneutral voltage at $600 \text{ }^\circ\text{C}$. Due to the existence of the electron hole conduction through the PCC electrolyte layer, the electrical efficiency reached around 65% depending on the operating temperatures. The PCCs exhibited a specific energy consumption between 54 and 66 kWh kg^{-1} , while showing systematically higher hydrogen production rates than commercial solid oxide cells at $600 \text{ }^\circ\text{C}$.

Finally, a new concept of metal-supported protonic ceramic cell (MS-PCC) electrolysis was developed and investigated. The metal-supported cells were manufactured by integrating various technologies including screen-printing, low-temperature co-sintering, and thin-film coating technology. Pulsed laser deposition (PLD) was used to fabricate a thin ($1 \text{ } \mu\text{m}$) and dense electrolyte layer, and to produce half-cells on $5 \times 5 \text{ cm}^2$ metal substrates. The MS-PCC with the developed BGLC positrode was tested in steam electrolysis mode, enabling apparent current densities as high as -850 mA cm^{-2} at 1.3 V and $600 \text{ }^\circ\text{C}$, demonstrating the feasibility of the concept.

Overall, this study paves the way for future protonic ceramic cells research. Positrode materials with double perovskite structures, like BGLC, can be used in practical applications due to their high electrocatalytic activity and superior stability at high applied current, which meets the requirements for industry. In addition, the metal-supported architecture has been proven to be feasible, thus opening the way for scaling up PCC technology. The current leakage and the low faradaic efficiency remain critical issues, especially in steam electrolysis. Increasing the faradaic efficiency under relevant operating conditions is identified as a key challenge to enable the scale-up and ramp-up of PCC technologies for electrolysis applications.

Zusammenfassung

Im Zuge der Energiewende sind elektrochemische Hochtemperatur-Energiewandler basierend auf Festoxidzellen (SOC) aufgrund ihrer schnellen Kinetik und einzigartig hohen Effizienz besonders attraktiv. Allerdings sind viele der eingesetzten Materialien bei den hohen Betriebstemperaturen von typischerweise 800 °C nicht langzeitstabil, was das Erreichen der benötigten Lebensdauer für industrielle Anwendungen erschwert. Eine Strategie, um die Lebensdauer zu erhöhen, ist die Reduzierung der Betriebstemperatur auf einen mittleren Bereich zwischen 500 °C und 700 °C. Protonenleitfähige Keramik-Zellen (PCCs) sind für den Betrieb in diesem Temperaturbereich besonders geeignet. Sie können im Brennstoffzellenmodus mit verschiedenen Brenngasen und im Elektrolysemodus für die elektrochemische Synthese (z.B. Wasserstoff, Ammoniak, Ethylen, Benzol usw.) betrieben werden. Allerdings befindet sich die Technologie noch in einem frühen Entwicklungsstadium und es gibt noch zahlreiche Herausforderungen bei der Entwicklung einer skalierbaren Zelltechnologie für praktische und industrielle Anwendungen: 1) die geringe Aktivität des Elektrokatalysators für die Sauerstoff- und Wasserdampfelektrode (Positrode) bei niedrigeren Temperaturen; 2) fehlende Untersuchungen zur Haltbarkeit und Zuverlässigkeit der Materialien über lange Zeiträume, insbesondere im Elektrolysebetrieb; 3) die schwierige Herstellung von Zellen in planarer Konfiguration aufgrund der hohen Sintertemperaturen von protonenleitfähigen Keramiken (d.h., Y-dotierte BaZrO₃-BaCeO₃ Mischkristalle). Bislang basiert das fortschrittlichste Zelldesign auf einer röhrenförmigen Geometrie, und es ist wünschenswert, ein planares Zelldesign zu entwickeln, das das Erreichen höherer Stromdichten ermöglicht.

In dieser Arbeit wurden Materialien mit Doppel-Perowskit-Struktur auf der Basis von Ba_{1-x}Gd_{0,8}La_{0,2+x}Co₂O_{6-δ} (BGLC) in Knopfzellenkonfiguration im Brennstoffzellen- und Elektrolysemodus untersucht. Das elektrochemische Verhalten wurde untersucht und der Einfluss von Betriebsparametern wie Gaszusammensetzung und Stromdichte wurde systematisch analysiert. Ein Ersatzschaltbildmodell der Elektrode wurde entwickelt, durch das die Auswirkung des durch die Positrode bedingten Leckagestroms durch den Elektrolyten untersucht wurde. Dies führte zu der Schlussfolgerung, dass der Wasserspaltungsprozess vorzugsweise an der Drei-Phasengrenze zwischen BGLC, BZCY und der Gasphase stattfindet. Bei der thermoneutralen Spannung für die Wasserstoffproduktion bei 600 °C betrug die

Faraday-Wirkungsgrad ungefähr 60%. Außerdem können eine niedrige Betriebstemperatur, ein hoher Dampfpartialdruck und ein niedriger Sauerstoffpartialdruck die Intensität des Leckagestroms verringern.

Bezüglich des Stabilitätsproblems wurde die hohe Zuverlässigkeit einer PCC mit BGLC/BZCY-Elektrode durch ihre Langzeitstabilität nachgewiesen, die im Elektrolysemodus über 1680 Stunden bei einer Stromdichte von -0.8 A cm^{-2} nahe der thermoneutralen Spannung bei 600 °C betrieben wurde. Aufgrund der Leitung von Elektronen/loch-Leitfähigkeit durch die PCC-Elektrolytschicht lag der elektrische Wirkungsgrad je nach Betriebstemperatur bei etwa 65%. Die PCCs wiesen einen spezifischen Energieverbrauch zwischen 54 und 66 kWh kg^{-1} auf, während die Wasserstoffproduktionsraten bei 600 °C systematisch höher waren als bei kommerziellen Festoxidzellen.

Schließlich wurde ein innovatives Konzept der Elektrolyse an den metallgestützten protonischen Keramikzellen (MS-PCC) entwickelt und untersucht. Die metallgestützten Zellen wurden durch die Kombination verschiedener Technologien hergestellt, darunter Siebdruck, Niedrigtemperatur-Co-Sintern und Dünnschichtbeschichtungstechnologie. Mithilfe von Laserstrahlverdampfen (PLD) wurde eine dünne ($1 \mu\text{m}$) und dichte Elektrolytschicht auf $5 \times 5 \text{ cm}^2$ Metallsubstrate aufgebracht, wodurch Halbzellen hergestellt wurden. Eine daraus hergestellte MS-PCC mit der entwickelten BGLC-Positrode wurde im Dampf-Elektrolyse-Modus getestet und ermöglichte scheinbare Stromdichten von bis zu -850 mA cm^{-2} bei 1.3 V und 600 °C , was die Machbarkeit des Konzepts nachweist.

Zusammengefasst ebnet die vorliegende Studie den Weg für zukünftige Forschungsarbeiten an protonischen Keramikzellen. Positroden-Materialien mit Doppel-Perowskit-Struktur, wie BGLC, können aufgrund ihrer hohen elektrokatalytischen Aktivität und überlegenen Stabilität bei hohen angelegten Stromdichten in realen Anwendungen eingesetzt werden, was den industriellen Anforderungen entspricht. Darüber hinaus hat sich die metallgestützte Architektur als praktikabel erwiesen und eröffnet somit einen neuen Weg zur Skalierung der PCC-Technologie. Die kritischen Probleme sind nach wie vor der Leckagestrom und der geringe Faraday-Wirkungsgrad, insbesondere bei der Dampfelektrolyse. Die Steigerung des Faraday-Wirkungsgrades bei den relevanten Betriebsbedingungen ist eine zentrale Herausforderung, um die Hochskalierung und das Hochfahren der PCC-Technologie für die Elektrolyseanwendung zu ermöglichen.

Table of contents

Acknowledgments	III
Author's declaration	IV
Abstract	V
Zusammenfassung	VII
Table of contents	IX
List of abbreviations	XIII
List of symbols	XV
1 Introduction	1
1.1 Background	1
1.2 Hydrogen production by water electrolysis at different temperatures	3
1.3 Aim and content	5
2 Background and fundamentals on protonic ceramic cells	6
2.1 Protonic ceramics	6
2.1.1 Formation and mobility of proton defects	6
2.1.2 Mixed ionic and electronic conductivity in Y-doped BaZrO ₃ -BaCeO ₃	7
2.2 Protonic ceramic cell components.....	9
2.2.1 Electrolyte	10
2.2.2 Fuel electrode (negatrode).....	12
2.2.3 Oxygen electrode (positrode)	13
2.3 Architectures of protonic ceramic cells	15
2.4 Fundamentals of protonic ceramic cells	18
2.4.1 Fuel cell operation	18

2.4.2 Steam electrolysis operation.....	18
2.4.3 Energy losses in electrolysis.....	20
2.4.4 Current leakage and energy efficiency in electrolysis.....	22
3 Motivation and interrelation between the studies/articles	25
4 Experimental methodologies	28
4.1 Materials preparation.....	28
4.2 Cells manufacturing	28
4.2.1 Different processing methods.....	28
4.2.2 Negatrode-supported protonic ceramic cells fabrication	30
4.2.3 Metal-supported protonic ceramic cells fabrication.....	31
4.3 Characterization techniques	32
4.3.1 X-ray diffraction.....	32
4.3.2 Dilatometric measurement	33
4.3.3 Scanning electron microscopy	33
4.3.4 Laser scanning microscopy	33
4.4 Electrochemical tests.....	34
4.4.1 Electrochemical test system installation	34
4.4.2 Hydrogen production measurement	35
4.4.3 Polarization curves	35
4.4.4 Electrochemical impedance spectroscopy.....	36
4.4.5 Electrochemical analysis methods	37
5 Publications.....	41
5.1 List of publications	41
5.2 Article I.....	43

5.3 Article II	60
5.4 Article III	71
6 Additional results and general discussion	92
6.1 Barium cobalt-based perovskite materials as promising positrodes	92
6.2 Current leakage and faradaic efficiency	97
6.3 Hydrogen production and durability of the performances	100
6.4 MS-PCCs for practical applications	102
7 Conclusions and outlook.....	104
7.1 Conclusions	104
7.2 Outlook.....	106
Appendix A: Supplementary information for Article I	109
Appendix B: Supplementary information for Article II.....	128
Appendix C: Supplementary information for Article III	136
Bibliography	149

List of abbreviations

AEL	Alkaline electrolysis
AEMEL	Anion exchange membrane electrolysis
BCO	BaCoO ₃
BGLC	Ba _{1-x} Gd _{0.8} La _{0.2+x} Co ₂ O _{6-δ}
BGLC1082	BaGd _{0.8} La _{0.2} Co ₂ O _{6-δ}
BGLC587	Ba _{0.5} Gd _{0.8} La _{0.7} Co ₂ O _{6-δ}
BLC	Ba _{0.5} La _{0.5} CoO _{3-δ}
BZCY	BaZr _{1-x-y} Ce _x Y _y O _{3-δ}
BZCY172	BaZr _{0.1} Ce _{0.7} Y _{0.2} O _{3-δ}
BZCY181	BaZr _{0.1} Ce _{0.8} Y _{0.1} O _{3-δ}
BZCY20	BaZr _{0.8-x} Ce _x Y _{0.2} O _{3-δ}
BZCY541	BaZr _{0.5} Ce _{0.4} Y _{0.1} O _{3-δ}
BZCY721	BaZr _{0.7} Ce _{0.2} Y _{0.1} O _{3-δ}
BZCYYb1711	BaZr _{0.1} Ce _{0.7} Y _{0.1} Yb _{0.1} O _{3-δ}
BZCYYb4411	BaZr _{0.4} Ce _{0.4} Y _{0.1} Yb _{0.1} O _{3-δ}
CCS	Carbon capture and storage
CNLS	Complex non-linear square
CPE	Constant phase element
DRT	Distribution of relaxation times
ECE	Energy conversion efficiency
ECM	Equivalent circuit model
EDX	Energy-dispersive X-ray
EIS	Electrochemical impedance spectroscopy
ES-PCCs	Electrolyte supported protonic ceramic cells
ET-AEL	Elevated temperature alkaline electrolysis
ET-PEMEL	Elevated temperature polymer electrolyte membrane electrolysis
FES-PCC	Fuel electrode supported protonic ceramic cell
GDC	Gadolinia-doped ceria
GHG	Greenhouse gas
IRENA	International renewable energy agency
KPI	Key performance indicator
LCOE	Levelized cost of electricity

LSCF	$\text{La}_{0.6}\text{Sr}_{0.4}\text{Co}_{0.2}\text{Fe}_{0.8}\text{O}_{3-\delta}$
LSM	$(\text{La}_{0.8}\text{Sr}_{0.2})_{0.95}\text{MnO}_{3-\delta}$
MEK	Methyl-ethyl-ketone
MIEC	Mixed ionic and electronic conductor
MSC	Metal supported cell
MS-PCC	Metal-supported protonic ceramic cell
NS-PCC	Negatrode-supported protonic ceramic cell
OCV	Open circuit voltage
OER	Oxygen evolution reaction
ORR	Oxygen reduction reaction
PBNO	$\text{Pr}_{2-x}\text{Ba}_x\text{NiO}_{4+\delta}$
PCC	Protonic ceramic cell
PCEC	Protonic ceramic electrolysis cell
PCFC	Protonic ceramic fuel cell
PEG	Polyethylene glycol
PEMEL	Polymer electrolyte membrane electrolysis
PLD	Pulsed laser deposition
PNO	$\text{Pr}_2\text{NiO}_{4+\delta}$
PPD	Peak power density
PVB	Polyvinyl butyral
RP	Ruddlesden-Popper
SEM	Scanning electron microscope
SMR	Steam methane reforming
SOC	Solid oxide cell
SSC	$\text{Sm}_{0.5}\text{Sr}_{0.5}\text{CoO}_{3-\delta}$
TEC	Thermal expansion coefficient
TPB	Triple phase boundary
XRD	X-ray diffraction
YSZ	Yttria-stabilized zirconia

List of symbols

Description	Symbol	Unit
Activation energy barrier	E_a	eV
Activation overpotential	η_{act}	V
Angular frequency	ω	s^{-1}
Apparent charge transfer coefficient	α	/
Arithmetic mean roughness	R_a	μm
Capacitance	C_p	F
Cell voltage	V_{cell}	V
Concentration overpotential	η_{con}	V
Current density	I	$A\ cm^{-2}$
Distribution function of relaxation times	$g(\tau)$	$\Omega\ s$
Electronic conductivity	σ_{elec}	$S\ m^{-1}$
Electronic resistance	$R_{\Omega,e}$	$\Omega\ cm^2$
Electronic transference number	t_e	/
Energy conversion efficiency	η_{ECE}	%
Exchange current density	I_0	$A\ cm^{-2}$
Exponent of constant phase	α	$0 < \alpha < 1$
Faradaic efficiency	η_{FE}	%
Faraday constant	F	$96485\ C\ mol^{-1}$
Gibbs free energy change	ΔG	$J\ mol^{-1}$
Imaginary part of the complex impedance	Z''	$\Omega\ cm^2$
Imaginary unit	j	$\sqrt{-1}$
Ionic resistance	$R_{\Omega,i}$	$\Omega\ cm^2$
Ionic transference number	t_i	/
Limiting current density	I_L	$A\ cm^{-2}$
Lower heating value of hydrogen	LHV_{H_2}	$33.33\ kWh\ kg^{-1}$
Mean peak to valley height roughness	R_z	μm
Measured hydrogen production rate	$n_{H_2,measured}$	$mol\ s^{-1}$

Molar enthalpy change	ΔH	J mol^{-1}
Number of electrons	z	/
Ohmic overpotential	η_{ohm}	V
Ohmic resistance	R_{Ω}	$\Omega \text{ cm}^2$
Operating temperature	T	k
Overall ohmic resistance	R_{ohmic}	$\Omega \text{ cm}^2$
Oxygen partial pressure	p_{O_2}	atm
Polarization resistance	R_{p}	$\Omega \text{ cm}^2$
Powder density	P	mW cm^{-2}
Pre-exponential factor	k	/
Reaction entropy	ΔS	$\text{J mol}^{-1} \text{ K}^{-1}$
Real part of the complex impedance	Z'	$\Omega \text{ cm}^2$
Real polarization resistance	$R_{\text{p,r}}$	$\Omega \text{ cm}^2$
Relaxation times	τ	s
Reversible potential	V_{rev}	V
Steam partial pressure	$p_{\text{H}_2\text{O}}$	atm
Theoretical potential	V_{N}	V
Thermoneutral voltage	V_{TN}	V
Thickness of the electrolyte	L	m
Total resistance	R_{t}	$\Omega \text{ cm}^2$
Universal gas constant	R	$8.3145 \text{ J K}^{-1} \text{ mol}^{-1}$
Water conversion rate	$X_{\text{H}_2\text{O}}$	%
Water latent heat	$\lambda_{\text{H}_2\text{O}}$	kJ kg^{-1}

1 Introduction

1.1 Background

Since the industrial revolution, energy consumption has increased dramatically, especially, in the last few decades (Figure 1.1) ¹. Traditional energy sources, including coal, oil, and natural gas, are the main primary energy sources, contributing to environmental pollution and to climate change ². Renewable energies, such as hydro-, solar, and wind power, have been developed and deployed at an accelerated pace in the recent past ³. However, these technologies depend strongly on environmental factors such as weather conditions and geography, which are hardly controllable. Intermittent by nature, the renewable electricity supply can hardly match with the energy consumption in the society without appropriate energy storage system. Electrochemical energy conversion technologies are especially attractive to storage and transform this primary electricity. For example, Lithium-ion batteries, as an electrochemical storage device, show high efficiency and flexibility, as illustrated in Figure 1.2, and have been used broadly in our daily lives ⁴. Whereas the application of the lithium-ion batteries is limited to small scales, i.e., less than a megawatt (MW), fuel cells and electrolyzers are more suited for larger power classes, i.e., in the range 1MW–1GW, and longer discharge times. An electrolyzer can convert renewable electricity into fuel gases (H₂, CO, and syngas) that can be converted into molecules such as CH₄ or liquid fuels for easy storage. Reversibly, the device can convert backward the produced chemical energy into electricity by operating in fuel cell mode. Among different fuel gases, hydrogen has the highest gravimetric energy density ⁵.

Green hydrogen, which is produced by electrolysis using renewable electricity, is a low CO₂ emission option for energy storage from solar and wind power that can significantly promote decarbonization ⁶. Hydrogen is used as the feed gas for many synthesis processes in the fuel and chemical industry, such as methane, ethylene, ethanol and ammonia, and also industrial processes like refining and steel production ⁷. In this thesis, novel types of electrolysis cells based on protonic ceramics were developed for hydrogen production at intermediate temperatures (500–700 °C).

Introduction

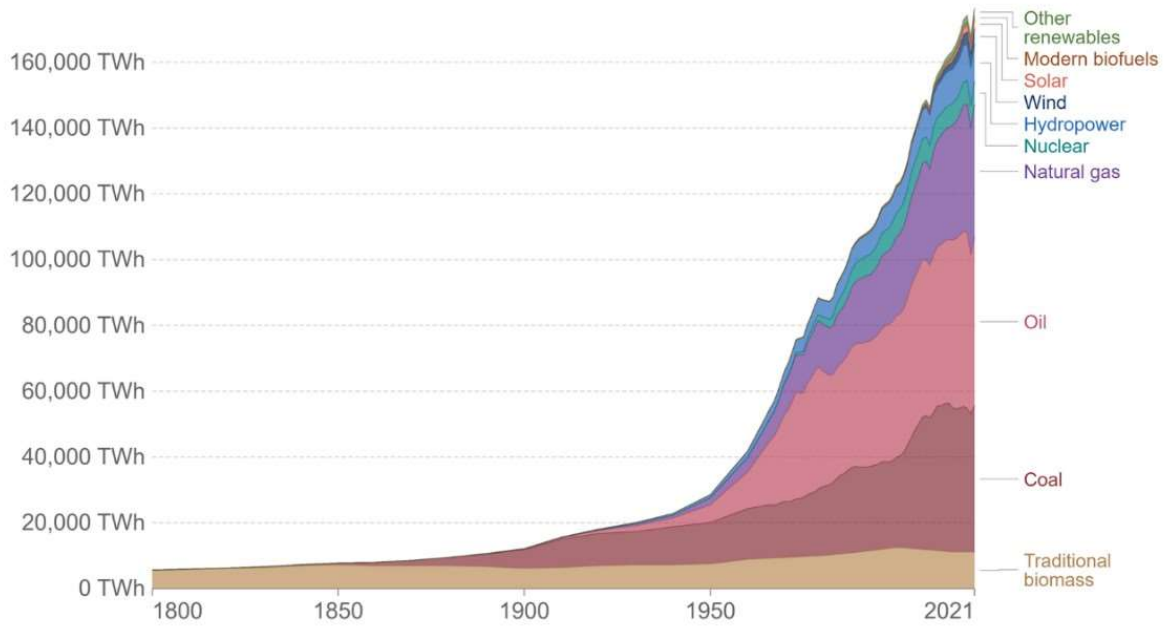


Figure 1.1: Global primary energy consumption by source, adapted from ref. ¹.

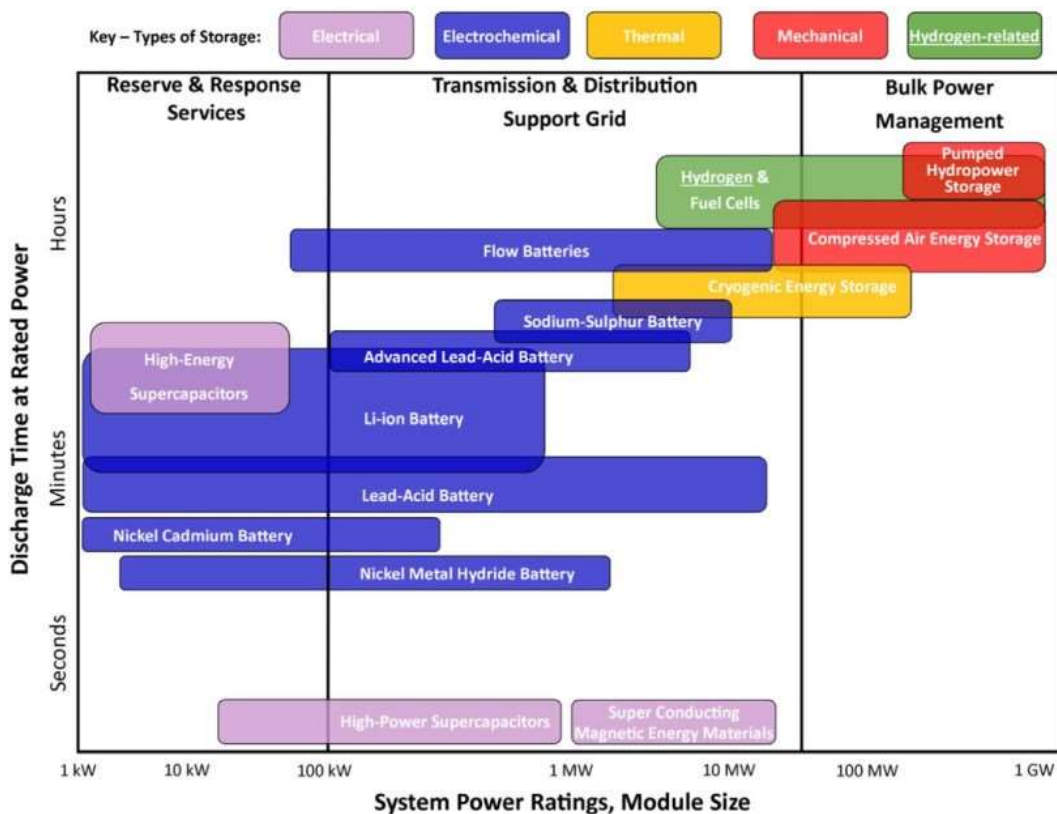


Figure 1.2: Comparison of different types of energy storage technologies in terms of storage capacity and discharge power duration, adapted from ref. ⁴.

1.2 Hydrogen production by water electrolysis at different temperatures

Today, the vast majority of hydrogen is produced with non-renewable sources, for example, ca. 80% of hydrogen is obtained by steam methane reforming (SMR), and ca. 18% by coal gasification, leading to considerable greenhouse gas (GHG) and pollution emissions^{8,9}. In principle, water electrolysis powered by renewable electricity can avoid GHG emissions. In 2021, only about 4–5% of hydrogen was produced by water electrolysis⁹. The high production cost is still a major barrier for scaling up this technology, as it can be 2–3 times more expensive than blue hydrogen, produced by steam methane reforming of natural gas and combined with carbon capture and storage (CCS) technologies¹⁰. At large scale (1000 kg/day), the highest percentage (more than 62%) of the total cost for green hydrogen production is the renewable electricity⁸. Therefore, increasing the electrical efficiency by enhancing electrolysis performance is a crucial strategy to facilitate industrial applications of water electrolysis.

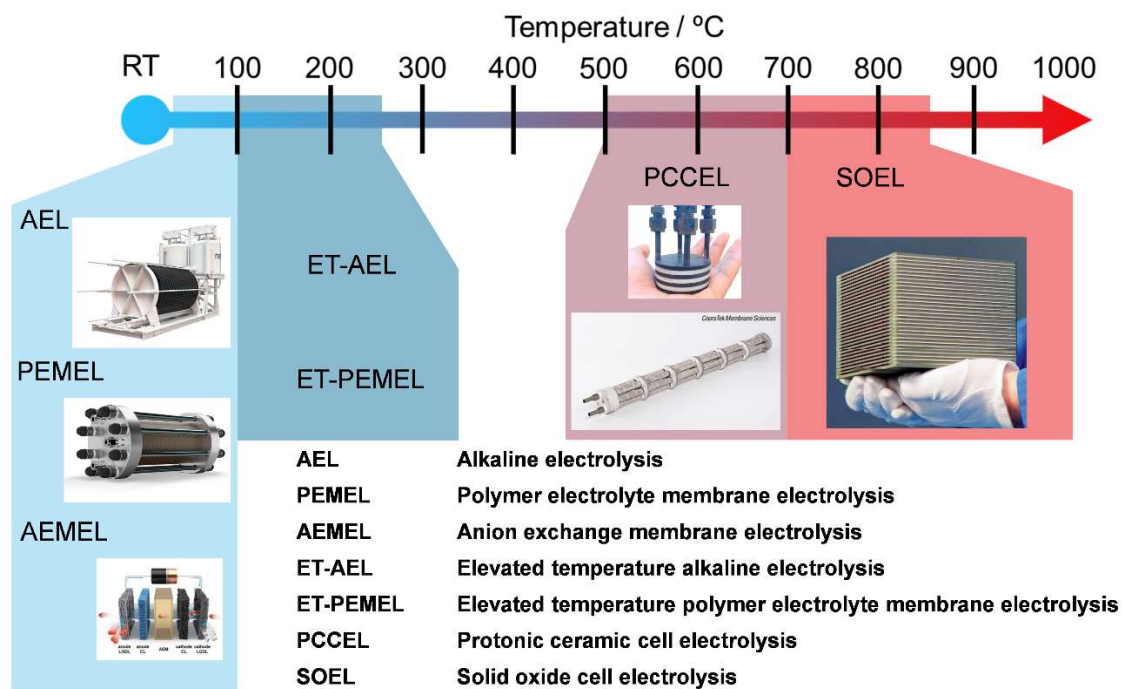


Figure 1.3: Different electrolysis techniques at representative working temperatures. (The AEL image is sourced from Nel Hydrogen; the PEMEL image is sourced from Hydrogen innovation GmbH; the AEMEL image is adapted from ref. ¹¹; The planar PCCEL image is adapted from ref. ¹²; the tubular PCCEL image is sourced from CoorsTek Membrane Sciences and the SOEL image is adapted from ref. ¹³)

Introduction

Different water electrolysis techniques are summarized in Figure 1.3 according to the operating temperatures. The low temperature electrolysis technologies are operated at temperatures lower than 100 °C. Consequently, these systems encompass both gases and liquids that need to be managed very well. Among the different technologies, alkaline electrolysis (AEL) is the most commonly used and commercially available. The typical working temperature for AEL ranges from 25 °C to 100 °C. The limited current density (less than 400 mA cm⁻²) and the insufficient voltage efficiency (50–68%) are the main challenges for AEL. Polymer electrolyte membrane electrolysis (PEMEL) can reach a high current density of around 2 A cm⁻² at 2.1 V and an operating temperature between 50 °C and 80 °C. However, scarce and expensive materials are needed in PEMEL, for instance, Pt as the cathode catalyst, IrO₂ as the anode catalyst, and Ti-based bipolar plates, which are hindering the deployment of this technology at a large scale. In recent years, anion exchange membrane electrolysis (AEMEL) has attracted more attention due to some technical advantages, such as the use of a non-noble metal catalyst and the use of a noncorrosive electrolyte. However, the development of AEMEL is still in the early stage and significant improvements are required to increase the performance and the durability.

Increasing the electrolysis temperature above 100 °C can enhance the reaction kinetics and simplify the water management. Therefore, the elevated-temperature polymer electrolyte membrane electrolysis (ET-PEMEL) was developed and the targeted working temperature is in the range of 100–250 °C. The enhanced electrochemical performance can alleviate the dependency on precious metal catalysts and provide an excellent dynamic response. In the meantime, new challenges regarding materials stability are imposed by the increase in operating temperatures.

To date, the most developed high temperature electrolyser is based on solid oxide cells (SOCs). SOCs typically operate at high temperatures, between 700 °C and 900 °C. The electrolyte materials are oxygen ion conductors (i.e., yttria-stabilized zirconia (YSZ) and gadolinia-doped ceria (GDC)). Compared with the low temperature technologies, the distinctive high operating temperatures offer advantages, for instance faster reaction kinetics, higher current density, and lower electrical energy demand. Nevertheless, the high operating temperatures can lead to accelerated elemental diffusion between the different components of the cell, causing a high degradation rate and a relatively fast aging of the interconnects and other stack and system components. Thus, reducing the operating temperature of the SOC has become an important direction of development.

From this perspective, protonic ceramic cells (PCCs) are ideally suited for operation between 400 °C and 700 °C. This is due to the lower activation energy of proton conduction (0.4–0.6 eV) compared to oxygen-ion conduction (> 0.8 eV)¹⁴. PCCs can be operated reversibly in both electrolysis and fuel cell mode as SOCs. The application for protonic ceramic cells were proposed and demonstrated by Iwahara *et al.*¹⁵ in the 1990s. Lowering the operation temperature offers advantages, for instance it can enable fast start-up, making PCCs suitable for coupling with intermittent energy sources (i.e., solar and wind power); moreover, it can contribute to extending the components lifetime, which has the potential to substantially decrease the manufacturing costs. Thus, PCCs exhibit a great potential for green hydrogen production through steam electrolysis at intermediate temperatures. While there has been considerable progress, the application of PCCs for steam electrolysis is still at a relatively low technology readiness level of around 3¹⁶, and some aspects related to the electrocatalysis as well as the cell architecture development still require research to completely unlock their potential and optimize their performance for green hydrogen production.

1.3 Aim and content

Given the global context of electrolysis development, this study concentrates on the development of a high-performance electrolysis cell at intermediate temperatures with protonic ceramic cells with a focus on the selection and qualification of the electrocatalytic material for the steam electrolysis and the development of a planar cell design.

Beyond this brief introduction in chapter 1, this cumulative thesis is structured around another six chapters. The necessary background and fundamentals of PCCs is given in chapter 2. In the chapter 3, the scientific questions addressed in this work together with the relation between the three different publications that compose this thesis is presented. The chapter 4 highlights the approaches used for this work, addressing both the manufacturing and the characterization methods. The three articles are presented in the chapter 5. The results are then discussed in the global research context presented in the introduction (chapter 6), and finally, a conclusion including perspectives for future research and development is given (chapter7).

(Note: References for chapters, excluding chapter 5, are at the end of the thesis, while the articles have their separate references in chapter 5 and the appendices.)

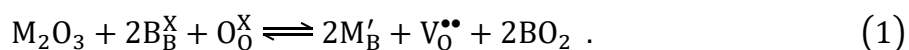
2 Background and fundamentals on protonic ceramic cells

In the previous chapter, the hydrogen production using protonic ceramic cells at intermediate temperatures was briefly introduced. As this technology is still in its early stages of development, the relevant background is presented in terms of the fundamentals of protonic ceramics, the typical materials and components, the different cell configurations, and the characteristics to evaluate energy conversion efficiency. The current state of development and scientific gaps regarding these aspects are presented in the following sections.

2.1 Protonic ceramics

2.1.1 Formation and mobility of proton defects

The proton conducting phenomenon was first speculated to occur in LaAlO_3 by Francis Forrat and co-workers in the 1960s¹⁷. Shortly afterwards, in 1966, Stotz and Wagner proposed the possibility of high temperature hydration by filling oxygen ion vacancies with hydroxyl ions in ceramics¹⁸. Since the 1980s, much of the important and pioneering research on the application of protonic ceramics has been carried out by Iwahara's group in Japan, including fuel cells, electrolysis, hydrogen separation and hydrogenation/dehydrogenation of hydrocarbons applications^{15, 19}. So far, the proton conduction has been confirmed in several types of oxides with different structures, for instance, the simple perovskite $\text{ABO}_{3-\delta}$, double perovskite $\text{A}_2\text{BB}'\text{O}_{6-\delta}$, Ruddlesden-Popper $\text{A}_2\text{BO}_{4+\delta}$, ortho-phosphates APO_4 , brownmillerites $\text{A}_2\text{B}_2\text{O}_5$ etc.¹⁹⁻²⁴. Specifically, Y-doped BaZrO_3 - BaCeO_3 solid solution materials ($\text{BaZr}_{1-x-y}\text{Ce}_x\text{Y}_y\text{O}_{3-\delta}$, BZCY) with the simple perovskite structure are considered as the most promising protonic ceramics^{19, 25-27}. In protonic ceramics, the formation of mobile protons requires the existence of oxygen vacancies ($\text{V}_\text{O}^{\bullet\bullet}$) in the lattice^{28, 29}. For ABO_3 perovskites, oxygen vacancies can be formed by doping M^{3+} on the B-site according to



In a humid gas atmosphere, steam dissociates and incorporates into the lattice via an acid-base hydration reaction^{14, 28, 30}:



Steam dissociates into a proton, which binds to a lattice oxygen, and a hydroxide ion, which fills an oxygen vacancy. This process is exothermic ¹⁴. Accordingly, the equilibrium constant of hydration (K_{Hydrat}) and the proton concentration ($[\text{OH}_0^\bullet]$) can be determined as:

$$K_{\text{Hydrat}} = \frac{[\text{OH}_0^\bullet]^2}{[\text{V}_0^{\bullet\bullet}][\text{O}_0^{\times}]p_{\text{H}_2\text{O}}} , \quad (3)$$

$$[\text{OH}_0^\bullet] = K_{\text{Hydrat}}^{\frac{1}{2}} [\text{V}_0^{\bullet\bullet}]^{\frac{1}{2}} [\text{O}_0^{\times}]^{\frac{1}{2}} p_{\text{H}_2\text{O}}^{\frac{1}{2}} , \quad (4)$$

where $p_{\text{H}_2\text{O}}$ is the partial pressure of steam.

A Grotthuss mechanism as shown in Figure 2.1 is considered as the most efficient proton transport mechanism to ensure its propagation through the oxide ^{14, 31}. The protons hop from one lattice oxygen to an adjacent lattice oxygen by breaking and forming O-H bonds alternatively. The migration energy barrier is typically around 0.5 eV, which is obviously lower than oxygen ion transport (0.8–1 eV) in perovskites ^{14, 32}.

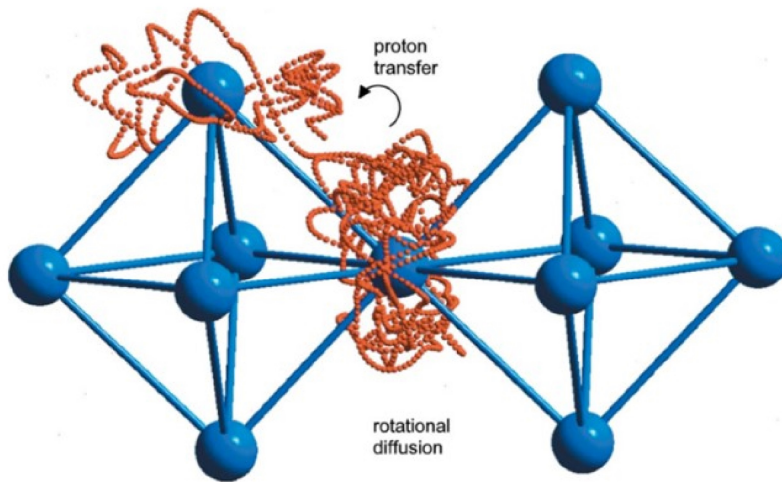


Figure 2.1: Proton transport in a perovskite (the blue sphere represents oxide ions and the red trace represents the trajectory of a proton), adapted from ref. ¹⁴.

2.1.2 Mixed ionic and electronic conductivity in Y-doped $\text{BaZrO}_3\text{-BaCeO}_3$

The formation of protonic defects relies on the presence of oxygen vacancies in the oxides implies such oxides show partial oxygen ion conductivity ³³. Furthermore, in an oxidizing

Background and fundamentals on protonic ceramic cells

atmosphere, p-type conductivity appears due to oxygen incorporation, which generates electron holes in the oxides³⁴,



The reaction equilibrium constant (K_O) and the electron holes concentration ($[h^\bullet]$) can be written as:

$$K_O = \frac{[O_O^x][h^\bullet]^2}{[V_O^{\bullet\bullet}]p_{O_2}^{\frac{1}{2}}}, \quad (6)$$

$$[h^\bullet] = K_O^{\frac{1}{2}}[V_O^{\bullet\bullet}]^{\frac{1}{2}}[O_O^x]^{-\frac{1}{2}}p_{O_2}^{\frac{1}{4}}. \quad (7)$$

where p_{O_2} is the partial pressure of oxygen.

Therefore, in protonic ceramics, the possible charge carriers are protons, oxygen-ions, and electron holes. The transference number of each species is a commonly used parameter for reflecting the transport properties of the oxides and it depends on the material, operating temperature, gas atmosphere, and applied current/voltage. Since the hydration reaction is exothermic, proton defects concentration decreases at elevated temperatures. Conversely, the increased temperature increases both oxygen ionic and electronic (p-type) conduction in humidified oxygen, which is the typical operating condition on the positrode side of a full cell. Generally, PCCs are recommended to operate at around 600 °C or lower temperatures, since the proton transport dominates the overall conductivity in protonic ceramics under wet hydrogen atmospheres within the proposed temperature range^{35,36}. Besides, the electron hole formation through oxygen incorporation competes with the generation of protonic defect via hydration reaction, as both processes consume oxygen vacancies in the lattice. In general, the appreciable p-type conductivity, yielding a low open circuit voltage (OCV) and a low energy conversion efficiency (ECE) of the cell, limits the application of protonic ceramic cells³⁷. The electron hole concentration can be given in terms of p_{H_2O} and p_{O_2} by combining the Equation 4 and Equation 7 as follows:

$$[h^\bullet] = K_{Hydrat}^{-\frac{1}{2}} K_O^{\frac{1}{2}} [OH_O^\bullet] [O_O^x]^{-1} p_{H_2O}^{-\frac{1}{2}} p_{O_2}^{\frac{1}{4}}. \quad (8)$$

Obviously, operating PCCs under high steam concentrations and low oxygen concentrations decreases the electron holes concentration. Apart from the gas atmosphere, the hole concentration is significantly influenced by the applied voltage:

$$[h^{\bullet}] = K_{OX} [OH_0^{\bullet}] P_{H_2O}^{-\frac{1}{2}} P_{O_2}^{\frac{1}{4}} = K_{OX} \exp \left[\frac{F(E - E^0)}{RT} \right], \quad (9)$$

where K_{OX} is water oxidation equilibrium constant and E is the potential³⁸. Therefore, a high potential enhances the electronic leakage.

Hence, electronic conductivity in the protonic ceramic electrolyte and its influence on the electrochemical characteristics of PCCs constituted a main focus of the thesis.

2.2 Protonic ceramic cell components

Protonic ceramic cells (PCCs) by using protonic ceramic membranes as the electrolyte can be operated for electricity generation (protonic ceramic fuel cell, PCFC) and hydrogen production (protonic ceramic electrolysis cell, PCEC), as illustrated in Figure 2.2. The typical cross-section images of PCCs (Figure 2.3) include the dense proton conducting electrolyte (ca. 10 μm), the porous oxygen electrode (positrode, with the thickness of ca. 30 μm), and the fuel electrode (negatrode, with the thickness of ca. 750 μm). The fuel electrode typically acts as the supporting layer, offering the necessary mechanical strength. In the following sections, different components of the full cells are explained and discussed.

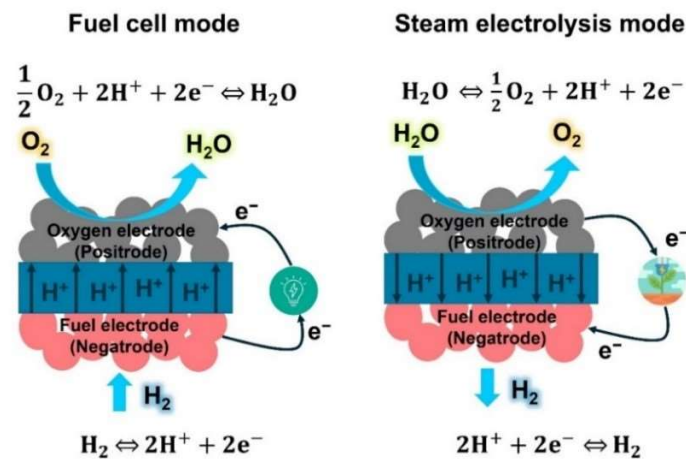


Figure 2.2: Schematic illustration of the protonic ceramic fuel cell (PCFC) and the protonic ceramic electrolysis cell (PCEC) for electricity generation and steam electrolysis.

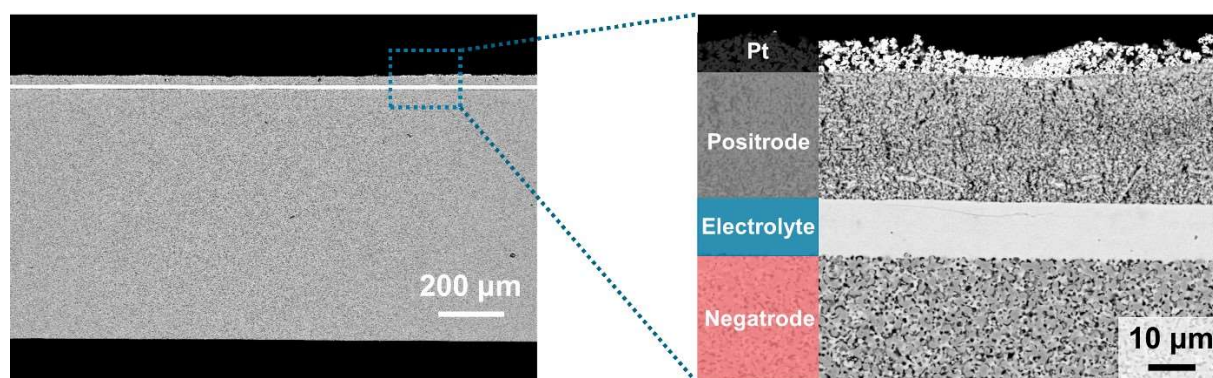


Figure 2.3: SEM cross-section images of the as-fabricated negatrode-supported protonic ceramic cells.

2.2.1 Electrolyte

As illustrated in Figure 2.2, the electrolyte of the PCCs is a dense layer that should possess adequate protonic conductivity and negligible electronic conductivity under the relevant operating conditions. Furthermore, the electrolyte materials require sufficient chemical stability in both oxidizing and reducing atmosphere, while being chemically and physically compatible with the electrode materials³⁹. The state-of-the-art electrolyte materials are derived from the yttrium-doped barium zirconate-cerate solid solution ($\text{BaZr}_{1-x-y}\text{Ce}_x\text{Y}_y\text{O}_{3-\delta}$, BZCY), which is developed based on the BaCeO_3 and BaZrO_3 perovskite materials.

In 1980s–1990s, Iwahara *et al.*^{19, 26, 27} reported that BaCeO_3 and BaZrO_3 based materials exhibit hydration capability and protonic conductivity. The drawbacks of those materials became evident after many studies. The BaCeO_3 based oxides are found to be unstable in humidified and/or CO_2 containing atmospheres, leading to significant performance degradation⁴⁰⁻⁴³. In contrast, BaZrO_3 based oxides exhibit good chemical stability in such atmospheres and high bulk protonic conductivity^{14, 44, 45}. However, the refractory nature of BaZrO_3 -based oxides, requiring densification temperatures above 1550 °C, poses considerable manufacturing challenges⁴⁶. Due to these factors, several sintering aids, for instance CuO , ZnO , and NiO , have been investigated to reduce the sintering temperatures⁴⁷⁻⁴⁹. Nevertheless, the addition of NiO into $\text{BaZr}_{0.8-x}\text{Ce}_x\text{Y}_{0.2}\text{O}_{3-\delta}$ (BZY20) results in a detrimental impact on protonic conductivity. Moreover, the minor secondary phases may appear at grain boundaries and enhance the electron hole conductivity⁵⁰.

Background and fundamentals on protonic ceramic cells

In recent decades, extensive research efforts have been devoted to the exploration and enhancement of BZCY-based oxides, aiming at refining their properties to align seamlessly with the theoretical property requirements of PCCs. As expected, the conductivity and the sinterability of BZCY can be improved with a higher Ce content, while a higher Zr content enhances its chemical stability¹⁹. Han *et al.*⁵¹ systematically studied the influence of Ce content in the $\text{BaZr}_{0.8-x}\text{Ce}_x\text{Y}_{0.2}\text{O}_{3-\delta}$ (BZCY20) on the hydration and transport properties of the materials. The results indicate that increasing the Ce content in BZCY20 leads to a higher dehydration temperature and a higher proton concentration, as well as a lower transport number of electron holes. This ultimately resulted in improved performance when using the BZCY electrolyte with a higher Ce content⁵¹. That is the reason why $\text{BaZr}_{0.1}\text{Ce}_{0.7}\text{Y}_{0.2}\text{O}_{3-\delta}$ (BZCY172) and $\text{BaZr}_{0.1}\text{Ce}_{0.8}\text{Y}_{0.1}\text{O}_{3-\delta}$ (BZCY181) have gained broad usage as the protonic ceramic electrolyte so far⁵²⁻⁵⁵. However, BZCY172 is found to be nearly completely decomposed into CeO_2 and BaCO_3 after 8 h exposure to 10% CO_2 / Ar atmosphere at 600 °C⁵⁶. In moist atmosphere, the BZCY ([Zr] \geq 40 at%) is not observed to react with steam to produce $\text{Ba}(\text{OH})_2$, and it is reported to be stable in a CO_2 rich atmosphere at the expected working temperature range of PCCs⁵⁷. In 2018, An *et al.*⁵⁸ successfully manufactured a PCFC with $\text{BaZr}_{0.3}\text{Ce}_{0.55}\text{Y}_{0.15}\text{O}_{3-\delta}$ as the electrolyte material and achieved a record high power density of 1.3 W cm^{-2} at 600 °C. This pioneering work demonstrates the possibility of manufacturing a planar cell with a size as big as $5 \times 5 \text{ cm}^2$ ⁵⁸. In the following year, a tubular PCC with an active area of 4.7 cm^2 , based on $\text{BaZr}_{0.7}\text{Ce}_{0.2}\text{Y}_{0.1}\text{O}_{3-\delta}$, was reported for high pressure (3 bar) steam electrolysis, exhibiting a remarkable stability over 700 h³⁸.

In addition, the incorporation of B-site doping in BZCY is an additional approach to improve the properties of the electrolyte materials. Liu's group developed the protonic ceramic of nominal composition $\text{BaZr}_{0.1}\text{Ce}_{0.7}\text{Y}_{0.1}\text{Yb}_{0.1}\text{O}_{3-\delta}$ (BZCYYb1711) by co-doping Y and Yb at the B-site⁵⁹. It is shown that BZCYYb1711 exhibits high ionic conductivity at intermediate temperatures, along with enhanced sulfur and coking tolerance. Since then, PCCs using BZCYYb1711 as the electrolyte were investigated in numerous studies. For example, Duan *et al.*⁶⁰ reported the cell with BZCYYb1711 electrolyte showing high performance and stability in fuel cell mode with hydrogen and methane fuel gases. Meanwhile, similar cells were tested for steam electrolysis and exhibited a high hydrogen production rate with high faradaic efficiency⁶¹. Additionally, the BZCYYb1711 phase remains stable under a dry, 100% CO_2 containing atmosphere at 600 °C for 50 h⁶¹. However, the long-term stability of BZCYYb1711

Background and fundamentals on protonic ceramic cells

may pose a challenge in H₂O or CO₂ atmospheric conditions as reported in other studies^{62,63}. These contradictory characteristics necessitate further exploration. Choi *et al.*⁶³ reported that the composition of BaZr_{0.4}Ce_{0.4}Y_{0.1}Yb_{0.1}O_{3- δ} (BZCYYb4411) with a higher Zr content at the B-site exhibits an enhanced CO₂ tolerance. Despite this, the preliminary PCC stack (with an active area of 5 cm²) by using BZCYYb4411 electrolyte shows a degradation rate of 3.3% kh⁻¹ at 0.4 A cm⁻² with a protecting layer at the interface between the electrolyte and the positrode in fuel cell mode¹². In a brief summary, PCCs with the BZCYYb series electrolyte possess high initial electrochemical performances in both fuel cell and steam electrolysis modes; but the relatively poor durability of the cells makes it difficult to match with the industrial application requirements, since high reliability is the most basic requirement. Further experimental and computational analyses are still required to fully understand the relationship between the composition, catalytic activity, and stability of these materials.

Based on these reports and promising results, electrolyte materials with a nominal composition of BaZr_xCe_{0.9-x}Y_{0.1}O_{3- δ} , with $x \geq 0.5$, were chosen and used in the present studies.

2.2.2 Fuel electrode (negatrode)

The fuel electrode, also referred to as the negatrode, is the site of the hydrogen oxidation (in fuel cell mode) and the hydrogen evolution (in steam electrolysis mode) reactions. Consequently, the materials of this electrode should possess high mixed protonic and electronic conductivity and demonstrate sufficient chemical stability under reducing conditions. By analogy with the mature and successful SOCs, the composite fuel electrode, consisting of Ni (which acts as the electronic conducting phase and possesses high catalytic activity towards hydrogen adsorption and hydrogen splitting) and a protonic ceramic phase (usually the electrolyte materials), has been broadly used as the negatrode in PCCs²⁰. The research on negatrode focuses on the optimization of the microstructure by selecting the best Ni/protonic ceramic ratio, particle size distribution, and sintering temperatures in order to maximize the triple phase boundary (TPB) length and achieve higher electrochemical performances⁶⁴⁻⁶⁷.

Since hydrogen is theoretically the only gaseous specie diffusing through the porous negatrode, the electrochemical properties of the cell are not greatly affected by the porosity of the electrode. Coors *et al.*⁶⁸ reported a negatrode without initial porosity, where the porous structure was created by reducing NiO to the metallic Ni, which is a particularly well-suited method for the

commercial fabrication of these electrochemical devices. Electrochemical performance tests demonstrate that the cells fabricated without the pore formers achieve the highest current and peak power densities compared to the cells with a high porosity negatrod⁶⁹. It is important to highlight that the negatrod-supported PCC is the most commonly used design so far; therefore adequate mechanical strength is a crucial aspect for this electrode^{70, 71}.

2.2.3 Oxygen electrode (positrod)

Due to the comparatively lower operating temperatures of PCCs compared to SOCs, the sluggish kinetics of the oxygen reduction reaction (ORR) and the oxygen evolution reaction (OER) make these processes dominating the polarization losses of the full cells^{20, 52}. The rational materials for the oxygen electrode, also known as the positrod, in PCCs should possess excellent electrocatalytic properties towards the OER and the ORR. Consequently, they are expected to demonstrate adequate conductivity for proton, oxygen ion, and electron transport simultaneously. Additionally, the positrod material requires sufficient chemical stability under high steam content atmospheres^{34, 72}.

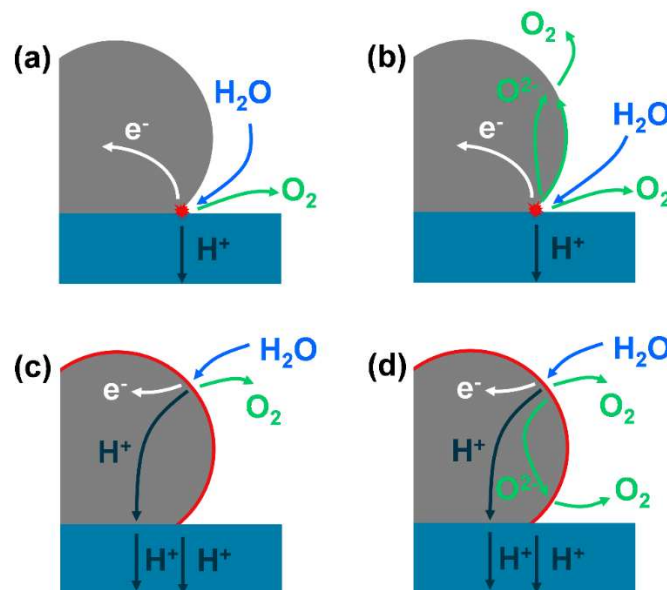


Figure 2.4: Schematic illustration of different positrod materials in PCCs for steam electrolysis operation: (a) electronic conductor, (b) mixed oxygen ionic and electronic conductor, (c) mixed protonic and electronic conductor, and (d) mixed protonic, oxygen ionic and electronic conductor. (Note: the red area represents the activity site for water-splitting process)

Background and fundamentals on protonic ceramic cells

Generally, four kinds of materials have been studied as the positive electrodes in PCCs, as summarized in Figure 2.4. In the early stages of PCC development, electronic conductors such as Pt and Pd were used as positive electrodes¹⁵. With these materials, the electrocatalytic active area (TPB) is confined at the interface between the electrolyte and the positive electrode. Referring to classical positive electrode materials in SOCs, the mixed ionic and electronic conductors (MIECs) have also been investigated in PCCs. Three main families of perovskite-related oxides (Figure 2.5) have been investigated as the potential PCC oxygen electrodes⁷³, namely: i) the cubic-type perovskite oxides, ii) the double perovskite oxides, and iii) the Ruddlesden-Popper phase oxides.

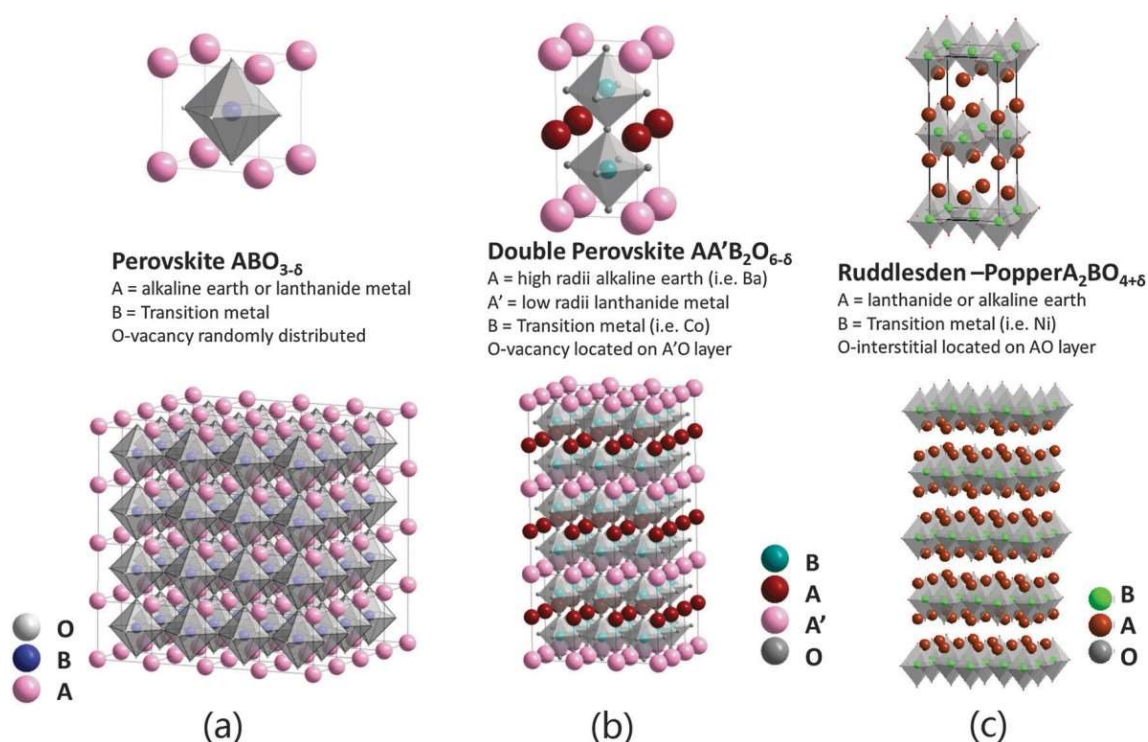


Figure 2.5: Crystal structures of the representative oxygen electrode materials: (a) Simple perovskite structure, (b) double perovskite structure, and (c) Ruddlesden-Popper structure. Adapted from ref.⁷³.

With cubic-type perovskite oxides, such as $Sm_{0.5}Sr_{0.5}CoO_{3-\delta}$ (SSC) and $La_{0.6}Sr_{0.4}Co_{0.2}Fe_{0.8}O_{3-\delta}$ (LSCF)^{74, 75}, the active areas are still limited at the interface between the electrolyte and the positive electrode as depicted in Figure 2.4b. To extend the electroactive area across the entire surface of the porous electrode, a material with sufficient bulk protonic conductivity is required. In principle, the entire electrode surface can serve as the active area by using perovskite oxides with mixed protonic and electronic conductivity (Figure 2.4c).

Background and fundamentals on protonic ceramic cells

In recent years, the concept of triple conducting oxides, as illustrated in Figure 2.4d, has been proposed. For example, $\text{BaCo}_{0.4}\text{Fe}_{0.4}\text{Zr}_{0.1}\text{Y}_{0.1}\text{O}_{6-\delta}$ ^{60, 61}, $\text{PrBa}_{0.5}\text{Sr}_{0.5}\text{Co}_{1.5}\text{Fe}_{0.5}\text{O}_{5+\delta}$ ⁷⁶, and $\text{NdBa}_{0.5}\text{Sr}_{0.5}\text{Co}_{1.5}\text{Fe}_{0.5}\text{O}_{5+\delta}$ ⁷⁷, have been demonstrated as triple conducting materials while showing good electrochemical performance in fuel cell and/or steam electrolysis mode. However, the role regarding the oxygen ion conductivity in the bulk is still under debate. There are two possible oxygen evolution pathways in the positrode: the bulk pathway (oxygen ion transfer through the bulk) and the surface pathway (oxygen species migrate along the surface). The favorable pathway relies on the properties of the materials (i.e., the surface exchange coefficient and the bulk oxygen ion diffusivity), the microstructure of the electrode, and the working conditions. For example, the Ruddlesden-Popper (RP) phase material $\text{Pr}_2\text{NiO}_{4+\delta}$ (PNO) was investigated as a triple conductive positrode in PCEC⁷⁸. Based on the PNO phase, the water-splitting performances of the new RP phase of $\text{Pr}_{2-x}\text{Ba}_x\text{NiO}_{4+\delta}$ (PBNO) by partially doping Ba at the A-site was improved, and the reaction mechanisms were analyzed⁷⁹. They found that the proton conductivity of PBNO is critical for active area extension in the positrode, and the oxygen-ion conductivity is not that significant for the water-splitting reaction; in comparison, the surface oxygen removal is found to be the most rate-limiting process; finally, the more active site combines proton conductivity and oxygen surface desorption capability⁷⁹.

As a protonic and electronic conductor, the double perovskite oxides of $\text{Ba}_{1-x}\text{Gd}_{0.8}\text{La}_{0.2+x}\text{Co}_2\text{O}_{6-\delta}$ (BGLC) have been extensively investigated in PCCs for steam electrolysis and have shown high performance and stability^{38, 80-82}. Most of the reported PCCs using BGLC as the positrode were in tubular cells, resulting in relatively low current density. Besides, perovskite oxides with Co on the B-site typically exhibit a high thermal expansion coefficient (TEC) compared to the protonic ceramic electrolyte ($8-11.2 \times 10^{-6} \text{ K}^{-1}$)⁸³, for example, LSCF ($15.3 \times 10^{-6} \text{ K}^{-1}$)⁸⁴, BGLC ($20 \times 10^{-6} \text{ K}^{-1}$)⁸⁵. The TEC mismatch between the electrolyte and the positrode is a challenge for the cell manufacturing. The most effective approach to mitigate this challenge is using composite electrodes by mixing the positrode materials and the electrolyte materials. In the present study, BGLC-based materials were investigated as positrodes in planar PPCs operating at high current densities for hydrogen production at intermediate temperatures.

2.3 Architectures of protonic ceramic cells

The protonic ceramic cells have two main geometries: the planar structure (Figure 2.6a) and the

Background and fundamentals on protonic ceramic cells

tubular structure (Figure 2.6b). For each type of cell, the thickest layer, known as the supporting layer, not only impacts the mechanical strength, but also plays a crucial role in determining the manufacturing process, the suitable operating window, and the electrochemical performance of the cell. In the planar cells, three types of configurations exist: the electrolyte-supported, the negatode-supported, and the metal-supported design (Figure 2.7).

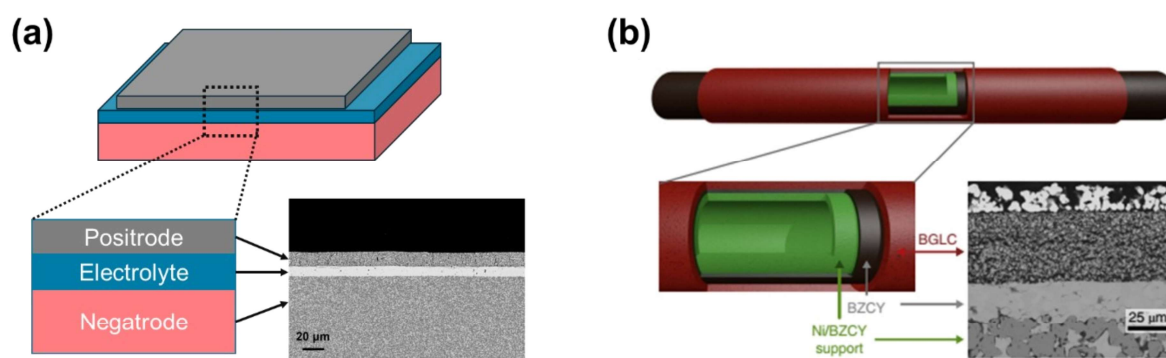


Figure 2.6: Schematic illustration of different geometries: (a) the planar cell and (b) tubular cell, adapted from ref. ³⁸.

Most mature SOC technologies use a planar cell geometry, which is currently being scaled up into systems in the multi-MW range. One can cite for instance, Bloom energy ⁸⁶, Sunfire ⁸⁷, Ceres Power ⁸⁸, and Elcogen ⁸⁹. In comparison, PCC is still at a very early stage of development. The first PCC stacks were successfully manufactured with the tubular geometry by Coors Tek Membrane Sciences AS and their partners ^{38,90,91}. The tubular cell architecture allows for easier sealing and operation under pressure. A 36-cell tubular PCC stack was operated as a hydrogen pump to produce hydrogen from NH₃, CH₄, and biogas at pressures exceeding 140 bar ⁹¹, which extremely facilitates storage of the produced hydrogen in pressure tanks of 350–700 bar ⁹². High added value chemicals, such as different aromatics, can be synthesized using this tubular PCC ⁹⁰. The tubular PCC has been demonstrated to operate in steam electrolysis mode at a total pressure of 3 bar ³⁸. On the other hand, the results revealed that the ohmic resistance of ca. 3 Ω cm² is nearly three times higher than the polarization resistance, which is less than 1 Ω cm² at 600 °C ³⁸. The high ohmic resistance is responsible for a lower energy density, potentially hindering the application of this technology.

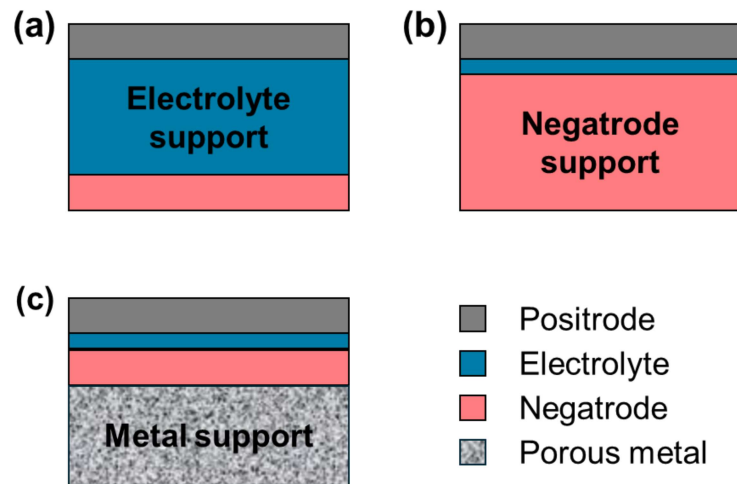


Figure 2.7: Schematic illustration of different PCCs: (a) electrolyte supported cell, (b) negatrode supported cell, and (c) metal supported cell.

Recently, several studies have shown the feasibility of producing large planar PCCs. For example, the $5 \times 5 \text{ cm}^2$ protonic ceramic cells were reported in fuel cell operation with a unit cell power of 20.8 W at $600 \text{ }^\circ\text{C}$ ⁵⁸. A PCC stack with three repeat units (each with an active area of ca. 5 cm^2) was demonstrated in fuel cell operation, and a single repeat unit was operated in steam electrolysis mode^{12,16}. The production of planar cells can be straightforward and feasible by combining different mature coating techniques, such as tape-casting, screen-printing, and co-sintering.

In terms of the cell configurations, the early demonstration of the protonic ceramic fuel cell and electrolysis concept was carried out using electrolyte supported PCCs (ES-PCCs). However, ES-PCCs usually possess a thick ($\geq 800 \text{ }\mu\text{m}$) layer of electrolyte, resulting in a high ohmic resistance. Furthermore, the refractory properties of the typical protonic ceramics pose challenges for scaling up ES-PCCs.

In the negatrode supported PCCs (NS-PCCs) design, a thick ($500\text{--}800 \text{ }\mu\text{m}$) negatrode works as the mechanical sustaining unit. Consequently, the electrolyte can be a thin-film layer of $5\text{--}10 \text{ }\mu\text{m}$ and the oxygen electrode only about $20 \text{ }\mu\text{m}$ thick^{70,93}. The configuration results in a significant reduction in ohmic losses, with the main losses attributed to the electrodes, particularly the oxygen electrode. To date, nearly all PCC-related research is based on the NS-PCC. A full functional NS-PCC consists of ca. 60 wt% of ceramic materials, which includes many critical raw elements (e.g., Ba, Y, Yb, La) and ca. 40 wt% of NiO. For manufacturing

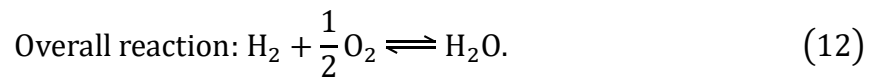
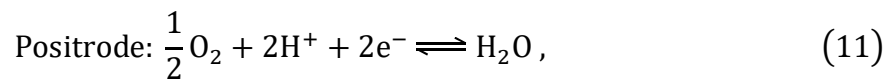
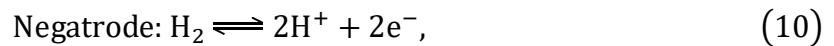
Background and fundamentals on protonic ceramic cells

megawatt PCC systems, the demand for these critical raw materials will significantly grow. A solution to this issue is to partially replace the fuel electrode support layer with inexpensive stainless-steel, thereby introducing the concept of metal supported cells (MSCs)⁹⁴. Additionally, the MSC design enables higher tolerance for both thermal and redox cycling.

2.4 Fundamentals of protonic ceramic cells

2.4.1 Fuel cell operation

The operating principle of the PCFCs with H₂ fuel gas is illustrated in Figure 2.2. The full cells consist of three main components: the porous positrode, the gas-tight protonic ceramic electrolyte, and the porous negatrode. At the negatrode, hydrogen is oxidized to H⁺, which is transported through the proton conducting electrolyte to the positrode side, where it reacts with oxygen to form steam. The two electrochemical reactions in the positrode and the negatrode, as well as the overall reaction, can be expressed as follows:



2.4.2 Steam electrolysis operation

Typically, high-temperature ceramic cells can be operated reversibly in both electrolysis mode and fuel cell mode using the same cell. As illustrated in Figure 2.2, steam is supplied to the positrode side and split on this side into protons and oxygen ions. Protons are transported across the protonic ceramic membrane and reduced to hydrogen on the negatrode side. The oxygen evolution reaction occurs on the positrode side and produces the oxygen as a by-product. The overall electrochemical reaction is as follows:



Steam electrolysis is a highly energy demanding process and equals to the molar enthalpy

change (ΔH) of the reaction (Equation 14), which can be expressed as:

$$\Delta H = \Delta G + T\Delta S , \quad (14)$$

where ΔG is the reaction Gibbs free energy change, ΔS is the reaction entropy and the operating temperature T . As illustrated in Figure 2.8, ΔG represents the electrical energy demand, and $T\Delta S$ corresponds to the heat demand as a function of temperature. As temperature increases, electricity demand decreases while heat demand increases. When the cell operates at thermoneutral voltage (V_{TN}), the entire energy demand is fulfilled by the electricity energy in adiabatic conditions⁹⁵. The V_{TN} can be defined as:

$$V_{TN} = \frac{\Delta H(T)}{zF} , \quad (15)$$

where z is 2 for the reaction (Equation 13) and F is the Faraday constant of 96485 C mol^{-1} . For example, under the typical working temperature of $600 \text{ }^\circ\text{C}$ and atmospheric conditions for PCCs, the enthalpy change of the water splitting reaction is 247 kJ mol^{-1} , and the thermoneutral voltage is 1.28 V .

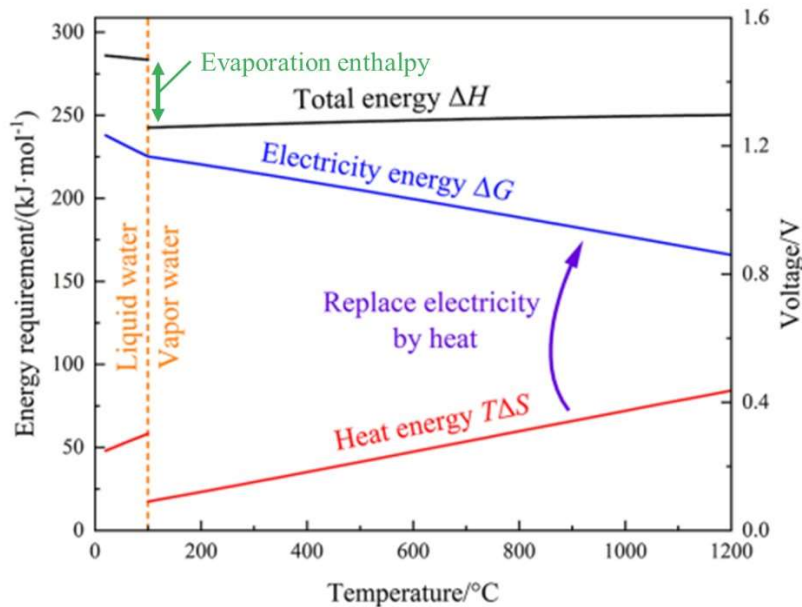


Figure 2.8: Thermodynamic properties of water electrolysis at different temperatures and atmospheric pressure. Reprinted and adapted from ref.⁹⁶.

Additionally, the Nernst potential or reversible cell voltage, which represents the minimum

Background and fundamentals on protonic ceramic cells

voltage required for the process to occur, can be defined as follows ⁹⁷:

$$V_{rev} = V_{rec}^0 + \frac{RT}{zF} \ln \left(\frac{p_{H_2} p_{O_2}^{1/2}}{p_{H_2O}} \right), \quad (16)$$

$$V_{rec}^0 = \frac{\Delta G^0}{zF}, \quad (17)$$

where V_{rec}^0 is the reversible voltage at standard conditions, p_i is the partial pressure of the corresponding component i .

2.4.3 Energy losses in electrolysis

The electrochemical performance of electrolysis cells is directly reflected by the polarization curves (I - V curves). The Figure 2.9 shows a typical I - V curve for high-temperature electrolysis. The voltage and the current density values are generally not linearly correlated due to various loss processes. The voltage (V_{cell}) applied to an electrolyser is typically higher than the reversible voltage to drive the electrolysis process ⁹⁷:

$$V_{cell} = V_{rev} + \eta_{act} + \eta_{ohm} + \eta_{con}, \quad (18)$$

where η_{act} is the activation overpotential, η_{ohm} is the ohmic overpotential, and η_{con} is the concentration overpotential. The activation overpotential originates from the reaction kinetics on both electrodes. It is influenced by the properties of the materials, such as the electrocatalytic activity and the electrode structure. The Butler-Volmer equation is used to determine the relationship between the activation overpotential and the current density (I) as follows ^{95, 98}:

$$I = I_0 \left[\exp \left(\frac{\alpha z F \eta_{act}}{RT} \right) - \exp \left(\frac{-(1 - \alpha) z F \eta_{act}}{RT} \right) \right], \quad (19)$$

where I_0 is the exchange current density, α is the apparent charge transfer coefficient. In electrochemistry, I_0 represents the activity of the electrode towards an electrochemical reaction and can be written as,

$$I_0 = k \exp \left(\frac{-E_a}{RT} \right), \quad (20)$$

where k represents the pre-exponential factor and E_a is the activation energy barrier. Therefore, a lower activation energy barrier and/or a higher working temperature result in a higher I_0 , indicating that a lower activation overpotential is sufficient to achieve a specified electrolysis current density (Equation 19).

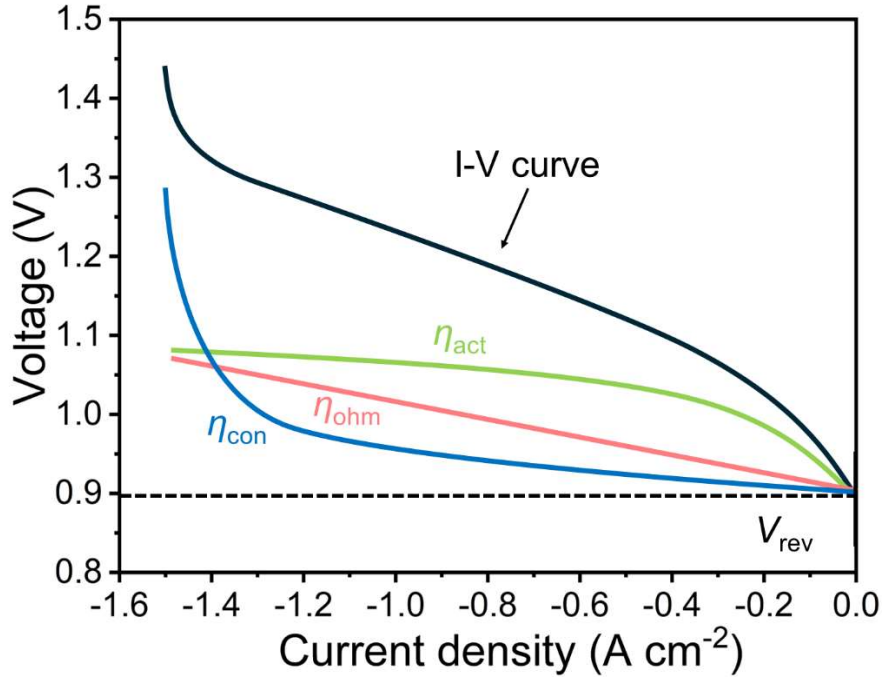


Figure 2.9: Typical polarization curve for steam electrolysis in high temperature ceramic cells.

The ohmic overpotential can be described based on Ohm's law ⁹⁷,

$$\eta_{ohm} = IR_{ohmic} = I(R_{elec} + R_{ionic} + R_{contact}) , \quad (21)$$

where R_{ohmic} represents the overall ohmic resistance resulting from the ionic (R_{ionic}) and electronic (R_{elec}) transport through all the components of the cells. In high temperature ceramic cells, the ohmic resistance is primarily governed by the ionic conductivity of the ceramic electrolyte. Additionally, for precise calculations, it is necessary to consider the contact resistance ($R_{contact}$) as well.

In terms of concentration overpotential, the diffusion of reactants and products is limited in the porous electrode. Additionally, the concentration of gases at the active sites differs between the inlet and outlet during reaction evolution. Moreover, an increased electrode thickness and a reduced porosity typically yields a high concentration overpotential. Larminie *et al.* ⁹⁹

Background and fundamentals on protonic ceramic cells

demonstrate the relationship between the η_{con} and the limiting current density (I_L), which is determined by the inlet gas flow rates and the structure of the electrodes, as follows^{98, 100}:

$$\eta_{con} = -\frac{RT}{2F} \ln \left(1 - \frac{I}{I_L} \right) . \quad (22)$$

In summary, the different overpotential contributions are responsible for the voltage increase at a given electrolysis current, which accounts for the additional electrical energy consumption for hydrogen production. Therefore, various studies have been carried out to develop new materials with higher conductivity, design new cell structures, and optimize the electrode microstructures in order to minimize the energy losses and thus increase the energy conversion efficiency (η_{ECE}).

2.4.4 Current leakage and energy efficiency in electrolysis

In cell-level analysis, the energy conversion efficiency can be defined as the ratio of the energy stored in the hydrogen (energy_{output}) to the electricity consumed (energy_{input}), as follows:

$$\eta_{ECE} = \frac{\text{energy}_{output}}{\text{energy}_{input}} = \frac{LHV_{H_2} \times n_{H_2,measured}}{V \times I} , \quad (23)$$

where LHV_{H_2} is the lower heating value of hydrogen (241.8 kJ mol⁻¹ or 33.33 kW h kg⁻¹), $n_{H_2,measured}$ is the measured hydrogen production rate, V is the cell voltage, and I is the current.

The faradaic efficiency (η_{FE}) is defined as the ratio of the measured hydrogen production to the theoretical hydrogen production at a given current, as follows:

$$\eta_{FE} = \frac{n_{H_2,measured}}{n_{H_2,theoretical}} = \frac{n_{H_2,measured}}{I \times (z \times F)^{-1}} . \quad (24)$$

In the ideal case, $\eta_{FE} = 1$. However, the current measured in PCCs during steam electrolysis is not completely utilized for hydrogen production, as illustrated in Figure 2.10a. The reaction of $\text{Null} \leftrightarrow \text{h}^\bullet + \text{e}^-$ (step 5) consumes electricity because of the p-type electronic conduction in the protonic ceramic membrane and leads to a decrease in energy efficiency. Figure 2.10b depicts the typical impact of this current leakage on the polarization curve. At a given voltage, the applied current (total current) is obviously higher than the effective electrolysis current,

which refers to the current utilized for hydrogen production.

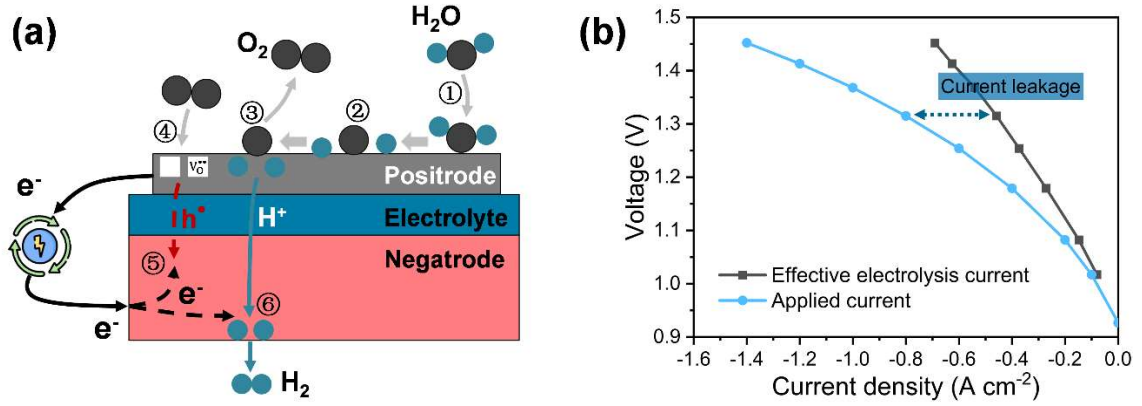


Figure 2.10: (a) Illustration of the reaction mechanism for steam electrolysis in PCCs; (b) A example of the I - V curve for steam electrolysis in PCCs. Adapted from Article II.

Therefore, the energy conversion efficiency (Equation 23) can be extended for PCEC as follows:

$$\eta_{ECE,1} = \frac{LHV_{H_2} \times \eta_{FE}}{z \times F \times V} \quad (25)$$

For high temperature electrolysis, the current density at V_{TN} is typically used as a key figure of merit for evaluating the electrochemical performance of the studied electrolysers. A high current density at V_{TN} demonstrates low overpotential and a higher hydrogen production rate. When the PCC is operated at V_{TN} or at a cell voltage higher than V_{TN} , the process is isothermal or exothermic, and therefore no additional thermal energy is required to maintain the operating temperature. Conversely, when the cell is operated at a voltage lower than V_{TN} , the process becomes endothermic. As a result, an external heat supply is required to maintain the working temperature of the cell. The additional heat supply could be compensated by integrating a suitable system with industrial waste heat. If the additional heat supply is not for free, then this part of energy should be accounted into the $energy_{input}$, which is defined as:

$$energy_{heat\ demand} = (V_{TN} - V) \times I \times \eta_{FE} \quad (26)$$

Consequently, the expression for energy conversion efficiency can be modified as:

$$\eta_{ECE,2} = \frac{LHV_{H_2} \times n_{H_2,measured}}{V \times I + energy_{heat\ demand}} = \frac{LHV_{H_2} \times \eta_{FE}}{z \times F \times V + (V_{TN} - V) \times \eta_{FE}} \quad (27)$$

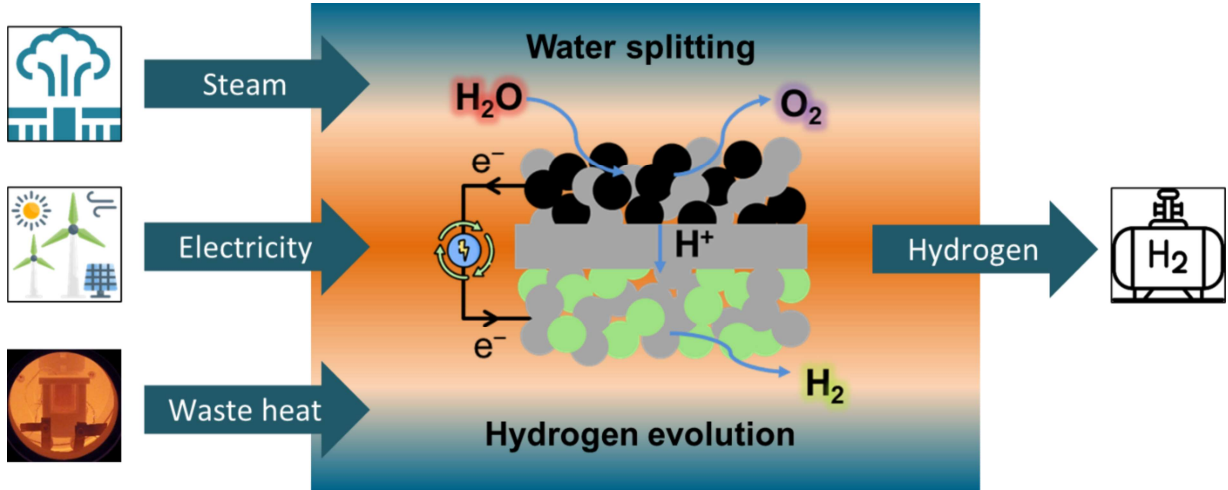


Figure 2.11: Illustration of energy conversion in PCCs for steam electrolysis operation with different external energy supplies, adapted from Article II.

Furthermore, the water evaporation process is also an energy consuming process, unless steam from other industrial sources is integrated into the system. This part of energy demand can be considered as:

$$energy_{\text{water vaporization}} = \frac{\lambda_{\text{H}_2\text{O}} \times I \times \eta_{\text{FE}}}{z \times F \times X_{\text{H}_2\text{O}}} , \quad (28)$$

where $\lambda_{\text{H}_2\text{O}}$ is the latent heat of vaporization and $X_{\text{H}_2\text{O}}$ is the water conversion rate. By adding this part of energy supply into the system, the energy conversion efficiency can be adjusted as follows:

$$\begin{aligned} \eta_{\text{ECE},3} &= \frac{LHV_{\text{H}_2} \times n_{\text{H}_2,\text{measured}}}{V \times I + energy_{\text{heat demand}} + energy_{\text{water vaporization}}} \\ &= \frac{LHV_{\text{H}_2} \times \eta_{\text{FE}}}{z \times F \times V + (V_{\text{TN}} - V) \times \eta_{\text{FE}} + \frac{\lambda_{\text{H}_2\text{O}} \times \eta_{\text{FE}}}{z \times F \times X_{\text{H}_2\text{O}}}} . \end{aligned} \quad (29)$$

The introduction in Chapter 1 highlights that state-of-the-art high-temperature electrolysis based on SOCs typically achieves an η_{FE} close to 100%. However, PCCs face issues with current leakage, which results in lower energy efficiency compared to SOCs.

3 Motivation and interrelation between the studies/articles

Given the background and fundamentals of PCCs, this work addresses key issues related to the development of high-performance planar cells with a focus on investigating and qualifying positrode materials at relevant operating conditions (high current density and high steam content atmosphere), and the investigation of planar protonic ceramic cells for hydrogen production at intermediate temperatures. This cumulative doctoral dissertation is structured around three publications, starting from the positrode materials, mechanism investigation and understanding of the water splitting reaction on the positrode, then focusing on the durability aspects of the materials as well as energy efficiency aspects in steam electrolysis mode, and finally the development and investigation of a new planar cell concept of metal-supported protonic ceramic cell. The alignment of these three articles with the overall objective of this work, as well as their interrelation and complementarity, is illustrated in Figure 3.1.

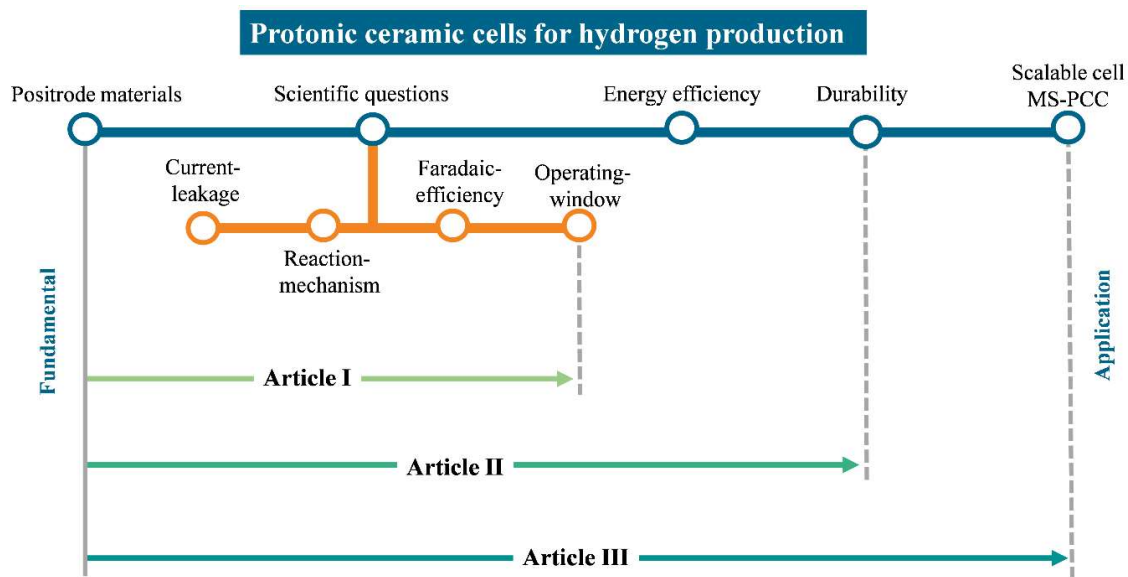


Figure 3.1: Outline of the interrelation of the articles.

With respect to the fundamentals and the background described, the key features of the three articles are detailed below.

Article I: A double perovskite oxygen electrode in Zr-rich proton conducting ceramic cells for efficient electricity generation and hydrogen production

Double perovskite material $\text{Ba}_{0.5}\text{Gd}_{0.8}\text{La}_{0.7}\text{Co}_2\text{O}_{6-\delta}$ (BGLC587) was investigated in lab-made

Motivation and interrelation between the studies/articles

planar NS-PCCs for both fuel cell and steam electrolysis operation. Electrochemical impedance spectroscopy (EIS), combined with the distribution of relaxation times (DRT) analysis and the equivalent circuit model (ECM) analysis, was used to investigate the exact influence of non-faradaic current on the behavior of planar PCCs. A specific ECM was developed to model the electronic conduction, enabling to extract parameters, such as electronic transference number, ionic resistance, and electronic resistance to figure out the certain number of this non-faradaic current under different operating conditions. In the meantime, a more complex ECM was proposed to study the reaction mechanisms of the water splitting process in the positrode in order to identify the rate-limiting process. This provides meaningful information for optimizing the materials and the electrode structure in order to further improve the electrochemical performance. Finally, the durability of PCCs with BGLC587-based positrode was investigated in both fuel cell and steam electrolysis modes for several hundred hours.

Article II: Hydrogen production at intermediate temperatures with proton conducting ceramic cells: Electrocatalytic activity, durability and energy efficiency

In this article, PCCs with BGLC1082-based positrode were further investigated for hydrogen production with a focus on durability and energy efficiency. Although the claim that PCCs exhibit higher performance than SOCs at intermediate temperatures has been frequently mentioned in previous publications, there has been a lack of direct evidence to support this viewpoint. Therefore, the results were compared with state-of-the-art SOCs in an attempt to position the PCCs in terms of performance. This article provides a thorough analysis of important parameters such as current density, activation energy, hydrogen production rate, energy consumption, and durability for the two technologies.

Article III: Hydrogen production with a protonic ceramic membrane reactor on porous Fe-Cr alloy

The high sintering temperature needed for protonic ceramic cells results in considerable manufacturing costs for large-scale cell production. Furthermore, this high sintering temperature is likely to cause failures in the cells, such as the formation of cracks and delamination across the various functional layers. For this reason, metal-supported protonic ceramic cells have been proposed and fabricated via a low temperature route (less than 1000 °C),

Motivation and interrelation between the studies/articles

combining wet ceramic processes with thin-film deposition techniques. The functionality of the MS-PCC full cell was demonstrated for steam electrolysis using the BGLC positrode developed in Article I and II.

4 Experimental methodologies

This chapter describes the overall experimental approaches and the methods employed in the work. It covers material synthesis, cell manufacturing, the development of the test platform, and the different characterization techniques used.

4.1 Materials preparation

The EDTA-citrate complexing sol-gel method was used for the synthesis of $\text{Ba}_{0.5}\text{Gd}_{0.8}\text{La}_{0.7}\text{Co}_2\text{O}_{6-\delta}$ (BGLC587) in a small amount in order to study the properties of this material. The processing details are described in Article I. The other materials, $\text{BaGd}_{0.8}\text{La}_{0.2}\text{Co}_2\text{O}_{6-\delta}$ (BGLC1082), $\text{Ba}_{0.5}\text{La}_{0.5}\text{CoO}_{3-\delta}$ (BLC), $\text{BaZr}_{0.7}\text{Ce}_{0.2}\text{Y}_{0.1}\text{O}_{3-\delta}$ (BZCY721), $\text{BaZr}_{0.5}\text{Ce}_{0.4}\text{Y}_{0.1}\text{O}_{3-\delta}$ (BZCY541), and NiO were purchased from Marion Technologies (France), and $(\text{La}_{0.8}\text{Sr}_{0.2})_{0.95}\text{MnO}_{3-\delta}$ (LSM) was purchased from fuelcellmaterials (US) in larger amounts (typically about 1 or 2 kg batches). These commercial materials were used to guarantee the reproducibility of the as-fabricated cells and, subsequently, for credible electrochemical investigation in Article I, II, and III. Porous ferritic stainless steel ITM from Plansee GmbH (Austria) was used as the substrate in Article III for the development of the MS-PCC.

4.2 Cells manufacturing

Two types of PCCs have been fabricated during the research on this topic: negatrode-supported PCCs and metal-supported PCCs. In this part, the rationale behind the selection of the experimental methods is explained, and the experimental parameters are detailed in the respective articles.

4.2.1 Different processing methods

Different processing methods (Figure 4.1) were considered for preparing the different functional layers in PCCs, based on the targeted physical and microstructural characteristics of each layer.

The dry-pressing method (Figure 4.1a) is a basic approach for making ceramic samples. The powder mixture is filled into a pellet die with a specified diameter to produce green ceramic bodies. This technique was used to manufacture 20 mm diameter NiO-BZCY541 negatrode

supporting layers, and BZCY721 targets for pulsed laser deposition (PLD).

The tape-casting method is a scalable method for producing ceramic films with a thickness ranging from ca. 10 μm to ca. 500 μm with a large area. This is possible by controlling the height of a doctor blade (Figure 4.1b). In this work, tape-casting has been used to produce different functional layers for the development of the MS-PCC samples.

The drop-coating method (Figure 4.1c) is a rudimentary way for thin-film coating used in various research fields. It was used to produce a thin-film electrolyte on the negatrod supported cells. Details of the electrolyte ceramic suspension preparation were described in Article I and II. The thickness of the coating layer can be controlled by adjusting the suspension concentration and the drop volume. Subsequently, a gas-tight electrolyte with high density was formed by sintering the coated layer at high temperatures.

The screen-printing method was used for the porous positrod preparation with an automatic screen-printing device (Figure 4.1d). The viscosity of the printing inks and the characteristics of the screens or meshes are crucial factors that determine the coating thickness and homogeneity.

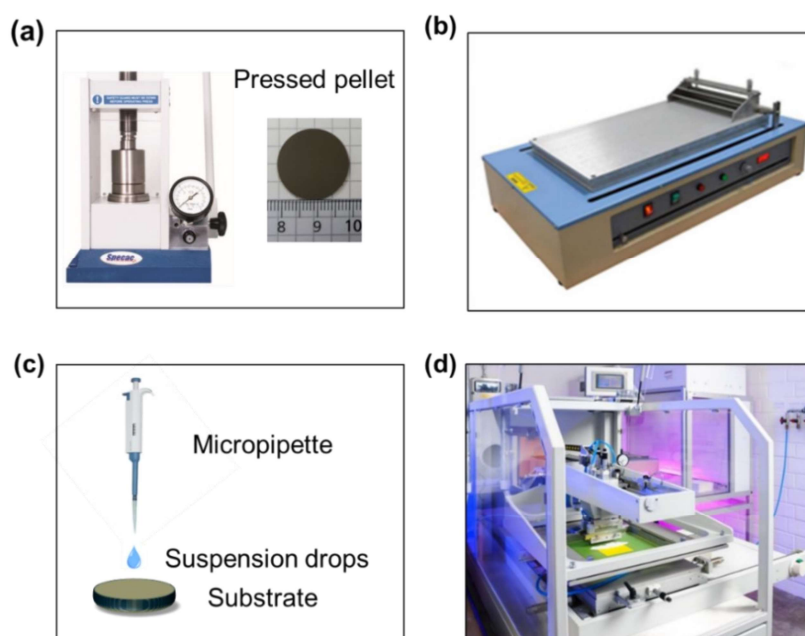


Figure 4.1: Images of different processing methods for preparing different functional layers in PCCs. (a) dry-pressing (Article I, II, III), (b) tape-casting (Article III), (c) drop-coating (Article I, II) and (d) Screen-printing (Article I, II, III).

Experimental methodologies

The preparation of green ceramic samples is typically followed by a sintering step to create the functional microstructure. Since different layers are designed for various functions, it is of great importance to choose an appropriate sintering temperature and dwell time. In this thesis, different types of furnaces were used for the sintering step, covering a broad range of temperatures between 700 °C and 1500 °C.

4.2.2 Negatrode-supported protonic ceramic cells fabrication

Negatrode-supported protonic ceramic cells (NS-PCCs) were fabricated for electrochemical investigation in Article I and II. The process flow for producing the NS-PCC is concisely outlined in Figure 4.2.

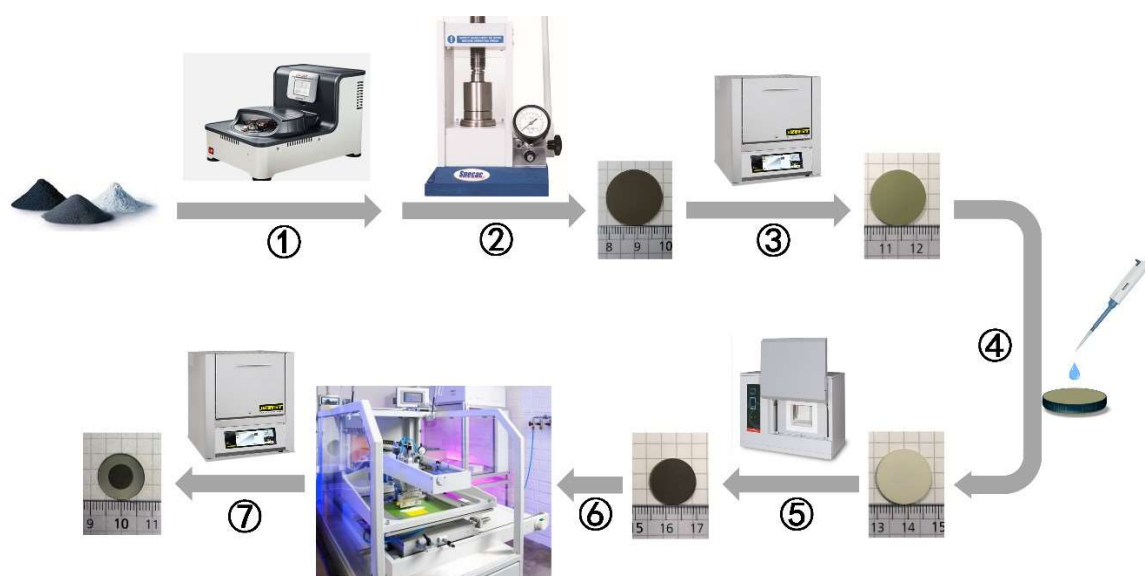


Figure 4.2: The flow chart of the manufacturing process for negatrode-supported protonic ceramic cells.

The NiO and BZCY541 powders from Marion Technologies were used. As the first step (step 1 in Figure 4.2), a well-mixed substrate powder was prepared by planetary ball-milling. The powder mixture was then pressed at a uniaxial pressure of 60 MPa to obtain a green-pellet as the substrate (step 2 in Figure 4.2). The pressed pellet was pre-sintered at 1150 °C for 2 h in air (step 3 in Figure 4.2) to increase the mechanical strength of the substrate for the following processes. The drop-coating approach was employed to produce the dense electrolyte layer on the substrate (step 4 in Figure 4.2). 200 μ L of the electrolyte suspension was dropped onto the NiO-BZCY541 substrate. After drying at 60 °C, the green half-cell was co-sintered at 1450 °C

for 5 h (step 5 in Figure 4.1). The fabricated half cells served as the model substrate for studying the electrocatalytic activity of different positrode materials. All the positrode were produced by screen-printing (step 6 in Figure 4.2). The corresponding positrode slurry was screen-printed onto the BZCY electrolyte surface and sintered at 900–1000 °C for 2 h (step 7 in Figure 4.2). The complete cells for electrochemical measurements have since been obtained. To ensure sufficient current connection, Pt paste (Heraeus GmbH, Germany) was brush-painted onto the surface of the oxygen electrode and sintered at 700 °C. The prepared cell has an active area of 0.5 cm².

4.2.3 Metal-supported protonic ceramic cells fabrication

The new concept of metal-supported protonic ceramic cell (MS-PCC) was successfully developed and demonstrated for steam electrolysis in Article III.

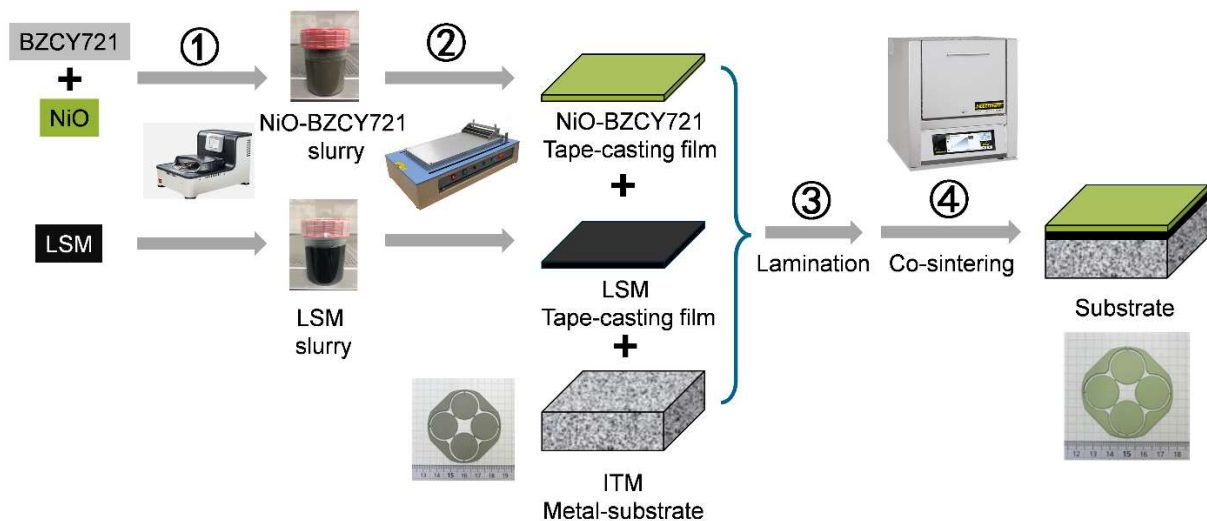


Figure 4.3: Process flowchart of MS-PCC substrates preparation with different functional layers for pulsed laser deposition.

Figure 4.3 illustrates the procedures for manufacturing MS-PCC half cells. The porous stainless ferritic steel was used as the supporting layer. The LSM diffusion barrier layer and the NiO-BZCY fuel electrode sheet were prepared by thin-film tape-casting. The tape-casting slurry was mixed using the planetary ball-milling device (step 1 in Figure 4.3). The slurry was then cast with a doctor blade into a green tape with a thickness of 10–20 μm (step 2 in Figure 4.3). The green tapes of LSM and NiO-BZCY were sequentially laminated onto the ITM substrate (step 3 in Figure 4.3), and the assembly was fired at 950 °C (step 4 in Figure 4.3).

Experimental methodologies

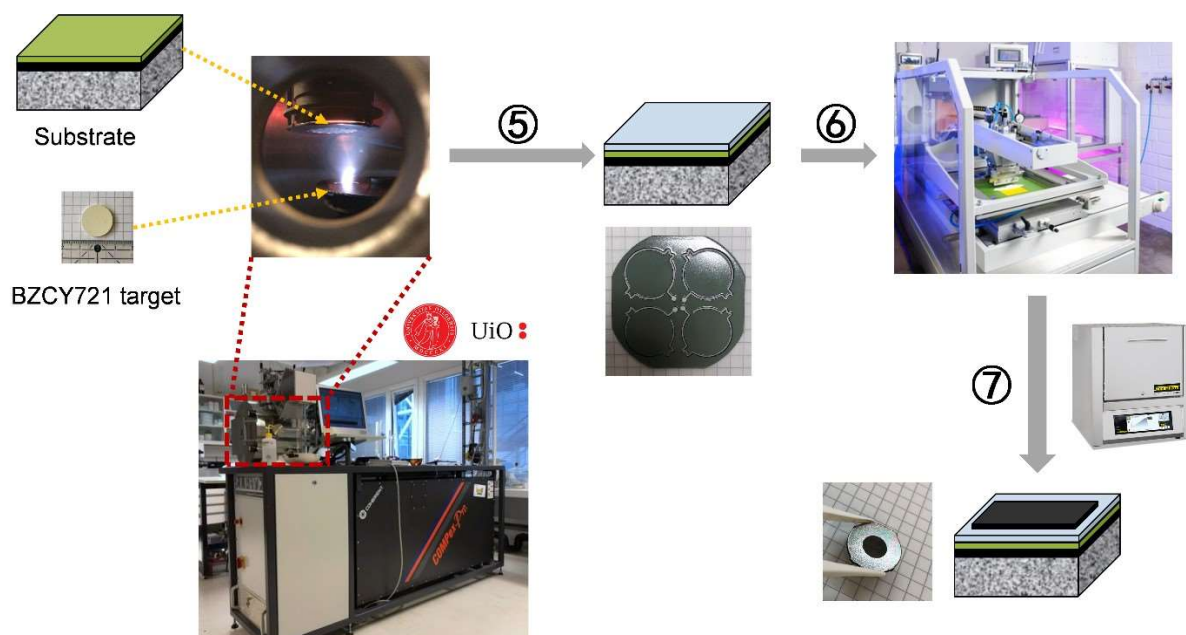


Figure 4.4: The process flowchart for the fabrication of thin-film electrolytes and porous oxygen electrodes by pulsed laser deposition (PLD) and screen-printing, respectively. (Note: The pulsed laser deposition process was carried out at University of Oslo)

Pulsed laser deposition (PLD) was used as the key method for a thin-film electrolyte deposition (step 5 in Figure 4.4). The experimental setup has been described in detail in previous work¹⁰¹. The positrode (Pt or BGLC-BZCY541) was screen-printed onto the thin-film BZCY electrolyte with the same procedure as described in the previous section (step 6 in Figure 4.4), but with a decreased sintering temperature of 700 °C (step 7 in Figure 4.4).

4.3 Characterization techniques

Various characterization techniques were used to evaluate the properties and the performance of the different samples that were produced.

4.3.1 X-ray diffraction

X-ray diffraction (XRD) analysis was used to identify the crystalline phases in powder samples and the fabricated cells by using a Bruker D8 Discover (Bruker AXS GmbH, Germany) with a $\text{CuK}\alpha$ X-ray source and equipped with a VANTEC-2000 area detector. To determine the optimal calcination temperature for BGLC587, XRD was used to analyze the crystallization of the calcined samples at various temperatures. Additionally, the chemical compatibility of the

composite oxygen electrode was investigated using XRD as well.

4.3.2 Dilatometric measurement

This measurement was frequently used to quantify the thermal expansion characteristics of the ceramic materials. Dilatometric measurements were performed using a DIL 402 C device (Netzsch, Germany) in the temperature range of 20 °C to 1200 °C, with a heating rate of 3 °C min⁻¹ in ambient air. A dense ceramic rod was prepared by isostatic pressing the powder in a latex tube at 460 MPa, followed by sintering at 1200 °C for 10 h. The relative density of the sintered specimen was higher than 95%.

4.3.3 Scanning electron microscopy

Scanning electron microscope (SEM) was used to observe the morphology of different samples, for example the ceramic powders, the surface of the sintered electrolyte, and the cross-sections of different PCCs. Furthermore, post-mortem analysis of the tested PCCs in steam electrolysis operation was carried out with an energy-dispersive X-ray (EDX) spectroscopy detector for analyzing elements distribution in components of the cells. For this purpose, a Zeiss Crossbeam 350 SEM (Car Zeiss AG, Germany) equipped with an Oxford ULTIM MAX 100 mm² EDX detector was used.

4.3.4 Laser scanning microscopy

For MS-PCCs development, the significant challenge lies in depositing a thin-film, gas-tight electrolyte using PLD on a substrate with a porous surface. A 3D laser scanning microscope (VK-X3000 series, Keyence) was used to quantitatively investigate the quality of the surface of different substrates with various functional layers. The parameters of arithmetic mean surface roughness (Ra) and ten-point mean roughness (Rz) were used for evaluation of the surface characteristics.

4.4 Electrochemical tests

4.4.1 Electrochemical test system installation

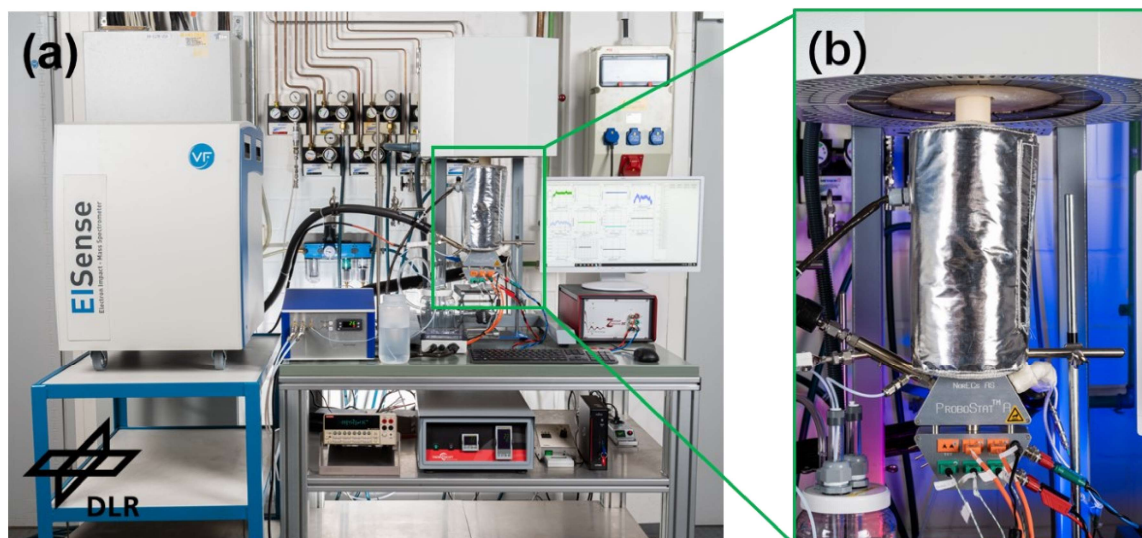


Figure 4.5: The installed electrochemical test system at DLR, TT-ECE.

During the preparation of this thesis, a new test system was installed for the electrochemical investigations, as shown in Figure 4.5. The system consists of two main parts: namely, the ProboStat system and the mass spectrometry. The ProboStat base unit was purchased from NORECS AS (Norway) with the base unit heating system for steam electrolysis operation (Figure 4.5b). One gas channel to the ProboStat base unit was regulated with 4 mass flow controllers (Red-y smart series, Vögtlin instruments GmbH, Switzerland) to ensure high-precision gas flow control. Another gas channel was controlled by a humidifier (HumiStat, NORECS AS, Norway), where steam can be added to the gas flow through a heating gas pipe with a maximum temperature of 150 °C. During steam electrolysis operation, the ProboStat base unit was heated above 100 °C, and the ceramic tube outside of the furnace was also heated by an additional heating jacket (MIL-HJ-350S, ISOHEAT, Germany) to a temperature higher than 100 °C in order to prevent steam condensation.

The upper part of the ceramic tube in the ProboStat base unit, where the cells are mounted, is placed in a tubular furnace (Thermconcept GmbH, Germany) to achieve desired operating temperatures. Additionally, two thermocouples were placed close to the measured cells to monitor and adjust the cell temperature to the designed working level. For cells mounting, the

cells were placed on top of the internal alumina tube, with both sides contacting a Pt mesh attached to two Pt wires for current collection. The “2-electrode 4-wire” method was used for the PCC measurement.

4.4.2 Hydrogen production measurement

As described in Chapter 2, due to the p-type conductivity in protonic ceramics, the electrical current applied to PCCs during steam electrolysis may not be fully utilized for H₂ production. Therefore, in order to understand electronic leakage during operation, it is essential to determine the composition of the gas at the outlet. A mass spectrometer (EISense, V&F Analyse und Messtechnik GmbH) was used for analyzing the actual H₂ production rate (Figure 4.5a). The mass spectrometer was calibrated before each measurement to ensure accurate detection. All the electrochemical measurements were performed using an electrochemical workstation (ZENNIUM XC, Zahner-Elektrik GmbH & Co. KG, Germany).

4.4.3 Polarization curves

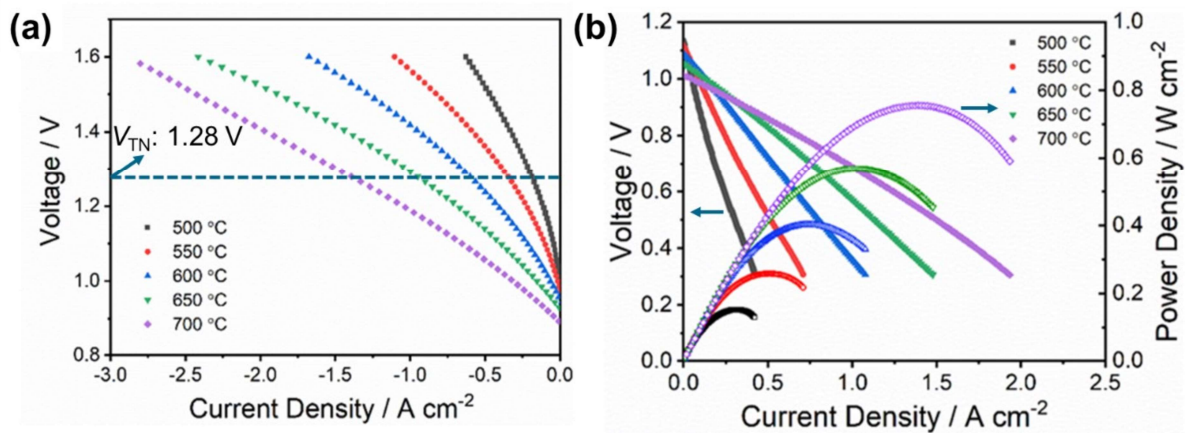


Figure 4.6: Polarization curves recorded from BGLC587-BZCY541 negatrode-supported protonic ceramic cells in (a) steam electrolysis and (b) fuel cell modes at different operating temperatures, adapted from Article I.

Polarization curves were recorded in steam electrolysis and fuel cell modes. As shown in Figure 4.6a, an exemplary diagram illustrates the electrolysis operation in PCCs⁸⁵. The polarization curves depict the behavior from open circuit voltages up to a maximum V_{cell} of 1.6 V. The apparent current density obtained at V_{TN} is commonly used as the key performance

Experimental methodologies

indicator (KPI) for the electrochemical performance of the cell. With the hydrogen production rate measurement, the non-faradaic current could be derived from the apparent current density.

For fuel cell operation, the power density as a function of current density can be calculated simply according to:

$$P = V_{\text{cell}} \times I. \quad (30)$$

Therefore, the I - V - P curves can be plotted as shown in Figure 4.6b⁸⁵. The peak power density serves as another KPI for evaluating cell performance in fuel cell mode.

4.4.4 Electrochemical impedance spectroscopy

In this thesis, electrochemical impedance spectroscopy (EIS) was employed as a powerful method to identify and quantify the influence of various operating parameters, for example operating temperatures, gas atmosphere, applied current or voltage, and operating mode (fuel cell mode and electrolysis mode) on the electrochemical properties of different types of PCCs.

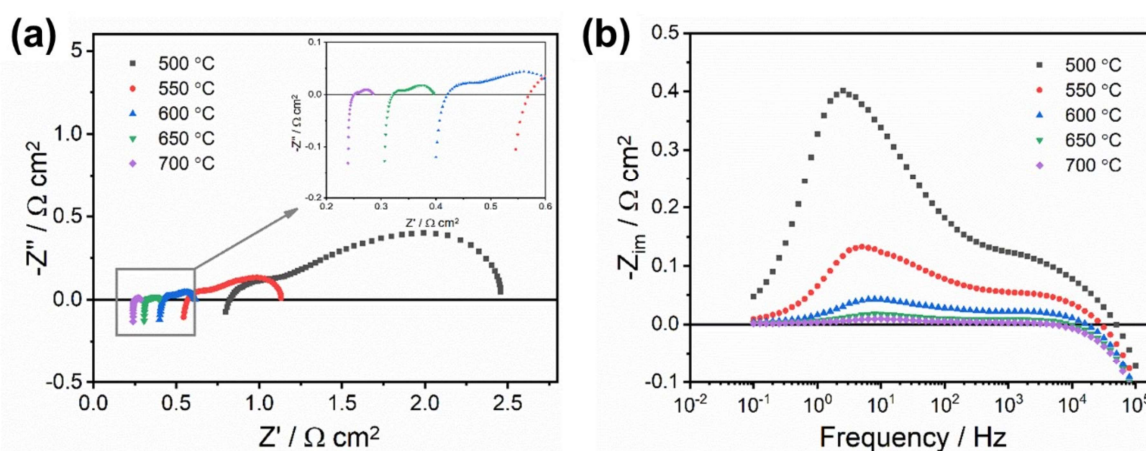


Figure 4.7: Typical (a) Nyquist and (b) imaginary impedance plots of protonic ceramic cells; PCC cells with BGLC587-BZCY541 positrode were measured at V_{OC} with wet air supplied to the positrode and wet H_2 supplied to the negatrode, adapted from Article I.

The Nyquist plot is a common way used to display the EIS results in high temperature ceramic cell research (Figure 4.7a). The plot typically consists of two compressed arcs (more arcs could be possible depending on the types of cells and the correlated test conditions) in the first quadrant of the axis. The first intersection with the x -axis in the high frequency region of the

Nyquist plot represents the ohmic resistance (R_{Ω}) of the investigated cells, which is mostly attributed to the resistance of the electrolyte. The intersection between high frequencies and low frequencies is usually considered as the polarization resistance (R_p), which comprises the electrochemical properties of the electrodes. The imaginary impedance plot (Figure 4.7b) provides insight into the characteristic frequencies that contribute to the overall resistance of the cell. Furthermore, deconstruction of the polarization resistance by means of the distribution of relaxation times (DRT) analysis and the equivalent circuit model (ECM) fitting can provide more details about the electrochemical behavior of the cell and the specific underlying processes.

4.4.5 Electrochemical analysis methods

In order to identify and characterize the contribution of different processes to an impedance spectrum, a complex non-linear square (CNLS) fitting with an appropriate ECM is frequently employed^{102, 103}. High-quality raw impedance data is the basic precondition, which is characterized by smooth arcs in the Nyquist plots. This is especially important at low frequencies, where the points can easily become scattered due to sudden voltage changes caused by small changes in the steam partial pressure¹⁰⁴. Furthermore, the ECM should be developed on the basis of reasonable physicochemical processes. The ECM typically consists of several common circuit elements (Figure 4.8) such as resistors, capacitors, and inductors connected in series or parallel.

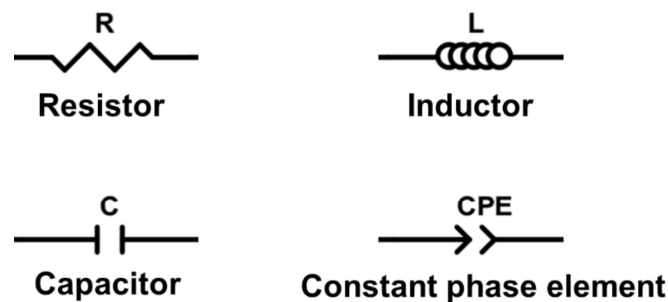


Figure 4.8: The most relevant equivalent circuit component used in high temperature ceramic cells.

The ohmic conduction process is typically modeled by a simple resistor (R_{Ω}). The impedance behavior of the electrochemical reaction process in the electrode can be modeled by a parallel

Experimental methodologies

combination of a resistor (R_p) and a capacitor (C_p). The R_p is the faradaic resistance and models the kinetics of the electrochemical reaction. The C_p represents the double layer capacitance and reflects the capacitive properties of the interface, assuming a smooth and regular interface in the electrode ⁹⁵. In reality, the irregular and porous electrodes can be better modeled with a constant phase element (CPE), often written as a Q element. Therefore, RQ elements are more frequently used for modeling the cells.

At high frequencies, the influence of the system inductance must be considered. This is typically due to the current in cables, wiring, and current collectors and can induce a non-negligible bias if the sample resistance is small. Twisting the cables can reduce the undesired effect to some extent ¹⁰⁵. However, some of commercial test rigs do not have the possibility to modify the connection path of the cables. Therefore, it is advised to add an inductor in the ECM to quantify the effect of inductance. With the basic elements introduced, the classical circuit models are presented and discussed further below.

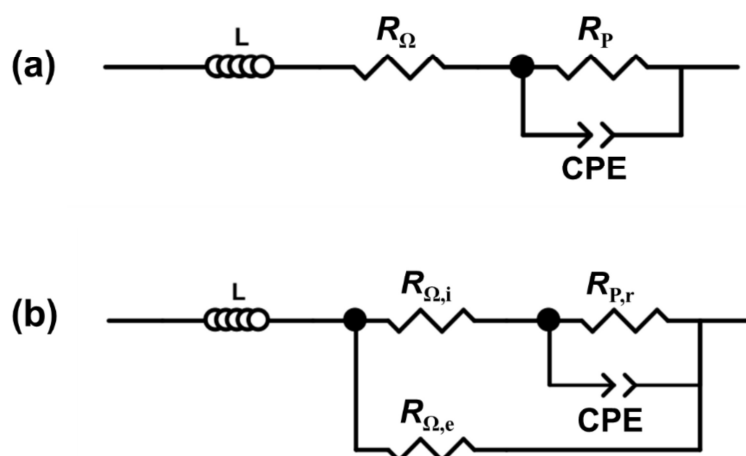


Figure 4.9: Equivalent circuit models for data deconvolution with one RQ-element representing the polarization process.

Figure 4.9a illustrates the frequently used basic ECM for data deconvolution in solid oxide ceramic cell related research. The ohmic resistance is modeled by a pure resistance (R_{Ω}). The polarization resistance is modeled by an RQ-element, which is a parallel combination of a resistor (R_p) and a constant phase element (CPE). The impedance of the CPE can be written as ¹⁰⁶:

$$Z_{\text{CPE}}(\omega) = \frac{1}{Q \times (i \times \omega)^\alpha} , \quad (31)$$

where Q is the admittance and α ($0 < \alpha < 1$) is the exponent of constant phase. If α equals 1, the behavior is that of an ideal capacitor. Otherwise, the pseudo-capacitance associated with the electrode process can be calculated according to¹⁰⁷:

$$C = \alpha \sqrt[\alpha]{\frac{Q}{R^{(\alpha-1)}}} . \quad (32)$$

In PCC, due to the mixed conduction property of the electrolyte materials (ionic and electronic conduction), an additional resistance $R_{\Omega,e}$, accounting for the electronic transport contribution, was introduced in parallel to the ionic resistance $R_{\Omega,i}$ (Figure 4.9b). Therefore, the total ohmic resistance is a combination of $R_{\Omega,e}$ and $R_{\Omega,i}$,

$$\frac{1}{R_{\Omega}} = \frac{1}{R_{\Omega,e}} + \frac{1}{R_{\Omega,i}} . \quad (33)$$

The $R_{\Omega,e}$ can be calculated by

$$R_{\Omega,e} = \frac{R_t}{1 - \frac{V_{\text{OC}}}{V_N}} , \quad (34)$$

where R_t is the total resistance ($R_t = R_{\Omega} + R_p$), V_N is the theoretical potential¹⁰⁸. With the calculated $R_{\Omega,e}$ and R_{Ω} from EIS results, $R_{\Omega,i}$ can be determined according to Equation 33. Subsequently, the average ionic transference number (t_i) and electronic transference number (t_e) can be calculated according to

$$t_i = \frac{R_e}{R_e + R_i} , \quad (35)$$

$$t_i + t_e = 1 . \quad (36)$$

Furthermore, the real polarization resistance ($R_{p,r}$) can be calculated based on the values of R_t , R_{Ω} , and t_i using the following equation:

$$R_{p,r} = \frac{R_{\Omega}(R_t - R_{\Omega})}{t_i[t_i R_t - (R_t - R_{\Omega})]} \quad (37)$$

As illustrated in Figure 4.9b, the model comprises only one RQ element. In a more complex model, there are more than one RQ element in the equivalent circuit, as discussed in Article I. Each RQ element denotes a distinct electrochemical process.

To determine the number of processes or RQ elements that should be included in the model, the distribution of relaxation times (DRT) method is a model-free approach that can help to determine both their numbers and their characteristic frequencies¹⁰⁹. As depicted in the imaginary impedance plot (Figure 4.7b), the contributions of different processes actually overlap due to similar time constants. Therefore, it is challenging to analyze such systems, especially with regard to the complex behavior of full cells. The DRT method assumes that the electrochemical system can be represented by a R_0 and an infinite number of RQ elements in series, and each RQ element is convergent in the impedance spectrum. The impedance can be expressed as follows¹¹⁰:

$$Z(\omega) = R_0 + Z_{pol}(\omega) = R_0 + R_{pol} \int_0^{\infty} \frac{g(\tau)}{1 + j\omega\tau} d\tau \quad (38)$$

With

$$\int_0^{\infty} g(\tau) d\tau = 1 \quad (39)$$

where R_0 is the ohmic resistance, $Z_{pol}(\omega)$ is the polarization impedance, R_{pol} is the polarization resistance, τ is the relaxation time, $g(\tau)$ is the distribution function of relaxation time, j is the imaginary unit, and ω is the angular frequency. In the present study, the DRT analysis was performed using the ec-idea software¹¹¹.

5 Publications

5.1 List of publications

This cumulative dissertation is based on three research articles, as listed below:

Article I: A double perovskite oxygen electrode in Zr-rich proton conducting ceramic cells for efficient electricity generation and hydrogen production

Haoyu Zheng, Matthias Riegraf, Noriko Sata and Rémi Costa

Journal of Materials Chemistry A, 2023, 11, 10955-10970

doi.org/10.1039/D3TA01298K

Contribution by Haoyu Zheng: Conceptualization, materials synthesis, test system installation, cell manufacturing and testing, evaluation, writing, and management of the submission and review process.

Article II: Hydrogen production at intermediate temperatures with proton conducting ceramic cells: Electrocatalytic activity, durability and energy efficiency

Haoyu Zheng, Feng Han, Noriko Sata, Rémi Costa

Journal of Energy Chemistry, 2023, 86, 437-446

doi.org/10.1016/j.jechem.2023.07.030

Contribution by Haoyu Zheng: Conceptualization, materials preparation, test system installation, cell manufacturing and testing, evaluation, writing, and management of the submission and review process.

Article III: Hydrogen production with a protonic ceramic membrane reactor on porous Fe-Cr alloy

Haoyu Zheng, Noriko Sata, Feng Han, Amir Masoud Dayaghi, Fumitada Iguchi, Katherine Develos-Bagarinao, Truls Norby, Marit Stange, Rémi Costa

The manuscript has been submitted.

Publications

Contribution by Haoyu Zheng: The cell manufacturing process, optimization of the cell structure, microscopic structure and thermo-mechanical stability analysis, electrochemical analysis of the cells, as well as results evaluation, writing, and submission.

Additionally, parts of this project have been published:

1. Rémi Costa, **Haoyu Zheng**, Feng Han, Noriko Sata, Amir Masoud Dayaghi, Truls Norby Marit Stange, *On the development of planar metal supported electrochemical cells with proton conducting ceramics*, 14th European SOFC & SOE Forum, 20-23 Oct. 2020.
2. **Haoyu Zheng**, Feng Han, Noriko Sata, Matthias Riegraf, Amir Masoud Dayaghi, Truls Norby, Rémi Costa, *Metal supported proton conducting ceramic cell with thin film electrolyte for electrolysis application*, ECS transactions, 103 (1) 693-700 (2021).
3. Noriko Sata, Feng Han, **Haoyu Zheng**, Amir Masoud Dayaghi, Truls Norby, Marit Stange, Robert Semerad, Rémi Costa, *Development of proton conducting ceramic cells in metal supported architecture*, ECS transactions, 103 (1) 1779-1789 (2021).
4. **Haoyu Zheng**, Noriko Sata, Matthias Riegraf, Amir Masoud Dayaghi, Truls Norby, Rémi Costa, *Proton conducting ceramic cells with $Ba_{1-x}Gd_{0.8}La_{0.2+x}Co_2O_{6-\delta}$ oxygen electrode for steam electrolysis application*, 15th European SOFC & SOE Forum, 5-8 July 2022.
5. Rémi Costa, **Haoyu Zheng**, Feng Han, Matthias Riegraf, Noriko Sata, *Progress in the development of metal-supported-cell architecture with proton conducting ceramics*, 15th European SOFC & SOE Forum, 5-8 July 2022.
6. **Haoyu Zheng**, Matthias Riegraf, Noriko Sata, Rémi Costa, *Investigation of the real performance of proton conducting ceramic cells with double perovskite positrode*, European materials research society (E-MRS), 2023 spring meeting, Strasbourg, France.

5.2 Article I

This article was published in *Journal of Materials Chemistry A*, 2023, 11, 10955-10970.

<https://doi.org/10.1039/D3TA01298K>

Cite this: *J. Mater. Chem. A*, 2023, 11, 10955

A double perovskite oxygen electrode in Zr-rich proton conducting ceramic cells for efficient electricity generation and hydrogen production†

Haoyu Zheng, *^{ab} Matthias Riegraf, ^a Noriko Sata ^a and Rémi Costa *^a

Proton conducting ceramic fuel cells and electrolyzers are nascent technologies. An operating temperature of about 600 °C calls for the development of specific oxygen electrodes with adequate catalytic activity and stability especially at high steam concentrations. An efficient composite oxygen electrode $\text{Ba}_{0.5}\text{Gd}_{0.6}\text{La}_{0.7}\text{Co}_2\text{O}_{6-\delta}-\text{BaZr}_{0.5}\text{Ce}_{0.4}\text{Y}_{0.1}\text{O}_{3-\delta}$ (BGLC587–BZCY541) with low polarization resistance and high durability in either mode is reported. Electronic leakage that occurs through the electrolyte due to intrinsic materials characteristics is a major issue that limits the faradaic efficiency (η_{FE}) especially in steam electrolysis. An equivalent circuit model was developed to deconvolute the effect of electronic leakage in the electrolyte and the oxygen electrode reaction process. The electronic (t_e) and ionic (t_i) transference numbers, real polarization resistance and η_{FE} are shown to be strongly related to $p_{\text{H}_2\text{O}}$, p_{O_2} , applied current density and operating temperatures. Distribution of relaxation time analysis of electrochemical impedance spectra revealed that the rate-limiting step for steam electrolysis is a surface-related oxygen electrode process in the low-frequency range and that a triple phase boundary process at the contact point BGLC587–BZCY541 is favored over a pure double phase boundary process at the surface of BGLC587 yielding the conclusion that composite electrode structures may have to be favored to achieve high performance.

Received 2nd March 2023
Accepted 19th April 2023

DOI: 10.1039/d3ta01298k

rsc.li/materials-a

1. Introduction

In the context of CO_2 emission abatement in the energy sector, hydrogen is asserting its position as a green energy carrier when produced by water electrolysis powered by low CO_2 electricity. Among the different water electrolysis technologies, high temperature electrolysis (typically above 600 °C) based on ceramic cells is especially attractive by allowing high energy conversion efficiency and the highest production rate of hydrogen at rated power. While electrolyzers based on solid oxide cells (SOCs) are approaching the pre-industrial scale with systems in the range of a few MW,¹ a technology based on proton conducting ceramic (PCC) cells is still nascent.

PCC cells typically use Y doped BaZrO_3 – BaCeO_3 solid solution materials ($\text{BaZr}_{1-x-y}\text{Ce}_x\text{Y}_y\text{O}_{3-\delta}$, BZCY) as an electrolyte, which are characterized by a lower activation energy for bulk proton transfer (0.3–0.5 eV) compared with oxygen ion conduction (0.8–0.9 eV) in solid oxide materials.² PCC cells are

ideally suited for operation between 400 °C and 600 °C, which makes them attractive to valorize waste heat from industrial processes available in the form of steam for hydrogen production.³ Moreover, beyond steam electrolysis application, a broad variety of ceramic membrane reactors can be built with PCC cells to convert electricity to high-value chemicals, such as ammonia, ethylene, acetylene and other hydrocarbons.^{4–7}

Similar to SOCs, PCC cells are reversible which means that they can be operated either in fuel cell (PCFC) or electrolysis (PCEC) mode. In PCC cells, steam generation or consumption occurs at the oxygen electrode, while only hydrogen is present at the fuel electrode. This is supposed to enable higher conversion rates and efficiency than in SOCs, because there is no dilution of hydrogen. Generally, the polarization losses in PCC cells are dominated by the oxygen electrode, due to the sluggish kinetics of the oxygen reduction reaction (ORR) or oxygen evolution reduction (OER) at low operating temperatures. The reaction rate limiting steps are usually associated with oxygen surface exchange and diffusion.^{8–10} In addition to high chemical stability at high steam content, it is thus desirable that a PCC oxygen electrode possesses high oxygen ionic, electronic and protonic conductivities. The preliminary research on PCC oxygen electrodes was based on simple perovskites ($\text{ABO}_{3-\delta}$) which generally are mixed (oxygen) ionic and electronic conductors (MIECs), including $\text{La}_{0.6}\text{Sr}_{0.4}\text{Co}_{0.2}\text{Fe}_{0.8}\text{O}_{3-\delta}$,¹¹ and $\text{Sm}_{0.5}\text{Sr}_{0.5}\text{CoO}_{3-\delta}$,¹² however, their performances are

^aInstitute of Engineering Thermodynamics, German Aerospace Center (DLR), Pfaffenwaldring 38–40, 70569 Stuttgart, Germany

^bInstitute for Building Energetics, Thermotechnology and Energy Storage (IGTE), University of Stuttgart, Pfaffenwaldring 31, 70569 Stuttgart, Germany. E-mail: zhenghaoyu01@gmail.com; remi.costa@dlr.de

† Electronic supplementary information (ESI) available. See DOI: <https://doi.org/10.1039/d3ta01298k>



inadequate, since the active sites are limited only to the triple phase boundaries (TPBs) between the oxygen electrode, proton conducting electrolyte and the gas phase. Double perovskite structure materials $A'A''B_2O_{6-\delta}$, where A is a trivalent lanthanide cation, A' is barium or strontium and B is a transition metal cation or mixture of different elements, such as $GdBaMn_2O_{6-\delta}$ and $GdBaCo_2O_{6-\delta}$,^{13,14} exhibit remarkably faster oxygen surface exchange, higher oxygen ion transfer rates and electronic conductivity compared with simple perovskite materials. In particular, $LnBaCo_2O_{6-\delta}$ (Ln being a lanthanide) based double perovskites, Ln–O and Ba–O layers are stacked alternately along the crystallographic *c*-axis leading oxygen vacancies to be localized preferably on the Ln–O layer,^{13,15} providing channels for rapid oxygen transport.¹⁶ Although the role of these defects has not been clearly identified, it is generally understood that oxygen vacancies promote surface reactions.¹⁷ Double perovskites $LnBaCo_2O_{6-\delta}$ with Ln = La, Pr, Nd, Sm and Gd have been explored in several studies. Among them, $Ba_{1-x}Gd_{0.8}La_{0.2+x}Co_2O_{6-\delta}$ (BGLC) was reported as a promising mixed protonic and electronic conductor in PCC cells,^{18,19} demonstrating high activity for the OER in photoelectrochemical devices even at room temperature.²⁰ Strandbakke *et al.*²¹ evaluated water incorporation of BGLC by exposure to a steam atmosphere at 400 °C. Vøllestad *et al.*²² reported a polarization resistance of a composite oxygen electrode $Ba_{0.5}Gd_{0.8}La_{0.7}Co_2O_{6-\delta}-BaZr_{0.7}Ce_{0.2}Y_{0.1}O_{3-\delta}$ in a tubular PCC cell below $1 \Omega \text{ cm}^2$ at 600 °C together with a good stability over 700 h when operated at -62.5 mA cm^{-2} and 1.5 bar steam in electrolysis mode. However, the large ohmic resistance of around $3 \Omega \text{ cm}^2$ at 600 °C, inherent to the tubular architecture and the issue of current collection did not allow for investigation of the electrode performance and stability at higher current densities.²³ This issue could be circumvented in a planar cell design. The further development of PCC cells and scale-up, especially for PCEC applications, requires tackling the challenges of performance and durability at more practical current densities, for example, around -0.5 A cm^{-2} and higher at nominal operating voltage.

The other particularity of PCC cells lies in the mixed-conducting properties of BZCY electrolyte materials, that under given conditions, exhibit in addition to proton conductivity, oxygen ion and p-type conductivities.²⁴ The transference numbers for each charge carrier depend on the chemical composition of the material, the operation atmosphere, the working temperature and the applied voltage. The presence of p-type charge carriers is especially critical as it typically induces electronic current leakage through the electrolyte which adversely affects the faradaic efficiency of the process.^{25,26} Several reports demonstrated that the impact of this electronic leakage is limited towards the faradaic efficiency for PCFCs.²⁷ However, it had dramatic influence on PCECs. Up to now, the state-of-the-art faradaic efficiency in PCECs was in the range of 30–70% at the thermal-neutral voltage (V_{TN} of around 1.3 V) which is below that in SOCs that reaches values close to 100% at V_{TN} .

Here, we report about the performance and electrochemical response of a composite $Ba_{0.5}Gd_{0.8}La_{0.7}Co_2O_{6-\delta}-BaZr_{0.5}Ce_{0.4}Y_{0.1}O_{3-\delta}$ (BGLC587–BZCY541) oxygen electrode in a planar PCC

cell operated as a PCFC and PCEC. The behavior of the composite oxygen electrode has been explored in full PCC cells by varying operating conditions such as temperature, gas atmosphere, and direct current (DC) bias. Furthermore, the characteristics of the different charge carrier transference numbers on the cell behavior as well as faradaic efficiency were evaluated in order to identify the most favorable operating conditions, particularly for electrolysis.

2. Results and discussion

2.1. Materials and morphology of the single cell

The crystalline structure of the as-prepared BGLC587 and the commercial BZCY541 powders were analyzed using XRD (Fig. 1a). The pattern of BGLC587 was consistent with the one reported in previous studies.²² The chemical compatibility between BGLC587 and BZCY541 was investigated by annealing the mixed powder in air at 1000 °C for 2 h. No secondary phase was observed in the XRD pattern of the BGLC587–BZCY541 mixture confirming adequate compatibility between the two components. Besides, the physical compatibility between the oxygen electrode and electrolyte is also a critical factor for the mechanical strength of full cells. Fig. S1† shows the thermal expansion feature of BGLC587. The average thermal expansion coefficient (TEC) value of BGLC587 at 300–700 °C is $20 \times 10^{-6} \text{ K}^{-1}$ and is indeed a common feature for cobalt-based perovskite structure materials. This is associated with the change in the spin state of Co^{3+} cations: the transition from a low-spin state to a high-spin state increasing the volume of CoO_6 octahedrons and thus causing lattice expansion.²⁸ By contrast, doped $BaCeO_3$ – $BaZrO_3$ electrolytes typically have a significantly lower TEC of ~ 10 – $12 \times 10^{-6} \text{ K}^{-1}$.²⁹ Such TEC mismatch can be the origin of a significant residual stress concentrated at the interface of the electrolyte/oxygen electrode and can ultimately yield to delamination and failure of the cell upon thermal cycles (*i.e.*, cell fabrication and operation). The use of a composite BGLC587–BZCY541 oxygen electrode allows mitigation of this issue. Fig. 1b and c depict the morphology of the BGLC587–BZCY541 composite oxygen electrode with a uniformly distributed porous structure.

Fig. 1d exhibits the XRD patterns of the NiO–BZCY541 fuel electrode and the BZCY541 electrolyte in the as-fabricated full cells without any secondary phases. An overview of the fabricated cell with a three-layer assembly is shown in Fig. 1f. The fuel electrode has a thickness of $\sim 800 \mu\text{m}$, shows good adhesion to the electrolyte and has a fine network distribution of NiO and BZCY541. The BZCY541 electrolyte layer (thickness of $\sim 12 \mu\text{m}$) exhibits a homogeneous and pin-hole free surface with a grain size of $\sim 2 \mu\text{m}$ (Fig. 1e). The composite BGLC587–BZCY541 oxygen electrode was about $35 \mu\text{m}$ thick with a good quality interface to the electrolyte layer without any evidence of cracks or delamination.

2.2. PCFC: fuel cell operation

The electrochemical performances of PCC cells with the BGLC587–BZCY541 oxygen electrode were evaluated in fuel cell



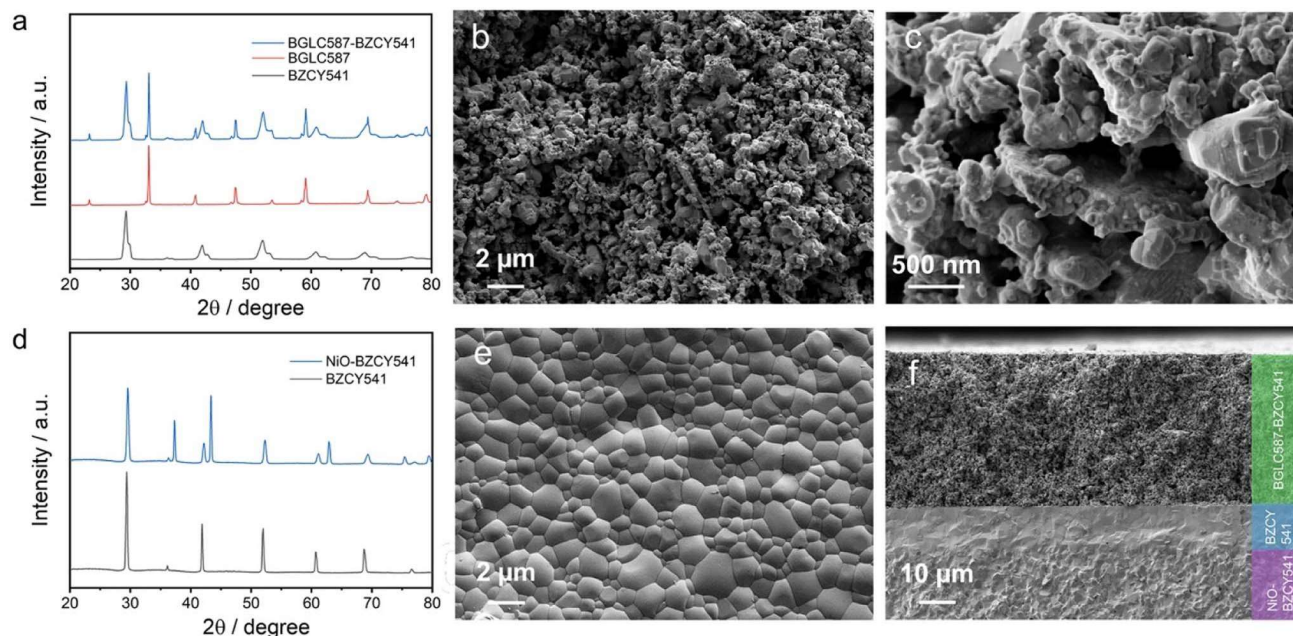


Fig. 1 (a) XRD patterns of commercial BZCY541, as-synthesized BGLC587 and BGLC587-BZCY541 mixture powder after calcining at 1000 °C for 2 h. (b) and (c) The morphology of a BGLC587-BZCY541 composite oxygen electrode at different magnifications. (d) XRD patterns of the BZCY541 electrolyte layer and a NiO-BZCY541 fuel electrode from the as-fabricated PCC cells. (e) Surface microstructure of the BZCY541 electrolyte layer after sintering at 1450 °C for 5 h. (f) Cross-section image of the as-fabricated PCC cells with different functional layers of NiO-BZCY541/BZCY541/BGLC587-BZCY541 (fuel electrode/electrolyte/oxygen electrode).

mode, first. The polarization characteristics are shown in Fig. 2a. Peak power densities (PPDs) reach 755, 570, 403, 259 and 152 mW cm^{-2} at 700, 650, 600, 550, and 500 °C, respectively, which are competitive values with the best performances reported so far for PCFCs with Zr-rich BZCY electrolyte. For comparison, Table S1† shows an overview of PPD values of different fuel electrode supported PCFCs with BZCY electrolyte in the literature. In most PCFCs with $\text{BaZr}_{0.9-x}\text{Ce}_x\text{Y}_{0.1}\text{O}_{3-\delta}$ ([Zr] > 40 at%) electrolyte and cobalt-containing oxide oxygen electrodes, the PPD is in the range between 100 and 300 mW cm^{-2} at 600 °C. Furthermore, good stability of the full cell with the BGLC587-BZCY541 oxygen electrode in fuel cell mode was demonstrated over 80 h at 0.2 A cm^{-2} and 650 °C (Fig. S2†).

The open circuit voltage (OCV; named V_{OC}) measured at 500 °C is 1.13 V which is close to the calculated theoretical Nernst voltage of 1.15 V (Fig. 2b). Such a small deviation suggests that a dense electrolyte with good gas-tightness and sealing was obtained. Nevertheless, the deviation between the measured and the theoretical voltage increased with temperature. For example, the OCV value is 1.09 V at 600 °C with the theoretical value being 1.13 V. Most likely, this increase in deviation is a manifestation of electronic leakage in the BZCY541 electrolyte, which is a typical property of proton conducting ceramics.

In proton conducting ceramics, the formation of mobile protonic charge carrier (OH_o^\cdot) is introduced by a hydration process and can be described by the Stotz-Wagner mechanism³⁰



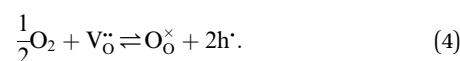
where one protonic defect is created by filling an oxygen vacancy with an OH^\cdot adsorbate that is derived from water dissociation, and a second defect is formed *via* the transfer of a proton to a lattice oxygen. This hydration reaction is exothermic. Consequently, proton migration is favored at low temperatures.

Based on eqn (1), the hydration equilibrium constant K_{H} and proton concentration can be defined as

$$K_{\text{H}} = \frac{[\text{OH}_\text{o}^\cdot]^2}{[\text{V}_\text{o}^{\cdot\cdot}][\text{O}_\text{o}^\times]p_{\text{H}_2\text{O}}} \quad (2)$$

$$[\text{OH}_\text{o}^\cdot] = K_{\text{H}}^{1/2} [\text{V}_\text{o}^{\cdot\cdot}]^{1/2} [\text{O}_\text{o}^\times]^{1/2} p_{\text{H}_2\text{O}}^{1/2} \quad (3)$$

From eqn (3), it is evident that a high steam content atmosphere serves to increase the protonic defect concentration. However, on further increasing operating temperatures, the molecular oxygen is incorporated into oxygen vacancies leading to the formation of electron holes according to^{31,32}



The equilibrium constant for oxygen incorporation K_{O} and the hole concentration can be formulated as

$$K_{\text{O}} = \frac{[\text{O}_\text{o}^\times][\text{h}^\cdot]^2}{[\text{V}_\text{o}^{\cdot\cdot}]p_{\text{O}_2}} \quad (5)$$

$$[\text{h}^\cdot] = K_{\text{O}}^{1/2} [\text{V}_\text{o}^{\cdot\cdot}]^{1/2} [\text{O}_\text{o}^\times]^{-1/2} p_{\text{O}_2}^{1/4} \quad (6)$$



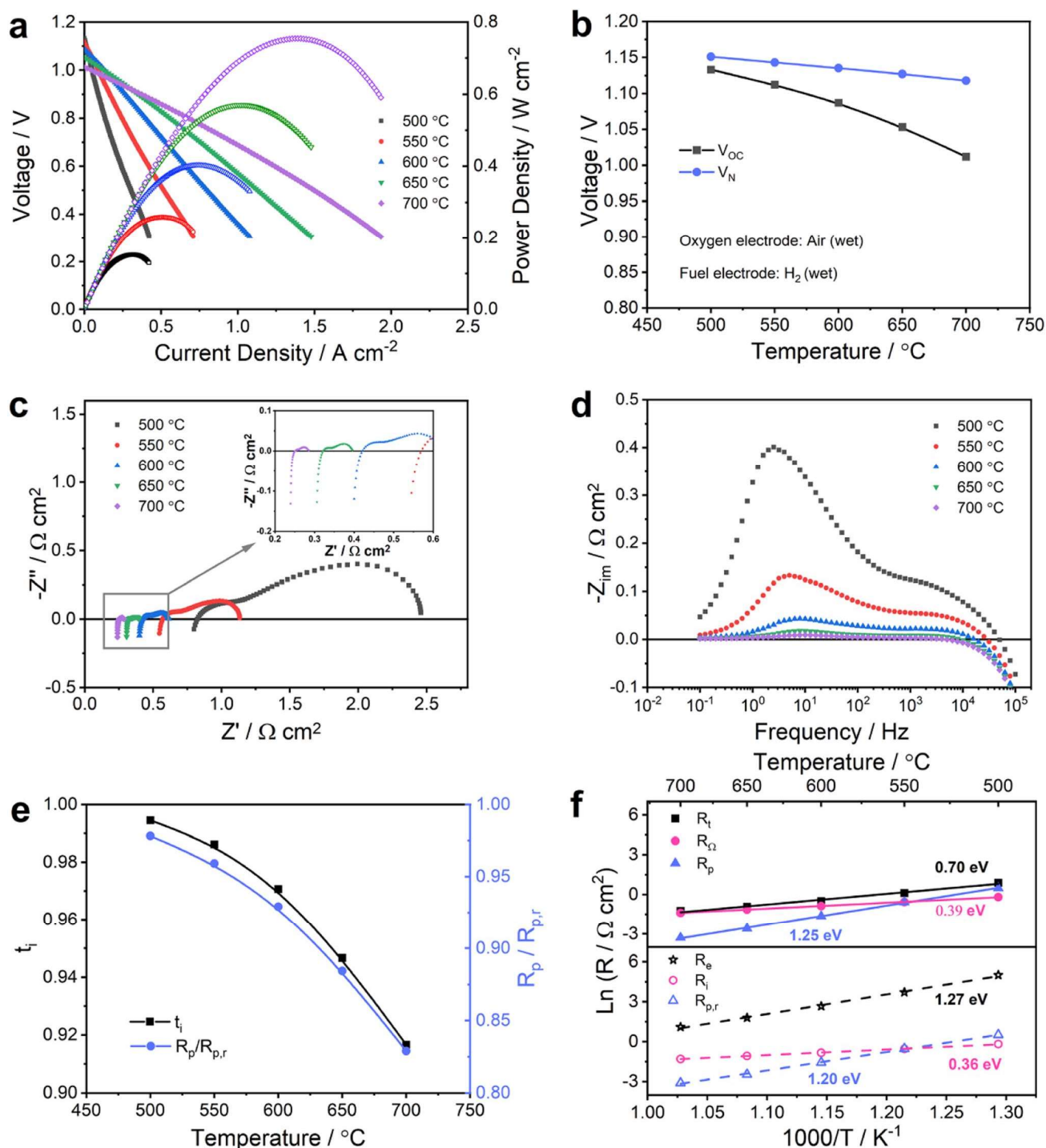


Fig. 2 Electrochemical performance of the PCC cells with the BGLC587–BZCY541 oxygen electrode in fuel cell mode with wet (~3% H₂O) hydrogen on the fuel electrode side and wet (~3% H₂O) air on the oxygen electrode side. (a) *I*–*V*–*P* curves of the PCC cells measured at 500, 550, 600, 650 and 700 °C, respectively. (b) Measured open circuit voltages (*V*_{OC}) and calculated theoretical Nernst voltages (*V*_N) as a function of temperature. (c) Nyquist and (d) imaginary impedance plots at OCV and different temperatures. (e) Temperature dependence of *R*_p/*R*_{p,r} ratios and ionic transference number (*t*_i) at OCV, and (f) temperature dependence of different resistances (*R*_v, *R*_Ω, *R*_p, *R*_e, *R*_i and *R*_{p,r}).

The formation of these electron holes is correlated with a p-type electronic conductivity in the BZCY541 electrolyte which, therefore, can explain the difference between the measured OCV and theoretical values.

To further reveal the impact of p-type conduction, electrochemical impedance spectra (EIS) were recorded at OCV and different temperatures (Fig. 2c and d) and analyzed using an equivalent circuit model as shown in Fig. 3a. Due to the mixed ionic and electronic conduction (MIEC) properties of the BZCY



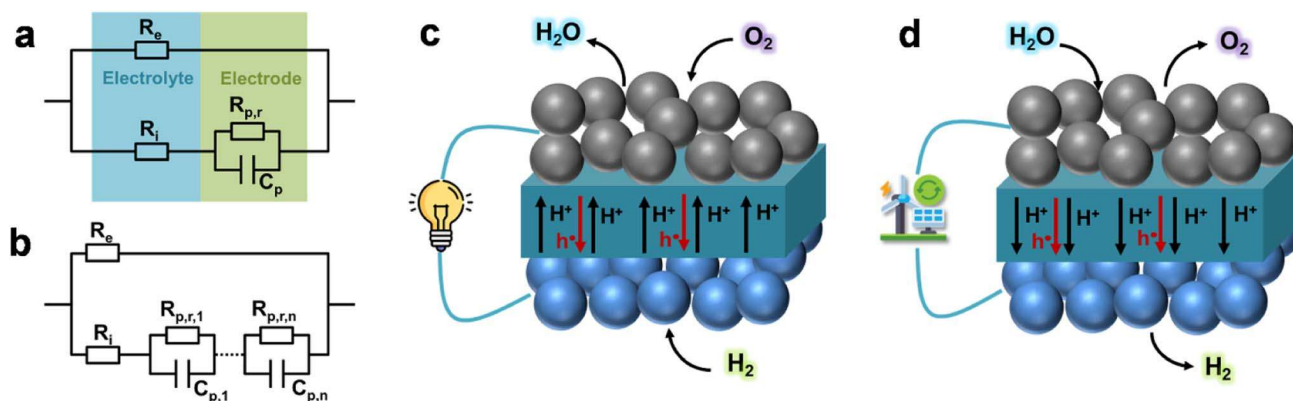


Fig. 3 (a) A simple equivalent circuit consisting of one RQ element to describe the polarization resistance of PCC cells with mixed conducting electrolytes; (b) a more complex equivalent circuit consisting of n (RQ) _{i} ($i = 1 \dots n$) elements in series for the polarization resistance. Schematic illustration of the PCC cells operated in fuel cell mode (c) and steam electrolysis mode (d).

electrolyte, the measured apparent ohmic resistance (R_{Ω}) contains contributions from both the ionic resistance (R_i) and the electronic resistance (R_e). Their relationship can be written as

$$R_{\Omega} = \frac{R_e R_i}{R_e + R_i} \quad (7)$$

For a MIEC material, the ionic transference number t_i ($t_i = R_e / (R_i + R_e)$) and electronic transference number t_e ($t_e + t_i = 1$) are usually used for evaluation of transport properties. When $t_i = 1$, there is no electronic conduction, the value of R_e is infinite and thus, R_i is equal to the measured R_{Ω} . If $0 < t_i < 1$, R_i and R_e can be calculated according to the literature (Note S1).^{†33}

Analogous to the apparent ohmic resistance, the apparent polarization resistance R_p also needs to be corrected since the real polarization resistance $R_{p,r}$ is parallel to the electronic resistance of the electrolyte (see Fig. 3a). The total resistance (R_t) can be expressed as a function of R_e , R_i and $R_{p,r}$:

$$R_t = \frac{R_e (R_i + R_{p,r})}{R_e + (R_i + R_{p,r})} \quad (8)$$

and then $R_{p,r}$ can be determined as:

$$R_{p,r} = \frac{R_{\Omega} (R_t - R_{\Omega})}{t_i [t_i R_t - (R_t - R_{\Omega})]} \quad (9)$$

Again, the value of $R_{p,r}$ is equal to R_p when t_i is 1, whereas for a mixed conductor ($t_i < 1$), the $R_{p,r}$ will be larger than R_p . For the determination of the total real polarization value of the cell, a simple equivalent circuit model as shown in Fig. 3a is sufficient and consequently,^{18,34} the EIS raw data shown in Fig. 2c and d were corrected and the results are represented in Fig. 2e and f (details are shown in Table S2[†]). For a more detailed analysis of the polarization resistance and a deconvolution of various polarization losses, a complex equivalent circuit consisting of n (RQ) _{i} elements that correspond to meaningful physicochemical processes needs to be developed (see Fig. 3b).

Fig. 2e shows that the ionic transference numbers decreased from 0.995 at 500 °C to 0.917 at 700 °C most likely due to the increased electronic conduction in the electrolyte at higher

temperatures. This is consistent with the observed increased deviation between measured and theoretical voltages as shown in Fig. 2b. The increases in electronic leakage with temperature also led to a change in $R_p/R_{p,r}$ which reduced from 0.98 at 500 °C to 0.82 at 700 °C, indicating an increased difference between apparent and real polarization resistances. Therefore, the necessity to correct the measured apparent resistance values is clearly demonstrated. Fig. 2f shows the Arrhenius plot of different resistances and the corresponding activation energies (E_a) are indicated as well. The activation energy barrier for the ionic resistance R_i of 0.36 eV is slightly lower than the 0.39 eV for R_{Ω} and agrees well with the migration energy associated with the activation energy of proton conduction (0.3–0.5 eV).² Similarly, the activation energy of $R_{p,r}$ of 1.20 eV was slightly lower than the 1.25 eV for R_p ; despite the corresponding resistance values of $R_{p,r}$ being larger than those of R_p . The activation energy of $R_{p,r}$ of the full cells matches well with the values of BGLC electrode symmetrical cells (0.8–1.25 eV).¹⁸ For fuel electrode supported cells, it is reported that the polarization resistance is dominated by the oxygen electrode.³⁵ The total losses of the cells are dominated by the ohmic contribution above 550 °C (Fig. 2f). In this study, BZCY541 was employed as the electrolyte. But it possesses relatively lower ionic conductivity in comparison to BZCY compositions with a larger Ce content on the B site (e.g., BZCY271) or with a higher level of doping on the B site with Y or Yb (e.g., BZCYyB).^{36,37} This could be the reason for the comparatively high ohmic losses. Table S3[†] summarizes the PCFC with the best performance reported so far (Note S2[†]). Nevertheless, the polarization resistance, which is dominated by the contribution of the oxygen electrode (e.g., $R_{p,r}$ is only 0.209 $\Omega \text{ cm}^2$ at 600 °C) is competitive for practical use.³⁵

2.3. PCEC: steam electrolysis operation

2.3.1. Temperature variation. To investigate the performance of PCC cells with the BGLC587–BZCY541 oxygen electrode in steam electrolysis mode, the oxygen electrode was supplied with 30% steam mixed with air. Polarization curves are shown in Fig. 4a. At an applied voltage of 1.3 V, the current densities reach -0.21 , -0.38 , -0.65 , -1.03 and -1.49 A cm^{-2} at



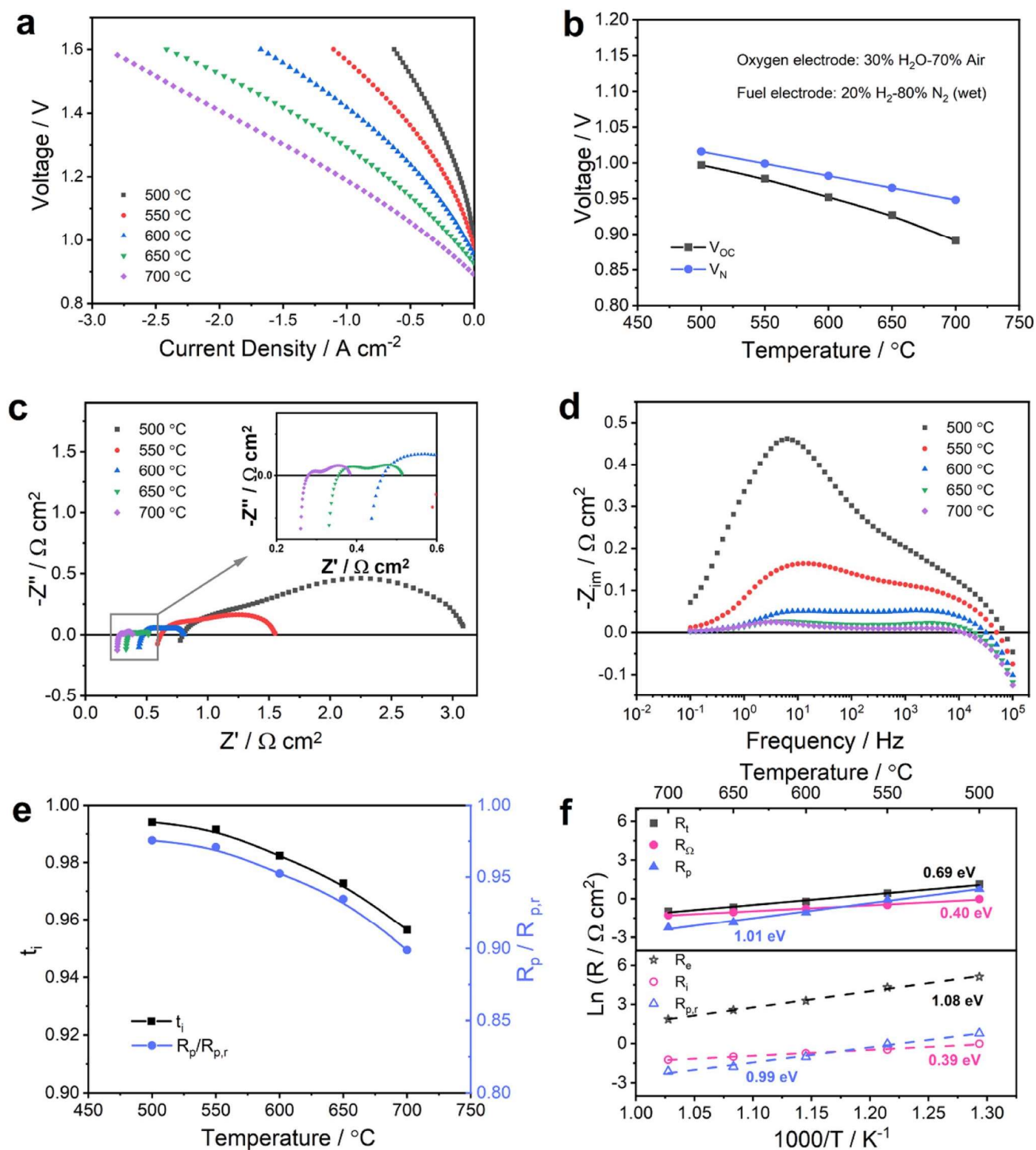


Fig. 4 Electrochemical performance of PCC cells with the BGLC587–BZCY541 oxygen electrode in steam electrolysis mode. (a) $I-V$ curves of the PCC cells measured at different temperatures with 20% H_2 -80% N_2 (wet) on the fuel electrode side and 30% H_2O -70% air on the oxygen electrode side. (b) Measured open circuit voltages (V_{OC}) and calculated theoretical Nernst voltages (V_N) as a function of temperature. (c) Nyquist and (d) imaginary impedance spectra at OCV and 500–700 °C. (e) Temperature dependence of $R_p/R_{p,r}$ ratios and ionic transference number t_i at OCV, and (f) temperature dependence of different resistances (R_t , R_Ω , R_p , R_e , R_i and $R_{p,r}$).

500, 550, 600, 650 and 700 °C, respectively. Table S4† shows comparison values for cells with similar architecture and electrolyte composition. The values in the present study match the highest ones among the comparison values, thus confirming

a high intrinsic OER electrocatalytic activity of the oxygen electrode. Furthermore, the reversible operation capability of the BGLC587–BZCY541 oxygen electrode shown in



Fig. 2a and 4a demonstrates its great electrocatalytic activity towards both the OER and ORR at low temperatures.

The OCV values are 0.997, 0.978, 0.952, 0.927 and 0.891 V at 500, 550, 600, 650 and 700 °C, respectively. Similar to fuel cell operation, the experimentally detected OCV values were slightly lower than the theoretical values (Fig. 4b). Nevertheless, the deviation between measured and theoretical voltages is mitigated compared with the difference shown in Fig. 2b, especially at high temperatures. This indicates a strong influence of the gas phase composition in the fuel electrode and oxygen electrode compartments on the electronic conductivity in the electrolyte. By combining eqn (3) and (6), the electron hole concentration can be determined in terms of steam partial pressure ($p_{\text{H}_2\text{O}}$) and oxygen partial pressure (p_{O_2}),

$$[\text{h}^{\bullet}] = K_{\text{H}}^{-\frac{1}{2}} K_{\text{O}}^{\frac{1}{2}} [\text{OH}_2\text{O}] [\text{O}_2^{\times}]^{-1} p_{\text{H}_2\text{O}}^{-\frac{1}{2}} p_{\text{O}_2}^{\frac{1}{4}} \quad (10)$$

Indeed, the observed voltage deviation is consistent with the hole concentration dependence on p_{O_2} and $p_{\text{H}_2\text{O}}$. The increment of steam content on the oxygen side decreased the p_{O_2} value by 28% (600 °C: 0.204 atm in Fig. 2a, 0.147 atm in Fig. 4a). Furthermore, the high $p_{\text{H}_2\text{O}}$ on the oxygen side thermodynamically favors the formation of proton defects and occupies more oxygen vacancies that in turn block the oxygen incorporation and the formation of electron holes on the oxygen electrode side.

The electrochemical impedance spectra recorded at OCV and various temperatures are shown in Fig. 4c and d and exhibit a typical thermally activated behavior. The spectra were modeled following the same approach as described in the previous section in order to calculate the real values of R_i , R_e and $R_{p,r}$. The results are shown in Fig. 4e and f (details are summarized in Table S5[†]). The ionic transference numbers range from 0.994 at 500 °C to 0.956 at 700 °C and are systematically higher than the ones determined from the gas compositions representative for fuel cell operation as shown in Fig. 2e. Consequently, the ratios of $R_p/R_{p,r}$ are also considerably higher, which means a decreased influence of electronic conduction on polarization resistance. Indeed, the electron hole concentration (eqn (10)) decreases while $p_{\text{H}_2\text{O}}$ increases and p_{O_2} decreases. Assuming comparable mobilities under both conditions, this behavior is also reflected in an increased electronic resistance of 14.6 $\Omega \text{ cm}^2$ under fuel cell conditions (Fig. 2f) compared to 26.5 $\Omega \text{ cm}^2$ under electrolysis conditions (Fig. 4f) at 600 °C. Due to the decreased electronic leakage under electrolysis conditions at OCV, the activation energies of R_i and $R_{p,r}$ are closer to the apparent values from R_{Ω} and R_p , respectively, in Fig. 4f. Furthermore, the activation energy for $R_{p,r}$ of 0.99 eV is lower than the corresponding value of 1.20 eV acquired as shown in Fig. 2f, suggesting that the electrocatalytic activity of the BGLC587–BZCY541 oxygen electrode is promoted at higher $p_{\text{H}_2\text{O}}$.

2.3.2. Steam partial pressure variation. As a next step, the steam/air ratio on the oxygen electrode side was verified to clarify its influence on performance and electronic leakage. Thus, polarization curves and EIS were recorded at 600 °C (Fig. 5a and b). At low overpotentials (until an overall voltage of

1.3 V), performance was higher with high $p_{\text{H}_2\text{O}}$. The performance changed slightly mainly due to the OCV change at different $p_{\text{H}_2\text{O}}$ and made the potentials different in this range. Impedance spectra at OCV show a slight apparent ohmic resistance decrease with increasing $p_{\text{H}_2\text{O}}$. Accordingly, the calculated ionic resistances decreased as well (Fig. 5c). Furthermore, the calculated ionic transference numbers were above 0.97 for all $p_{\text{H}_2\text{O}}$ and reached 0.99 at 70% steam supply as shown in Fig. 5c and Table S6[†]. These values clearly clarified that the electrolyte conductivity is dominated by ionic charge carriers at high $p_{\text{H}_2\text{O}}$ and 600 °C. An increase in $p_{\text{H}_2\text{O}}$ and a simultaneous decrease in p_{O_2} will decrease the electron hole concentration and reduce the electronic leakage according to eqn (10), which would lead to an increase in apparent ohmic resistance. Nevertheless, the measured apparent ohmic resistance decreased with increasing $p_{\text{H}_2\text{O}}$ /decreasing p_{O_2} which can be explained using a simultaneous increased protonic concentration according to eqn (3). In addition, both the apparent and the real polarization resistances (R_p and $R_{p,r}$) increased with $p_{\text{H}_2\text{O}}$. Based on the imaginary impedance plot (Fig. S4[†]), the increase was mainly attributed to the high frequency range ($\sim 10^3$ Hz) which is thus, most likely related to the BGLC587–BZCY541 oxygen electrode. The significant change in resistance is likely caused by the change of electronic conductivity in the BGLC587–BZCY541 oxygen electrode at different gas atmospheres which follows the behavior in eqn (10). At high $p_{\text{H}_2\text{O}}$ /low p_{O_2} the formation rate of electron holes decreases which has a detrimental effect on electrode performance and increases the polarization resistance. Additionally, a higher polarization resistance in a wet atmosphere than in a dry atmosphere was confirmed in the BGLC oxygen electrode symmetrical cells at 650 °C,¹⁸ suggesting that the protons are not involved in the rate limiting process at the oxygen electrode.

Furthermore, impedance spectra were recorded at various applied voltages to investigate the cell's behavior under electrical bias. Both the high frequency and low frequency arcs in the Nyquist impedance plot reduced with increasing voltages as shown in Fig. S5[†]. The values of t_i , R_e , R_i and $R_{p,r}$ were calculated and presented in Table S7.[†] Notably, t_i dropped dramatically from 0.982 at OCV (0.955 V) to 0.889 at OCV + 0.2 V (1.155 V), indicating increased electronic conduction in the electrolyte at high overpotentials. Vøllestad *et al.* have determined the electron hole concentration as a function of potential E ,²²

$$[\text{h}^{\bullet}] = K_{\text{OX}} [\text{OH}_2\text{O}] p_{\text{H}_2\text{O}}^{-\frac{1}{2}} p_{\text{O}_2}^{\frac{1}{4}} = K_{\text{OX}} \exp \left[\frac{F(E - E^0)}{RT} \right], \quad (11)$$

where K_{OX} is the water oxidation equilibrium constant. It is demonstrated that the electron hole concentration could increase at a high cell voltage. Besides, the defect transport flux of electronic holes J_h can be defined using the Nernst–Planck formulation according to diffusion due to concentration gradients and migration due to electrostatic potential gradients as

$$J_h = -D_h \left(\nabla[\text{h}^{\bullet}] + \frac{z_h F}{RT} [\text{h}^{\bullet}] \nabla \phi \right), \quad (12)$$



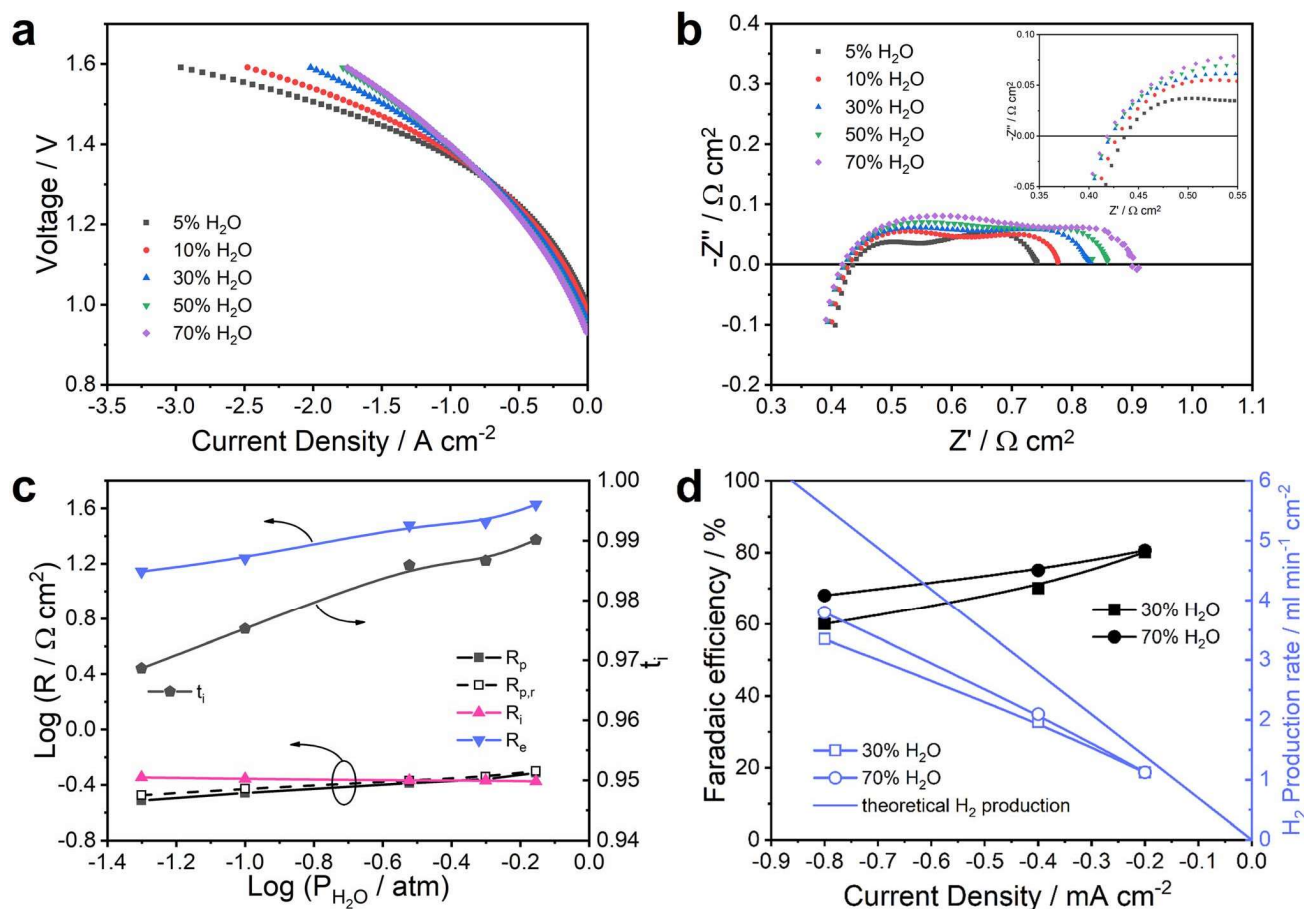


Fig. 5 Electrochemical performance of PCC cells with the BGLC587–BZCY541 oxygen electrode in steam electrolysis mode at 600 °C. (a) I – V curves of the cell measured with various H_2O concentrations (5–70%) mixed with air at the oxygen electrode, and the corresponding (b) Nyquist impedance spectra at OCV. (c) Steam partial pressure dependence of different resistances and ionic transference numbers. (d) Faradaic efficiency and H_2 production rates at different applied current densities with 30% and 70% H_2O mixed with air at the oxygen electrode.

where D_{h} , z_{h} and ϕ are the electron hole defect diffusion coefficient, charges of the defect carrier and the local electrostatic potential, respectively. In one spatial dimension, the ϕ increases with applied potential. An increased electron hole concentration (eqn (11)) at the interface between the electrolyte and the oxygen electrode combined with an increased electric field at higher applied potential can yield a higher electronic leakage through electrolyte. This is experimentally verified by the increase of t_{e} at higher cell voltage (e.g., 0.05 at OCV + 0.1 V to 0.11 at OCV + 0.2 V). The feature is consistent with the simulation results of $\text{BaZr}_{0.9}\text{Y}_{0.1}\text{O}_{3-\delta}$ electrolyte in PCC cells, showing the p-type conductivity increasing with electrolysis current density.²⁵ Accordingly, the resistance associated with electron hole transport decreased by nearly one order of magnitude from $26.5 \Omega \text{ cm}^2$ (OCV) to $3.8 \Omega \text{ cm}^2$ (OCV + 0.2 V). This behavior can also explain the obvious flattening of the I – V curves in Fig. 5a at high overpotentials (higher than 1.3 V). This flattening indicates a resistance decrease; however, it is most likely to be caused in large part by the electronic leakage at high p_{O_2} , low $p_{\text{H}_2\text{O}}$ and high overpotentials. Besides, at terminal voltages higher than the thermal-neutral voltage (~ 1.3 V), the

local heating due to the exothermic process tends to raise the temperature and thus further enhance the current leakage. In other words, the apparent current density is not necessarily representative of the actual electrolysis current density that is converted into hydrogen. Therefore, additional insights obtained *via* exhaust gas analysis are described in the following sections.

2.3.3. Faradaic efficiency. Faradaic efficiency and H_2 production rates were calculated based on mass spectrometry measurements and are depicted in Fig. 5d. The measured faradaic efficiency reduced with increasing current density, for instance, from 81% at -0.2 A cm^{-2} to 68% at -0.8 A cm^{-2} with 70% steam mixed with air at 600 °C. Furthermore, there is a trend that the faradaic efficiency increases with increasing steam concentrations/decreasing oxygen concentrations, consistent with the dependency of the hole concentration on these parameters as described using eqn (10). This feature is accentuated at high current densities. In order to evaluate the relative influence of $p_{\text{H}_2\text{O}}$ and p_{O_2} , separately, the faradaic efficiency was measured at -0.6 A cm^{-2} with different feed gases on the oxygen electrode side (Table 1). The polarization



curves (Fig. S6†) show only minor differences and cross each other upon variation of either $p\text{H}_2\text{O}$ or $p\text{O}_2$. A similar trend was already reported upon $p\text{O}_2$ variation.⁴⁰ However, the faradaic efficiency increased from 59% to 66% when the $p\text{H}_2\text{O}$ was increased from 0.3 atm to 0.7 atm and $p\text{O}_2$ was kept constant at 0.2 atm. An increased steam partial pressure shifts the equilibrium towards a lower hole concentration (eqn (11)) yielding a higher efficiency. Besides, the faradaic efficiency decreased clearly from 59% at 0.2 atm $p\text{O}_2$ to 50% at 0.4 atm $p\text{O}_2$ and 40% at 0.7 atm $p\text{O}_2$. This corroborates a particularly severe current leakage upon an increase in $p\text{O}_2$. Similar results have been reported in the literature.^{22,35,41} In recent years, many performance reports on PCECs have shown a high current density over 1 A cm^{-2} at 1.3 V (Table S8†). However, in some cases low faradaic efficiencies were evidenced, suggesting considerable energy losses due to current leakage through the electrolyte. Achieving high faradaic efficiency at high current density appears to be a determining challenge to be addressed for developing high performance PCECs. For cells with Y doped $\text{BaZrO}_3\text{-BaCeO}_3$ solid solution materials as the electrolyte, it can thus be recommended to maintain a high $p\text{H}_2\text{O}$ together with a low $p\text{O}_2$ on the oxygen electrode side, in order to obtain a high faradaic efficiency and a high energy conversion efficiency.

In conclusion, the gas atmosphere and applied DC bias both showed a remarkable impact on the faradaic efficiency. For practical application, that is at high steam conversion rates, the produced O_2 on the oxygen electrode side will increase the local $p\text{O}_2$ significantly resulting in an increased current leakage. Nonetheless, the applied DC bias is likely to have a greater impact on the faradaic efficiency for steam electrolysis compared with the $p\text{O}_2$ evolution. Optimization of the operating window may not be the sole and best solution to address such inherent p-type current leakage. Recently, different approaches were suggested by optimizing the cell design to suppress the current leakage, for instance, *via* the employment of an additional layer able to block the diffusion of p-type charge carriers or the development of novel electrolyte materials for PCECs.⁴² However, the investigation and the evaluation of such approaches go beyond the scope of the present study.

2.3.4. Water splitting process in the oxygen electrode. The polarization resistance observed in impedance spectra normally reflects the electrochemical reaction process in the electrode. Different impedance spectra recorded upon separate variations of $p\text{H}_2\text{O}$ and $p\text{O}_2$ are shown in Fig. 6a and b. R_Ω decreased at high $p\text{H}_2\text{O}$ (Fig. 6a) as well as the calculated R_i (Table S9†),

which is likely caused by the enhanced hydration and the associated higher proton concentration in the BZCY electrolyte at high $p\text{H}_2\text{O}$ (eqn (1)). Concomitantly, the calculated t_i increased from 0.970 with 5% steam to 0.992 with 50% steam. By contrast, $R_{p,r}$ was increased from 0.320 $\Omega \text{ cm}^2$ with 5% steam to 0.362 $\Omega \text{ cm}^2$ with 50% steam. This is consistent with a study by Strandbakke *et al.* who observed that for BGLC in a symmetrical cell,¹⁸ the apparent polarization resistance in a wet atmosphere is higher than that in a dry atmosphere at 650 °C, indicating that the rate limiting electrode process is not related to protons or protonic species. The authors suggested that most likely oxygen or/and oxide ion related surface adsorption and diffusion play essential roles, and these processes are hindered by adsorbed steam at the reactive sites.

Turning to $p\text{O}_2$ variation, both R_Ω and R_p decreased with increasing $p\text{O}_2$ as depicted in Fig. 6b and d. In this case, the decreased R_Ω can be attributed to the increased hole conduction through the electrolyte in more oxidizing atmospheres (eqn (4)). This is reflected by an increase in t_e , increasing from 0.011 with 10% oxygen to 0.016 with 70% oxygen on the oxygen electrode side. In addition, it is speculated that cobalt in the BGLC phase is present in a high oxidation state at high $p\text{O}_2$ and primarily contributes to the electronic defect concentration,²² which may affect the reaction process on the oxygen electrode side. Generally, the oxygen exchange rate on the oxygen electrode side increases in more oxidizing atmospheres. One should notice that the p-type conduction in the oxygen electrode may increase, and this could be one of the reasons for the R_p decrease with increasing $p\text{O}_2$ as well.

In the imaginary impedance plot (Fig. 6c and d), the change in R_p upon variation of $p\text{H}_2\text{O}$ occurred in the frequency range of $10^3\text{-}10^4$ Hz and to a smaller extent between $10^0\text{-}10^1$ Hz. Differently, the change in R_p caused by varying $p\text{O}_2$ occurred across the whole frequency range of $10^0\text{-}10^4$ Hz. The Nyquist and imaginary impedance plots exhibit distinctly different behaviors of the polarization resistance changing with the variation in $p\text{H}_2\text{O}$ or $p\text{O}_2$. As a result, the observed change in polarization resistance is a cumulation of discrete polarization components corresponding to $p\text{H}_2\text{O}$ and/or $p\text{O}_2$ variation. Distinguishing the different processes becomes challenging when their respective characteristic time constants are close to each other.

To deconvolute the total polarization resistance more precisely into individual processes, the distribution of relaxation time (DRT) analysis of the spectra was performed with the impedance responses to $p\text{H}_2\text{O}$ or $p\text{O}_2$ variations, as shown in Fig. 7a and b. The DRT results identify that for both gas variations, the polarization response can be discretized into four main contributions or processes, namely P1, P2, P3 and P4, which appear at frequencies of approximately 10^4 , 10^3 , $10^1\text{-}10^2$ and $10^0\text{-}10^1$ Hz, respectively. Therefore, an equivalent circuit model was proposed with the elements $L\text{-}R_0\text{-}(R_1Q_1)\text{-}(R_2Q_2)\text{-}(R_3Q_3)\text{-}(R_4Q_4)$ (Fig. S7†), where L represents an inductance, R_0 represents the ohmic resistance and the four RQ -elements represent the four peaks in the DRT plots. In this notation, Q represents a constant phase element (CPE). All fitting parameters are listed in Table S10.† Since this equivalent

Table 1 Overview of the electrochemical characteristics of a PCEC with a BGLC587–BZCY541 oxygen electrode at 600 °C as a function of the $p\text{H}_2\text{O}$ and the $p\text{O}_2$; voltage and FE refer to the measured voltage and faradaic efficiency at -0.6 A cm^{-2}

	$p\text{H}_2\text{O}/(p\text{O}_2 = 0.20 \text{ atm})$		$p\text{O}_2/(p\text{H}_2\text{O} = 0.3 \text{ atm})$		
	0.30 atm	0.70 atm	0.20 atm	0.40 atm	0.70 atm
Voltage/V	1.25	1.23	1.25	1.25	1.24
FE/%	59	66	59	50	40



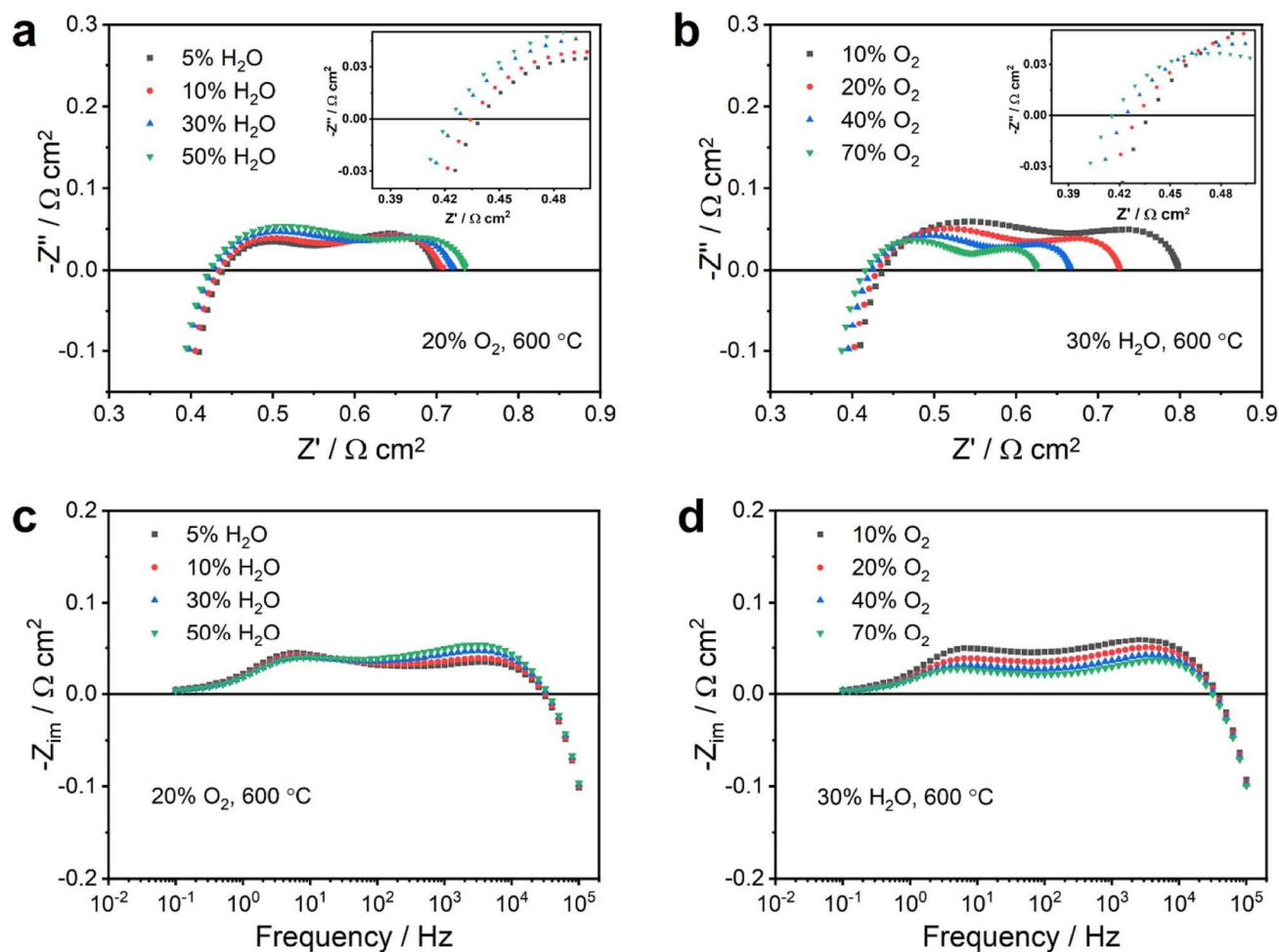


Fig. 6 (a) Nyquist and (c) imaginary impedance spectra as a function of H_2O partial pressure on the oxygen electrode side at 600 °C and OCV, and (b) Nyquist and (d) imaginary impedance spectra as a function of O_2 partial pressure on the oxygen electrode side at 600 °C and OCV.

circuit model thread is parallel to an electronic resistance as well (see Fig. 3), a correction of R_1 – R_4 was carried out after fitting to obtain the real resistance values according to the procedure described above (details are shown in Table S11†). Accordingly, the activation energy for R_1 , R_2 , R_3 and R_4 derived from Fig. 4c was calculated and presented in Fig. S8,† and the values are 0.59, 1.28, 1.07 and 0.81 eV, respectively.

Based on these results, the resistance of all oxygen electrode-related loss processes can be empirically described according to

$$R_i \propto (p\text{O}_2)^{-m_i}(p\text{H}_2\text{O})^{-n_i} \quad (13)$$

where R_i is the polarization resistance for each loss process and m_i and n_i are the reaction orders with respect to the partial pressures. The values of these exponents can then reveal in-depth mechanistic insights about the nature of the loss process. For this reason, extensive reaction networks for the most probable mechanisms for the oxygen reduction/evolution reaction on proton-conducting ceramics have been compiled before.^{18,43–45} Furthermore, the characteristic exponents of $p\text{H}_2\text{O}$ and $p\text{O}_2$ in the equilibrium exchange rate were derived for the different elementary steps. Thus, the comparison of the

reaction orders, in other words the exponents, in eqn (13) determined by equivalent circuit model fitting and the derived characteristic values shown in Fig. 7c and d can lead to the identification of the rate-limiting steps in the respective loss process. As summarized in Table S12,† an overview of elementary reactions for a mixed protonic and electronic conducting oxygen electrode is presented. This reaction network comprises H_2O adsorption, H_2O dissociation, proton transfer, charge transfer, oxygen association and desorption processes.

As a result of the equivalent circuit fitting, the dependence of R_4 on $p\text{O}_2^{-m}$ and $p\text{H}_2\text{O}^{-n}$ with $m_4 = 0.26$ and $n_4 = 0.08$, respectively, was obtained. The dependence on $p\text{H}_2\text{O}$ is very weak (n close to zero). P4 has a summit frequency between 10^0 and 10^1 Hz. The pseudo-capacitance C_4 was calculated and showed a value of 10^{-1} – 10^0 F cm^{-2} .¹⁸ Such values are in line with the reaction orders proposed when oxygen surface diffusion from the TPB to the BGLC surface is the rate-limiting step.^{44,46} Moreover, P4 has an E_a of 0.81 eV, which is close to the apparent activation energy of the oxygen surface exchange coefficient for ordered perovskite cobaltites (0.6–0.9 eV).^{47,48} The relative contribution of P4 to the total polarization decreased strongly by changing from a pure BGLC ($C_4 = 0.016$ F cm^{-2}) to



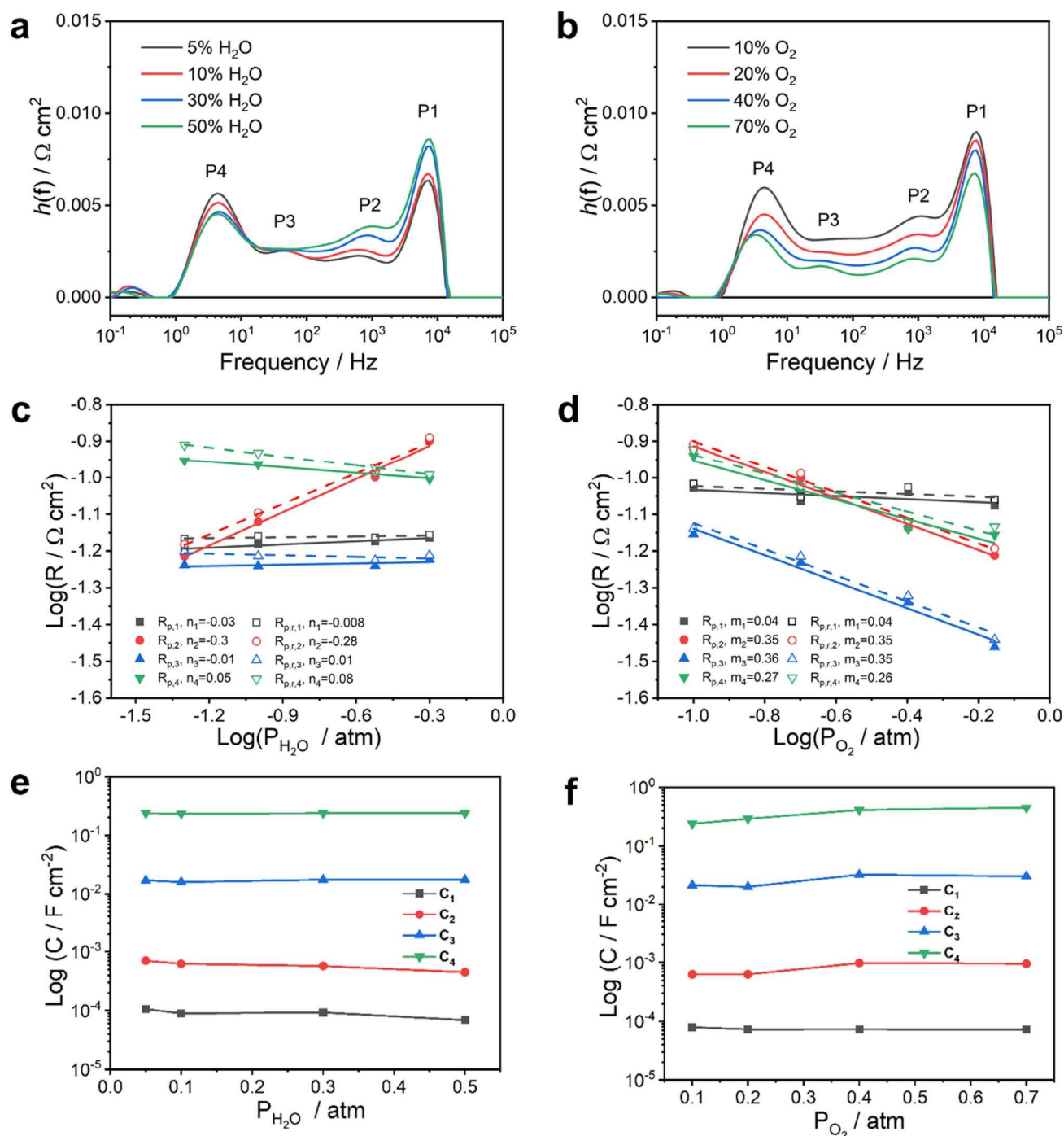


Fig. 7 Distribution of relaxation time (DRT) results as functions of $p\text{H}_2\text{O}$ (a) and $p\text{O}_2$ (b) at 600 °C. Dependence of P1, P2, P3 and P4 polarization resistances on (c) $p\text{H}_2\text{O}$ and (d) $p\text{O}_2$, and dependence of the corresponding capacitances on (e) $p\text{H}_2\text{O}$ and (f) $p\text{O}_2$, respectively. The fuel electrode side was fed with wet ($\sim 3\%$ H_2O) 20% H_2 –80% N_2 .

a BGLC587–BZCY541 composite oxygen electrode (Fig. S9†). All in all, this suggests that P4 is related to a process occurring at the surface of the BGLC and that the TPB reaction at the contact point BGLC587–BZCY541 is favored over a pure DPB process at the surface of BGLC as illustrated in Fig. 8.

Regarding the middle frequency range, the related index of P3 on $p\text{O}_2$ is 0.35 and hence, close to 3/8, while it is relatively independent of $p\text{H}_2\text{O}$ ($n_3 = 0.01$). These values are consistent

with what has previously been proposed for the electron transfer of an adsorbed O^- to the proton conductor and the formation of neutral oxygen. But it has to be pointed out that the existence of neutral oxygen on perovskite phases is considered to be energetically unfavorable.^{43,49} Comparing the corresponding E_a of 1.07 eV and related capacitance of $10^{-2} \text{ F cm}^{-2}$,³⁴ it could suggest a surface process involving a charge transfer on oxygen.



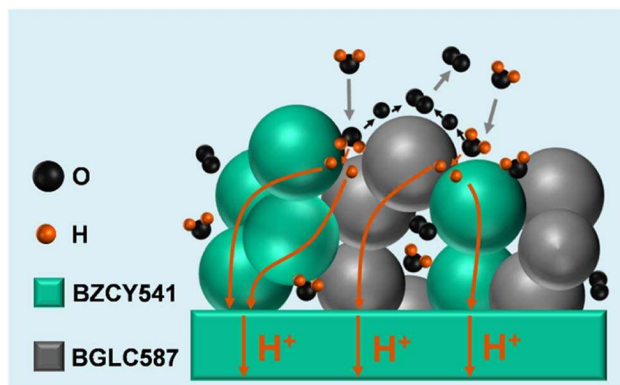


Fig. 8 The schematic diagram of the proposed reaction mechanisms in the BGLC587–BZCY541 oxygen electrode for steam electrolysis.

The capacitance C_1 (10^{-4} – 10^{-5} F cm $^{-2}$) associated with P1 is consistent with the high-frequency process in symmetrical BGLC cells.^{18,50} The capacitance values are significantly lower than what is generally observed for gas and surface diffusion processes and processes related to a chemical capacitance. The magnitude of the capacitance could rather indicate a charge transfer process associated with a double layer capacitance. In the present study, a weak dependence of R_1 on pO_2 ($m_1 = 0.04$) and pH_2O ($n_1 = -0.008$) was observed, also consistent with a previous study where this process was assigned to a process at the buried interface between the electrolyte and the oxygen electrode in a symmetrical BGLC cell since such processes are generally considered to be independent of gas atmosphere variation. The activation energy of R_1 is 0.59 eV, which is within an acceptable range for proton transfer despite being slightly higher than the E_a of R_1 from Fig. 4f corresponding to protonic transport in the electrolyte and far below the value expected for oxygen ion diffusion.

The process P2 (10^3 Hz, 10^{-3} – 10^{-4} F cm $^{-2}$) shows the indices $m = 0.35$ and $n = -0.28$ and based on these identified reaction orders no clear assignment based on the proposed framework can be made. By considering only the correlation with pO_2 , P2 may involve a charge transfer. But the dependency of P2 on pH_2O should not exist. The increase in R_2 was observed at high pH_2O or low pO_2 , most likely because this step is dominated by electron–hole transfer related steps. As mentioned above, the high steam content atmosphere may promote the hydration process and could hinder oxygen incorporation to some extent, which results in an electronic conductivity decrease. On the other hand, low pO_2 may decrease the electronic conductivity as well. Further studies are still demanded for better clarification of P2 in the composite oxygen electrode.

The experimental results show that oxygen reactions at the surface of BGLC are determining factors for the performance of the oxygen electrode in PCC cells and that a composite structure may be beneficial to achieve higher performance. It needs to be stated that the deconvolution of the PCC full cell impedance is challenging due to the lack of mechanistic studies on the processes. A mechanistic interpretation of the water splitting reaction should ideally be performed with electrodes of defined

geometries. Conditions in realistic porous electrodes are frequently a lot more complex and thus, their analysis with the above-mentioned models as provided in the present study can explain major trends rather than unequivocally identify mechanisms.

2.4. Durability in steam electrolysis operation

To assess the stability of the full cells with the BGLC587–BZCY541 oxygen electrode for steam electrolysis, different stability tests and post-mortem degradation analysis were carried out and the results are provided in Fig. 9. The cell was first tested in galvanostatic mode at different current densities and temperatures. The voltage evolution suggests good short-term stability. A slight improvement was observed in each step, particularly at high current density, which could be attributed to slight heating caused by exothermic operation at voltages higher than V_{TN} or improvement of contact between the Pt current collector and the oxygen electrode, resulting in a decrease in the ohmic resistance. Additionally, another fresh cell was investigated at -0.8 A cm $^{-2}$ and 600 °C with 30% H $_2$ O (Fig. S11†). Within 60 h, the voltage decreased from 1.44 V to 1.37 V, and it reached a similar voltage as shown in Fig. 8b, indicating high reproducibility of the cells in this study. The reduction of the ohmic resistance from 0.635 Ω cm 2 to 0.527 Ω cm 2 was the main contribution to the overpotential decrease, resulting in the improvement of the cell performance, which is a common feature of improved contact over time by using a Pt current collector.

After the short-term stability tests as shown in Fig. 9a and b, the cell was examined at -0.4 mA cm $^{-2}$ and 600 °C for 366 h in total (Fig. 9c). The oscillation of the voltage was associated with an unstable steam supply. In the first 200 h at 10% H $_2$ O, the voltage remained constant at around 1.22 V. In the following 166 h at 30% H $_2$ O, the voltage increased slightly from 1.213 V to 1.219 V corresponding to a degradation rate of 36 mV per 1000 h. The durability results confirmed the high stability of the cell with the BGLC587–BZCY541 oxygen electrode. Post-mortem cross-sectional microstructures were obtained *via* SEM after operation. Fig. 9d shows a distinct three-layer structure, including the dense BZCY541 electrolyte layer, the porous Ni–BZCY541 fuel electrode and the BGLC587–BZCY541 oxygen electrode. After operation the fuel electrode (Fig. S12†) is more porous compared to that after manufacturing (Fig. 1f), due to the nickel particle shrinkage associated with the reduction of nickel oxide. Notably, electrolyte and the fuel electrode were still bonded well without any delamination after the operation under a high steam content atmosphere. Moreover, the interface between the BGLC587–BZCY541 oxygen electrode and electrolyte also remained crack-free without any evidence of delamination. The microstructure of the oxygen electrode shown in Fig. 9e exhibits well-distributed porosity, and the particles did not show any obvious agglomeration or growth after durability operation, which is consistent with the stable electrolysis voltage at different applied current densities and steam content. The durability results together with the microstructural analysis confirmed good prospects in terms of



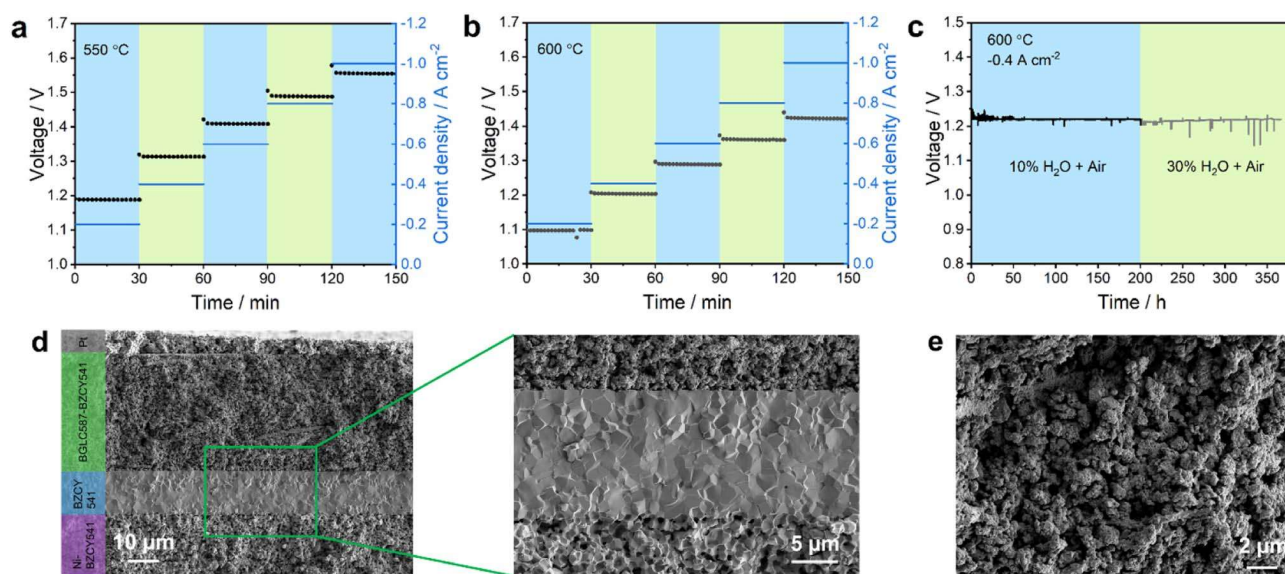


Fig. 9 Stability characteristics of the PCC cells with the BGLC587–BZCY541 oxygen electrode in steam electrolysis mode. The short-term stability of measured voltages as a function of time at different current densities as indicated on the left y-axis at 550 °C (a) and 600 °C (b). (c) Long-term stability of voltage evolution at 600 °C and a fixed current density of -0.4 A cm^{-2} . (d) Cross-sectional images of the full cell and (e) the BGLC587–BZCY541 oxygen electrode after long term operation at different magnifications.

stability of the cell with the BGLC587–BZCY541 oxygen electrode.

3. Experimental section

3.1. Synthesis of $\text{Ba}_{0.5}\text{Gd}_{0.8}\text{La}_{0.7}\text{Co}_2\text{O}_{6-\delta}$

$\text{Ba}_{0.5}\text{Gd}_{0.8}\text{La}_{0.7}\text{Co}_2\text{O}_{6-\delta}$ (BGLC587) powder was prepared using the EDTA-citrate complexing sol-gel method. The raw materials were $\text{Ba}(\text{NO}_3)_2$ (Alfa Aesar), $\text{Gd}(\text{NO}_3)_3 \cdot 6\text{H}_2\text{O}$ (Alfa Aesar), $\text{La}(\text{NO}_3)_3 \cdot 6\text{H}_2\text{O}$ (Alfa Aesar), and $\text{Co}(\text{NO}_3)_2 \cdot 6\text{H}_2\text{O}$ (Alfa Aesar). The different precursor salts were dissolved in distilled water allowing for the targeted stoichiometric ratio to be achieved. For the solution, EDTA and citric acid were added as complexing agents with a molar ratio of 1 : 1 : 1.5 (total metal ions : EDTA : citric acid). pH was adjusted to 8 by adding $\text{NH}_3 \cdot \text{H}_2\text{O}$. The obtained solution was heated at 80 °C under magnetic stirring until a viscous gel was obtained. The gel was fired at 240 °C for 10 h to form the precursor, which was subsequently crushed thoroughly in a mortar. Then the combusted powder was calcined at 1150 °C for 5 h in air.

3.2. Cell manufacturing

Fuel electrode supported proton conducting ceramic cells with BGLC587–BZCY541 composite oxygen electrodes were fabricated.

3.2.1. Substrate fabrication. NiO and $\text{BaZr}_{0.5}\text{Ce}_{0.4}\text{Y}_{0.1}\text{O}_{3-\delta}$ (BZCY541) powders from Marion Technologies were used as received. For the substrate, NiO, BZCY541 and starch as a pore former were mixed in 2-propanol with a weight ratio of 6 : 4 : 1 and treated by planetary ball milling to obtain homogeneous mixtures. The mixed powder was dried and pressed in a 20 mm diameter pellet die with a uniaxial pressure of 60 MPa. The

pellet was pre-sintered at 1150 °C for 2 h in air to obtain substrates.

3.2.2. Electrolyte fabrication. The electrolyte layer was applied by drop-coating. An electrolyte suspension was prepared by adding 1.25 g of BZCY541 powder, 12 g of absolute ethanol as solvent, 0.05 g of polyvinyl butyral as a plasticizer, 0.05 g of polyethylene glycol as a dispersant, 0.05 g of triethanolamine as an emulsifier and 1 mm diameter zirconium oxide beads. Afterwards, the mixture was roll-milled for 12 h. 200 μL of the electrolyte suspension solution was dropped onto the NiO–BZCY541 substrate. After drying at 60 °C, the green half cells were co-sintered at 1450 °C for 5 h.

3.2.3. Oxygen electrode fabrication. Double perovskite BGLC587 was mixed with BZCY541 in a weight ratio of 6 : 4. The corresponding electrode powders were mixed with a binder (6 wt% ethyl cellulose in terpineol) in a weight ratio of 65 : 35 to form a slurry. The slurry was screen-printed onto the BZCY541 electrolyte surface and subsequently sintered at 1000 °C for 2 h. Platinum paste (Heraeus GmbH, Germany) was brush-painted onto the surface of the oxygen electrode as a contact layer and sintered at 700 °C for 1 h. The active area of the full cell was 0.5 cm^2 .

3.3. Characterization

The synthesized powders and fabricated cells were investigated using X-ray diffractometers (Bruker AXS, Germany) for crystal-line phase characterization. The morphology of the cells' functional layers was observed using a scanning electron microscope (Zeiss ULTRA PLUS SEM, Carl Zeiss AG, Germany). Dilatometry measurement was performed on a DIL 402C device (Netzsch, Germany) in the temperature range of 20–1200 °C with a heating rate of 3 °C min^{-1} in ambient air. A dense



ceramic rod was prepared by isostatic pressing the powder in a latex tube at 460 MPa and sintering at 1200 °C for 10 h. The relative density of the sintered specimen was higher than 95%.

Full cells were electrochemically investigated in fuel cell and electrolysis modes on a commercial test system (ProboStat, NORECS AS, Norway). On the fuel side, 50 sccm gas was fed into a bubbler at room temperature adding approximately 3% of steam. On the oxygen side, a humidifier (HumiStat, NORECS AS, Norway) was used to enable steam contents of 3–70%. The total gas flow rate on the oxygen side was fixed at 50 sccm. Platinum meshes were attached to both the fuel and the oxygen electrodes as the current collector. Each platinum mesh was connected with two platinum wires and the 2-electrode 4-probe method was used for electrochemical measurements. Cells were sealed using a ceramic sealant (Ceramabond 552, AREMCO, USA) and a glass paste (617, AREMCO, USA) to ensure gas-tight sealing. After the sealing process, the fuel electrode was reduced at 700 °C for 12 h with a 20% H₂/80% N₂ (wet, ~3%) gas mixture while the oxygen electrode side was flushed with air. When reduction was complete and open circuit voltage (OCV) reached a steady state, the initial electrochemical cell performance was recorded first in fuel cell mode with wet air on the oxygen electrode side and humidified (~3% H₂O) H₂ on the fuel side. All electrochemical measurements were performed using a Zennium XC (Zahner, Germany). Polarization curves were carried out from OCV to 0.3 V in fuel cell mode and from OCV up to 1.6 V in electrolysis mode with a scanning rate of 0.005 V s⁻¹. Electrochemical impedance spectroscopy (EIS) was performed in a frequency range from 0.1 Hz to 100 kHz with an amplitude of 20 mV. Distribution of relaxation times (DRT) analysis was performed by using the modelling software ecidea. A regularization parameter of 0.5 was chosen since it led to a small difference between the reconstructed and measured impedance spectra while avoiding over-regularization.⁵¹ Equivalent circuit model (ECM) fitting was carried out with ZView®.

For PCEC operation, 30% steam and 70% air were fed to the oxygen electrode side and a wet (~3% H₂O) gas mixture of 20% H₂ and 80% N₂ was fed to the fuel electrode side. During the test, polarization curves and EIS were recorded. The cells were operated in steady state operation for 30 min at current densities of -0.2, -0.4, -0.6, -0.8 and -1.0 A cm⁻² at temperatures of 550 and 600 °C, respectively. Long-term stability was also examined at different partial pressures of steam (10% and 30%) and a current load of -0.4 A cm⁻² and -0.8 A cm⁻² for 366 h and 62 h, respectively. The production rate of H₂ was analyzed using a mass spectrometer (EISense, V&F Analyse-und Messtechnik GmbH). The mass spectrometer was calibrated before each experiment. Then, the faradaic efficiency (η_{FE}) was calculated in steam electrolysis mode under various operating conditions as the ratio between the measured hydrogen production rate and the theoretical one:

$$\eta_{FE} = \frac{n_{\text{measured}}}{n_{\text{theoretical}}} = \frac{n_{\text{measured}}}{I \times (n \times F)^{-1}}, \quad (14)$$

where n_{measured} is the actual hydrogen production rate (mol s⁻¹), I is the applied current (A), n is 2 for hydrogen production and F is the faradaic constant (96485 C mol⁻¹).

4. Conclusions

In summary, PCC cells with a BGLC587–BZCY541 composite oxygen electrode have been systematically investigated for fuel cell and steam electrolysis application at intermediate temperatures (500–700 °C). A peak power density of ~400 mW cm⁻² in fuel cell mode and a current density of -650 mA cm⁻² at 1.3 V in steam electrolysis mode were reached at 600 °C, demonstrating good performance in both modes. The durability test in steam electrolysis up to 366 h at -0.4 A cm⁻² and 30% steam content has shown an extrapolated degradation rate of 36 mV/1000 h which is at this stage very encouraging for further development.

Detailed analysis of the impedance response of the PCC cells showed that the polarization resistance is dominated by the oxygen electrode. The oxygen evolution reaction was investigated by deconvolution of impedance spectra under various p_{O_2} and p_{H_2O} atmospheres. In PCECs, the experimental results suggest that oxygen reactions at the surface of BGLC587 are determining factors for the cell performance. Furthermore, the study suggests that a triple phase boundary process at the contact point between gas phase, BGLC587 and BZCY541 is favored over a pure double phase boundary process at the surface of BGLC587. Approaches including morphological optimization, a decrease in the sintering temperatures and the use of finer grain sizes could be explored to enhance the exchange surface area of the oxygen electrode with the gas phase and thus further reduce the polarization resistance. The faradaic efficiency was shown to be strongly dependent on the atmosphere at the oxygen electrode. The variation of the faradaic efficiency upon p_{H_2O} , p_{O_2} and current density revealed that operation at high p_{H_2O} and low p_{O_2} could mitigate the issue of low faradaic efficiency by hindering the formation of electron holes and thus their diffusion throughout the electrolyte yielding current leakage. However, the current leakage became more severe at higher current density, that is at higher overpotential. For instance, the faradaic efficiency decreased from 80% to 68% when the applied current density was increased from -200 mA cm⁻² to -800 mA cm⁻² at 600 °C.

It is important to point out that this study was performed on cells with an active area of 0.5 cm² and at relatively low steam conversion rates. In industrial operating conditions, for example, on cells with large active areas and at high steam conversion, the issue of current leakage through the electrolyte may become more prominent as the concentration of oxygen increases along the gas channel which is likely to affect the transport properties of the electrolyte. We anticipate that this as an important challenge to be addressed for the scale-up of planar PCC cells for electrolysis application.

Conflicts of interest

There are no conflicts to declare.

Acknowledgements

The China Scholarship Council is acknowledged for the doctoral scholarship of Haoyu Zheng (201806160173). The



German Federal Ministry for Education and Research is acknowledged for funding via the projects DAICHI (01DR18002) and ARCADE (03SF0580A). We would like to thank the University of Bayreuth, Chair for Electrical Energy Systems, for providing the impedance analysis and modelling software ec-idea (<https://www.ees.uni-bayreuth.de/en/ec-idea>).

References

- 1 Sunfire GmbH, *Hydrogen the Renewable Feedstock and Energy Carrier*, <https://www.sunfire.de/en/hydrogen>, 2020.
- 2 K. D. Kreuer, *Annu. Rev. Mater. Res.*, 2003, **33**, 333–359.
- 3 C. Duan, J. Tong, M. Shang, S. Nikodemski, M. Sanders, S. Ricote, A. Almansoori and R. O'Hayre, *Science*, 2015, **349**, 1321–1326.
- 4 W. Wu, L.-C. Wang, H. Hu, W. Bian, J. Y. Gomez, C. J. Orme, H. Ding, Y. Dong, T. He, J. Li and D. Ding, *ACS Catal.*, 2021, **11**, 12194–12202.
- 5 M. Li, B. Hua, L.-C. Wang, J. D. Sugar, W. Wu, Y. Ding, J. Li and D. Ding, *Nat. Catal.*, 2021, **4**, 274–283.
- 6 V. Kyriakou, I. Garagounis, A. Vourros, E. Vasileiou and M. Stoukides, *Joule*, 2019, **4**, 142.
- 7 C. C. Duan, R. Kee, H. Y. Zhu, N. Sullivan, L. Z. Zhu, L. Z. Bian, D. Jennings and R. O'Hayre, *Nat. Energy*, 2019, **4**, 230–240.
- 8 F. Baumann, J. Maier and J. Fleig, *Solid State Ionics*, 2008, **179**, 1198–1204.
- 9 J. Fleig, *Annu. Rev. Mater. Res.*, 2003, **33**, 361–382.
- 10 J. Fleig and J. Maier, *J. Eur. Ceram. Soc.*, 2004, **24**, 1343–1347.
- 11 E. Fabbri, L. Bi, D. Pergolesi and E. Traversa, *Energy Environ. Sci.*, 2011, **4**, 4984–4993.
- 12 L. Yang, C. Zuo, S. Wang, Z. Cheng and M. Liu, *Adv. Mater.*, 2008, **20**, 3280–3283.
- 13 A. A. Taskin, A. N. Lavrov and Y. Ando, *Appl. Phys. Lett.*, 2005, **86**, 091910.
- 14 A. Taskin, A. Lavrov and Y. Ando, *Prog. Solid State Chem.*, 2007, **35**, 481–490.
- 15 D. Ávila-Brandé, G. King, E. Urones-Garrote, A. Llobet and S. García-Martín, *Adv. Funct. Mater.*, 2014, **24**, 2510–2517.
- 16 J. Kim, S. Sengodan, G. Kwon, D. Ding, J. Shin, M. Liu and G. Kim, *ChemSusChem*, 2014, **7**, 2811–2815.
- 17 M. Papac, V. Stevanovic, A. Zakutayev and R. O'Hayre, *Nat. Mater.*, 2020, **20**, 301–313.
- 18 R. Strandbakke, V. A. Cherepanov, A. Y. Zuev, D. S. Tsvetkov, C. Argirusis, G. Sourkouni, S. Prunte and T. Norby, *Solid State Ionics*, 2015, **278**, 120–132.
- 19 E. Vøllestad, M. Schrade, J. Segalini, R. Strandbakke and T. Norby, *J. Mater. Chem. A*, 2017, **5**, 15743–15751.
- 20 J. Zhu, J. B. Guðmundsdóttir, R. Strandbakke, K. G. Both, T. Aarholt, P. A. Carvalho, M. H. Sørby, I. J. T. Jensen, M. N. Guzik, T. Norby, H. Haug and A. Chatzitzakis, *ACS Appl. Mater. Interfaces*, 2021, **13**, 20313–20325.
- 21 R. Strandbakke, E. Vøllestad, S. A. Robinson, M.-L. Fontaine and T. Norby, *J. Electrochem. Soc.*, 2017, **164**, F196–F202.
- 22 E. Vøllestad, R. Strandbakke, M. Tarach, D. Catalan-Martinez, M. L. Fontaine, D. Beaff, D. R. Clark, J. M. Serra and T. Norby, *Nat. Mater.*, 2019, **18**, 752–759.
- 23 H. Zhu and R. J. Kee, *J. Power Sources*, 2007, **169**, 315–326.
- 24 K. Nomura and H. Kageyama, *Solid State Ionics*, 2007, **178**, 661–665.
- 25 H. Zhu and R. J. Kee, *Int. J. Hydrogen Energy*, 2016, **41**, 2931–2943.
- 26 R. J. Kee, H. Zhu, B. W. Hildenbrand, E. Vøllestad, M. D. Sanders and R. P. O'Hayre, *J. Electrochem. Soc.*, 2013, **160**, F290–F300.
- 27 C. Duan, J. Huang, N. Sullivan and R. O'Hayre, *Appl. Phys. Rev.*, 2020, **7**, 011314.
- 28 K. Huang, H. Y. Lee and J. B. Goodenough, *J. Electrochem. Soc.*, 1998, **145**, 3220–3227.
- 29 S. Yamanaka, M. Fujikane, T. Hamaguchi, H. Muta, T. Oyama, T. Matsuda, S.-i. Kobayashi and K. Kurosaki, *J. Alloys Compd.*, 2003, **359**, 109–113.
- 30 S. Stotz and C. Wagner, *Ber. Bunsenges. Phys. Chem.*, 1966, **70**, 781–788.
- 31 T. Schober, W. Schilling and H. Wenzl, *Solid State Ionics*, 1996, **86**, 653–658.
- 32 T. Norby and Y. Larring, *Curr. Opin. Solid State Mater. Sci.*, 1997, **2**, 593–599.
- 33 M. Liu and H. Hu, *J. Electrochem. Soc.*, 1996, **143**, L109–L112.
- 34 D. Poetzsch, R. Merkle and J. Maier, *J. Power Sources*, 2013, **242**, 784–789.
- 35 Y. Zhou, E. Liu, Y. Chen, Y. Liu, L. Zhang, W. Zhang, Z. Luo, N. Kane, B. Zhao, L. Soule, Y. Niu, Y. Ding, H. Ding, D. Ding and M. Liu, *ACS Energy Lett.*, 2021, **6**, 1511–1520.
- 36 L. Yang, S. Wang, K. Blinn, M. Liu, Z. Liu, Z. Cheng and M. Liu, *Science*, 2009, **326**, 126–129.
- 37 D. Han, X. Liu, T. S. Bjørheim and T. Uda, *Adv. Energy Mater.*, 2021, **11**, 2003149.
- 38 H. Hu and M. Liu, *Solid State Ionics*, 1998, **109**, 259–272.
- 39 D. Huan, W. Wang, Y. Xie, N. Shi, Y. Wan, C. Xia, R. Peng and Y. Lu, *J. Mater. Chem. A*, 2018, **6**, 18508–18517.
- 40 S. Rajendran, N. K. Thangavel, H. Ding, Y. Ding, D. Ding and L. M. Reddy Arava, *ACS Appl. Mater. Interfaces*, 2020, **12**, 38275–38284.
- 41 H. Ding, W. Wu, C. Jiang, Y. Ding, W. Bian, B. Hu, P. Singh, C. J. Orme, L. Wang, Y. Zhang and D. Ding, *Nat. Commun.*, 2020, **11**, 1907.
- 42 Y. Matsuzaki, Y. Tachikawa, Y. Baba, K. Sato, G. Kojo, H. Matsuo, J. Otomo, H. Matsumoto, S. Taniguchi and K. Sasaki, *J. Electrochem. Soc.*, 2020, **167**, 084515.
- 43 D. Poetzsch, R. Merkle and J. Maier, *J. Electrochem. Soc.*, 2015, **162**, F939–F950.
- 44 F. He, T. Wu, R. Peng and C. Xia, *J. Power Sources*, 2009, **194**, 263–268.
- 45 H. Tian, W. Li, L. Ma, T. Yang, B. Guan, W. Shi, T. L. Kalapos and X. Liu, *ACS Appl. Mater. Interfaces*, 2020, **12**, 49574–49585.
- 46 T. Kobayashi, K. Kuroda, S. Jeong, H. Kwon, C. Zhu, H. Habazaki and Y. Aoki, *J. Electrochem. Soc.*, 2018, **165**, F342–F349.
- 47 M. Burriel, J. Peña-Martínez, R. J. Chater, S. Fearn, A. V. Berenov, S. J. Skinner and J. A. Kilner, *Chem. Mater.*, 2012, **24**, 613–621.



- 48 M. V. Ananyev, V. A. Eremin, D. S. Tsvetkov, N. M. Porotnikova, A. S. Farlenkov, A. Y. Zuev, A. V. Fetisov and E. K. Kurumchin, *Solid State Ionics*, 2017, **304**, 96–106.
- 49 R. Merkle and J. Maier, *Phys. Chem. Chem. Phys.*, 2002, **4**, 4140–4148.
- 50 J. Dailly, F. Mauvy, M. Marrony, M. Pouchard and J.-C. Grenier, *J. Solid State Electrochem.*, 2010, **15**, 245–251.
- 51 M. Hahn, S. Schindler, L.-C. Triebs and M. A. Danzer, *Batteries*, 2019, **5**, 43.



Publications

5.3 Article II

This article was published in Journal of Energy Chemistry, 2023, 86, 437-446.

<https://doi.org/10.1016/j.jechem.2023.07.030>



Hydrogen production at intermediate temperatures with proton conducting ceramic cells: Electrocatalytic activity, durability and energy efficiency

Haoyu Zheng^{a,b,*}, Feng Han^a, Noriko Sata^a, Rémi Costa^{a,*}

^a Institute of Engineering Thermodynamics, German Aerospace Center (DLR), Stuttgart 70569, Germany

^b Institute for Building Energetics, Thermotechnology and Energy Storage (IGTE), University of Stuttgart, Stuttgart 70569, Germany

ARTICLE INFO

Article history:

Received 25 May 2023

Revised 21 July 2023

Accepted 22 July 2023

Available online 11 August 2023

Keywords:

Steam electrolysis

Hydrogen production

Proton conducting ceramics

Intermediate temperature

Energy efficiency

ABSTRACT

Proton conducting ceramic cells (PCCs) are an attractive emerging technology operating in the intermediate temperature range of 500 to 700 °C. In this work, we evaluate the production of hydrogen at intermediate temperatures by proton conducting ceramic cell electrolysis (PCCEL). We demonstrate a high-performance steam electrolysis owing to a composite positrode based on BaGd_{0.8}La_{0.2}Co₂O_{6-δ} (BGLC1082) and BaZr_{0.5}Ce_{0.4}Y_{0.1}O_{3-δ} (BZCY541). The high reliability of PCCEL is demonstrated for 1680 h at a current density as high as -0.8 A cm^{-2} close to the thermoneutral cell voltage at 600 °C. The electrolysis cell showed a specific energy consumption ranging from 54 to 66 kW h kg⁻¹ that is comparable to state-of-the-art low temperature electrolysis technologies, while showing hydrogen production rates systematically higher than commercial solid oxide ceramic cells (SOCs). Compared to SOCs, the results verified the higher performances of PCCs at the relevant operating temperatures, due to the lower activation energy for proton transfer comparing with oxygen ion conduction. However, because of the p-type electronic conduction in protonic ceramics, the energy conversion rate of PCCs is relatively lower in steam electrolysis. The faradaic efficiency of the PCC in electrolysis mode can be increased at lower operating temperatures and in endothermic conditions, making PCCEL a technology of choice to valorize high temperature waste heat from industrial processes into hydrogen. To increase the faradaic efficiency by optimizing the materials, the cell design, or the operating strategy is a key challenge to address for future developments of PCCEL in order to achieve even more superior techno-economic merits.

© 2023 Science Press and Dalian Institute of Chemical Physics, Chinese Academy of Sciences. Published by ELSEVIER B.V. and Science Press. This is an open access article under the CC BY license (<http://creativecommons.org/licenses/by/4.0/>).

1. Introduction

The global hydrogen demand reached 94 million tons (Mt) in 2021 representing 2.5% of the global energy consumption [1]. The current hydrogen production is mainly based on steam methane reforming and coal gasification [2], which is responsible for more than 900 Mt of CO₂ emissions annually [3]. Hydrogen is commonly used in refineries for the petrochemistry and chemical industry, and a growing demand of hydrogen is expected from the hard-to-abate sector such as the aviation, heavy industry, shipping, heavy-duty transportation, or district heating [1]. Hydrogen production by water electrolysis powered by renewable

resources has low CO₂ emission and is of utmost importance for the decarbonization of the energy and transportation sectors [4]. Water electrolysis is an endothermic process. It is especially efficient at high temperatures when steam is used as the feedstock, as a significant portion of the energy required for the water splitting is supplied in the form of heat [5]. High temperature steam electrolysis based on solid oxide electrolysis (SOEL) performed typically at temperatures above 800 °C is proven to be the most efficient technology compared to the low temperature ones such as alkaline electrolysis (AEL), polymer exchange membrane electrolysis (PEMEL) and anion exchange membrane electrolysis (AEMEL) [5].

SOEL is usually performed under isothermal conditions, that is at a cell voltage close or slightly higher than the thermoneutral voltage (V_{TN} , $\sim 1.28 \text{ V}$). At V_{TN} and under ideal adiabatic conditions, the electrical energy conversion in the cell is 100%. In reality, the voltage is maintained slightly above V_{TN} to enable a slight heat

* Corresponding authors.

E-mail addresses: zhenghaoyu01@gmail.com (H. Zheng), remi.costa@dlr.de (R. Costa).

generation and to balance the heat losses to the environment, keeping the cell or the stack in isothermal conditions. SOEL operation in isothermal condition is favoured by the supply of superheated steam at a temperature very close to the nominal stack operating temperature in order to avoid critical thermal gradient along the gas channels. In SOEL, the water splitting occurs at the fuel electrode (negatrode) of the solid oxide ceramic cells (SOCs) which is generally made of a cermet of nickel mixed with an oxygen ion conducting ceramic, for example, yttria-stabilized zirconia (YSZ) or gadolinia-doped ceria (GDC) [6,7]. The supplied steam is mixed with a fraction of 5% to 10% hydrogen in order to maintain constant reducing conditions and to avoid the oxidation of the nickel in the cermet electrode. The electrolysis process yields typically a 70%–80% hydrogen-rich stream at the stack outlet, with unconverted steam as the balance. This large fraction of steam in the outlet stream together with the high temperature poses the significant challenge of the recirculation and heat recovery in terms of materials selection, design, and durability of the blower and the heat exchangers, respectively [8–10]. Moreover, the remaining steam must be removed in most of the use cases of the produced hydrogen.

High temperature electrolysis in the intermediate range that is typically around 600 °C is less demanding for the structural materials and offers, therefore, significant perspectives for a superior longevity compared to SOEL [11,12]. Moreover, the intermediate operating temperature range is especially attractive for valorising the waste heat from industrial processes. The Carnot waste heat recovery potential for high temperature waste heat, i.e., at temperature above 300 °C, exceeds 150 terawatt-hour (TW h) per year in the European industry alone with iron and steel and non-metallic minerals industries as major sources [13,14]. Proton conducting ceramic cells (PCCs) can be operated at intermediate temperatures (400–700 °C) in electrolysis (PCCEL) due to a lower activation energy for proton transfer compared to oxygen ion transfer in SOCs [15–17]. In PCCs, Y-doped BaZrO₃–BaCeO₃ solid solution materials, i.e., BaZr_{1-x-y}Ce_xY_yO_{3-δ} (BZCY), are state-of-the-art electrolytes. BZCY exhibits mixed ionic and electronic conductivity. The charge carriers in BZCY are electron holes, protons, and oxygen ions, and their respective prevalence is influenced by the precise materials composition itself, the operating temperature and the gas atmosphere [18]. Electron holes are formed in BZCY electrolyte materials upon oxygen incorporation, which is given by



The reaction is endothermic, meaning that the formation of electron holes is enhanced at higher temperatures. The prevalence of electron holes causes electronic leakage through the electrolyte layer, which leads to a low faradaic efficiency and, thus, to a low electrical efficiency. The electronic leakage is minimal in fuel cell operation [19,20]. In electrolysis mode, however, the operating conditions favor p-type conduction in the electrolyte, and the faradaic efficiency shows a strong dependency on the oxygen partial pressure (*p*O₂), steam partial pressure (*p*H₂O), working temperature and the anodic overpotential at the oxygen electrode (positrode). To date, the observed faradaic efficiency values exhibit a wide range spanning from ~30% to ~85% under thermoneutral conditions (Table S1). Furthermore, operation in the intermediate temperature range is concomitant with lower reaction rates in relation with the oxygen reduction reaction (ORR) and the oxygen evolution reaction (OER) at the oxygen electrode (positrode) [21]. Therefore, positrode materials with high electrocatalytic activities are crucial for the development of high-performance PCC technology [22]. Double perovskite structure materials based on Ba_{1-x}Gd_{0.8}La_{0.2+x}Co₂O_{6-δ} (*x* = 0–0.5) (BGLC) with water uptake properties have been thoroughly investigated [23,24]. The electrochemical behavior of Ba_{0.5}–

Gd_{0.8}La_{0.7}Co₂O_{6-δ} (BGLC587) mixed with BZCY541 into composite positrode has been investigated as a function of the gas atmosphere, the temperature, and the applied electrical bias. The effect of these operating conditions on the current leakage and faradaic efficiency in electrolysis mode was extensively discussed [25]. It was demonstrated by Vøllestad et al. that BGLC with *x* = 0 (BGLC1082) possesses the largest concentration of oxygen vacancies and shows the highest electrical conductivity in a useful *p*O₂ and temperature range, that is between 1 and 10⁻⁵ atm and between room temperature and 800 °C, respectively [26].

Here, we evaluated the production of hydrogen at intermediate temperatures by steam electrolysis with PCCs in terms of performance, durability and figure of merits compared to other electrolysis technologies. Since the formation of protonic defect (OH^{*}) by hydration reaction consumes oxygen vacancies, the composition BGLC1082 is likely to possess the highest electrocatalytic activity among the BGLC compounds (with *x* ≥ 0.1). We manufactured a proton conducting ceramic cell with a composite positrode of BGLC1082–BZCY541. High performance and durable PCCEL at a current density as high as –0.8 A cm⁻² at thermoneutral voltages over 1680 h operation was achieved. Furthermore, steam electrolysis at intermediate temperatures with PCCs was systematically compared with the state-of-the-art SOCs for hydrogen production. The PCC exhibited systemically higher hydrogen production rate. However, due to the existence of current leakage across the electrolyte, PCCs demonstrated a lower energy conversion efficiency compared to SOCs. The endothermic operating regime in combination with waste heat recovery is highlighted as the most promising operating strategy for PCCEL to achieve high energy efficiency.

2. Experimental

2.1. Materials preparation

BaGd_{0.8}La_{0.2}Co₂O_{6-δ} (BGLC1082) and BaZr_{0.5}Ce_{0.4}Y_{0.1}O_{3-δ} (BZCY541) commercial powders (Marion Technologies, Verniole, France) were used in this study. The BZCY541 raw powder was annealed in air at 1400 °C for 5 h before using. The BGLC1082 raw powder was treated at 600 °C for 65 h with 30% steam/Air in order to investigate its stability in moist atmosphere.

2.2. Full cells fabrication

Proton conducting ceramic cells: negatrode supported proton conducting ceramic full cells were fabricated. NiO (Marion Technologies, Verniole, France), BZCY541 and starch (REMY FG P, BENEIO GmbH, Germany) (weight ratio of 6:4:1) were mixed in 2-propanol by planetary ball milling for 3 h, and the obtained mixture was dried in an oven at 65 °C. 1 g of the mixture was pressed in a 20 mm diameter die at 60 MPa uniaxial. The green pellet was pre-sintered at 1150 °C for 2 h to enhance the mechanical strength for the next processing steps. BZCY541 electrolyte was deposited on NiO–BZCY substrate by drop-coating. The suspension was prepared by mixing BZCY541 raw powder, ethanol, polyvinyl butyral, polyethylene glycol and triethanolamine on a roll-miller for 12 h. When a homogeneous suspension was formed, 200 μL of the electrolyte suspension was dropped on the surface of the NiO–BZCY541 substrate. After drying, the assembly was co-sintered in air at 1450 °C for 5 h, resulting in the formation of half cells. During sintering, the sample was covered by the raw powder to prevent Ba evaporation. For the positrode, BGLC1082 and BZCY541 with the weight ratio of 6:4 were mixed in ethanol, ball-milled for 5 h with 400 r min⁻¹ in a planetary ball mill, and finally dried at 60 °C. A fraction of the obtained powder mixture was annealed in air at 1000 °C for 2 h to check the chemical compatibility of the two com-

ponents while the rest was blended with an ink vehicle (6 wt.% ethyl cellulose in terpineol) in a three-roll mill to form a homogenous ink. This ink was subsequently screen printed onto the surface of the BZCY541 electrolyte of the half cells and calcined at 900 °C for 2 h. A Pt paste (Heraeus GmbH, Germany) was painted on the positrode and fired at 700 °C for 1 h as a current contacting layer. The active area of the full cell was 0.5 cm².

Solid oxide ceramic cells: commercial SOCs (ASC-400B) from Elcogen AS (Estonia) were used in this study. The SOCs consist of a NiO-YSZ substrate (400 ± 30 μm) with a diameter of 20 mm, a NiO-YSZ negatrode layer (~10 μm), a YSZ electrolyte (3 ± 1 μm), a GDC barrier layer (2 ± 1 μm) and an LSC (La_{0.6}Sr_{0.4}CoO_{3-δ}) positrode (15 ± 5 μm). The active area of the SOC full cell is 0.79 cm². A Pt paste was brushed on the top of the LSC positrode and calcined at 700 °C for 1 h to keep the consistency of the experiments with PCCs measurements.

2.3. Characterization

X-ray diffraction (XRD) with a D8 Discover GADDS and equipped with a VANTEC-2000 area detector was used to analyze the ceramic powders (Bruker AXS, Germany). The diffraction pattern was recorded using a tuned monochromatic and collimated Cu K_α radiation source in Bragg-Brentano geometry. The ICDD database was used to identify crystal phases. Microstructures of the different functional layers and elemental mapping were observed using a Zeiss Crossbeam 350 scanning electron microscope (SEM, Carl Zeiss AG, Germany) with the energy dispersive X-ray spectroscopy (EDS) detector of Oxford ULTIM MAX 100 mm².

2.4. Electrochemical measurement

The as-prepared proton conducting ceramic cells with BGLC1082–BZCY541 positrode were investigated in steam electrolysis operation using an electrochemical test system. The system comprises the ProboStat base unit (NORECS AS, Norway) as the cell housing, humidifier (HumiStat, NORECS AS, Norway) for water evaporation, mass flow controllers (Vögtlin Instruments GmbH, Switzerland) and a mass spectrometer (EISense, V&F Analyse und Messtechnik GmbH) for outlet gas analysis. For the test, Pt meshes were attached on both positrode and negatrode as the current collectors, and each Pt mesh was connected with two Pt wires. The 2-electrodes 4-wires method was used for all the electrochemical measurements. A ceramic sealant (Ceramabond 552, AREMCO, USA) together with a glass paste (617, AREMCO, USA) were used to ensure gas-tight sealing between the two electrodes. After curing the sealants, the cells were heated up to 700 °C by 3 °C min⁻¹ with 5%H₂/N₂ supplied to the negatrode and air supplied to the positrode. After 12 h reduction, the gas feed to the negatrode was switched to pure H₂ until the open circuit voltage (OCV) became stable. The electrochemical performance of the PCCs was tested in fuel cell mode first with wet air supplied to the positrode side and wet H₂ to the negatrode side. Polarization curves were recorded at the voltages from OCV to 0.3 V with a scanning rate of 0.005 V s⁻¹.

In steam electrolysis operation, polarization curves were recorded from OCV to 1.5 V at the operation temperatures from 500 to 700 °C with 30%H₂O/air was supplied to the positrode and wet (~3% H₂O) 20%H₂/N₂ was supplied to the negatrode. A long-term stability test was performed in galvanostatic mode, lasting for a total of 1680 h. The SOCs were tested in the same apparatus following a similar protocol. Air was supplied to the positrode, and 30%H₂O–20%H₂–50%N₂ was supplied to the negatrode at a flow rate of 50 sccm on both electrode sides. Polarization curves and electrochemical impedance spectra (EIS) at OCV were recorded in the temperature range of 550–700 °C. Electrochemical impedance

measurements were performed in the frequency range from 100 kHz to 0.1 Hz at the amplitude of 20 mV. Equivalent circuit model (ECM) fitting was carried out using ZView[®]. The faradaic efficiency (η_{FE}) of PCCs for steam electrolysis was calculated by analyzing the deviation between theoretical hydrogen production rate with the actual hydrogen production rate.

3. Results and discussion

3.1. PCCEL at intermediate temperatures

In PCCEL, the water splitting process occurs at the positrode, and the generated mobile protons, which are introduced by the hydration process ($V_O + O_O^x + H_2O \rightleftharpoons 2OH_O$) in a wet atmosphere, transfer from the positrode to the negatrode. On the negative electrode, the protons are reduced to hydrogen ($2H^+ + 2e^- \rightarrow H_2$), while the oxygen evolution process ($2O^{2-} \rightarrow O_2 + 4e^-$) takes place on the positrode side to produce the by-product of oxygen, as shown in Fig. 1(a). We have used a negatrode supported planar PCC with the composite positrode of BGLC1082–BZCY541 for hydrogen production.

By the XRD analysis, the BGLC1082 powder displayed a layered perovskite structure in tetragonal P4/mmm space group (Fig. S1a) [24,27]. Recently, a water-induced surface modification phenomenon and performance enhancement was observed in double perovskite structure materials with cobalt on B-site [28–30]. The in-situ exsolved BaCoO_{3-δ} phase was shown to be the active site for rapid oxygen adsorption and dissociation process. In BGLC1082, the BaCoO_{3-δ} phase was detected by treating the raw powder in 30% steam/air at 600 °C for 65 h (Fig. S1b). Exploring the mechanism of BaCoO_{3-δ} exsolution in the BGLC1082 goes beyond the scope of this study. Chemical compatibility between BGLC1082 and BZCY541 was confirmed by checking the phases of the mixture of BGLC1082–BZCY541 annealed in air at 1000 °C for 2 h. No secondary phase formation or decomposition was observed (Fig. S1a).

The PCC consists of a ~800 μm thick negatrode (Ni–BZCY541), a ~10 μm thick electrolyte (BZCY541) and the composite positrode (BGLC1082–BZCY541) of 30 μm in thickness (Fig. 1b). Current densities of –1.60, –1.23, –0.83, –0.51 and –0.27 A cm⁻² were achieved at thermoneutral voltage (~1.28 V) and the operating temperatures of 700, 650, 600, 550 and 500 °C, respectively (Fig. 1c). The measured current density is 8 times higher than the previous research in a tubular cell with a similar positrode, in which the current density was limited to around –0.10 A cm⁻² at ~1.28 V and 600 °C [24]. This is also higher than our previous work with BGLC587–BZCY541 composite positrode cells (–0.65 A cm⁻² at 1.3 V and 600 °C) [25]. Furthermore, we demonstrated an excellent performance of the cell with peak power densities of 506, 667 and 833 mW cm⁻², respectively, at 600, 650 and 700 °C in fuel cell mode as well (more details see Note S1 and Fig. S2). The results confirmed that the BGLC1082–BZCY541 composite positrode exhibits remarkable electrocatalytic activity towards both the ORR and OER processes.

The measured (V_{OC}) and theoretical (V_T) open circuit voltages revealed increasing discrepancies upon temperature increase (Fig. 1c). For a better understanding of this phenomenon, electrochemical impedance spectra (EIS) measurements were performed at OCV (Fig. 1d). An equivalent circuit model (Fig. S4a) was used for the EIS data fitting. The ohmic resistance (R_{Ω}) is determined by the high frequency intercept with the real axis. Considering the mixed ionic and electronic transport properties of the BZCY541 electrolyte, R_{Ω} is the sum of ionic resistance ($R_{\Omega,i}$) and electronic resistance ($R_{\Omega,e}$). The ionic transference number (t_i) and the electronic transference number (t_e) can be calculated (Fig. S5), accordingly [23,31,32]. The value of t_i decreased from 0.996 at 500 °C to

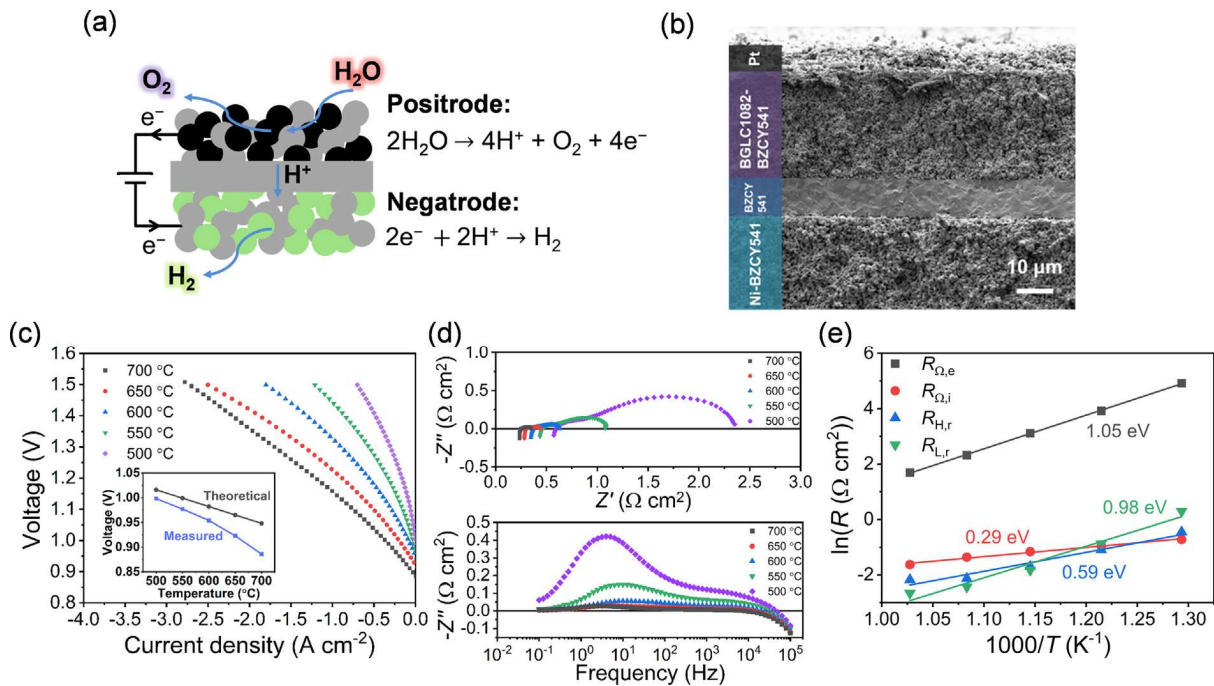


Fig. 1. (a) Schematic illustration of the PCCs for steam electrolysis. (b) SEM cross-section image of the as-prepared PCCs. (c) Polarization curves recorded in steam electrolysis mode with 30% steam/air supplied to the positrode and 20% H_2/N_2 to the negatrode (inside, the comparison between the measured open circuit voltages and the theoretical values); and the corresponding electrochemical impedance spectra recorded at OCV (d). (e) Arrhenius plot of the electronic resistance ($R_{\Omega,e}$), ionic resistance ($R_{\Omega,i}$), and corrected polarization resistance ($R_{H,r}$ and $R_{L,r}$).

0.965 at 700 °C, indicating the increased electronic conductivity at higher temperatures. By neglecting the contact resistances, the conductivity of the electrolyte (σ_{Ω}) can be calculated using the following equation

$$\lim_{\omega \rightarrow \infty} \{Z\} = R_{\Omega} + R_{\text{contact}} \approx \frac{L}{\sigma_{\Omega}} \quad (2)$$

where L is the thickness of the electrolyte. Therefore, the ionic ($\sigma_{\Omega,i}$) and electronic ($\sigma_{\Omega,e}$) conductivities of the electrolyte can be determined (Fig. S6). Both $\sigma_{\Omega,i}$ and $\sigma_{\Omega,e}$ increased at elevated temperatures, with $\sigma_{\Omega,i}$ ranging from 0.002 to 0.006 S cm^{-1} between 500 and 700 °C, which is in good agreement with the previously reported BZCY541 conductivity values [33]. Besides, the $\sigma_{\Omega,e}$ is more than 2 orders of magnitude lower than $\sigma_{\Omega,i}$ at low temperatures. To quantify this electronic leakage based on the EIS results, we employed the method developed by Choi et al. [34]

$$I_{\text{OC}}(e^-) = -I_{\text{OC}}(H^+) = -\frac{V_{\text{OC}}}{R_t} \left(1 - \frac{V_{\text{OC}}}{V_N}\right) \quad (3)$$

where $I_{\text{OC}}(e^-)$ and $I_{\text{OC}}(H^+)$ are the electronic and protonic current densities at open circuit voltages, and R_t is the total resistance at V_{OC} . The current leakage was estimated to be between 0.007 A cm^{-2} at 500 °C, and 0.163 A cm^{-2} at 700 °C, confirming the impact of the p-type electronic conduction through the electrolyte and an accelerated current leakage at higher temperatures.

The polarization resistance (R_p) is given by the intercepts between high and low frequencies with the real axis. In the Nyquist plot, the impedance curve shows a predominant low frequency arc ($R_{L,r}$) that is generally assigned to a surface related diffusion process and a high frequency arc ($R_{H,r}$) that is assigned to a charge transfer process. The real polarization resistance at high frequencies ($R_{H,r}$) and low frequencies ($R_{L,r}$) are obtained from the same equivalent circuit model fitting. Current leakage leads to discrepancies between apparent values and true polarization values, that is determined by considering the current leakage (as pre-

sented in Table S2). The activation energy (E_a) is calculated by using the corrected resistance values obtained from the fitting results. The calculated E_a of R_i is 0.29 eV, which is relatively low in comparison with the reported E_a values of proton migration through the bulk [35]. Besides, the E_a of $R_{H,r}$ and $R_{L,r}$ are 0.59 and 0.98 eV, respectively. For negatrode-supported PCCs, the polarization resistance is demonstrated mainly from the positrode [25,28], and the E_a of $R_{L,r}$ is quite close to the reported E_a of the oxygen surface exchange coefficient for ordered cobaltites [36,37]. The E_a of R_e shows the highest values of 1.05 eV.

3.2. Current leakage and faradaic efficiency in PCCCEL

Under polarization, the conduction of electron holes through the BZCY electrolyte leads to the current leakage during electrolysis, resulting in a net reduction of the effective current for proton reduction at the negatrode (step 5 in Fig. 2a). Zhu et al. [19] reported that the flux of all charge carriers under high polarization current is dominated by the migration flux which is directly proportional to the conductivity of the electrolyte under the conditions at positrode side and thus, related to the transference number of the corresponding charge carriers, as at open circuit conditions.

The total current density, that is the applied current density, and the terminal voltages are summarized in Fig. 2(b). The faradaic efficiency was calculated by comparing the detected H_2 production rate with the theoretical values (Fig. 2c). The measurement was performed under galvanostatic mode at each measurement point for more than 30 min until the detected outlet gas composition was stable. At V_{TN} , the maximum faradaic efficiency reached 64% at 550 °C (Fig. 2c), which is competitive with previous reports as summarized in Table S1. At a given voltage, the faradaic efficiency decreased upon temperature increase. Moreover, the faradaic efficiency reduced dramatically with the increase of terminal voltage.

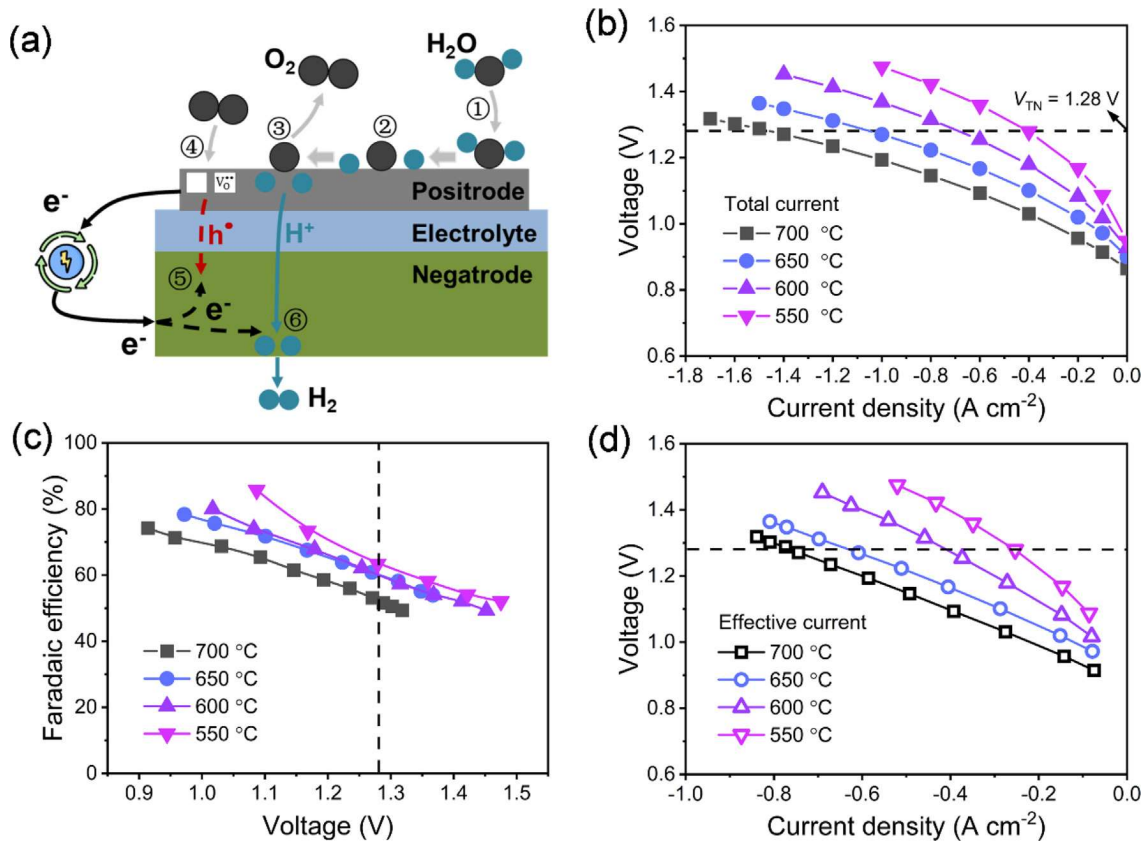


Fig. 2. Characterizations of PCCs with BGLC1082-BZCY541 composite positrode for steam electrolysis at different operating temperatures. (a) Schematic illustration of the PCCs for steam electrolysis accompanied with electronic current leakage (step 1: water adsorption, step 2: incorporation, step 3: oxygen release and proton transfer, step 4: oxygen incorporation, step 5: $\text{Null} = \text{h}^* + \text{e}^-$, step 6: proton reduction [24]). (b) Apparent polarization curves. (c) The measured faradaic efficiency as a function of voltage. (d) Polarization curves corrected by the corresponding faradaic efficiency and plotted as a function of the effective current density.

Vøllestad et al. [24] demonstrated the relation between the concentration of electron holes and the potential E

$$[\text{h}^*] = K_{\text{OX}} [\text{OH}_0] p_{\text{H}_2\text{O}}^{-\frac{1}{2}} p_{\text{O}_2}^{\frac{1}{4}} = K_{\text{OX}} \exp \left[\frac{F(E - E^0)}{RT} \right] \quad (4)$$

Additionally, as reported by Duan et al. [12] the steam partial pressure ($p_{\text{H}_2\text{O}}$) and oxygen partial pressure (p_{O_2}) at the interface of electrolyte/positrode can be estimated using Fick's first law. The $p_{\text{H}_2\text{O}}$ at the interface is decreased during electrolysis operation at high current density, and the generation of oxygen increases the p_{O_2} . Since higher p_{O_2} and lower $p_{\text{H}_2\text{O}}$ conditions promote the formation of electron holes, this leads to a negative feedback loop resulting in a more pronounced decrease of the faradaic efficiency at higher current density. Therefore, the effective current yielding net hydrogen production is reduced to -0.26 , -0.41 , -0.63 and -0.76 A cm^{-2} at 1.28 V and temperatures of 550, 600, 650 and 700 °C, respectively (Fig. 2d).

3.3. Long-term durability of PCCEL

The durability of electrolysis cells and stacks is a crucial factor in determining the success of a novel technology. To date, results about degradation of PCCs during long-term experiments are scarce as the technology is nascent. The study conducted by Zhou et al. reported a voltage drift of 40 mV/1000 h during PCCEL at -1.0 A cm^{-2} and 650 °C over a period of 1833 h [28]. In the present study, the short-term stability of PCCEL under variable electrolysis current was investigated first at 550 and 600 °C with 30% H_2O supplied to the positrode (Fig. S8). By increasing the current

density from -0.2 to -1.0 A cm^{-2} , the terminal voltage remained stable and constant at each step, demonstrating the stability of the cell at various current densities. Another fresh cell was tested for 1680 h to assess the long-term durability. The corresponding life cycle is shown in Fig. 3(a). In the first 300 h, a mixture of 10% H_2O in air was supplied to the positrode, and the cell was operated at -0.4 A cm^{-2} , corresponding to a cell voltage of 1.180 V. The cell voltage remained constant over the period, suggesting a negligible degradation. At $t = 300 \text{ h}$, the current density was set to -0.8 A cm^{-2} , corresponding to a terminal voltage of 1.294 V that is slightly above V_{TN} (1.28 V). The cell was operated in these conditions for 215 h. The power interruption at $t = 432 \text{ h}$ did not cause any significant damage to the cell, as the nominal operating voltage of $\sim 1.294 \text{ V}$ was recovered, demonstrating the robustness of the tested cell.

At $t = 515 \text{ h}$, the steam content in the positrode gas feed was increased to 30%, while the current was kept constant at -0.8 A cm^{-2} . The cell was operated in these conditions until $t = 1680 \text{ h}$. By increasing the steam content from 10% to 30%, the terminal voltage dropped by 23 mV from ~ 1.294 to $\sim 1.271 \text{ V}$. The cell voltage was nearly stable or slightly decreasing for several hundred hours until another power supply failure occurred at $t = 1251 \text{ h}$. After the power recovery, the voltages turned back to 1.291 V. Although there is still a difference of $\sim 20 \text{ mV}$, the results confirm the excellent stability of the cell with BGLC1082-BZCY541 and its robustness when operated at -0.8 A cm^{-2} . After this long-term experiment, the cell was investigated by means of SEM (Fig. 3b). No indication of delamination could be detected between the two electrode/electrolyte interfaces. Moreover, the elemental

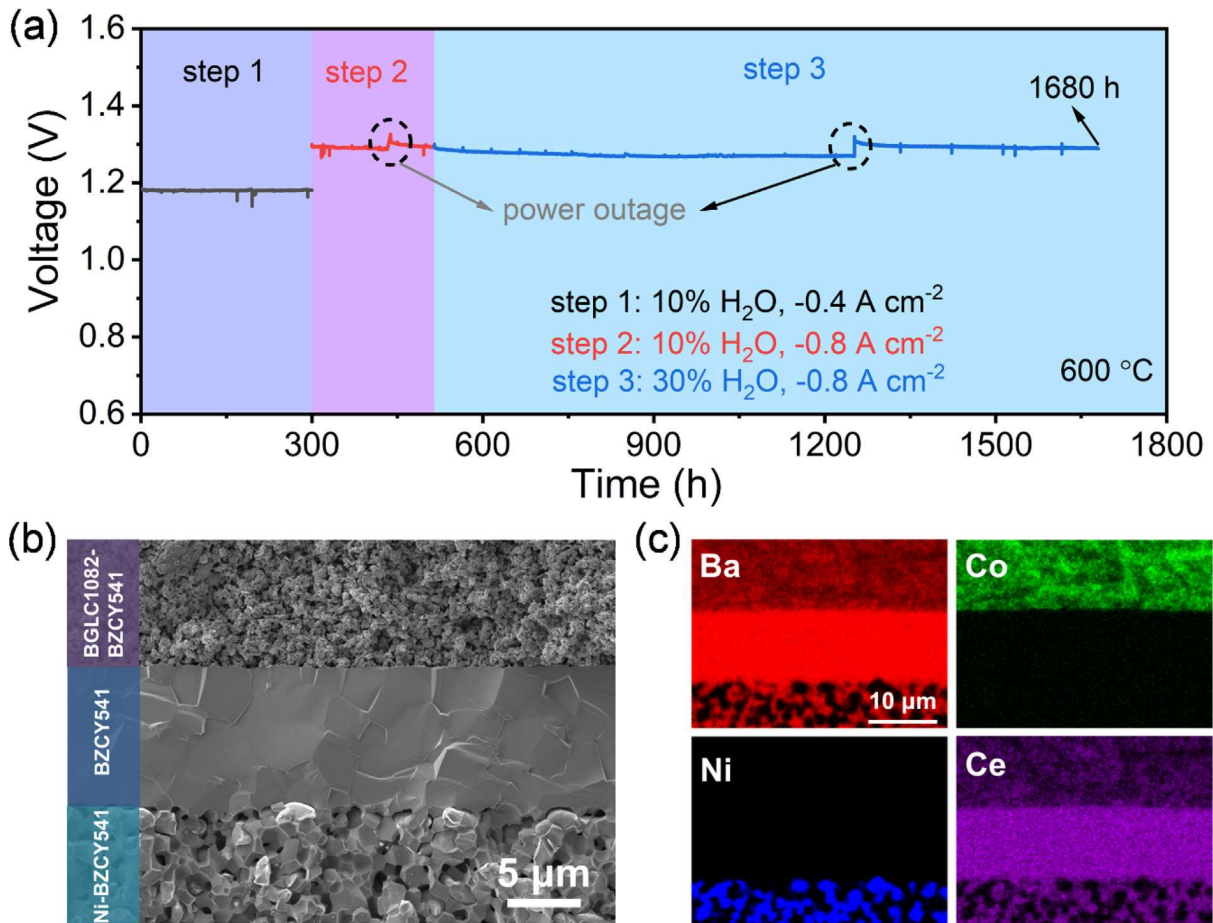


Fig. 3. Long-term stability of PCCs measured in steam electrolysis mode. (a) The voltage evolution in galvanostatic mode with 10%–30% steam/air in the positrode and 20% H₂/N₂ in the negatrode at 600 °C for 1680 h. (b) Cross-section SEM image and (c) EDX elemental mapping of the PCC after long-term steam electrolysis measurement for 1680 h.

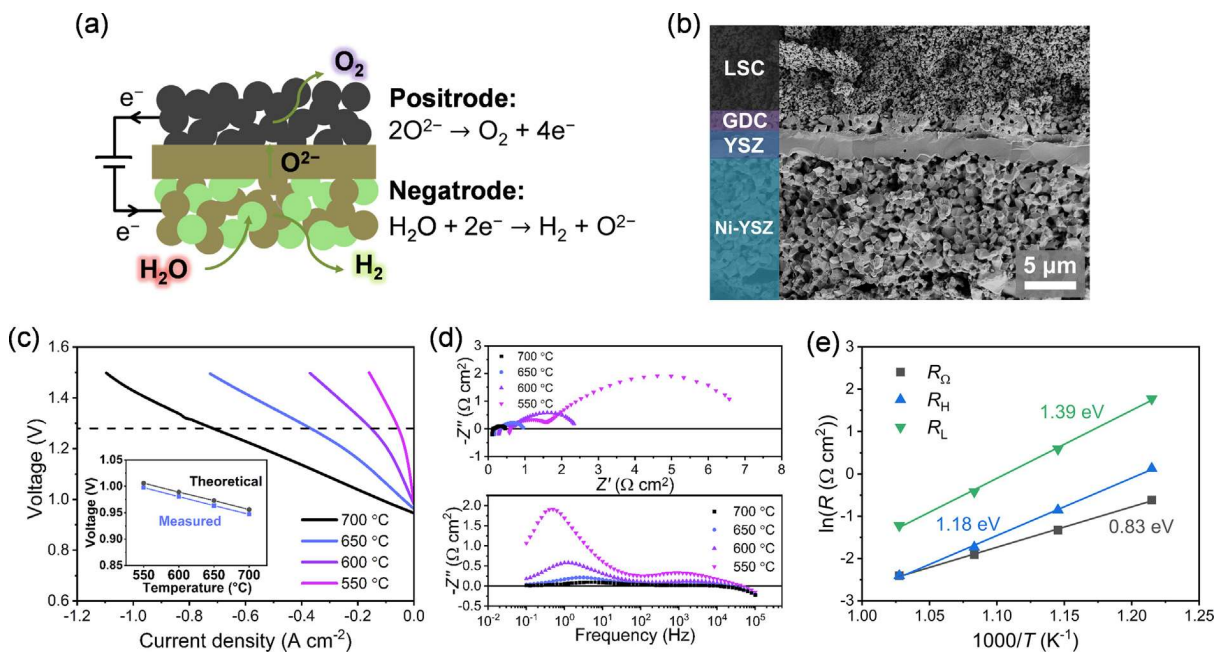


Fig. 4. Characterization of a state-of-the-art commercial SOC for steam electrolysis. Air was supplied to the positrode and a mixture of 20% H₂-30% H₂O-50% N₂ was supplied to the negatrode. (a) Schematic illustration of SOCs for steam electrolysis. (b) SEM cross-section image of the commercial SOC. (c) Polarization curves as a function of current density (inside, the comparison between the measured open circuit voltage and the theoretical value). (d) Nyquist and Bode plots of the electrochemical impedance spectra recorded at OCV. (e) Arrhenius plots of the ohmic resistance (R_{Ω}) and the polarization resistance (R_H and R_L).

distribution remained homogeneous within the different materials (Fig. 3c, additional elements showing in Fig. S9). It should be noted that Ni migration was not observed at the negatrod after the long time PCCEL operation, despite a current density as high as -0.8 A cm^{-2} . SEM images with higher magnifications in Fig. S10 did not show any evidence of microstructural change in both electrodes, demonstrating the high reliability of the PCC under the tested conditions. This feature is to be compared with the voltage drift of about 40 mV kh^{-1} reported for negatrod supported SOCs operated in steam electrolysis [38], whose Ni-YSZ cermet electrode is prone to degradation. Though its origin is not clearly elucidated, this degradation is possibly related to Ni migration via surface diffusion of Ni(OH)_x species especially at high operating current density and high relative humidity content, leading to the high degradation rate in SOCs [8,9,39]. This suggests that optimization strategies for mitigating degradation in electrolysis are likely to differ between PCCs and SOCs.

3.4. Hydrogen production and energy efficiency at intermediate temperatures

State-of-the-art commercial SOCs (ASC-400B, Elcogen AS, Estonia) were tested for the sake of comparison between SOEL and PCCEL at intermediate temperatures. The same test apparatus and comparable testing conditions to PCCEL were used for SOEL, and the results are shown in Fig. 4. In principle, one of the main differences between SOEL and PCCEL (Fig. 1a) is that in SOEL, the steam is supplied to the SOC negatrod (Fig. 4a). A distinctive feature of the reference SOC is the $\sim 3 \mu\text{m}$ thin YSZ electrolyte (Fig. 4b), which was developed for intermediate SOEL operation. During electrolysis, the current densities at V_{TN} reach -0.055 , -0.153 , -0.368 and -0.716 A cm^{-2} at 550, 600, 650 and 700 °C, respectively. The apparent values of the current density obtained in SOEL were lower than those obtained in PCCEL over the entire temperature range. In contrast, the deviation between V_{OC} and V_{T} in SOEL is limited (less than 1%) compared to PCCEL and does not show any temperature dependence (insert Fig. 4c). The small difference is supposed to be originating from a fraction of gas leakage at the sealing area. Since YSZ electrolyte can be considered as a pure oxygen ion conductor in the tested operating range, the faradaic efficiency of SOEL is considered to be close to 100% [40–42]. Fig. 4(d) shows the EIS recorded at OCV. The R_{Ω} mainly represents the losses associated to the oxygen ion transport through the electrolyte. R_{Ω} values in the SOC are 0.54, 0.27, 0.15 and $0.09 \Omega \text{ cm}^2$ at 550, 600, 650 and 700 °C, respectively. The corresponding activation energy of 0.83 eV for R_{Ω} in SOCs agrees with oxygen ion transport (Fig. 4e) [43,44]. In the PCC, the corresponding values of $R_{\Omega,i}$ are 0.38, 0.31, 0.26 and $0.20 \Omega \text{ cm}^2$ with an associated activation energy of 0.29 eV for $R_{\Omega,i}$ for the transport of protons (Fig. 1e). The ohmic losses in SOCs were lower than in PCCs at temperatures above 600 °C. While, below this temperature, the ohmic losses in PCCs became lower than in SOCs. The thin electrolyte in the commercial SOCs enable to reduce the ohmic resistance significantly [45]. However, the higher activation energy for oxygen ion conduction compared to proton conduction, makes it challenging to achieve high performance at low temperatures, i.e., below 600 °C with state-of-the-art YSZ electrolyte. The higher proton conductivity values (Fig. S7) in conjunction with a lower activation energy makes PCCs more suited for operation at lower temperatures. By analogy with SOCs, the reduction of electrolyte thickness in PCCs can be a suitable strategy to further improve cell performance at lower temperatures, though its relative impact will be reduced in magnitude due to the lower activation energy value. It is important to note that a reduced electrolyte thickness is likely to increase the current leakage through the PCC electrolyte which may in fine be unfavorable from an energetic point of view. PCCs optimization

with thin film electrolyte pose an interesting challenge that deserves further study [46].

The Nyquist plot in Fig. 4(d) suggests 2 depressed arcs; therefore, the EIS spectra recorded on the SOC were fitted by the equivalent circuit with 2 RQ elements (Fig. S4b). The E_a corresponding to high frequency resistances (R_{H}) and low frequency resistances (R_{L}) are 1.18 and 1.39 eV, respectively. Again, both values are higher than the characteristic ones in PCCs (Fig. 1e). At low frequency, the main difference may be attributed to the steam diffusion. The diffusion length of steam on positrod side in PCCs is typically $\sim 30 \mu\text{m}$ (Fig. 1a), whereas it is about $400 \mu\text{m}$ in the reference SOC negatrod we tested, which is more than an order of magnitude greater. Considering various overpotential losses in the full cells, the losses originating from the gas diffusion make one of the major distinctions between proton conducting and oxygen ion conducting ceramic cells especially at high current density. By using a mathematical analysis, Zheng et al. reported that PCCs possess lower concentration overpotentials compared to SOCs in the negatrod-supported cell configuration [47].

The H_2 production rate in PCCEL was calculated as a function of the terminal voltage at different temperatures (Fig. 5a). The production rates are 1.78, 2.86, 4.39 and $5.30 \text{ mL min}^{-1} \text{ cm}^{-2}$ at 550, 600, 650 and 700 °C and 1.28 V. The H_2 production rates in SOEL were calculated based on the polarization curves upon the reasonable assumption of a 100% faradaic efficiency (Fig. 5b). PCCEL demonstrated a higher H_2 production rate than SOEL at all tested temperatures.

In addition to the hydrogen production rate, the electricity consumption is also a very important factor that determines the price of the produced hydrogen. The electricity consumption was calculated for 1 kg H_2 production at V_{TN} for PCCEL and SOEL by considering the current densities and hydrogen production rate (Fig. 6a–c). In a single cell level analysis, only the electricity supplied to the cells was considered as the power input which can be defined as

$$\text{power(input)} = V \times I \quad (5)$$

where I is the current and V is the terminal voltage. The energy conversion efficiency can be described as

$$\eta_{\text{ECE}} = \frac{\text{power(output)}}{\text{power(input)}} \quad (6)$$

where the power (output) is the chemical energy of the produced hydrogen. Considering the lower heating value for hydrogen, the power (output) can be written as

$$\text{power(output)} = \frac{I \times \eta_{\text{FE}}}{z \times F} \times \Delta H_{\text{H}_2, \text{LHV}} \quad (7)$$

where I is the current, η_{FE} is faradaic efficiency, z is 2 for steam electrolysis, F is Faraday's constant and $\Delta H_{\text{H}_2, \text{LHV}}$ is the low heating value for hydrogen ($241.8 \text{ kJ mol}^{-1}$ or $33.33 \text{ kW h kg}^{-1}$).

At V_{TN} for SOEL, the electricity consumption is $\sim 34 \text{ kW h kg}^{-1}$, which is very close to the lower heating value of hydrogen and remains temperature independent. Thus, η_{ECE} remains close to 100% over the entire temperature range for SOEL (Fig. 6c). However, in PCCEL, the specific electricity consumption was consistently higher and increased from 54 to 66 kW h kg^{-1} upon temperature increase from 550 up to 700 °C at V_{TN} (Fig. 6c). This specific energy consumption is to be compared with other electrolysis technologies at low temperature such as PEMEL ($47\text{--}66 \text{ kW h kg}^{-1}$), AEL ($47\text{--}66 \text{ kW h kg}^{-1}$) and AEMEL ($51.5\text{--}66 \text{ kW h kg}^{-1}$) [48].

In PCCEL, the energy consumption above $33.33 \text{ kW h kg}^{-1}$ of produced hydrogen is an energy that must be supplied to the cell without being converted into hydrogen molecules. This additional energy demand is due to the current leakage through the electrolyte, resulting in the lower faradaic efficiency. This corresponds

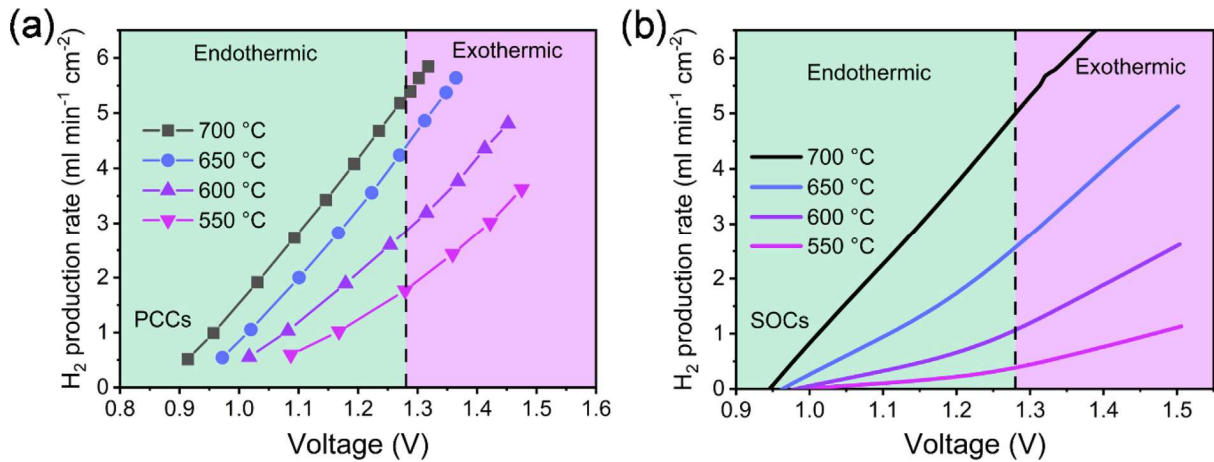


Fig. 5. Hydrogen production rate as a function of voltage at temperatures of 550–700 °C in PCCEL (a) and SOEL (b).

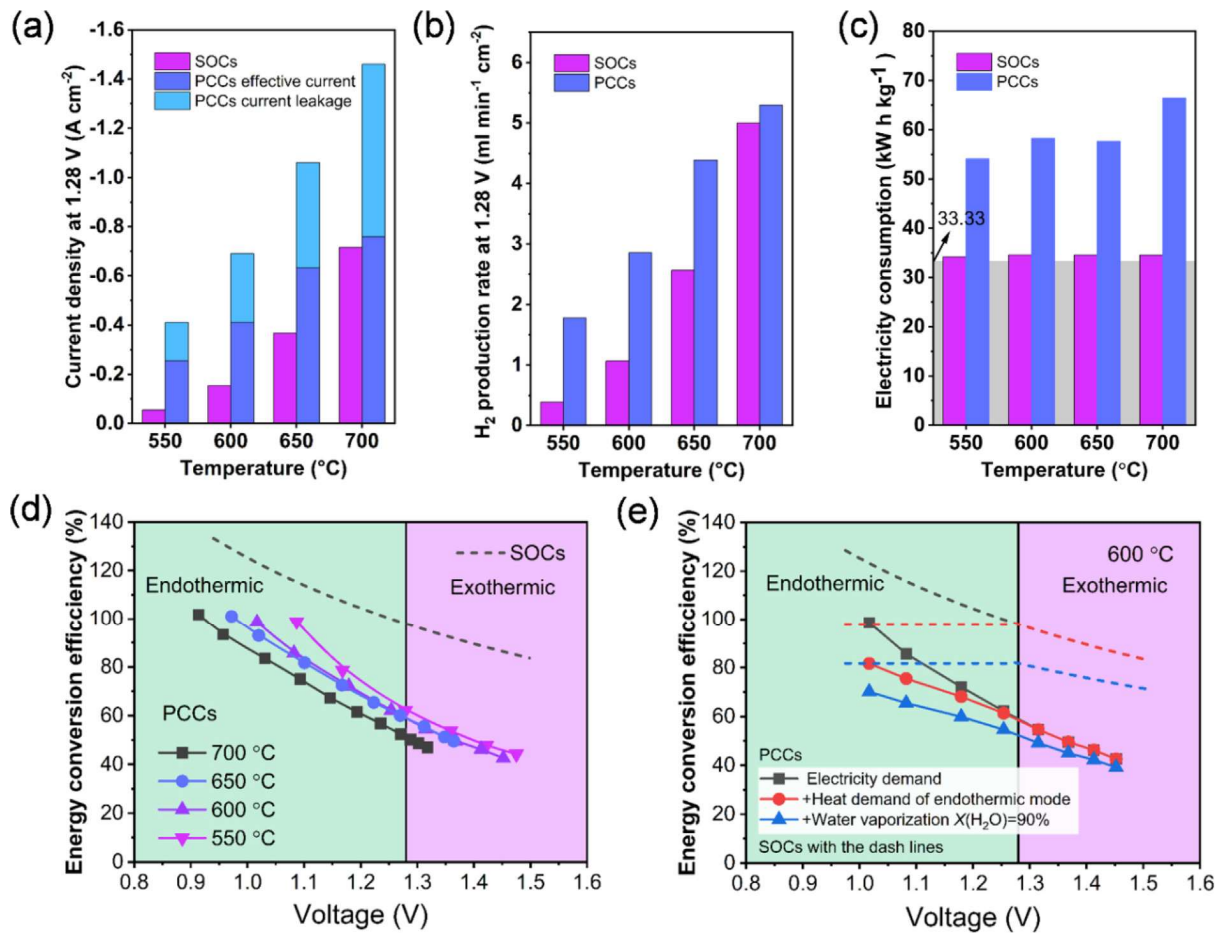


Fig. 6. Comparison between PCCEL and SOEL at thermal neutral voltage (~1.28 V). (a) The current density, (b) hydrogen production rate and (c) electricity consumption for producing 1 kg hydrogen as a function of operating temperatures from 550 to 700 °C. (d) Calculated energy conversion efficiencies of PCCEL and SOEL considering free heat sources. (e) Energy conversion efficiencies of PCCEL and SOEL considering additional heat demand for endothermal operation and water vaporization.

to an energy conversion efficiency η_{ECE} of 62% and 52%, at 550 and 700 °C, respectively (Fig. 6d). Therefore, a lower operating temperature is favorable to reduce current leakage and thus to promote the energy efficiency in PCCEL. Endothermal operation, which is at a terminal voltage below V_{TN} , is an attractive feature of this electrolysis technology, as electrical efficiencies above 100% can be reached at the cell level in SOCs. In endothermal operating regime

that is at low overpotential, η_{ECE} for PCCEL ranges from ~60% to ~100% (Fig. 6d). Nonetheless, endothermal operation consumes energy that must be accounted into the energy input unless provided by a free heat source for a more accurate evaluation. This part of energy can be written as

$$\text{power } (V_{\text{cell}} < V_{\text{TN}}) = (V_{\text{TN}} - V_{\text{cell}}) \times I \times \eta_{FE} \quad (8)$$

Additionally, the vaporization of water is energy consumption as well, and this part of energy can be written as

$$\text{Power}(\text{watervaporization}) = \frac{\lambda_{\text{H}_2\text{O}} \times I \times \eta_{\text{FE}}}{z \times F \times X(\text{H}_2\text{O})} \quad (9)$$

where $\lambda_{\text{H}_2\text{O}}$ is the water latent heat and $X(\text{H}_2\text{O})$ is the water conversion rate. For the calculation, a high conversion rate was assumed to be 90%, which is aligned with industrial values for SOEL. Considering electricity as the energy source for endothermal operation, the η_{ECE} for SOEL decreased down to around 100% (Fig. 6e). The energy demand for water vaporization accounts for additional ~20 points of efficiency. In PCCEL, the energy conversion efficiency remains lower than for SOEL, however with a reduced gap in the endothermal operating zone. At the system level, the gap can be further reduced to the benefit of PCCEL if one considers the necessary purification of hydrogen. Due to the ambipolar transport of oxygen ions and protons in PCC electrolyte, a small steam partial pressure of ~0.3% is established on the negatrod side [24], depending on the oxygen ion transference number. In SOEL, steam content can be as high as 20% in the outlet gas. If water vapor is separated by condensation, there are approximately two orders of magnitude of thermal energy in water vapor that could be wasted in SOEL compared to PCCEL.

In summary, considering the overpotential dependency of the hole concentration and, consequently, the faradaic efficiency (Eq. (4)), PCCEL operated in an endothermal mode appears even more meaningful than for any other electrolysis technology and is to be favored to maximize energy conversion efficiency. This would require an external heat source at sufficient temperature in order to maintain the system at the right operating temperature and avoid cooling. Considering that a temperature of 600 °C is more favorable for the handling of superheated steam than a temperature of 800 °C that would be required for conventional SOEL, this makes PCCEL a technology of choice for the valorization of high temperature waste heat.

4. Conclusions

The BGCL1082-BZCY541 composite positrode for PCCs exhibits high electrocatalytic activity towards ORR and OER at intermediate temperatures (500–700 °C). We demonstrated a PCC cell with excellent durability in electrolysis mode at ~1.28 V for 1680 h with a current density as high as -0.8 A cm^{-2} . This is 8 times higher than the previous report on tubular cells. The electrolysis cell operated at intermediate temperatures with a specific energy consumption comprised between 54 and 66 kW h kg^{-1} , which is comparable to low temperature electrolysis technologies, while showing a hydrogen production rate systematically higher than SOEL performed with a commercial reference cell. In other words, at the rated hydrogen production, PCCEL requires less active surface area than SOEL. The reduced faradaic efficiency and comparatively low energy conversion efficiency in PCCEL are caused by the current leakage through the BZCY electrolyte. This can be mitigated by operation at reduced temperatures and in endothermal mode, which makes PCCEL a technology of choice to valorize high temperature waste heat from industrial processes into hydrogen. To increase the faradaic efficiency, by optimizing materials, the cell design, or the operating strategy is a key challenge to address for future developments of PCCEL in order to achieve even more superior techno-economic merits.

Declaration of competing interest

The authors declare that they have no known competing financial interests or personal relationships that could have appeared to influence the work reported in this paper.

Acknowledgments

The China Scholarship Council is acknowledged for the doctoral scholarship of Haoyu Zheng (201806160173). The German Federal Ministry for Education and Research is acknowledged for funding via the Project ARCADE (03SF0580A).

Appendix A. Supplementary material

Supplementary data to this article can be found online at <https://doi.org/10.1016/j.jechem.2023.07.030>.

References

- [1] IEA, Global Hydrogen Review 2022, <https://www.iea.org/reports/global-hydrogen-review-2022>, 2022.
- [2] M. Younas, S. Shafique, A. Hafeez, F. Javed, F. Rehman, Fuel 316 (2022).
- [3] IEA, Hydrogen, <https://www.iea.org/reports/hydrogen>, 2022.
- [4] T. Terlou, C. Bauer, R. McKenna, M. Mazzotti, Energ. Environ. Sci. 15 (2022) 3583–3602.
- [5] W. Zhang, M. Liu, X. Gu, Y. Shi, Z. Deng, N. Cai, Chem. Rev. 123 (2023) 7119–7192.
- [6] A. Hauch, S.H. Jensen, S. Ramousse, M. Mogensen, J. Electrochem. Soc. 153 (2006) A1741–A1747.
- [7] A. Sciazko, T. Shimura, Y. Komatsu, N. Shikazono, J. Therm. Sci. Technol. 16 (2021) JTST0013.
- [8] M.P. Hoerlein, M. Riegraf, R. Costa, G. Schiller, K.A. Friedrich, Electrochim. Acta 276 (2018) 162–175.
- [9] M.B. Mogensen, M. Chen, H.L. Frandsen, C. Graves, A. Hauch, P.V. Hendriksen, T. Jacobsen, S.H. Jensen, T.L. Skafte, X. Sun, Fuel Cells 21 (2021) 415–429.
- [10] A. Faes, A. Hessler-Wyser, A. Zryd, J. Van Herle, Membranes 2 (2012) 585–664.
- [11] L. Bi, S. Boulfrad, E. Traversa, Chem. Soc. Rev. 43 (2014) 8255–8270.
- [12] C. Duan, J. Huang, N. Sullivan, R. O'Hayre, Appl. Phys. Rev. 7 (2020).
- [13] G.P. Panayiotou, G. Bianchi, G. Georgiou, L. Aresti, M. Argyrou, R. Agathokleous, K.M. Tsamos, S.A. Tassou, G. Florides, S. Kalogirou, P. Christodoulides, Energy Procedia 123 (2017) 335–345.
- [14] G. Bianchi, G.P. Panayiotou, L. Aresti, S.A. Kalogirou, G.A. Florides, K.M. Tsamos, S.A. Tassou, P. Christodoulides, Energy Ecol. 4 (2019) 211–221.
- [15] H. An, H.-W. Lee, B.-K. Kim, J.-W. Son, K.J. Yoon, H. Kim, D. Shin, H.-I. Ji, J.-H. Lee, Nat. Energy 3 (2018) 870–875.
- [16] C. Duan, J. Tong, M. Shang, S. Nikodemski, M. Sanders, S. Ricote, A. Almansoori, R. O'Hayre, Science 349 (2015) 1321–1326.
- [17] C.C. Duan, R. Kee, H.Y. Zhu, N. Sullivan, L.Z. Zhu, L.Z. Bian, D. Jennings, R. O'Hayre, Nat. Energy 4 (2019) 230–240.
- [18] D. Han, X. Liu, T.S. Bjørheim, T. Uda, Adv. Energy Mater. 11 (2021) 2003149.
- [19] H. Zhu, S. Ricote, C. Duan, R.P. O'Hayre, D.S. Tsvetkov, R.J. Kee, J. Electrochem. Soc. 165 (2018) F581–F588.
- [20] H. Zhu, S. Ricote, C. Duan, R.P. O'Hayre, R.J. Kee, J. Electrochem. Soc. 165 (2018) F845–F853.
- [21] Y. Zhang, R. Knibbe, J. Sunarso, Y. Zhong, W. Zhou, Z. Shao, Z. Zhu, Adv. Mater. 29 (2017) 1700132.
- [22] N. Wang, C. Tang, L. Du, R. Zhu, L. Xing, Z. Song, B. Yuan, L. Zhao, Y. Aoki, S. Ye, Adv. Energy Mater. 12 (2022) 2201882.
- [23] R. Strandbakke, V.A. Cherepanov, A.Y. Zuev, D.S. Tsvetkov, C. Argiris, G. Soukouni, S. Prunte, T. Norby, Solid State Ion. 278 (2015) 120–132.
- [24] E. Vøllestad, R. Strandbakke, M. Tarach, D. Catalan-Martinez, M.L. Fontaine, D. Beaff, D.R. Clark, J.M. Serra, T. Norby, Nat. Mater. 18 (2019) 752–759.
- [25] H. Zheng, M. Riegraf, N. Sata, R. Costa, J. Mater. Chem. A 11 (2023) 10955–10970.
- [26] E. Vøllestad, M. Schrade, J. Segalini, R. Strandbakke, T. Norby, J. Mater. Chem. A 5 (2017) 15743–15751.
- [27] K. Leonard, J. Druce, V. Thoreton, J.A. Kilner, H. Matsumoto, Solid State Ion. 319 (2018) 218–222.
- [28] Y. Zhou, E. Liu, Y. Chen, Y. Liu, L. Zhang, W. Zhang, Z. Luo, N. Kane, B. Zhao, L. Soule, Y. Niu, Y. Ding, H. Ding, D. Ding, M. Liu, ACS Energy Lett. 6 (2021) 1511–1520.
- [29] J.H. Kim, S. Yoo, R. Murphy, Y. Chen, Y. Ding, K. Pei, B. Zhao, G. Kim, Y. Choi, M. Liu, Energ. Environ. Sci. 14 (2021) 1506–1516.
- [30] Y. Chen, Y. Choi, S. Yoo, Y. Ding, R. Yan, K. Pei, C. Qu, L. Zhang, I. Chang, B. Zhao, Y. Zhang, H. Chen, Y. Chen, C. Yang, B. deGlee, R. Murphy, J. Liu, M. Liu, Joule 2 (2018) 938–949.
- [31] M. Liu, H. Hu, J. Electrochem. Soc. 143 (1996) L109–L112.
- [32] D. Huan, W. Wang, Y. Xie, N. Shi, Y. Wan, C. Xia, R. Peng, Y. Lu, J. Mater. Chem. A 6 (2018) 18508–18517.
- [33] K. Katahira, Y. Kohchi, T. Shimura, H. Iwahara, Solid State Ion. 138 (2000) 91–98.
- [34] S. Choi, T.C. Davenport, S.M. Haile, Energ. Environ. Sci. 12 (2019) 206–215.
- [35] K.D. Kreuer, Annu. Rev. Mat. Res. 33 (2003) 333–359.
- [36] M. Burriel, J. Peña-Martinez, R.J. Chater, S. Fearn, A.V. Berenov, S.J. Skinner, J.A. Kilner, Chem. Mater. 24 (2012) 613–621.

- [37] M.V. Ananyev, V.A. Eremin, D.S. Tsvetkov, N.M. Porotnikova, A.S. Farlenkov, A. Y. Zuev, A.V. Fetisov, E.K. Kurumchin, *Solid State Ion.* 304 (2017) 96–106.
- [38] F. Tietz, D. Sebold, A. Brisse, J. Schefold, *J. Power Sources* 223 (2013) 129–135.
- [39] M.B. Mogensen, A. Hauch, X. Sun, M. Chen, Y. Tao, S.D. Ebbesen, K.V. Hansen, P. V. Hendriksen, *Fuel Cells* 17 (2017) 434–441.
- [40] J. Schefold, A. Brisse, F. Tietz, *J. Electrochem. Soc.* 159 (2011) A137–A144.
- [41] J. Schefold, A. Brisse, M. Zahid, *ECS Trans.* 28 (2010) 357–367.
- [42] C.M. Stoots, J.E. O'Brien, K.G. Condie, J.J. Hartvigsen, *Int. J. Hydrog. Energy* 35 (2010) 4861–4870.
- [43] C. Korte, A. Peters, J. Janek, D. Hesse, N. Zakharov, *PCCP* 10 (2008) 4623–4635.
- [44] R. Devanathan, W. Weber, S. Singhal, J. Gale, *Solid State Ion.* 177 (2006) 1251–1258.
- [45] F. Han, R. Mücke, T. Van Gestel, A. Leonide, N.H. Menzler, H.P. Buchkremer, D. Stöver, *J. Power Sources* 218 (2012) 157–162.
- [46] Y. Matsuzaki, Y. Tachikawa, Y. Baba, K. Sato, G. Kojo, H. Matsuo, J. Otomo, H. Matsumoto, S. Taniguchi, K. Sasaki, *J. Electrochem. Soc.* 167 (2020).
- [47] K.-Q. Zheng, M. Ni, Q. Sun, L.-Y. Shen, *Acta Mech. Sin.* 29 (2013) 388–394.
- [48] IRENA (2020), *Green Hydrogen Cost Reduction: Scaling up Electrolysers to Meet the 1.5 °C Climate Goal*, International Renewable Energy Agency, Abu Dhabi.

5.4 Article III

Hydrogen production with a protonic ceramic membrane reactor on porous Fe-Cr alloy

Haoyu Zheng, Noriko Sata, Feng Han, Amir Masoud Dayaghi, Fumitada Iguchi, Katherine Develos-Bagarinao, Truls Norby, Marit Stange, Rémi Costa

The manuscript has been submitted.

Hydrogen production with a protonic ceramic membrane reactor on porous Fe-Cr alloy

*Haoyu Zheng^{1,2}, Noriko Sata¹, Feng Han¹, Amir Masoud Dayaghi³, Fumitada Iguchi⁴,
Katherine Develos-Bagarinao⁵, Truls Norby³, Marit Stange⁶, Rémi Costa^{1*}*

¹ Institute of Engineering Thermodynamics, Electrochemical Energy Technology, German Aerospace Center (DLR), Pfaffenwaldring 38-40, D-70569 Stuttgart, Germany

² Institute of Building Energetics, Thermotechnology and Energy Storage (IGTE), University of Stuttgart, Pfaffenwaldring 31, D-70569 Stuttgart, Germany

³ Department of Chemistry, Centre for Materials Science and Nanotechnology (SMN), University of Oslo, NO-0315 Oslo, Norway

⁴ Department of Mechanical Engineering, College of Engineering, Nihon University, Koriyama, Fukushima 963-8642, Japan

⁵ Global Zero Emission Research Center, National Institute of Advanced Industrial Science and Technology, Tsukuba, Ibaraki 305-8569, Japan

⁶ SINTEF, Forskningsveien 1, NO-0373 Oslo, Norway

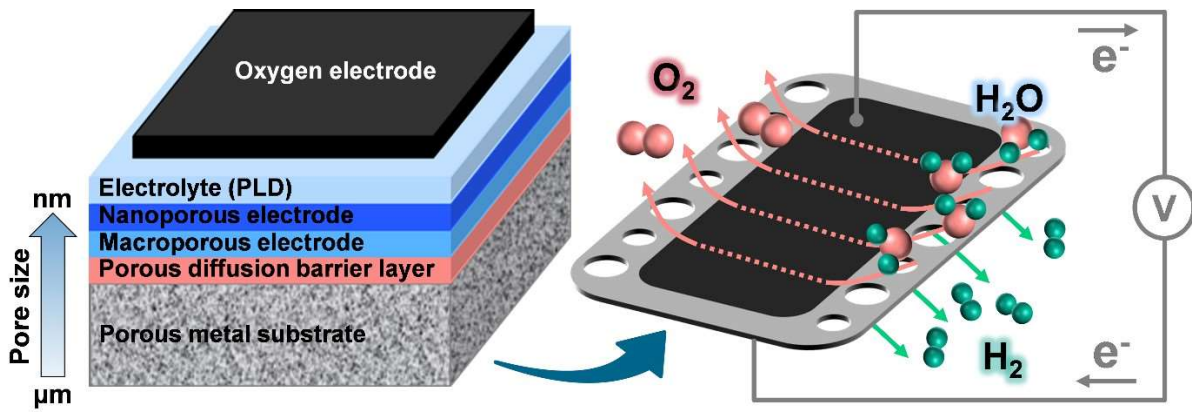
* Corresponding author.

Email: remi.costa@dlr.de

ABSTRACT

A metal supported design is desirable for ceramic electrochemical cells for its robustness. Yet, a strong alkaline character and a refractory nature of the electrolyte material makes it challenge to be densified onto a steel component. Here we show a metal supported protonic ceramic cell (MS-PCC) concept enabling ~90% ceramic materials savings compared to traditional cell design. The manufacturing route combines wet ceramic processing with sintering and thin film deposition at temperatures below 1000 °C. The critical diffusive elements were sufficiently confined, and the volume variation of the different functional layers limited to maintain the integrity of the thin film electrolyte. Applied to steam electrolysis for hydrogen production, the MS-PCC enabled a current density of about -0.84 A cm^{-2} at 600 °C at a terminal voltage of 1.3 V. This concept offers incomparable perspectives for scale-up and opens up a broad range of applications for hydrogen or Power-to-X applications.

Table of Contents Graphic



MAIN TEXT

Electrolysis is a key building block for Power-to-X technologies, where X can be hydrogen, syngas or hydrocarbons.¹ High temperature electrochemical cells operating at temperatures typically above 500 °C are especially attractive due to unrivalled energy conversion efficiency and fast kinetics.¹ Solid oxide cells (SOCs) and protonic ceramic cells (PCCs) are built upon oxygen ion conducting or proton conducting ceramic materials, respectively. Their mechanical robustness, sufficient for handling, stacking and operating at high temperature, is conferred by increasing the thickness of one of the constitutive cell layers that can be either the electrolyte or one out of the two electrodes. This requires a substantial amount of ceramic containing critical raw materials and often enforces compromises in terms of performance.

The metal supported cell design aims at replacing thick ceramic based electrode supports by a metallic substrate, capable of withstanding both oxidizing and reducing environment in temperature and capable of supporting thin ceramic functional layers. The use of a metal substrate made of ferritic stainless-steel results in cells with a high mechanical strength and allows to reduce dramatically the amount of ceramic materials.²⁻¹² Nowadays, different metal supported solid oxide cells (MS-SOCs) are based on oxygen ion conducting ceramic membranes. MS-SOCs from the company CERES are currently approaching commercialization, as prototypes in the power range of 100 kW to 1 MW have recently been demonstrated for fuel cell and electrolysis application.^{13, 14} This technology relies on a gadolinia-doped ceria (GDC) based electrolyte.¹⁵ The amphoteric nature of ceria, characterized by a Smith acid-base parameter $\alpha = -2.7$, mitigates excessive reactivity with volatile amphoteric or slightly acidic compounds, such as, chromium oxides (Cr_2O_3), granting thus a good thermo-chemo-mechanical compatibility with the ferritic stainless-steel components.^{16, 17} Yet in protonic ceramics, strong electropositive cations such as Ba confer a strong alkaline behaviour ($\alpha \sim -10.8$) to perovskites from the solid solution $\text{BaZr}_{1-x-y}\text{Ce}_x\text{Y}_y\text{O}_{3-\delta}$ (BZCY),¹⁸ broadly acknowledged as the state-of-the-art PCC electrolyte material. This is a desired property to enable the incorporation of protonic defects by water uptake ($\text{H}_2\text{O} + v\ddot{\text{O}} + \text{O}_\text{O}^x \leftrightarrow 2\text{OH}_\text{O}$ in Kröger Vink notation). However, this intrinsic property makes it highly reactive with many compounds presenting an amphoteric or acidic character, such as the volatile oxidized Cr and SiO_2 ($\alpha = 0.9$) species that could be formed and released by the stainless steel in the presence of oxygen or steam at high temperature.³ Even though the sintering temperature can be reduced from above 1500 °C to around 1300 °C, phase decomposition and contamination of

Publications

the electrolyte layer by the acidic oxides are commonly observed in MS-PCCs manufactured by sintering.¹⁹ The strong alkaline character of protonic ceramics changes the paradigm of developing a metal supported cell architecture. The promising potential of PCCs has been demonstrated recently by remarkably high performances in $5\times 5\text{ cm}^2$ sized cells and in reversible operation with a conventional fuel electrode supported design.^{20, 21} It comprises a thick ($>600\text{ }\mu\text{m}$) fuel electrode supporting layer, which is normally a cermet of NiO mixed with the electrolyte compound. Here we demonstrate a metal-supported protonic ceramic cell (MS-PCC) concept together with its manufacturing route (Figure S1) applied to steam electrolysis (Figure 1a). The thick cermet support is replaced by a porous metal support based on a Fe-Cr alloy, enabling an estimated $\sim 90\%$ ceramic materials saving - including a 95.7% reduction in NiO, which is a strategic material for the energy transition - compared to the state-of-the-art fuel electrode supported cell architecture (Figure 1b-d).

The strategy to realize a thin and dense electrolyte is based on the fabrication of a pore graded multi-layer assembly.^{22, 23} Over manufacturing, the temperature never exceeds $1000\text{ }^\circ\text{C}$ in order to prevent excessive Cr release. In this paper, we report a successful coating of dense BaZrO₃-based perovskite electrolyte layer on the porous metal supported substrate using pulsed laser deposition (PLD) as the key process, which is a well acknowledged thin-film fabrication technique for multi-elements materials of refractory nature.

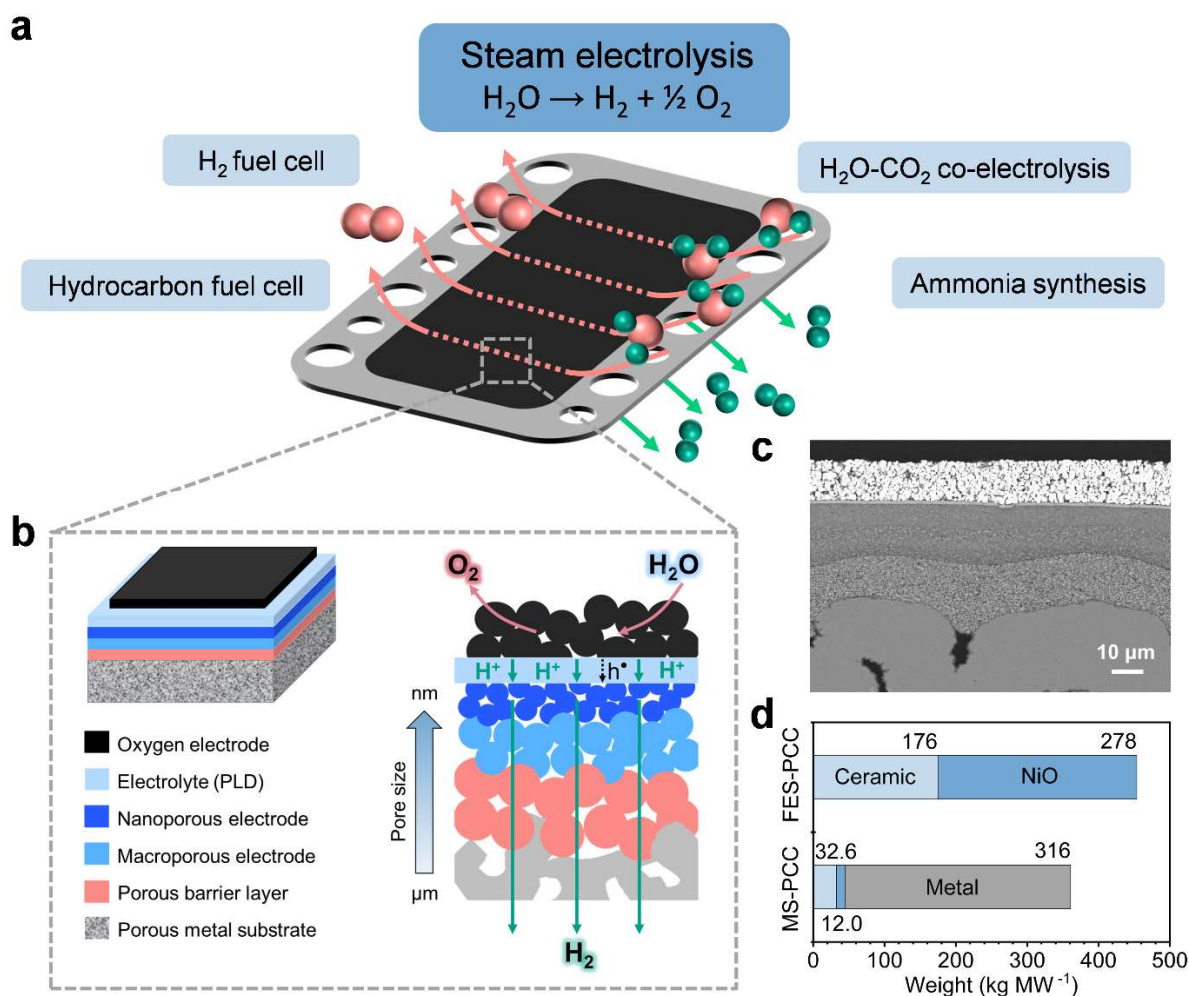


Figure 1. Concept of MS-PCC with thin-film electrolyte. (a) Schematic diagram of a MS-PCC stack cassette for Power-to-X application. (b) Illustration of the cross-sectional structure of a MS-PCC and the operating principals for steam electrolysis. (c) Cross-section SEM image of the MS-PCC with Pt oxygen electrode. (d) Estimated need of ceramic, NiO and metal for manufacturing a MW system comparing the MS-PCC with the fuel electrode supported protonic ceramic cell (FES-PCC) design. For the comparison, the performance values at 600 °C and 1.3 V were considered, as reported previously for FES-PCC,²⁴ and in this work, assuming the same faradaic efficiency. A thickness of 500 µm was set for the fuel electrode supporting layer.

The designed cell structure contains a porous metal substrate (Figure S2), an electronic conductive diffusion barrier layer of $(\text{La}_{0.80}\text{Sr}_{0.20})_{0.95}\text{MnO}_{3-\delta}$ (LSM) to avoid excessive reactivity of Cr species with the protonic ceramic material, the fuel electrode I of NiO mixed with $\text{BaZr}_{0.7}\text{Ce}_{0.2}\text{Y}_{0.1}\text{O}_{3-\delta}$ (NiO-BZCY721), the fuel electrode II of NiO mixed with $\text{BaZr}_{0.5}\text{Ce}_{0.4}\text{Y}_{0.1}\text{O}_{3-\delta}$ (NiO-BZCY541), a thin-film electrolyte $\text{BaZr}_{0.7}\text{Ce}_{0.2}\text{Y}_{0.1}\text{O}_{3-\delta}$ (BZCY721),

Publications

and an oxygen electrode of Pt or a composite electrode of $\text{Ba}_{0.5}\text{Gd}_{0.8}\text{La}_{0.7}\text{Co}_2\text{O}_{6-\delta}$ mixed with $\text{BaZr}_{0.5}\text{Ce}_{0.4}\text{Y}_{0.1}\text{O}_{3-\delta}$ (BGLC-BZCY541) shown in Figure 1b. The different ceramic functional layers (FLs) are manufactured on top of the porous metal substrate (Figure 1c, the full cross-sectional image shown in Figure S3). A good match of the thermal expansion coefficients (TECs) between the different layers is critical to avoid the cell failure. TECs of the half-cell components are listed in the Table 1.

Table 1. List of materials of the half-cell components in this work.

Acronym	Composition	TEC / 10^{-6} K^{-1}	Functionality
BZCY721	$\text{BaZr}_{0.7}\text{Ce}_{0.2}\text{Y}_{0.1}\text{O}_{3-\delta}$	9.3 ²⁵ 10.2 @650-1000 °C ²⁶	Electrolyte
NiO-BZCY541	$\text{NiO-BaZr}_{0.5}\text{Ce}_{0.4}\text{Y}_{0.1}\text{O}_{3-\delta}$	11.9 @200-1100 °C	Fuel electrode
NiO-BZCY721	$\text{NiO-BaZr}_{0.7}\text{Ce}_{0.2}\text{Y}_{0.1}\text{O}_{3-\delta}$	-	
LSM	$(\text{La}_{0.80}\text{Sr}_{0.20})_{0.95}\text{MnO}_{3-\delta}$	12.4 ²⁷	Barrier layer
ITM	Ferritic steel (26% Cr)	11.3 @ RT-900 °C	Metal support

A smooth surface of the fuel electrode FL is the key to grow the thin electrolyte in good crystallinity.²⁸ The pore size of the metal substrate (ca. 30 μm , Figure S2) is reduced down to submicron size by adding the LSM barrier layer and further reduced to ca. 200 nm by NiO-BZCY FLs (Figure 2a-d), and no obvious defects can be observed in the FLs at lower magnification in SEM images (Figure S4). The pore size reduction resulted in the refinement of the surface roughness (Figure 2e-h) compared to the ITM substrate (Figure S5) with an arithmetic mean roughness R_a of $\sim 0.058 \mu\text{m}$ and a maximum peak to valley height of the profile R_z of $\sim 0.238 \mu\text{m}$ at the NiO-BZCY541 FL (Figure 2i). The microstructure of the MS-PCC is optimized by inserting this second fuel electrode NiO-BZCY541 (Figure S6) as described in detail in Note S1. This high-quality surface is essential for the manufacturing of the dense electrolyte with good transport properties in order to limit the risk of pinhole formation due to the non-coverage of the underlying pores during thin film deposition. Figure S7 shows the picture of MS-PCC half-cell sample ($5 \times 5 \text{ cm}^2$) with the thin-film BZCY721 electrolyte on the top.

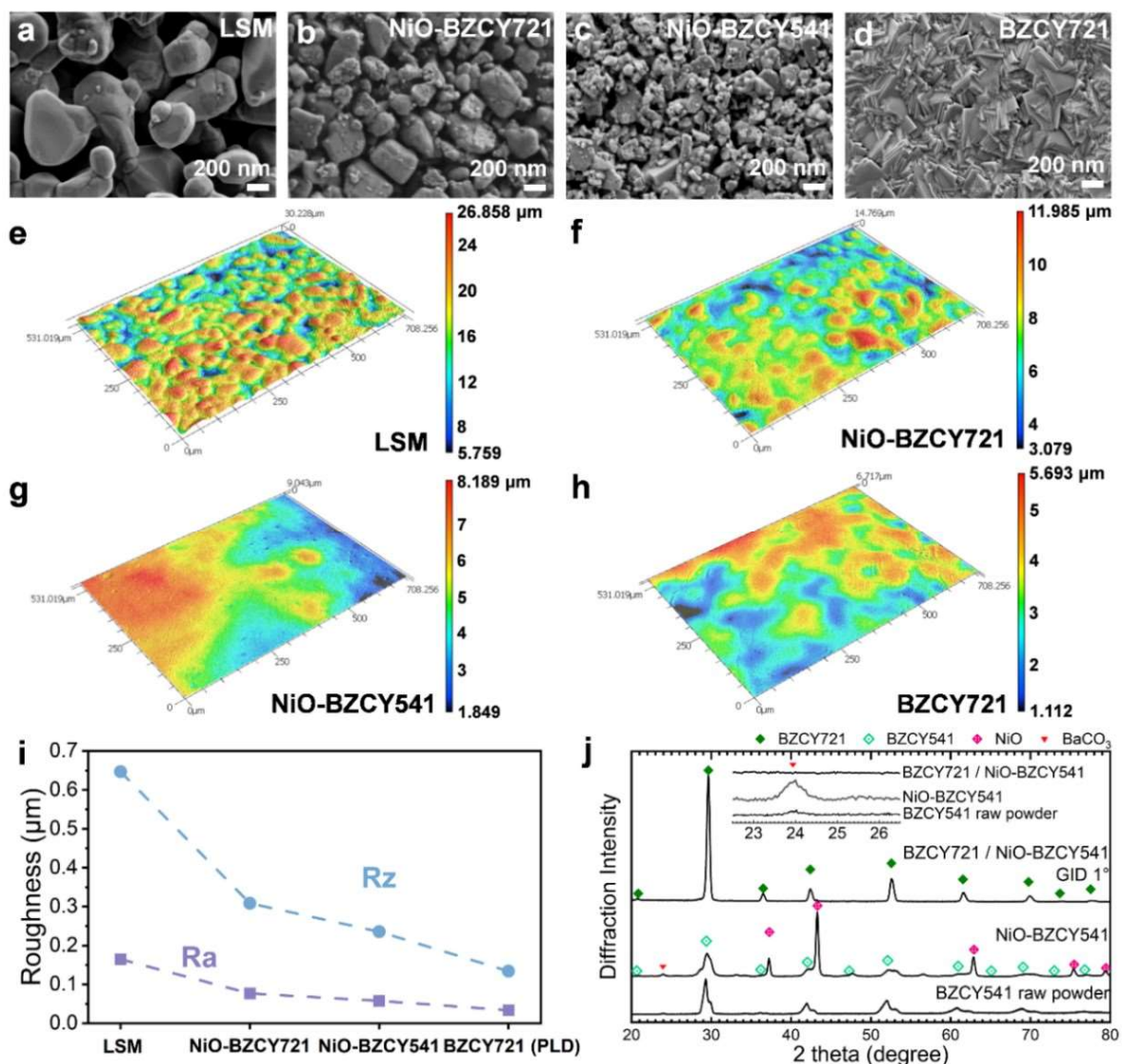


Figure 2. Investigation of the thin-film electrolyte MS-PCCs half cells. (a-d) SEM surface images of different FLs: LSM, NiO-BZCY721, NiO-BZCY541 and BZCY721, respectively. (e-h) The corresponding 3D images with topographic contrast reconstructed from the laser scanning microscope. (i) Surface roughness levels of Ra and Rz in different layers. (j) XRD diffractograms of the half cell. The diffractogram of the NiO-BZCY541 was recorded before PLD process and that of the BZCY721 electrolyte was recorded by a grazing incidence diffraction (GID, incident angle=1°).

Figure 2j displays the X-ray diffractograms of the MS-PCC before and after deposition of the BZCY721 electrolyte. Without electrolyte layers, NiO, BZCY541 and a small amount of BaCO₃ were detected. The BaCO₃ originates mainly from the raw powder. The diffraction pattern of BZCY541 in the NiO-BZCY541 FL is very similar to the one of the raw powders

Publications

that is characterized by a broad peak profile. This demonstrates that grain growth or phase change did not take place during the thermal treatment below 1000 °C necessary for the cell manufacturing. The electrolyte pattern was recorded by grazing incident diffraction (GID) at the incident angle of 1°, which allows to distinguish the electrolyte layer. The diffraction pattern demonstrated that the PLD coating is a well crystallized ceramic layer of the targeted BZCY721 phase.

The mechanical stability of the ceramic layers both during the manufacture process and under operational conditions is crucial to achieve the desired functionality of the MS-PCC. A high stress in the electrolyte layer may cause its fracture that would immediately degrade the cell performance. Assuming an ideal manufacturing process, the expected residual thermal stress values can be calculated with a simple model using the elastic properties²⁹ and thermal expansion coefficients of the materials used in the MS-PCC. By using the layer thicknesses, sintering temperatures, cermet compositions, and porosity values corresponding to the MS-PCC, the calculated stress value was –355 MPa (compressive) for a 1 µm thick BZCY721 electrolyte layer. The residual stress assessment by XRD confirmed that the electrolyte layer had a compressive stress after thin film deposition (Figure S8). The stress was close to or smaller than the calculated value when the thin film electrolyte was deposited in optimal conditions (II-1 and 2 in Figure S8). When the conditions were not appropriate, the electrolyte layer could be delaminated. The samples I-1 and 2 are such examples. They presented two diffraction peaks of the PLD layer originating from the different parts grown during the deposition process due to high laser power (detail discussion in Note S2). One of these two peaks showed remarkably larger stress values which might have an origin other than purely thermal, likely in relation with the crystal growth mechanism, and that yielded to the electrolyte delamination. Besides, the sufficient thermomechanical stability of the MS-PCC with a double fuel electrode layer and an optimal electrolyte was confirmed through annealing tests of the half-cells at 700 °C for 30 h (Figure S9).

The open circuit voltages (OCVs) in a H₂/O₂ concentration cell showed a double dependency in the H₂ concentration (p_{H_2}) (Figure 3a) and in the temperature (Figure S10). In isothermal conditions, the peak OCV was obtained for a H₂ stream diluted with N₂ with an increased viscosity – N₂ being of bigger size than the H₂ molecule – compared to a pure H₂ stream. The share of hydrogen in the gas mixture corresponding to the peak OCV decreased upon temperature increase as the diffusivity of gases increases. This betrayed an imperfect tightness

of the electrolyte or the sealing. This was confirmed by the small voltage spikes when the stability of the OCV was assessed over time (Figure 3b). The voltage spikes are likely the result of sudden variations of $p\text{H}_2$ and oxygen concentration ($p\text{O}_2$) on either side of the electrolyte due to burning. Additionally, the current leakage in the protonic ceramic electrolyte could be another reason leading to the OCV decrease.³⁰ Still the electrolyte is sufficiently tight to enable the cell to develop OCVs above 0.8 V at 600 °C and to be polarized.

In PCC operated in steam electrolysis at 600 °C, the oxygen evolution reaction (OER, $2\text{H}_2\text{O} \rightarrow \text{O}_2 + 4\text{H}^+ + 4\text{e}^-$) is rate limiting. Ideally, the OER electrocatalyst should possess good proton, oxygen ion and electron transport properties. Finding a high performance and durable OER catalyst for PCC is an enduring challenge which attracts significant research focus.³¹ By using Pt as an OER catalyst, a current density of ca. -170 mA cm^{-2} at 600 °C and $\sim 1.3 \text{ V}$ (Figure 3c) could be measured in steam electrolysis operation. By using a composite oxygen electrode of $\text{Ba}_{0.5}\text{Gd}_{0.8}\text{La}_{0.7}\text{Co}_2\text{O}_{6-\delta}$ (BGLC) and BZCY541 (BGLC-BZCY541) with superior electrocatalytic and durability feature,^{24,32} the current density increased up to ca. -840 mA cm^{-2} at 1.3 V and 600 °C (Figure 3c). At 600 °C, the evolution of the polarization curve is almost linear over the whole range of current density which is the reflect of a nearly constant total cell resistance (R_t). At OCV, R_t is dominated by the ohmic contribution (R_Ω), which is one order of magnitude higher than the polarization resistance (R_p) at 600° C as determined by electrochemical impedance spectroscopy (Figure 3e and 3f). R_Ω showed an evolution in temperature between 500 °C and 600 °C that can be modelled by an Arrhenius equation with an activation energy of about 0.49 eV (Figure 3d). Though it was difficult to deconvolute the relative contributions from the metal substrate currently, the LSM layer and the electrolyte layer that are expected to dominate R_Ω , an activation energy of 0.48 eV is consistent with protons as main charge carriers in the electrolyte material.³³ In addition, the activation energy of R_p (1.25 eV) is close to the values reported from a BGLC symmetrical cell,³⁴ inferring that the total MS-PCC polarization resistance is dominated by the oxygen electrode contribution. This is also consistent with the fact that the OER is rate limiting in PCC.

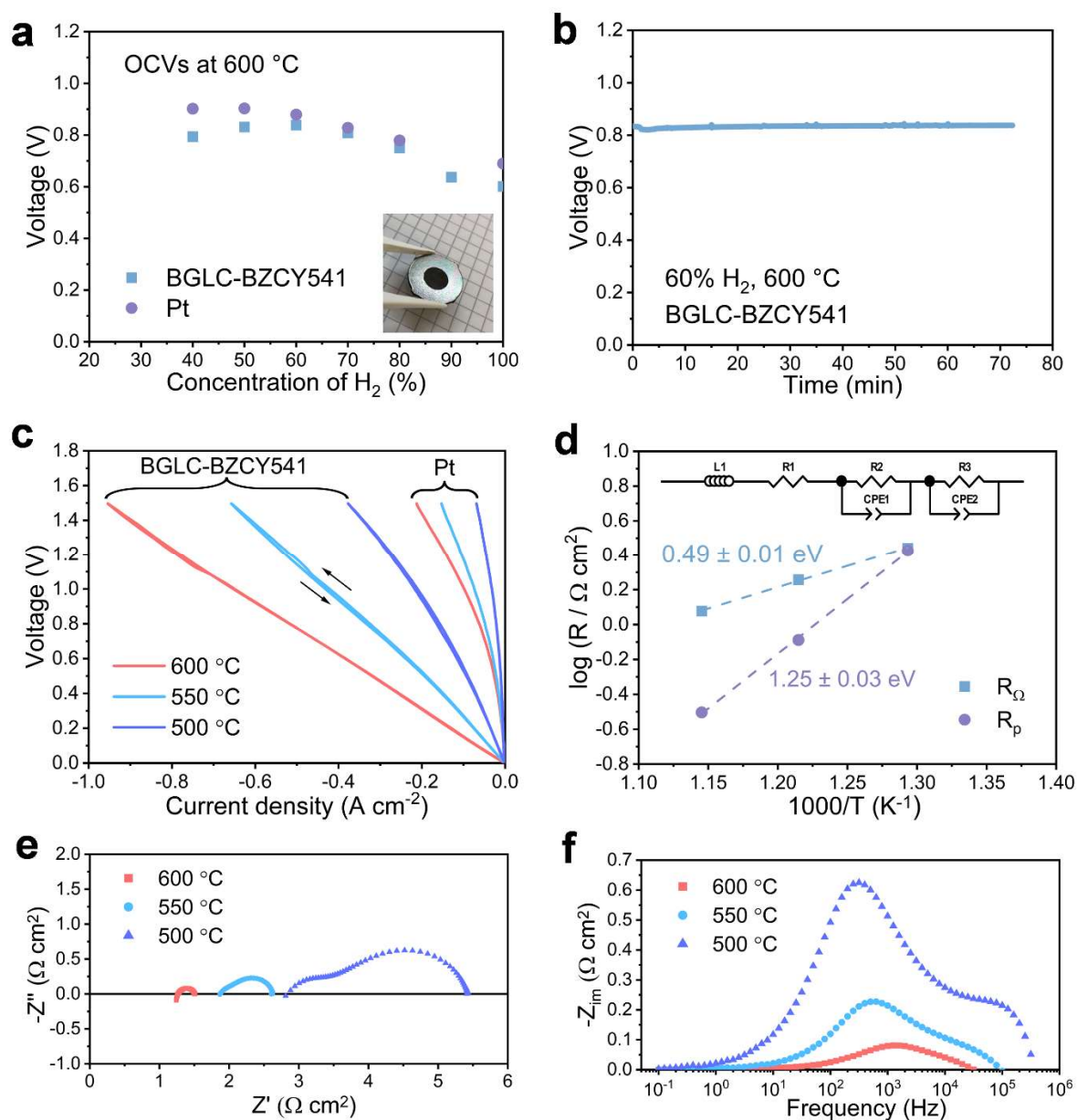


Figure 3. Electrochemical characterization of PCCs in steam electrolysis operation. (a) OCVs of MS-PCCs with Pt or BGLC-BZCY541 oxygen electrode obtained with different H₂ concentration varied from 40% to 100% with N₂ balanced in the feed gas stream on fuel electrode side, and oxygen electrode side was supplied with 20% O₂ – 80% N₂; inset is the sample photo of the MS-PCC. (b) The OCV profile of the MS-PCC with 60% H₂ on fuel electrode side. (c) Polarization curves obtained from MS-PCCs with Pt and BGLC-BZCY541 as oxygen electrode material at temperatures between 500 °C and 600 °C. N₂ with ~3 vol% H₂O was supplied to the fuel electrode, and a mixture of 10% H₂O and 90% air to the oxygen electrode. In these conditions the OCV was a few mV as a result of the gas conditions (no hydrogen at the fuel electrode and small p_{H₂O} gradient), the possible gas cross over due to the

presence of pinhole defects in the electrolyte layer and the p-type charge carriers in the electrolyte, originating from the wet oxidizing gas conditions.³⁵ The formation of hydrogen at the fuel electrode upon polarization, was evidenced with a portable hydrogen sensor at the outlet. The electrochemical impedance spectra were recorded at OCV; (d) Arrhenius-type plot of R_{Ω} and R_p with BGLC-BZCY541 oxygen electrode MS-PCC, and the corresponding Nyquist impedance plot in (e), the imaginary impedance plot in (f).

Beyond the electrochemical performance, the mechanical and the chemical stabilities of the cells under operational conditions determine their lifetime. Figure 4a displays the elemental mapping on the cross-section of the as-prepared half-cell (left in Figure 4a) and after deposition of the oxygen electrode and electrochemical operation (right in Figure 4a) acquired with high-resolution secondary ion mass spectrometry (SIMS) imaging.

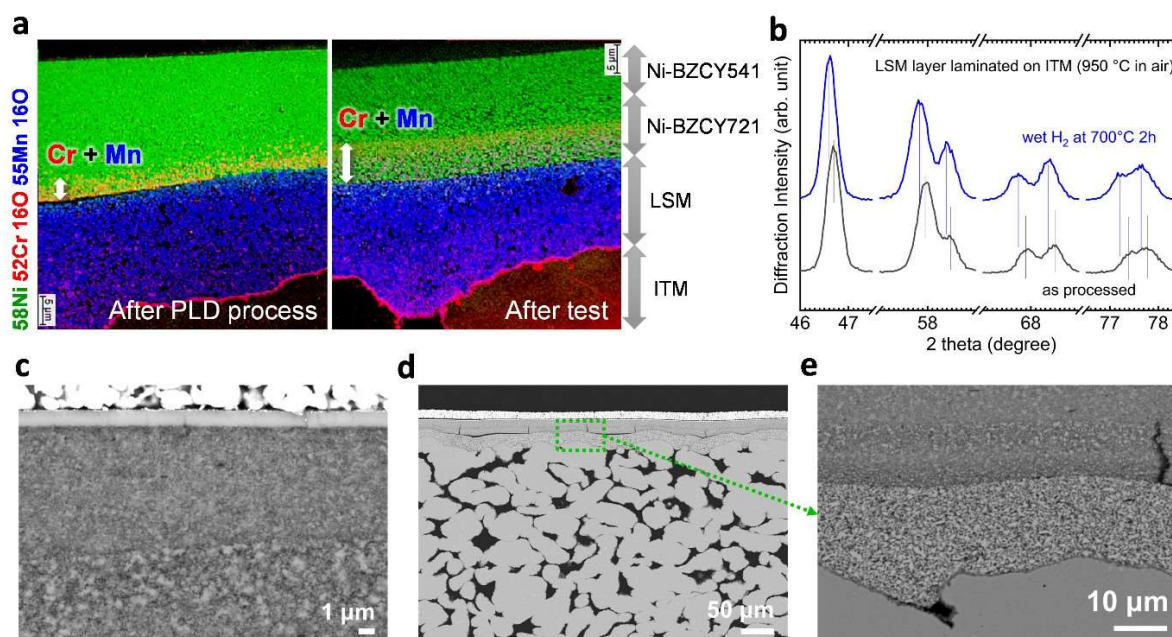


Figure 4. Degradation aspects of the MS-PCC after 200 h in temperature for electrochemical investigation. (a) Elemental mapping of the cross sections of the as-prepared (left) and tested (right) MS-PCC acquired using Nano-SIMS. For the as-prepared half-cell, it is clear that Cr and Mn diffuse into the NiO-BZCY721 layer by a few μm from the interface with LSM whereas this region extends to about $10\ \mu\text{m}$ after cell test. The secondary ions are represented as follows: $^{58}\text{Ni}^-$ in green; $^{52}\text{Cr}^{16}\text{O}^-$ in red; $^{55}\text{Mn}^{16}\text{O}^-$ in blue. (b) Comparison of XRD of LSM layer on ITM annealed in dry and wet hydrogen. (c) SEM polished cross section with phase contrast showing the thin film electrolyte that remain crack free and well bonded with the FLs. (d-e) SEM

Publications

polished cross section of the MS-PCC at different magnifications showing partial delamination between the FL and the LSM layer and crack formation in the FL.

For both samples before and after test operation, Cr₂O₃ scales (represented by regions coloured in red on Figure 4a) with a thickness of about 1 µm was observed on the ITM surfaces. However, the extent of Cr diffusion into the adjacent LSM layers appears more significant for the sample after operation; this can be seen as spreading of pink-coloured areas adjacent to the LSM-ITM interfaces. The regions indicated by arrows on the Nano-SIMS images in Figure 4a also show evidence of Cr and Mn diffusion into the Ni-BZCY721 FL. The diffusion length from the LSM/Ni-BZCY721 FL interface was a few micrometres in the as-prepared cell, whereas it extended across nearly 10 µm in the tested cell in which the pores became apparently larger after the reduction. This suggests that, upon testing, Cr and Mn could be transported further into the FL due to its relatively large pore size compared to the as-prepared cell. The diffusion seems to have stopped in the middle of Ni-BZCY721 layer. At first, Cr₂O₃ vaporises and diffuses through the pores in the LSM layer during the sintering step in air at 950 °C.¹⁶ The diffusion could be decelerated in the functional layer for several reasons, such as a decreasing pore size and reaction of the diffusing elements with the LSM to form Cr-Mn oxides. Cr and Mn could then also further diffuse during the firing of the oxygen electrode at 700 °C in oxidizing atmosphere and during the electrochemical test performed at 500~600 °C for a few hundred hours in the wet reducing conditions as applied to the fuel side in operation.¹⁷ Though no Cr was found near the Ni-BZCY541 FL/electrolyte interface after entire electrochemical characterization, it is conceivable that Cr and Mn diffusion at longer term would cause fatal degradation of the cells. For the long-term operation, it is therefore of high importance to minimise vaporization of Cr from the metal support during both manufacturing and operation while reducing the use of a Mn source. A dense protective coating on the metal support is thus highly desirable.

Cracks in the layers and delamination at the interfaces could happen when the stress is high enough to fracture or detach the layers. This can yield a significant performance loss, or even operational failure of the cell. In the electrochemical ceramic cells, the most critical is the electrolyte layer which should remain stable. SEM cross sections of tested cells (Figure 4c-e) revealing that the thin BZCY electrolyte layer exhibits no noticeable defects after operation. Observed mechanical defects are partial delamination along the LSM/Ni-BZCY721 FL interface and through-plane cracks initiated at the interface LSM/Ni-BZCY721 FL and stopped

in the Ni-BZCY721 FL. From the SEM picture, it is observed that cracks are located where the delamination started. Considering the small difference of the TEC values among the components as shown in Table 1 and the fact that there is no crack in the freshly fabricated cell, the crack should have been formed during operation when exposed to the reducing atmosphere. The LSM layer calcined on ITM substrate were annealed at 700 °C for 2 h in reducing atmosphere and assessed by XRD (Figure S11). In dry hydrogen (99,999% purity) most of LSM phase was changed into $\text{La}_{1.3}\text{Sr}_{0.5}\text{MnO}_{3.95}$ and MnO , indicating Mn^{3+} reduction towards Mn^{2+} .³⁶ On the other hand, the LSM phase remained in wet hydrogen (~3 vol% H_2O , ~97 vol% H_2). Since the electrochemical operation was performed under wet atmospheres, the LSM layer might have been stable. The chemical lattice expansion in wet hydrogen was about 0.22 % with respect of the as processed LSM layer (Figure 4b). The isothermal dilatometry analysis of NiO-BZCY541 cermet has determined the dimensional change in reducing condition to be at least about -0.3 % (Figure S12). The dimensional change due to chemical expansion of LSM and NiO reduction in the cermet fuel electrode might be responsible for the partial delamination at the LSM/Ni-BZCY721 FL interface and for the tensile stress that resulted in the crack formation in the FL.

Compared to the concepts involving manufacturing steps at high temperature, our approach of MS-PCC based on a pore graded structure processed at a temperature below 1000 °C and thin film technology is shown to be effective for application in steam electrolysis. Improvement of the Cr retention in the metal support and optimization of the different material compositions to reduce TEC mismatch between the layers and avoid excessive chemical expansion are key directions for further improving the cell performance.³⁷ The implementation of other physical vapor deposition techniques to deposit the thin film electrolyte that are more industrialisable than PLD could be crucial for the scale-up of the technology.

In the context of limited resources in critical and strategic raw materials for the key technologies of the energy transition, the metal supported architecture may be a key asset for the market to decide about further developments. The multi-layer assembly of the PCC in this architecture can also offer large selections for the counter-electrode material in replacement of the chosen oxygen electrode in this work. This opens up a broad range of applications for which the PCC cells are unique. This can include electrochemical hydrogen pumping,³⁸ fuel cell, co-electrolysis and diverse electrosynthesis processes including ammonia synthesis (Figure 1).

Publications

In a context of the decarbonation of the energy systems, these market applications are likely to be the driver of the future developments and the ramp-up of the technology.

ASSOCIATED CONTENT

Supporting information available: Experimental section, SEM, laser scanning confocal microscopy image of ITM substrate, the MS-PCC sample photo, residual stress analysis of PLD coatings, and measured OCV values of the MS-PCC.

AUTHOR INFORMATION

Corresponding Authors

Rémi Costa- Institute of Engineering Thermodynamics, Electrochemical Energy Technology, German Aerospace Center (DLR), Pfaffenwaldring 38-40, D-70569 Stuttgart, Germany; Email: remi.costa@dlr.de

Authors

Haoyu Zheng - Institute of Engineering Thermodynamics, Electrochemical Energy Technology, German Aerospace Center (DLR), Pfaffenwaldring 38-40, D-70569 Stuttgart, Germany; Institute of Building Energetics, Thermotechnology and Energy Storage (IGTE), University of Stuttgart. Pfaffenwaldring 31, D-70569 Stuttgart, Germany

Noriko Sata - Institute of Engineering Thermodynamics, Electrochemical Energy Technology, German Aerospace Center (DLR), Pfaffenwaldring 38-40, D-70569 Stuttgart, Germany

Feng Han - Institute of Engineering Thermodynamics, Electrochemical Energy Technology, German Aerospace Center (DLR), Pfaffenwaldring 38-40, D-70569 Stuttgart, Germany

Amir Masoud Dayaghi - Department of Chemistry, Centre for Materials Science and Nanotechnology (SMN), University of Oslo, NO-0315 Oslo, Norway

Fumitada Iguchi - Department of Mechanical Engineering, College of Engineering, Nihon University, Koriyama, Fukushima 963-8642, Japan

Katherine Develos-Bagarinao - Global Zero Emission Research Center, National Institute of Advanced Industrial Science and Technology, Tsukuba, Ibaraki 305-8569, Japan

Truls Norby - Department of Chemistry, Centre for Materials Science and Nanotechnology (SMN), University of Oslo, NO-0315 Oslo, Norway

Marit Stange - SINTEF, Forskningsveien 1, NO-0373 Oslo, Norway

Notes

The approach of manufacturing is based on a German patent application DE102016112125A1 “Verfahren zur Herstellung eines Festelektrolyts, Festelektrolyt und Festoxidbrennstoffzelle” since 1st of July 2016. The application is co-owned by DLR and Ceraco GmbH, and involves F.H. and R.C., and is pending (status 08.11.2023)

Author Contributions

H.Z. worked on the cell manufacture process, conducted microscopic structure analysis, and performed the electrochemical analysis of the cell. N.S optimized the PLD process, contributed to the structural optimization, and conducted material assessment by XRD and dilatometry. F. H. performed the early development of the cell concept and engineered the design of the metal substrate and prepared the samples for dilatometry. A.M.D. contributed to the PLD deposition, layer analysis and electrochemical test during the development phase of the thin film electrolyte. F.I. contributed to the mechanical property assessment, performed the calculation of residual stress and the XRD residual stress analysis. K.D.B. performed the investigation by Nano-SIMS. T.N. provided resources and supervision. M.S. provided resources, R.C. designed the cell and the study, provided resources and supervised the study. All co-authors discussed the results. R.C., H.Z. and N.S., prepared the first draft with the support of all co-authors.

ACKNOWLEDGMENT

The China Scholarship Council is acknowledged for the doctoral scholarship of Haoyu Zheng (201806160173). The German Federal Ministry for Education and Research (project 01DR18002), the Research Council of Norway (project 284389) and JST SICORP (project JPMJSC17C5) are acknowledged for funding of the project DAICHI in the frame of the EIG CONCERT-Japan.

REFERENCES

- (1) Hauch, A.; Kungas, R.; Blennow, P.; Hansen, A. B.; Hansen, J. B.; Mathiesen, B. V.; Mogensen, M. B. Recent advances in solid oxide cell technology for electrolysis. *Science* **2020**, *370* (6513), eaba6118.
- (2) Bance, P.; Brandon, N. P.; Girvan, B.; Holbeche, P.; O’Dea, S.; Steele, B. C. H. Spinning-out a fuel cell company from a UK University—2 years of progress at Ceres Power. *J. Power Sources* **2004**, *131* (1-2), 86-90.
- (3) Brandon, N. P.; Blake, A.; Corcoran, D.; Cumming, D.; Duckett, A.; El-Koury, K.; Haigh, D.; Kidd, C.; Leah, R.; Lewis, G.; et al. Development of Metal Supported Solid Oxide Fuel Cells for Operation at 500-600 °C. *J. Fuel Cell Sci. Technol.* **2004**, *1* (1), 61-65.
- (4) Oishi, N.; Yoo, Y. Fabrication of Cerium Oxide Based SOFC Having a Porous Stainless Steel Support *ECS Trans.* **2009**, *25* (2), 739-744.
- (5) Leah, R. T.; Brandon, N. P.; Aguiar, P. Modelling of cells, stacks and systems based around metal-supported planar IT-SOFC cells with CGO electrolytes operating at 500–600 °C. *J. Power Sources* **2005**, *145* (2), 336-352.
- (6) Hui, S.; Yang, D.; Wang, Z.; Yick, S.; Decès-Petit, C.; Qu, W.; Tuck, A.; Maric, R.; Ghosh, D. Metal-supported solid oxide fuel cell operated at 400–600 °C. *J. Power Sources* **2007**, *167* (2), 336-339.
- (7) Xie, Y.; Neagu, R.; Hsu, C.-S.; Zhang, X.; Decès-Petit, C. Spray Pyrolysis Deposition of Electrolyte and Anode for Metal-Supported Solid Oxide Fuel Cell. *J. Electrochem. Soc.* **2008**, *155* (4), B407-B410.
- (8) Hui, R.; Berghaus, J. O.; Decès-Petit, C.; Qu, W.; Yick, S.; Legoux, J.-G.; Moreau, C. High performance metal-supported solid oxide fuel cells fabricated by thermal spray. *J. Power Sources* **2009**, *191* (2), 371-376.
- (9) Haydn, M.; Ortner, K.; Franco, T.; Uhlenbruck, S.; Menzler, N. H.; Stöver, D.; Bräuer, G.; Venskutonis, A.; Sigl, L. S.; Buchkremer, H.-P.; et al. Multi-layer thin-film electrolytes for metal supported solid oxide fuel cells. *J. Power Sources* **2014**, *256*, 52-60.

- (10) Dayaghi, A. M.; Kim, K. J.; Kim, S.; Park, J.; Kim, S. J.; Park, B. H.; Choi, G. M. Stainless steel-supported solid oxide fuel cell with $\text{La}_{0.2}\text{Sr}_{0.8}\text{Ti}_{0.9}\text{Ni}_{0.1}\text{O}_{3-\delta}$ /yttria-stabilized zirconia composite anode. *J. Power Sources* **2016**, *324*, 288-293.
- (11) Udomsilp, D.; Rechberger, J.; Neubauer, R.; Bischof, C.; Thaler, F.; Schafbauer, W.; Menzler, N. H.; de Haart, L. G. J.; Nanning, A.; Opitz, A. K.; et al. Metal-Supported Solid Oxide Fuel Cells with Exceptionally High Power Density for Range Extender Systems. *Cell Rep. Phys. Sci.* **2020**, *1* (6), 100072.
- (12) Pirou, S.; Talic, B.; Brodersen, K.; Hauch, A.; Frandsen, H. L.; Skafte, T. L.; Persson, A. H.; Høgh, J. V. T.; Henriksen, H.; Navasa, M.; et al. Production of a monolithic fuel cell stack with high power density. *Nat. Commun.* **2022**, *13* (1), 1263.
- (13) Leah, R.; Bone, A.; Hjalmarsson, P.; Selcuk, A.; Lankin, M.; Rahman, M.; Clare, A.; Reade, G.; Felix, F.; De Vero, J.; et al. Commercialization of the Ceres Power SteelCell® Technology: Latest Update. *ECS Trans.* **2021**, *103* (1), 679-684.
- (14) Leah, R.; Bone, A.; Hjalmarsson, P.; Selcuk, A.; Lankin, M.; Rahman, M.; Felix, F.; De Vero, J.; Macauley, C.; Charbonneau, C. Commercialization of Ceres SteelCell® Technology for power generation and electrolysis. *ECS Trans.* **2023**, *111* (6), 121-131.
- (15) Leah, R. T.; Bone, A.; Selcuk, A.; Corcoran, D.; Lankin, M.; Dehaney-Steven, Z.; Selby, M.; Whalen, P. Development of highly robust, volume-manufacturable metal-supported SOFCs for operation below 600 °C. *ECS Trans.* **2011**, *35* (1), 351-367.
- (16) Stenzel, A.; Fähsing, D.; Schütze, M.; Galetz, M. C. Volatilization kinetics of chromium oxide, manganese oxide, and manganese chromium spinel at high temperatures in environments containing water vapor. *Mater. Corros.* **2019**, *70* (8), 1426-1438.
- (17) Huang, W.; Huang, T.; Song, P.; Chen, R.; Zheng, B.; Wang, C.; Li, C.; Lu, J. $\text{CrO}_2(\text{OH})_2$ volatilization rate and oxidation behavior prediction of the NiCr coating in air-H₂O environment at 650 °C. *Corros. Sci.* **2021**, *182*, 109303.
- (18) Portier, J.; Poizot, P.; Campet, G.; Subramanian, M. A.; Tarascon, J. M. Acid–base behavior of oxides and their electronic structure. *Solid State Sci.* **2003**, *5* (5), 695-699.
- (19) Wang, R.; Lau, G. Y.; Ding, D.; Zhu, T.; Tucker, M. C. Approaches for co-sintering metal-supported proton-conducting solid oxide cells with $\text{Ba}(\text{Zr,Ce,Y,Yb})\text{O}_{3-\delta}$ electrolyte. *Int. J.*

Publications

Hydrog. Energy **2019**, *44* (26), 13768-13776.

(20) An, H.; Lee, H.-W.; Kim, B.-K.; Son, J.-W.; Yoon, K. J.; Kim, H.; Shin, D.; Ji, H.-I.; Lee, J.-H. A 5×5 cm² protonic ceramic fuel cell with a power density of 1.3 W cm⁻² at 600 °C. *Nat Energy* **2018**, *3* (10), 870-875.

(21) Duan, C. C.; Kee, R.; Zhu, H. Y.; Sullivan, N.; Zhu, L. Z.; Bian, L. Z.; Jennings, D.; O'Hayre, R. Highly efficient reversible protonic ceramic electrochemical cells for power generation and fuel production. *Nat Energy* **2019**, *4* (3), 230-240.

(22) Feng, H.; Costa, R.; Robert, S. Verfahren zur Herstellung eines Festelektrolyts, Festelektrolyt und Festoxidbrennstoffzelle. DE102016112125A1, Germany 2018.

(23) Costa, R.; Han, F.; Szabo, P.; Yurkiv, V.; Semerad, R.; Cheah, S. K.; Dessemond, L. Performances and Limitations of Metal Supported Cells with Strontium Titanate based Fuel Electrode. *Fuel Cells* **2018**, *18* (3), 251-259.

(24) Zheng, H.; Riegraf, M.; Sata, N.; Costa, R. A double perovskite oxygen electrode in Zr-rich proton conducting ceramic cells for efficient electricity generation and hydrogen production. *J. Mater. Chem. A* **2023**, *11* (20), 10955-10970.

(25) Løken, A.; Ricote, S.; Wachowski, S. Thermal and Chemical Expansion in Proton Ceramic Electrolytes and Compatible Electrodes. *Crystals* **2018**, *8* (9), 365.

(26) Hudish, G.; Manerbino, A.; Coors, W. G.; Ricote, S. Chemical expansion in BaZr_{0.9-x}Ce_xY_{0.1}O_{3-δ} (x = 0 and 0.2) upon hydration determined by high-temperature X-ray diffraction. *J. Am. Ceram. Soc.* **2017**, *101* (3), 1298-1309.

(27) Tietz, F. Thermal expansion of SOFC materials. *Ionics* **1999**, *5*, 129-139.

(28) Sata, N.; Han, F.; Zheng, H.; Dayaghi, A. M.; Norby, T.; Stange, M.; Semerad, R.; Costa, R. Development of proton conducting ceramic cells in metal supported architecture. *ECS Trans.* **2021**, *103* (1), 1779-1789.

(29) Hinata, K.; Sata, N.; Costa, R.; Iguchi, F. High Temperature Elastic Modulus of Proton Conducting Ceramics Y-Doped Ba (Zr, Ce) O₃. In *Electrochemical Society Meeting Abstracts prime2020*, 2020; The Electrochemical Society, Inc.: pp 2617-2617.

- (30) Zhu, H.; Ricote, S.; Kee, R. J. Faradaic efficiency in protonic-ceramic electrolysis cells. *J. Phys. Energy* **2022**, *4* (1), 014002.
- (31) Papac, M.; Stevanovic, V.; Zakutayev, A.; O'Hayre, R. Triple ionic-electronic conducting oxides for next-generation electrochemical devices. *Nat. Mater.* **2020**, *20*, 301-313.
- (32) Vøllestad, E.; Strandbakke, R.; Tarach, M.; Catalan-Martinez, D.; Fontaine, M. L.; Beeff, D.; Clark, D. R.; Serra, J. M.; Norby, T. Mixed proton and electron conducting double perovskite anodes for stable and efficient tubular proton ceramic electrolyzers. *Nat. Mater.* **2019**, *18* (7), 752-759.
- (33) Kreuer, K. D. Proton-conducting oxides. *Annu. Rev. Mater. Res.* **2003**, *33* (1), 333-359.
- (34) Strandbakke, R.; Cherepanov, V. A.; Zuev, A. Y.; Tsvetkov, D. S.; Argirusis, C.; Sourkouni, G.; Prunte, S.; Norby, T. Gd- and Pr-based double perovskite cobaltites as oxygen electrodes for proton ceramic fuel cells and electrolyser cells. *Solid State Ion.* **2015**, *278*, 120-132.
- (35) Zhu, H.; Kee, R. J. Membrane polarization in mixed-conducting ceramic fuel cells and electrolyzers. *Int. J. Hydrog. Energy* **2016**, *41* (4), 2931-2943.
- (36) Miyoshi, S.; Hong, J.-O.; Yashiro, K.; Kaimai, A.; Nigara, Y.; Kawamura, K.; Kawada, T.; Mizusaki, J. Lattice expansion upon reduction of perovskite-type LaMnO₃ with oxygen-deficit nonstoichiometry. *Solid State Ion.* **2003**, *161* (3-4), 209-217.
- (37) Dayaghi, A. M.; Haugsrud, R.; Stange, M.; Larring, Y.; Strandbakke, R.; Norby, T. Increasing the thermal expansion of proton conducting Y-doped BaZrO₃ by Sr and Ce substitution. *Solid State Ion.* **2021**, *359*, 115534.
- (38) Wang, Q.; Luo, T.; Tong, Y.; Dai, M.; Miao, X.-Y.; Ricote, S.; Zhan, Z.; Chen, M. Large-area protonic ceramic cells for hydrogen purification. *Sep. Purif. Technol.* **2022**, *295*, 121301.

6 Additional results and general discussion

This work falls within the scope of the development of PCC based technologies for energy applications, focusing on hydrogen production by steam electrolysis at intermediate temperatures. In particular, the focus was set on the materials selection, their qualification in terms of performance and durability, corresponding to application in a planar cell design (Figure 6.1). Furthermore, the additional results presented in this chapter on PCCs with the BLC positrode for steam electrolysis are being prepared for an upcoming article.

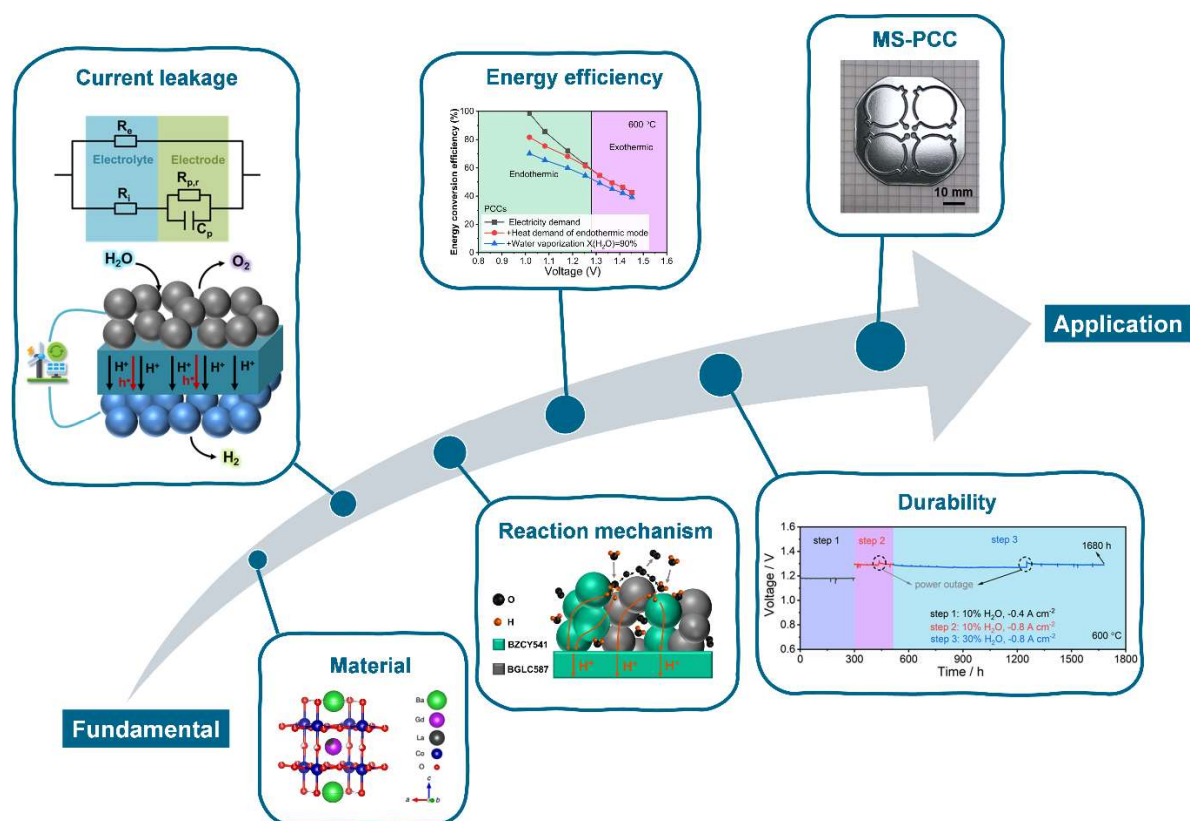


Figure 6.1: Schematic illustration of the critical scientific aspects represented in the thesis. (the image of material is adapted from ref. ³⁸)

6.1 Barium cobalt-based perovskite materials as promising positrodes

The electrocatalytic activity of different barium cobalt-based perovskite materials, including $Ba_{1-x}Gd_{0.8}La_{0.2+x}Co_2O_{6-\delta}$ (BGLC) with different Ba contents at the A-site (i.e., $x = 0$ and $x = 0.5$), and $Ba_{0.5}La_{0.5}CoO_{3-\delta}$ (BLC), was investigated in planar button cells of as-prepared NS-PCCs in both steam electrolysis and fuel cell operation. The key performances are

summarized in Table 6.1.

Table 6.1: Summary of current densities at V_{TN} in steam electrolysis mode and peak power densities achieved in fuel cell mode using different positrodes in PCCs.

Positrode materials	Cell architecture	Current density $A\ cm^{-2}$ at V_{TN} (ca. 1.3 V)	Peak power density $mW\ cm^{-2}$	Ref.
BGLC587-BZCY721	Tubular	ca. -0.15 at $600\ ^\circ C$	/	38
BGLC587-BZCY541	Planar	-0.65 at $600\ ^\circ C$	403 at $600\ ^\circ C$	This work
BGLC1082-BZCY541	Planar	-0.83 at $600\ ^\circ C$	506 at $600\ ^\circ C$	This work
BLC	Planar	ca. -0.35 at $600\ ^\circ C$	/	112
BLC-BZCY541	Planar	-0.828 at $600\ ^\circ C$	586 at $600\ ^\circ C$	This work

With BGLC587-BZCY541 positrode planar PCCs, the current density reaches $-0.65\ A\ cm^{-2}$ at V_{TN} , which is 4 times higher than that of the tubular cells³⁸. Additionally, the peak power density (PPD) reaches $403\ mW\ cm^{-2}$ at $600\ ^\circ C$. These initial electrochemical performances exceed most reported PCC performances with a similar BZCY electrolyte ($Zr \geq 50\ at\%$). To explain the water splitting process in the positrode, the electrochemical model developed aforementioned in Chapter 4 was employed to describe and model the contribution of electron hole conduction to the polarization resistance, making it possible to extract the real polarization resistances for reaction kinetics analysis. Two sets of elementary reaction steps corresponding to different processes were developed^{113, 114}. With the variation of pH_2O , $R_{p,r}$ increased at high pH_2O . We found that the reaction orders calculated from the apparent polarization resistance did not show obvious differences from those obtained with the corrected real polarization resistance at the measured temperature of $600\ ^\circ C$, suggesting a low non-faradaic current at this temperature. The water splitting process on BGLC587-BZCY541 is found to be rate limited by the surface related process in the low frequency region, and the TPB area exhibits higher activity towards the reaction.

It is important to note that the reaction orders are theoretical and some more complex processes were not considered in the elementary reaction steps. For instance, the diffusion of neutral oxygen and differently charged oxygen species on the electrode surface was not accounted for.

Additional results and general discussion

Additionally, the proposed method for determining the interpretation of mechanisms could be employed on electrodes with defined geometries, which may provide more detailed information in future research. As a preliminary investigation, the analysis can still provide valuable information with regard to exploring the rate-limiting reaction process. For instance, the TPB area exhibits high catalytic activity in the BGLC587-BZCY541 positrode. Therefore, optimizing the porous structure of the electrode to create more TPB could be a feasible technical approach to further enhance the initial performance of the PCC.

By increasing the Ba content in the material, namely BGLC1082, the performance was further improved. For example, the PPD increased to 506 mW cm^{-2} at $600 \text{ }^\circ\text{C}$ in fuel cell mode, and the current density increased to -0.83 A cm^{-2} at V_{TN} and $600 \text{ }^\circ\text{C}$ in electrolysis mode. The secondary phase of BaCoO_3 (BCO) was detected by treating the BGLC1082 raw powder in a wet atmosphere. Similarly, the formation of BCO in other host matrix materials has been reported, with the BCO phase demonstrated as the active site for the rapid oxygen adsorption and dissociation process^{115,116}. The oxygen-ion related surface diffusion processes are suggested to be the rate-limiting process in the BGLC587 positrode. Therefore, the higher electrochemical performance of BGLC1082 compared to BGLC587 can be explained by the highly active secondary phase of BCO formation. In the last decade, the release of metal or alloy nanoparticles from host materials has received increased attention due to the high activity levels of the exsolved nanoparticles¹¹⁷. The behavior observed in this study, concerning the release of another crystalline phase on the host oxide lattice, could open a new route for materials design.

The results demonstrated that the BGLC-based positrode shows high electrocatalytic activity towards water splitting in planar PCCs at intermediate temperatures, together with promising long-term stability – proven for 1680 h – at a current density as high as -0.8 A cm^{-2} . However, Strandbakke *et al.*¹¹⁸ recently reported that BGLC with different Ba contents ($x=1-0.5$) contains a range of crystallographic phases, including minor amounts of BaCO_3 , Gd_2O_3 , and Co_3O_4 (at least two of the phases). Specifically, the amount of BaCO_3 is higher than 3.2 wt% in all the different BGLC compositions, which is suspected to be inert compared to the host matrix materials^{119,120}. The complexity of the structure and the multi-phase characteristics of the raw BGLC materials raise concerns about their stability over very long time and under operating parameters such as high current and high conversion rates, which stand as the basic technical requirements for their application. Therefore, another barium cobalt-based perovskite

material, $\text{Ba}_{0.5}\text{La}_{0.5}\text{CoO}_{3-\delta}$ (BLC), with a simple cubic structure and fewer elements, was investigated as well.

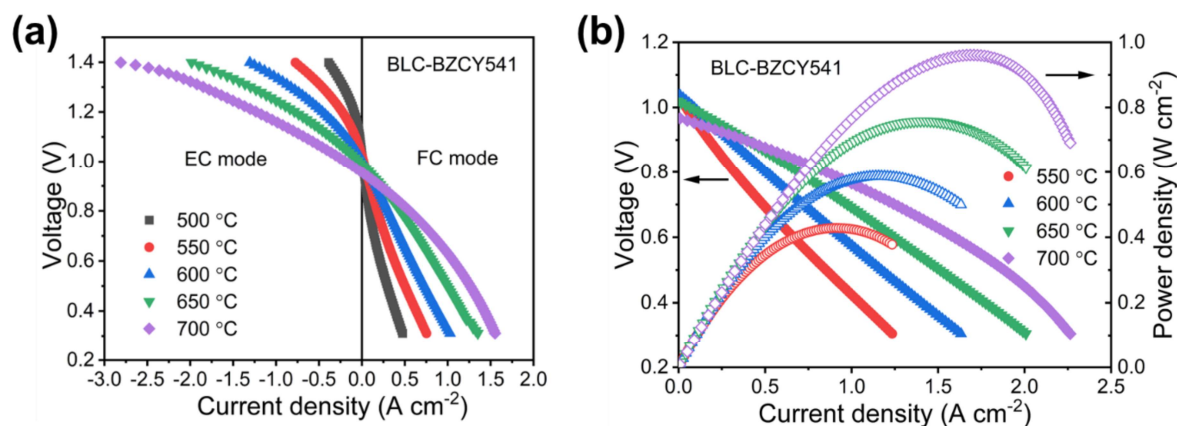


Figure 6.2: Electrochemical characterization of PCCs with the BLC-BZCY541 positrode. (a) Polarization curves of reversible operation with wet H_2 supplied to the negatrotrode and 30% $\text{H}_2\text{O}/\text{air}$ supplied to the positrode. (b) Polarization curves of the cell operated in fuel cell mode with wet air on the positrode side.

The composite positrode of BLC-BZCY541 was tested in a similar NS-PCC, and the cell exhibited an even higher PPD in fuel cell mode, as summarized in Table 6.1. Moreover, the polarization curves change smoothly from EC mode to FC mode (Figure 6.2), indicating the good reversibility of the cells. To explore the reason behind this, the variation of the electrode response with respect to $p\text{H}_2\text{O}$ was performed as well. Conversely, a distinct feature was observed in the PCC with the BLC-BZCY541 positrode, as shown in Figure 6.3. Both R_Ω and R_p decreased when the atmosphere was switched from dry to moist conditions due to increased protonic conduction in the BZCY541 phase. By further increasing the $p\text{H}_2\text{O}$, R_Ω did not exhibit significant differences; however, R_p decreased continuously. This suggests that the protonic conductivity in the BLC phase continued to improve with higher $p\text{H}_2\text{O}$, in contrast to the electrode response observed in the BGLC582 positrode. As demonstrated by Wachowski *et al.*¹²¹, BLC shows water uptake property. Therefore, it is suggested that the reaction mechanism discussed in Article I, corresponding to the existence of reaction sites over the entire electrode surface, is the reasonable process in the BLC-BZCY541 positrode.

Additional results and general discussion

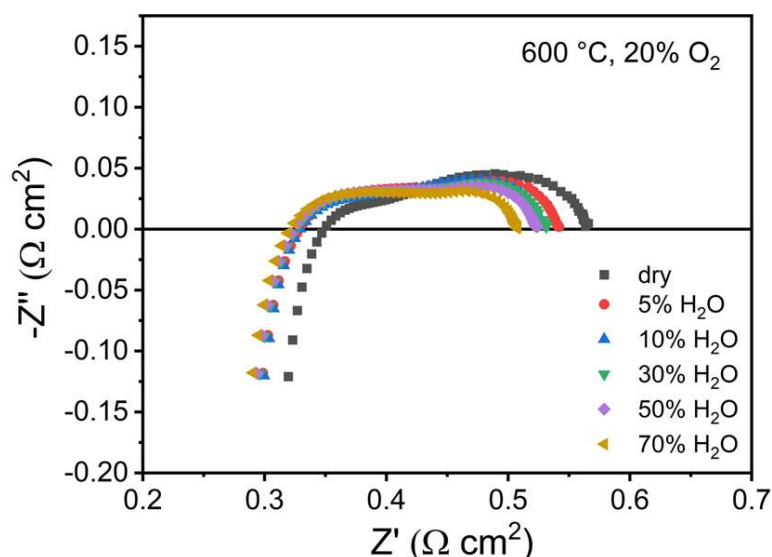


Figure 6.3: Electrochemical impedance spectra of a PCC with the BLC-BZCY541 positrode under OCV and various $p\text{H}_2\text{O}$ (balanced with N_2) conditions.

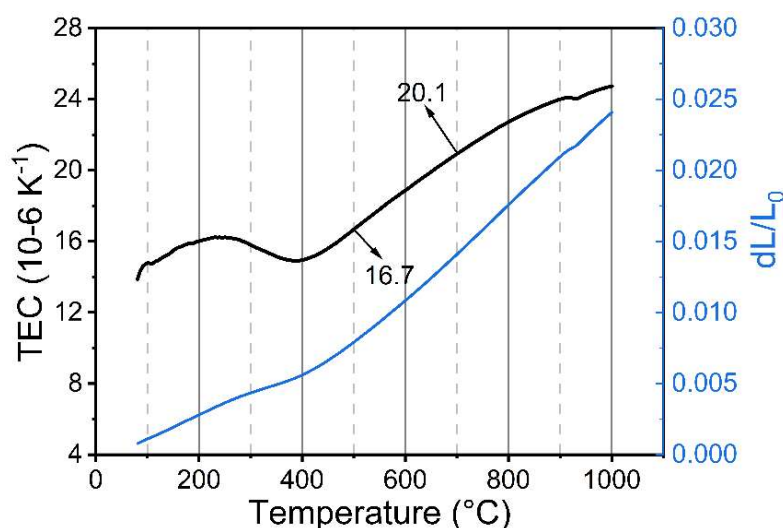


Figure 6.4: Thermal expansion behavior of BLC-BZCY541 from 80 °C to 1000 °C in air.

All the results demonstrate that barium cobalt-based perovskite materials can act as a highly active electrocatalytic positrode. In the perspective of large-scale application, other factors than the purely electrocatalytic considerations come into consideration: The thermo-mechanical stability of the interfaces between adjacent layers is a critical factor for scale-up. The state-of-the-art protonic ceramics, such as BZCY, typically exhibit a TEC value of $10\text{--}12 \times 10^{-6} \text{ K}^{-1}$ ¹²². In contrast, perovskite materials with Co at the B-site typically have a higher TEC value due to the change in the spin state of the Co^{3+} cation¹²³. For example, the

average TEC of BGLC587 is $20 \times 10^{-6} \text{ K}^{-1}$ at 300-700 °C. Regarding BLC, the TEC value increased from $16.7 \times 10^{-6} \text{ K}^{-1}$ at 500 °C to $20.1 \times 10^{-6} \text{ K}^{-1}$ at 700 °C, as depicted in Figure 6.4. It is worth mentioning that the planar PCC investigated in the present study was still at the button cell level. With a small active area, using the composite positrode by mixing the barium cobalt-based perovskite materials with BZCY can avoid a significant mismatch between the different functional layers, as confirmed by the durability measurement. However, when scaling up to manufacture larger cells with $5 \times 5 \text{ cm}^2$ or even $10 \times 10 \text{ cm}^2$ of the active area, the mismatch in TEC between the positrode and the electrolyte can become critical and lead to delamination at the interface.

Therefore, a focus of future research on the development of barium cobalt-based perovskite to reduce the TEC value to close to $11 \times 10^{-6} \text{ K}^{-1}$ appears meaningful. For instance, doping with transition metals (e.g., Ni, Fe, Cu) could be a solution to optimize this characteristic and it has been demonstrated as a feasible approach. Through partial substitution of Co with Ni, the TEC value of the materials can be reduced without compromising the conductivity of the material¹²³.

6.2 Current leakage and faradaic efficiency

The electronic conductive properties have been extensively studied in relevant protonic ceramics, indicating enhanced electronic conductivity under oxidizing and high temperature conditions. The increment of electronic conductivity can promote the electrochemical process in electrode. Whereas the existence of electronic conductivity in the electrolyte cases current leakage (non-faradaic current), leading to a low η_{FE} . As investigated in Article I and II, the PCCs with BGLC-based positrodes have a relatively low η_{FE} of ca. 60% at V_{TN} . In comparison, the η_{FE} is close to 100% in SOCs. The low η_{FE} results in a low energy efficiency. Therefore, it is crucial to thoroughly investigate the causes and effects of the non-faradaic current in full cells in order to address this issue.

As described in Chapter 2, the electronic hole concentration depends on various external conditions, including $p\text{H}_2\text{O}$, $p\text{O}_2$, operating temperature, and applied V or I . In steam electrolysis mode, the electronic transference number (t_e) increased obviously from 0.006 at 500 °C to 0.044 at 700 °C, suggesting that operating the cell at lower temperatures can partially block the non-faradaic current.

In addition to the working temperatures, the results from variation in gas contents confirmed

Additional results and general discussion

that higher $p_{\text{H}_2\text{O}}$ and lower p_{O_2} can reduce the non-faradaic current. For example, the t_e decreased from 0.03 to 0.008 by increasing $p_{\text{H}_2\text{O}}$ from 0.05 atm to 0.5 atm and also decreased from 0.016 to 0.011 by decreasing the p_{O_2} from 0.7 atm to 0.1 atm. Plotting $\log(t_e)$ as a function of $\log(p)$ (Figure 6.5) reveals the dependence of the electronic transference number on $p_{\text{H}_2\text{O}}$ and p_{O_2} , which is consistent with the theoretical electron hole concentration (Equation 8). This confirms that the non-faradaic current is more influenced by $p_{\text{H}_2\text{O}}$. Similar trends were found in the faradaic efficiency analysis: low operating temperature, high $p_{\text{H}_2\text{O}}$, and low p_{O_2} tend to increase the faradaic efficiency.

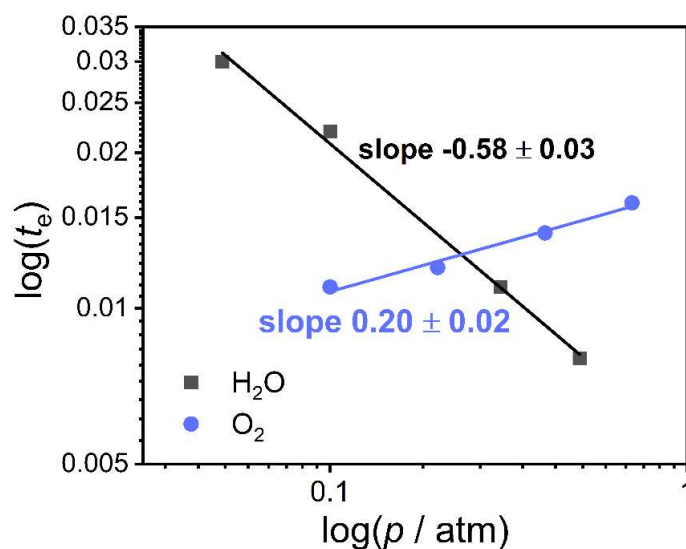


Figure 6.5: $\log(t_e)$ vs $\log(p_{\text{H}_2\text{O}})$ and $\log(p_{\text{O}_2})$ at 600 °C in the PCC cells with the BGLC587-BZCY541 positrode.

Moreover, the faradaic efficiency was dramatically influenced by the applied I or V . It is noteworthy that achieving a faradaic efficiency of $\geq 80\%$ at low overpotential or current density may not adequately reflect the high faradaic efficiency potential of the cells. In the present study, the faradaic efficiency can reach values as high as 80%–90% at -0.1 A cm^{-2} (for PCCs with BGLC1082-BZCY541 positrode in Article II); however, it decreases to ca. 60% at V_{TN} . As described in Equation 9, the electronic hole concentration increases upon the applied V . Moreover, at higher V , the local $p_{\text{H}_2\text{O}}$ at the interface of electrolyte/positrode could be more than 50% lower than the $p_{\text{H}_2\text{O}}$ at the inlet³⁴. Additionally, the local p_{O_2} increases by O_2 production during electrolysis. These combined changes together could potentially lead to an increase in non-faradaic current through the electrolyte. On this basis, we have concluded that the non-faradaic current can be partially blocked by increasing $p_{\text{H}_2\text{O}}$ and decreasing p_{O_2} . Apart

from the results obtained from Article I and II with BGLC-based positrode, the faradaic efficiency analysis was performed in a PCC with BLC-BZCY541 positrode as the additional results, as depicted in Figure 6.6. The finding reveals comparable trends to those observed in the PCC with BGLC-BZCY541.

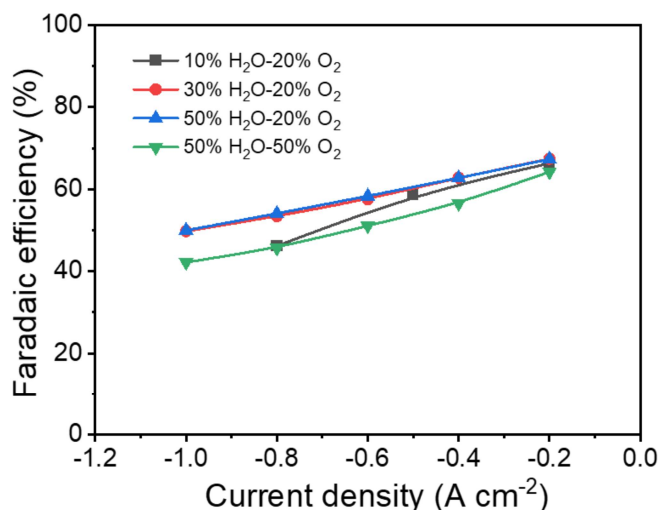


Figure 6.6: Faradaic efficiency analysis of a PCC with the BLC-BZCY541 positrode at 600 °C and different gas contents on the positrode side. The gas mixture was balanced with N₂.

It is important to note that all the results are based on the evaluation of the PCCs in button cells. At this scale, the cells typically do not face the gas conversion losses during operation as they are tested at low conversion rate. Therefore, the gas concentrations do not change significantly over the active area. In large cells and for practical application of stacks, the steam conversion rate could be as high as 80% to 90%¹²⁴, which would result in a significant decrease in $p_{\text{H}_2\text{O}}$ together with an increase in p_{O_2} along the gas channel. Thus, it is speculated that the non-faradaic current may not be significantly reduced by simply controlling the inlet gas content. Hence, it is worth emphasizing that further research aiming at reducing non-faradaic current and, consequently, increasing electricity efficiency shall be one of the primary focal points for future PCC development.

The strategies to increase the faradaic efficiency can be carried out from the aspects as illustrated in Figure 6.7. With a given functional cell, optimizing the operating conditions might be the easiest way to increase the faradaic efficiency, for instance, under high $p_{\text{H}_2\text{O}}$, low p_{O_2} and low T . Additionally, the issue of low faradaic efficiency may be addressed by exploring use cases at reduced oxygen partial pressure; for instance, working as a hydrogen pumping can

Additional results and general discussion

achieve a faradaic efficiency close to 100%^{125, 126}.

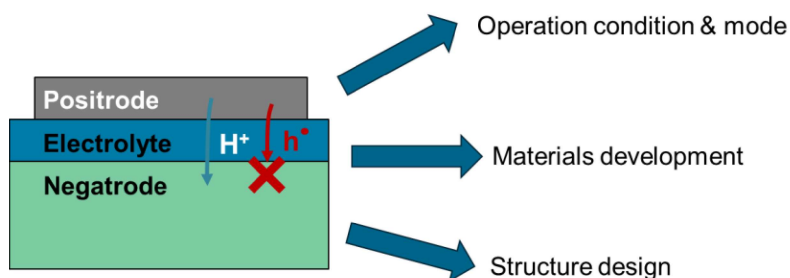


Figure 6.7: Strategies to increase the faradaic efficiency of PCCs.

Furthermore, the development of protonic ceramic with low electronic conductivity could be the optimal solution. In the present study, we tested different composite positrodes in the same half cells. The faradaic efficiency did not show big differences. Replacing the BZCY541 electrolyte by other protonic ceramics could be a viable solution to increase the faradaic efficiency. For instance, PCCs with BZCYYb4411 exhibit ca. 80% faradaic efficiency at -0.8 A cm^{-2} ¹²⁷. However, a faradaic efficiency of only about 48% has also been reported at V_{TN} by using BZCYYb4411⁷⁶. As discussed in Chapter 2, BZCYYb exhibits conflicting stability characteristics in H_2O and CO_2 atmospheres from different publications, which could be the reason for the different faradaic efficiency reported. Therefore, more detailed investigations should be carried out with this series of materials. Regarding the cell structure, since BZCY is a p-type conductor, by inserting the additional layer with an n-type conductor at the interface of the electrolyte and the electrode could be another approach to investigate in order to block the current leakage. Further research is needed to develop new types of materials that can meet the above criteria.

6.3 Hydrogen production and durability of the performances

The investigated PCCs were comprehensively compared with state-of-the-art SOCs for hydrogen production at intermediate temperatures, in order to elucidate the advantages and disadvantages of PCC technology. PCCs exhibit significantly lower activation energy in terms of both ohmic resistance and polarization resistance. Remarkably, despite having an electrolyte thickness of ca. $10 \mu\text{m}$, PCCs demonstrate higher electrochemical performance than commercial SOCs with an electrolyte thickness of ca. $3 \mu\text{m}$. Since the majority of ohmic losses are attributed to the electrolyte layer, it is reasonable to expect that the performance of PCCs

can be further enhanced by employing a thinner electrolyte, as evidenced in several publications already^{58, 127}. Consequently, the operating temperatures can be further reduced to around 450 °C. This will extend the potential applications of PCC to various industrial sectors, including the automotive industry. It is important to note that a reduced electrolyte thickness may accelerate non-faradaic current¹²⁸. Achieving a balance between high electrocatalytic activity and elevated faradaic efficiency is a crucial factor to be considered.

In terms of durability, the sufficient short-term stability was demonstrated by testing the PCCs with BGLC58-BZCY541 and BGLC1082-BZCY541 composite positrodes at different applied currents ranging from -0.2 A cm^{-2} to -1 A cm^{-2} , which gives the possibility to couple PCC with renewable electricity to reduce the cost for green hydrogen production. As reported by IRENA, for instance, the global weighted-average levelized cost of electricity (LCOE) of new onshore wind projects was USD 0.033/kWh, which is 52% lower than the cheapest fossil fuel-fired power plant of USD 0.069/kWh in 2022¹²⁹. Given the fluctuating nature of intermittent renewable electricity generation, which varies daily and seasonally, it is essential for the electrolyser to respond rapidly and maintain stability when transitioning from periods of peak to trough power supply. These promising results demonstrate the possibility of coupling PCCs with the intermittent energy sources from solar and wind farms in order to reduce the costs of electricity compared to the electricity generated by fossil fuels.

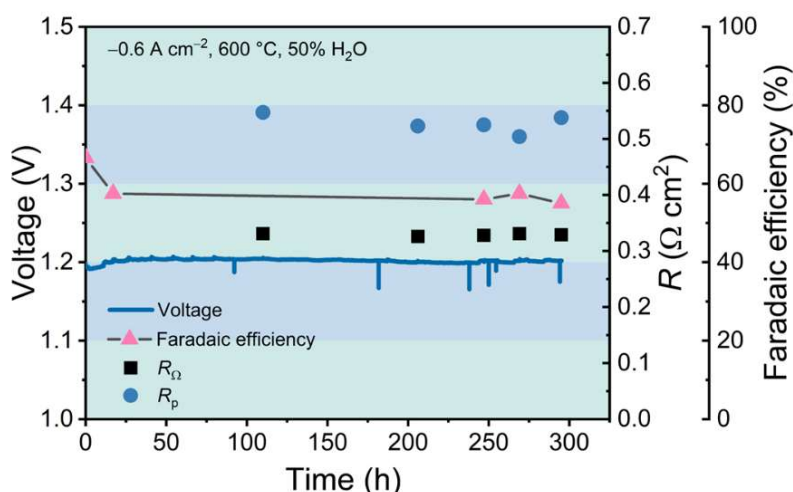


Figure 6.8: Durability measurement of PCCs with the BLC-BZCY541 positrode for hydrogen production.

Additionally, a 300 h stability assessment was conducted on the PCC with a BLC-BZCY541

Additional results and general discussion

positrode, as depicted in Figure 6.8. Throughout the evaluation, there were no significant changes in resistances, including R_{Ω} and R_p , cell voltage and faradaic efficiency. Furthermore, the exceptional long-term durability of the PCC at intermediate temperature was further verified by an extended measurement of 1680 hours in Article II. During the measurement, we did not find the obvious changes of the terminal voltages under different test conditions (i.e., $p\text{H}_2\text{O}$ and current density). Through post-mortem analysis, Ni migration was not observed via EDX-mapping, which is one of the primary reasons for performance degradation in SOCs^{130,131}. The lower operating temperature together with the lower $p\text{H}_2\text{O}$ on the negatrode side could explain the reason for the high reliability of the PCCs.

6.4 MS-PCCs for practical applications

The state-of-the-art protonic ceramics are $\text{BaZr}_{1-x-y}\text{Ce}_x\text{Y}_y\text{O}_{3-\delta}$ (BZCY). The refractory property of BZCY requires high sintering temperature ($\geq 1450\text{ }^\circ\text{C}$) to produce the dense electrolyte layer, resulting in significant energy consumption during the manufacturing process. At such high sintering temperatures, cracks and delamination of different functional layers may occur because of the mismatch shrinkage rates in different layers. Until now, the majority of PCC-related research has been confined to the button cell level, with a diameter of around 20 mm. In addition, several studies have demonstrated the possibility of scaling up PCC with a $5 \times 5\text{ cm}^2$ substrate^{58,132}. A stack with a single NS-PCC unit design exhibits a relatively high degradation rate of $3.3\% \text{ kh}^{-1}$ at 0.4 A cm^{-2} and $500\text{ }^\circ\text{C}$ ¹². Therefore, significant improvements are required for scaling up planar PCCs (e.g., $10 \times 10\text{ cm}^2$) with a cermet supported structure.

We have preliminarily proven the MS-PCC concept as a feasible development option for scaling up PCC, while several critical aspects also discussed. The diffusion of Cr from the metal substrate into the barrier layer and partially into the negatrode layer was observed, resulting in the formation of secondary phases. In order to prevent elemental diffusion, it is necessary to develop a new barrier layer with a thermal expansion coefficient of approximately $12 \times 10^{-6}\text{ K}^{-1}$, while also exhibiting sufficient electronic conductivity and dimensional stability in reducing atmospheres. The thin film barrier layer should preferably cover the entire surface of the metal substrate. Methods such as dip-coating and infiltration can be used¹³³. Additionally, the ITM substrate used in this study, with a 3D porous structure, presents challenges in achieving uniform coating coverage across the entire surface of the substrate. Using a metal substrate with regularly straight holes created by laser drilling can facilitate the flow of the

coating solution and ensure uniform distribution.

For the future development of MS-PCCs, an interesting parallel with the MS-SOCs developed by Ceres Power could be envisioned. The SteelCell® demonstrates rapid progress towards commercialization. A low-sintering (less than 1100 °C) approach is used to sinter dense ceria layer on stainless steel¹³⁴. The MS-SOCs have been integrated into 1 kW and 5 kW stack platforms in 2019¹³⁵. A 100 kW scale electrolysis module has been demonstrated using the MS-SOCs in 2023¹³⁶. Indeed, a key issue for the future development of the MS-PCC may be the scalability of the thin film electrolyte deposition method for industrial application.

Materials saving is an important aspect that can promote the development of MS-PCCs. One benefit of using a stainless-steel substrate is the reduction in the consumption of critical raw materials (Figure 6.9). For a megawatt (MW) electrolysis system, the demand for ceramic materials decreased obviously from 175.5 kg with negatrode-supported cells to 32.6 kg with MS-PCCs, especially for the elements of Ba, Zr, Ce, and Y. It is worth mentioning that the metal substrate with a thickness of ca. 600 µm was not optimized in the present study. The thickness of the metal substrate can be easily reduced while still offering sufficient mechanical strength compared to the cermet substrate. This enables higher volumetric power density within the stacks, facilitating device size miniaturization.

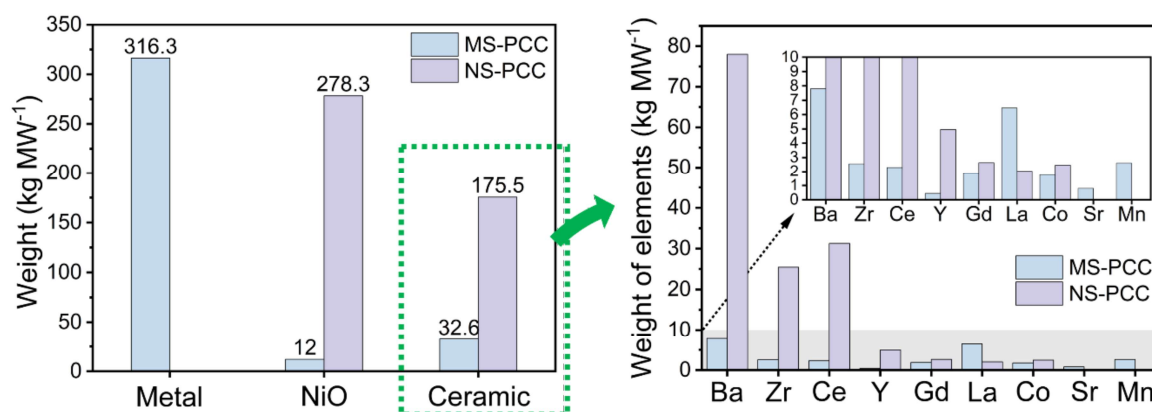


Figure 6.9: Consumption of different materials in NS-PCC and MS-PCC configurations.

In summary, despite the various technical challenges facing MS-PCCs at this early stage, it remains worthwhile to continue research in this area as it offers promising solutions for scaling up PCCs.

7 Conclusions and outlook

7.1 Conclusions

This doctoral dissertation encompasses thorough research concentrated on the investigation of positrode materials with high electrocatalytic activity and reliability for integration into a scalable planar protonic ceramic cell for hydrogen production at intermediate temperatures. The focus of the study is the exploration of the precise impact of the non-faradaic current in the protonic ceramic electrolyte on the electrochemical behavior, faradaic efficiency, energy conversion efficiency, and durability of the cell.

Barium cobalt-based perovskite materials, including $\text{Ba}_{1-x}\text{Gd}_{0.8}\text{La}_{0.2+x}\text{Co}_2\text{O}_{6-\delta}$ (BGLC) and $\text{Ba}_{0.5}\text{La}_{0.5}\text{CoO}_{3-\delta}$ (BLC), exhibited high electrochemical performance in both steam electrolysis and fuel cell mode in a planar protonic ceramic cell (PCC) configuration, allowing operation at a high current density compared to PCC in a tubular design. An equivalent circuit model (ECM) containing a parallel channel representing the electronic conductivity was proposed to analyze the electrochemical impedance spectroscopy (EIS) recorded in the PCCs under various operating conditions, such as working temperature (T), particle pressure of steam ($p\text{H}_2\text{O}$), particle pressure of oxygen ($p\text{O}_2$), and applied current (I). The faradaic efficiency could reach ca. 60% at V_{TN} with a current density as high as -0.8 A cm^{-2} in the PCCs with different positrode materials. Consequently, the energy conversion efficiency is ca. 55–60%, and the efficiency is still competitive with low temperature electrolysis techniques. Moreover, it was found that the PCCs display higher faradaic efficiency under low T , high $p\text{H}_2\text{O}$, low $p\text{O}_2$, and low I condition. The findings provide meaningful guidelines for defining a proper operational window for PCCs in order to achieve a higher energy conversion rate. However, operating the cell at low I may conflict with economically viable practical applications. The results emphasized that the development of new protonic ceramic materials with low electronic conductivity and the optimization of the cell structure with the implementation of a non-faradaic current blocking layer should be the focus of future work.

As demonstrated in this research, operating a PCC at the reduced temperature of 600 °C yields several significant benefits compared to mature solid oxide cell (SOCs) technology with a typical operating temperature higher than 800 °C. PCCs exhibit a higher hydrogen production rate compared to state-of-the-art SOCs under similar conditions, despite experiencing current

leakage issues. The further development of PCCs provides interesting prospects for accelerating the commercialization of green hydrogen production technology by addressing this issue in the foreseeable future.

The good short-term stability of PCCs at different current densities allows them to be coupled with intermittent renewable electricity. Furthermore, a 300 h durability test at 600 °C demonstrated the stability of key parameters such as the cell voltage, resistance, and faradaic efficiency over time. Eventually, the excellent long-term reliability over 1680 h in steam electrolysis mode at a high current density of -0.8 A cm^{-2} and 600 °C was examined. The Ni migration phenomenon, which is considered as the main cause of SOC degradation in electrolysis, was not observed by EDX-mapping analysis in the tested PCC. The low operating temperature mitigates the elemental diffusion between the different cell components, which suggests interesting prospects for the life-time of PCC stacks and systems.

Finally, this study demonstrates, for the first time, a novel concept of metal-supported protonic ceramic cells (MS-PCC) as a technically realizable design for practical application. Pulsed laser deposition was employed as the key technology for making a thin-film protonic ceramic electrolyte on a $5 \times 5 \text{ cm}^2$ metal substrate. All the manufacturing processes were conducted at temperatures lower than 1000 °C. In comparison, the conventional manufacturing method requires sintering temperatures higher than 1500 °C, resulting in high costs and the formation of cracks or delamination in different layers due to the different thermal expansion of cell components. Moreover, by replacing the thick negative cermet layer with the metal substrate, the consumption of critical raw materials can be reduced by ca. 80%. The electrochemical performance of MS-PCC was examined in steam electrolysis mode and exhibited a current density as high as -0.84 A cm^{-2} at V_{TN} and 600 °C.

With the outcomes of this thesis, the reduction of the non-faradaic current in the electrolyte at high current density is identified as a key remaining challenge. Furthermore, long-term stability over a significant extended period of ca. 10 000 h still needs to be explored. Planar PCC stacks with $10 \times 10 \text{ cm}^2$ unit cells have not been reported yet and still need to be demonstrated. Given the numerous advantages highlighted in this study, PCCs clearly merit further scientific research and development.

7.2 Outlook

The excellent properties of proton-conducting ceramic cells in fuel cell and steam electrolysis operation have been demonstrated in this work. However, several critical challenges remain to be overcome for the further commercialization of this technology. Especially, specific directions for future work are outlined below:

1) *Enhancing electrochemical performance*

This thesis mainly focused on the operation of PCCs at 600 °C. By further increasing the electrochemical performance of the cell with a higher volumetric power density, the operating temperature can be further reduced to ca. 450 °C, enabling faster start up. Consequently, the PCFCs could be utilized in the automobile industry. The lower operating temperature enables the reuse of waste steam in other industrial sectors for hydrogen production purposes.

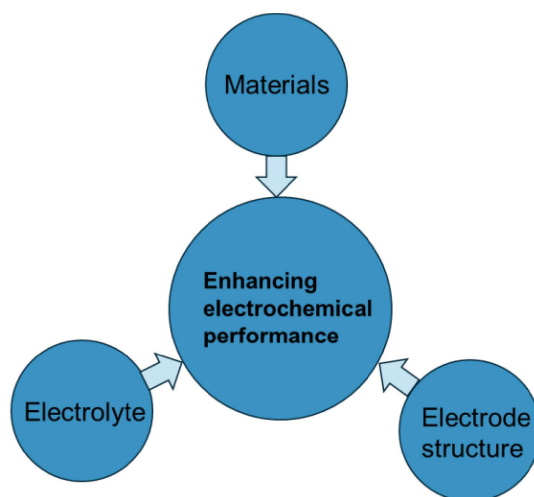


Figure 7.1: Strategies to increase the cell's electrochemical performance.

To increase the electrochemical performance further, we can focus on various aspects (Figure 7.1), such as materials design, electrolyte, and electrode structure optimization. Since the sluggish kinetics at the positive electrode cause the majority of the activation losses. Thus, the materials should exhibit sufficiently high electronic and protonic conductivities together with high surface catalytic activity towards oxygen-ion related surface processes. Recently, promising results from high-entropy oxides have shown high catalytic activity at low operating temperatures, making them potential candidates for use as the positive electrode in PCCs. However, the durability of high-entropy oxides under extreme working conditions (high current density and

high $p_{\text{H}_2\text{O}}$) needs to be assessed. Furthermore, based on the reaction kinetics analysis method proposed in the study, the rate limiting steps can be figured out. Therefore, the electrode structure can be optimized accordingly on the basis of the specific results with a given particular system. Lastly, the use of a thin film electrolyte can reduce ohmic losses. However, the thin film electrolyte can present challenges in terms of manufacturability and scalability. In addition, the reduced electrolyte thickness may increase the non-Faradaic current in the electrolyte. All these aspects deserve further investigation to increase cell performance and reduce the operating temperature to about 450 °C.

2) Other potential applications with PCCs

Having protons as the main charge carrier in the electrolyte expands the potential applications of PCCs, particularly for the synthesis of ammonia and high-value hydrocarbon products (Figure 7.2).

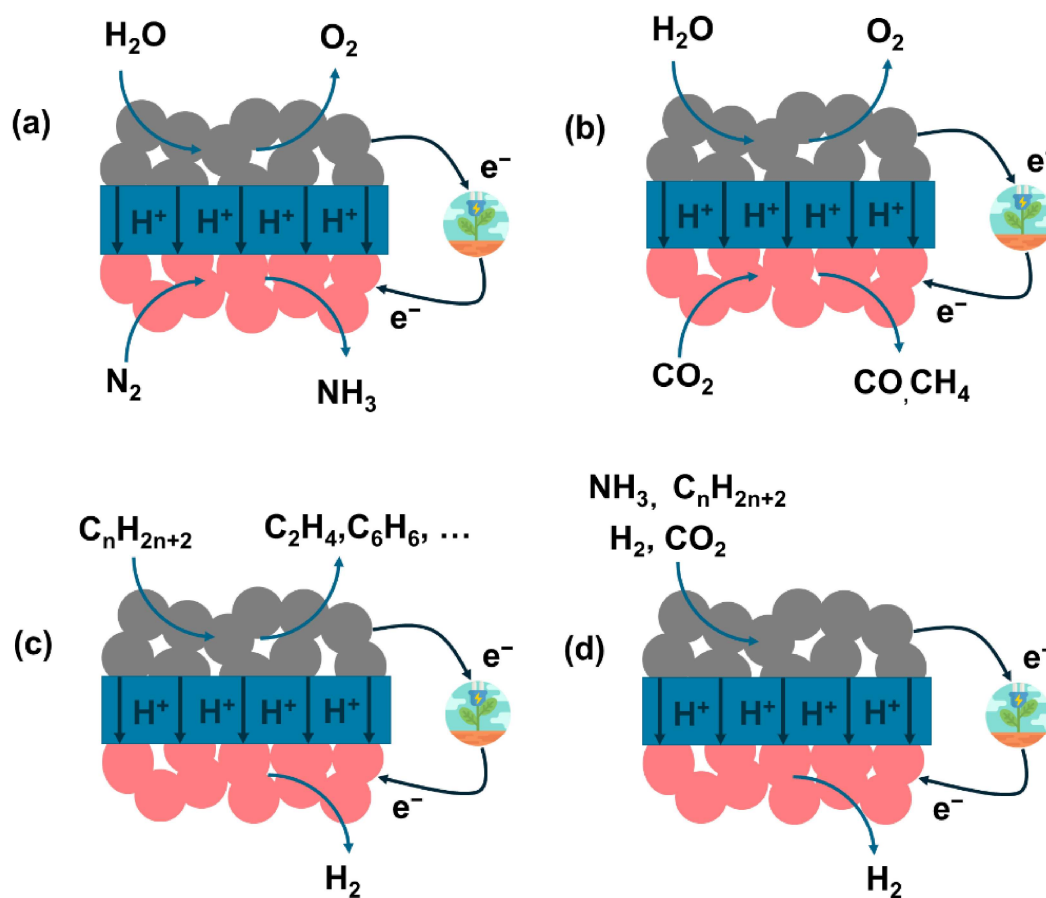


Figure 7.2: Different electrochemical use-cases with PCCs at intermediate temperatures.

Conclusions and outlook

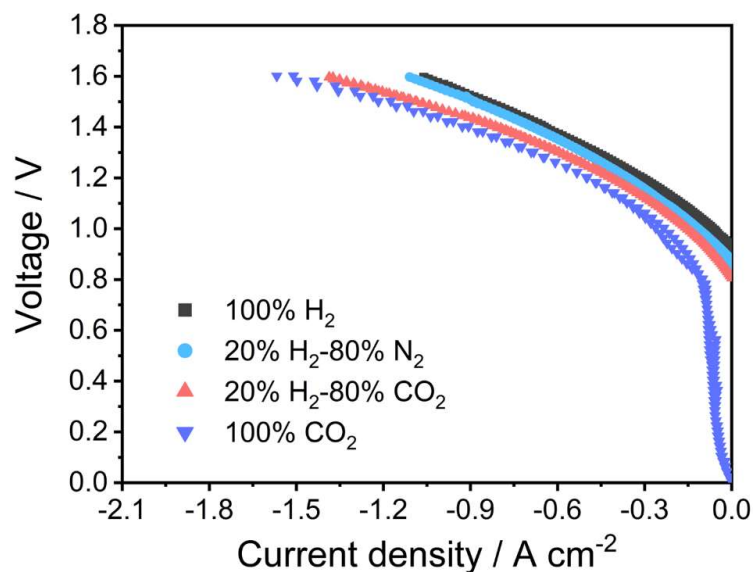


Figure 7.3: Preliminary results for $\text{CO}_2\text{-H}_2\text{O}$ co-electrolysis in PCCs with the BGLC-BZCY positrode. The polarization curves were recorded with 30% steam/air on the positrode side and various gases on the negatrode side at 700 °C.

PCCs can be used as a reactor to produce CH_4 by $\text{CO}_2\text{-H}_2\text{O}$ co-electrolysis (Figure 7.2b). Preliminary tests with the prepared PCCs for this reaction (Figure 7.3) were conducted using polarization curves. The cell exhibits a higher current density in co-electrolysis mode compared to steam electrolysis conditions. The next step involves analyzing the outlet gases and identifying a suitable catalyst with higher CH_4 conversion activity in the negatrode.

Additionally, as illustrated in Figure 7.2a, PCCs can serve as the reactor for ammonia synthesis through the extraction of protons from the water-splitting process¹³⁷. However, it is worth noting that the produced O_2 on the positrode side leads to an increase in $p\text{O}_2$ and the formation of electronic holes. Therefore, the development of a highly faradaic efficient PCC stands as a pivotal step to achieve a high conversion rate for NH_3 or CO/CH_4 . Alternatively, the use of PCCs for specific reactions within a low oxidizing atmosphere can inherently circumvent the non-faradaic current, for example as a hydrogen pumping device (Figures 7.2c and 7.2d). As next steps, the primary focus will shift towards exploring highly active and durable catalysts, as well as scaling up PCCs.

Appendix A: Supplementary information for Article I

Supplementary Information

A double perovskite oxygen electrode in Zr-rich proton conducting ceramic cells for efficient electricity generation and hydrogen production

Haoyu Zheng,^{*ab} Matthias Riegraf,^a Noriko Sata^a and Rémi Costa^{*a}

^a Institute of Engineering Thermodynamics, German Aerospace Center (DLR),
Pfaffenwaldring 38-40, 70569 Stuttgart, Germany

^b Institute for Building Energetics, Thermotechnology and Energy Storage (IGTE), University
of Stuttgart. Pfaffenwaldring 31, 70569 Stuttgart, Germany

E-mail: zhenghaoyu01@gmail.com; remi.costa@dlr.de

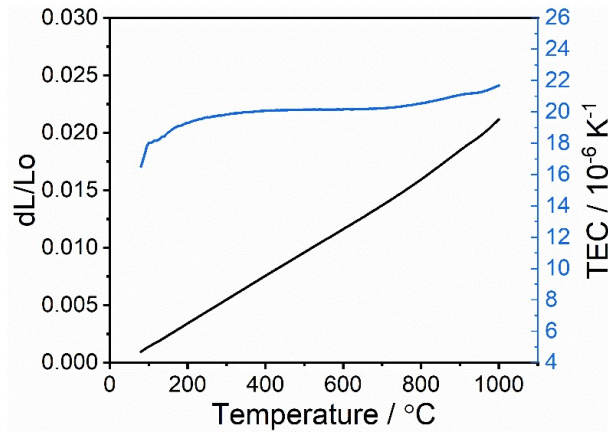


Figure S1. Thermal expansion behavior of BGLC587 from 80 °C to 1000 C in air.

Table S1. Comparison of BGLC587-BZCY541 oxygen electrode PCCs in fuel cell mode at 600 °C with perovskite-based oxygen electrode PCCs in previous studies.

Air electrode	electrolyte	Fuel electrode	PPD (mW cm ⁻²)		Ref.
			600 °C	650 °C	
BGLC587-BZCY541	BZCY541	Ni-BZCY541	403	570	This work
LiNi _{0.8} Co _{0.2} O ₂ - BaZr _{0.1} Ce _{0.7} Y _{0.2} O _{3-δ}	BaZr _{0.1} Ce _{0.7} Y _{0.2} O _{3-δ}	Ni-BaZr _{0.1} Ce _{0.7} Y _{0.2} O _{3-δ}		410	¹
SrSc _{0.175} Nb _{0.025} Co _{0.8} O _{3-δ}	BaZr _{0.1} Ce _{0.7} Y _{0.2} O _{3-δ}	Ni-BaZr _{0.1} Ce _{0.7} Y _{0.2} O _{3-δ}	~260	~360	²
PrBa _{0.5} Sr _{0.5} Co ₂ O _{5+δ} - BaZr _{0.1} Ce _{0.7} Y _{0.2} O _{3-δ}	BaZr _{0.1} Ce _{0.7} Y _{0.2} O _{3-δ}	Ni-BaZr _{0.1} Ce _{0.7} Y _{0.2} O _{3-δ}	274	395	³
Ba _{0.5} Sr _{0.5} Co _{0.8} Fe _{0.2} O _{3-δ}	BaCe _{0.8} Y _{0.2} O _{3-δ}	Ni-BaCe _{0.8} Y _{0.2} O _{3-δ}	~280	~400	⁴
Ba _{0.5} Sr _{0.5} Co _{0.8} Fe _{0.2} O _{3-δ}	BaZr _{0.4} Ce _{0.4} Y _{0.2} O _{3-δ}	Ni-BaZr _{0.4} Ce _{0.4} Y _{0.2} O _{3-δ}	~155	~170	⁴
Ba _{0.5} Sr _{0.5} Co _{0.8} Fe _{0.2} O _{3-δ}	BaZr _{0.8} Y _{0.2} O _{3-δ}	Ni-BaZr _{0.8} Y _{0.2} O _{3-δ}	~23	~32	⁴
Pr ₂ NiO _{4+δ}	BaZr _{0.4} Ce _{0.4} Y _{0.2} O _{3-δ}	Ni-BaZr _{0.85} Y _{0.15} O _{3-δ}	102	158	⁵
Ba _{0.5} Sr _{0.5} (Co _{0.8} Fe _{0.2}) _{0.9} Ti _{0.1} O _{3-δ} - BaZr _{0.4} Ce _{0.4} Y _{0.2} O _{3-δ}	BaZr _{0.4} Ce _{0.4} Y _{0.2} O _{3-δ}	Ni-BaZr _{0.4} Ce _{0.4} Y _{0.2} O _{3-δ}	194	243	⁶
La _{0.6} Sr _{0.4} Co _{0.2} Fe _{0.8} O _{3-δ}	BaZr _{0.4} Ce _{0.4} Y _{0.2} O _{3-δ}	Ni-BaZr _{0.4} Ce _{0.4} Y _{0.2} O _{3-δ}	279	340	⁷
La _{0.6} Sr _{0.4} Co _{0.2} Fe _{0.8} O _{3-δ}	BaZr _{0.6} Ce _{0.2} Y _{0.2} O _{3-δ}	Ni-BaZr _{0.6} Ce _{0.2} Y _{0.2} O _{3-δ}	336	396	⁷
La _{0.6} Sr _{0.4} Co _{0.2} Fe _{0.8} O _{3-δ}	BaZr _{0.7} Ce _{0.1} Y _{0.2} O _{3-δ}	Ni-BaZr _{0.7} Ce _{0.1} Y _{0.2} O _{3-δ}	111		⁷
La _{0.6} Sr _{0.4} Co _{0.2} Fe _{0.8} O _{3-δ}	BaZr _{0.8} Y _{0.2} O _{3-δ}	Ni-BaZr _{0.8} Y _{0.2} O _{3-δ}	102		⁷
Sm _{0.5} Sr _{0.5} CoO _{3-δ} -Ce _{0.8} Sm _{0.2} O _{3-δ}	BaZr _{0.8} Y _{0.2} O _{3-δ}	Ni-BaZr _{0.1} Ce _{0.7} Y _{0.2} O _{3-δ}	55	70	⁸
La _{0.6} Sr _{0.4} Co _{0.2} Fe _{0.8} O _{3-δ} - BaCe _{0.7} Zr _{0.15} Y _{0.15} O _{3-δ}	BaCe _{0.7} Zr _{0.15} Y _{0.15} O _{3-δ}	Ni-BaCe _{0.7} Zr _{0.15} Y _{0.15} O _{3-δ}	~190	~260	⁹
BaZr _{0.1} Ce _{0.7} Y _{0.2} O _{3-δ} - Sm _{0.5} Sr _{0.5} CoO _{3-δ}	BaZr _{0.1} Ce _{0.7} Y _{0.2} O _{3-δ}	Ni-BaZr _{0.1} Ce _{0.7} Y _{0.2} O _{3-δ}	445	598	¹⁰

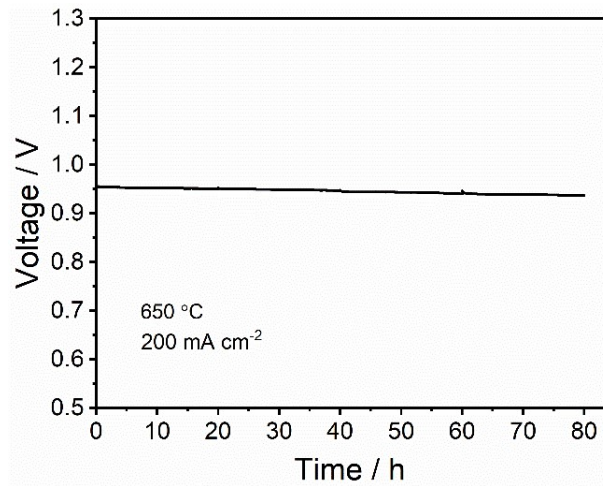


Figure S2. Durability test of the PCC cell at 200 mA cm^{-2} and 650 °C in fuel cell mode with wet hydrogen on the fuel electrode side and wet air on the oxygen electrode side.

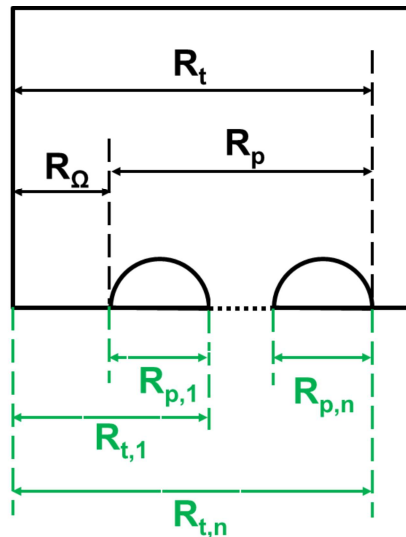


Figure S3. Simulated Nyquist plot of impedance spectra for the circuit containing n (RQ)_{*i*} elements.

Note S1

Typically, in Nyquist plots (Figure S3) of SOCs with YSZ electrolyte which is a pure oxygen ion conductor, the first x -axis intercept at the high frequency regime could be considered as ohmic resistance (R_Ω), which normally arises from the bulk resistance in electrolyte, while the intercept of the squashed arcs in between corresponds to the polarization resistance (R_p), which is related with the electrochemical reaction in both fuel electrode and oxygen electrode. In PCC cells, however, the existence of electronic conduction through the electrolyte makes the real polarization resistance ($R_{p,r}$) different from the apparent polarization resistance (R_p). Therefore,

the electronic resistance (R_e) was introduced parallelly into the equivalent circuit shown in Figure 3a. At the high frequency intercept, the polarization capacitance could be assumed to be short-circuited. Hence, R_Ω representing the apparent ohmic resistance is given as

$$R_\Omega = \frac{R_e R_i}{R_e + R_i} \quad , \quad (1)$$

where R_e and R_i indicate electronic resistance and ionic resistance in the electrolyte. At lower frequencies, the polarization resistance contributes to the impedance and the total resistance (R_t) can be expressed as

$$R_t = \frac{R_e (R_i + R_{p,r})}{R_e + (R_i + R_{p,r})} \quad , \quad (2)$$

where $R_{p,r}$ represents the real polarization resistance under the influence of electronic conduction through electrolyte. Since R_e can be expressed as

$$R_e = \frac{R_t}{1 - \frac{V_{OC}}{V_N}} \quad , \quad (3)$$

where V_{OC} and V_N are the measured open circuit voltage and computed Nernst voltage, respectively.¹¹ Consequently, the average ionic transference number (t_i) and R_i can be expressed and calculated by

$$t_i = \frac{R_e}{R_e + R_i} = 1 - \frac{R_\Omega}{R_t} \left(1 - \frac{V_{OC}}{V_N}\right) \quad , \quad (4)$$

$$R_i = \frac{R_\Omega}{t_i} \quad . \quad (5)$$

Substitution of equation (3) and (4) into (2), the real polarization resistance can be calculated based on R_t , R_Ω and t_i , as expressed below

$$R_{p,r} = \frac{R_\Omega (R_t - R_\Omega)}{t_i [t_i R_t - (R_t - R_\Omega)]} \quad . \quad (6)$$

In practical resistance analysis, there will be more than one RQ element required in the equivalent circuit based on the physico-chemical processes as shown in Figure 3b. The real polarization resistance ($R_{p,r,i}$) for each $(RQ)_i$ element can be calculated as well by using equation (6).

Table S2. Electrochemical characteristics of representative PCC cells at OCV in fuel cell mode.

T °C	R_t $\Omega \text{ cm}^2$	R_Ω $\Omega \text{ cm}^2$	R_p $\Omega \text{ cm}^2$	$R_{p,r}$ $\Omega \text{ cm}^2$	R_i $\Omega \text{ cm}^2$	R_e $\Omega \text{ cm}^2$	t_i	t_e
500	2.460	0.823	1.637	1.673	0.827	153.999	0.995	0.005
550	1.131	0.569	0.562	0.585	0.577	42.021	0.986	0.014
600	0.615	0.421	0.194	0.209	0.434	14.589	0.971	0.029
650	0.397	0.322	0.075	0.085	0.340	6.092	0.947	0.053
700	0.287	0.250	0.037	0.045	0.273	3.014	0.917	0.083

Table S3. Comparison of the PCFC with BGLC587-BZCY541 oxygen electrode at 600 °C in this study with the best performance PCFCs using different proton conducting electrolytes.

Air electrode	Electrolyte	Fuel electrode	PPD	R_Ω	R_p	Ref.
BGLC587-BZCY541	BaZr _{0.5} Ce _{0.4} Y _{0.1} O _{3-δ} ~12 μm	Ni- BaZr _{0.5} Ce _{0.4} Y _{0.1} O _{3-δ}	403	0.421	0.194	This work
NBSCF	BaZr _{0.1} Ce _{0.7} Y _{0.1} Yb _{0.1} O _{3-δ} ~15 μm	Ni- BaZr _{0.1} Ce _{0.7} Y _{0.1} Yb _{0.1} O _{3-δ}	690	0.128	0.283	¹²
PBCC	BaZr _{0.1} Ce _{0.7} Y _{0.1} Yb _{0.1} O _{3-δ} ~10 μm	Ni- BaZr _{0.1} Ce _{0.7} Y _{0.1} Yb _{0.1} O _{3-δ}	1060	~0.1	~0.2	¹³
PBCFN	BaZr _{0.1} Ce _{0.7} Y _{0.1} Yb _{0.1} O _{3-δ} ~10 μm	Ni- BaZr _{0.1} Ce _{0.7} Y _{0.1} Yb _{0.1} O _{3-δ}	723	~0.15	~0.28	¹⁴
BSCF	BaCe _{0.55} Zr _{0.3} Y _{0.15} O _{3-δ} 5 μm	Ni- BaCe _{0.55} Zr _{0.3} Y _{0.15} O _{3-δ}	1302	0.09	0.09	¹⁵
LSC (Pulsed laser deposition)	BaZr _{0.85} Y _{0.15} O _{3-δ} ~2 μm (Pulsed laser deposition)	Ni- BaZr _{0.85} Y _{0.15} O _{3-δ}	740	~0.1	~0.15	¹⁶
LSC (Pulsed laser deposition)	BaCe _{0.55} Zr _{0.3} Y _{0.15} O _{3-δ} ~1 μm (Pulsed laser deposition)	Ni- BaCe _{0.55} Zr _{0.3} Y _{0.15} O _{3-δ} (Pulsed laser deposition)	1100	~0.06	~0.23	¹⁷

NBSCF=NdBa_{0.5}Sr_{0.5}Co_{1.5}Fe_{0.5}O_{5+δ};PBCC= PrBa_{0.8}Ca_{0.2}Co₂O_{5+δ};PBCFN= PrBaCo_{1.6}Fe_{0.2}Nb_{0.2}O_{5+δ};BSCF= Ba_{0.5}Sr_{0.5}Co_{0.8}Fe_{0.2}O_{3-δ};LSC=La_{0.6}Sr_{0.4}CoO_{3-δ};

Note S2

Table S3 summarizes some of the best PCFC performances published in recent years. The relatively high ohmic losses of our BZCY541 electrolyte could be explained by the Zr-rich phase of the material compared to those of the other cells in this table. However, the low polarization resistance is still competitive.

Table S4. Comparison of the PCC cell with BGLC587-BZCY541 oxygen electrode in steam electrolysis mode at 600 °C with PCC cells from previous studies.

Air electrode	Electrolyte	Fuel electrode	Air electrode gas composition	Current density at 1.3 V (A cm ⁻²)	Ref.
BGLC587-BZCY541	BZCY541	Ni-BZCY541	Air (30% H ₂ O)	-0.650	This work
La _{0.6} Sr _{0.4} Co _{0.2} Fe _{0.8} O _{3-δ} -BaZr _{0.8} Y _{0.2} O _{3-δ}	BaZr _{0.8} Y _{0.2} O _{3-δ}	Ni-BaZr _{0.8} Y _{0.2} O _{3-δ}	Air (3% H ₂ O)	-0.053	¹⁸
Sm _{0.5} Sr _{0.5} CoO _{3-δ} -BaCe _{0.5} Zr _{0.3} Y _{0.2} O _{3-δ}	BaCe _{0.5} Zr _{0.3} Y _{0.2} O _{3-δ}	Ni-BaCe _{0.5} Zr _{0.3} Y _{0.2} O _{3-δ}	Air (50% H ₂ O)	-0.190	¹⁹
Sr ₂ Fe _{1.5} Mo _{0.5} O _{6-δ} -BaZr _{0.8} Y _{0.2} O _{3-δ}	BaZr _{0.8} Y _{0.2} O _{3-δ}	Ni-BaZr _{0.8} Y _{0.2} O _{3-δ}	Air (3% H ₂ O)	-0.210	²⁰
Pr ₂ NiO _{4+δ} -BaZr _{0.2} Ce _{0.6} Y _{0.2} O _{3-δ}	BaZr _{0.2} Ce _{0.6} Y _{0.2} O _{3-δ}	Ni-BaZr _{0.2} Ce _{0.6} Y _{0.2} O _{3-δ}	Air (40% H ₂ O)	-0.600	²¹
SrEu ₂ Fe _{1.8} Co _{0.2} O _{7-δ} -BaZr _{0.5} Ce _{0.3} Y _{0.2} O _{3-δ}	BaZr _{0.5} Ce _{0.3} Y _{0.2} O _{3-δ}	Ni-BaZr _{0.5} Ce _{0.3} Y _{0.2} O _{3-δ}	Air (10% H ₂ O)	-0.350	²²
Sr _{2.8} La _{0.2} Fe ₂ O _{7-δ}	BaCe _{0.5} Zr _{0.3} Y _{0.2} O _{3-δ}	Ni-BaCe _{0.5} Zr _{0.3} Y _{0.2} O _{3-δ}	Air (20% H ₂ O)	-0.460	²³
La _{1.2} Sr _{0.8} NiO ₄	BaCe _{0.7} Zr _{0.1} Y _{0.2} O _{3-δ}	Ni-BaCe _{0.7} Zr _{0.1} Y _{0.2} O _{3-δ}	Air (20% H ₂ O)	-0.420	²⁴
Pr _{1.2} Sr _{0.8} NiO ₄	BaCe _{0.7} Zr _{0.1} Y _{0.2} O _{3-δ}	Ni-BaCe _{0.7} Zr _{0.1} Y _{0.2} O _{3-δ}	Air (20% H ₂ O)	-0.350	²⁴
(PrBa _{0.8} Ca _{0.2}) _{0.95} Co ₂ O _{6-δ}	BaCe _{0.4} Zr _{0.4} Y _{0.1} Yb _{0.1} O _{3-δ}	Ni-BaCe _{0.4} Zr _{0.4} Y _{0.1} Yb _{0.1} O _{3-δ}	O ₂ (20% H ₂ O)	-0.720	²⁵
PrBa _{0.8} Ca _{0.2} Co ₂ O _{6-δ}	BaCe _{0.4} Zr _{0.4} Y _{0.1} Yb _{0.1} O _{3-δ}	Ni-BaCe _{0.4} Zr _{0.4} Y _{0.1} Yb _{0.1} O _{3-δ}	O ₂ (20% H ₂ O)	-0.505	²⁵

Table S5. Electrochemical characteristics of representative PCC cells at OCV in steam electrolysis operation.

T °C	R_t $\Omega \text{ cm}^2$	R_Ω $\Omega \text{ cm}^2$	R_p $\Omega \text{ cm}^2$	$R_{p,r}$ $\Omega \text{ cm}^2$	R_i $\Omega \text{ cm}^2$	R_e $\Omega \text{ cm}^2$	t_i	t_e
500	3.117	0.975	2.142	2.196	0.980	166.678	0.994	0.006
550	1.554	0.617	0.937	0.965	0.622	73.926	0.992	0.008
600	0.809	0.464	0.345	0.362	0.473	26.481	0.982	0.018
650	0.514	0.355	0.159	0.170	0.365	13.053	0.973	0.027
700	0.385	0.279	0.106	0.118	0.292	6.397	0.956	0.044

Table S6. Electrochemical characteristics of representative PCC cells at OCV in steam electrolysis operation at different steam concentrations mixed with air on the oxygen electrode side.

$p_{\text{H}_2\text{O}}$ atm	V_{OC} V	V_E V	R_t $\Omega \text{ cm}^2$	R_Ω $\Omega \text{ cm}^2$	R_p $\Omega \text{ cm}^2$	$R_{p,r}$ $\Omega \text{ cm}^2$	R_i $\Omega \text{ cm}^2$	R_e $\Omega \text{ cm}^2$	t_i	t_e
0.05	0.998	1.055	0.744	0.437	0.308	0.335	0.451	13.918	0.969	0.031
0.1	0.982	1.028	0.778	0.430	0.348	0.374	0.440	17.334	0.975	0.025
0.3	0.954	0.982	0.832	0.422	0.410	0.427	0.428	29.986	0.986	0.014
0.5	0.930	0.956	0.860	0.422	0.438	0.456	0.428	31.621	0.987	0.013
0.7	0.914	0.934	0.905	0.418	0.487	0.502	0.422	42.410	0.990	0.010

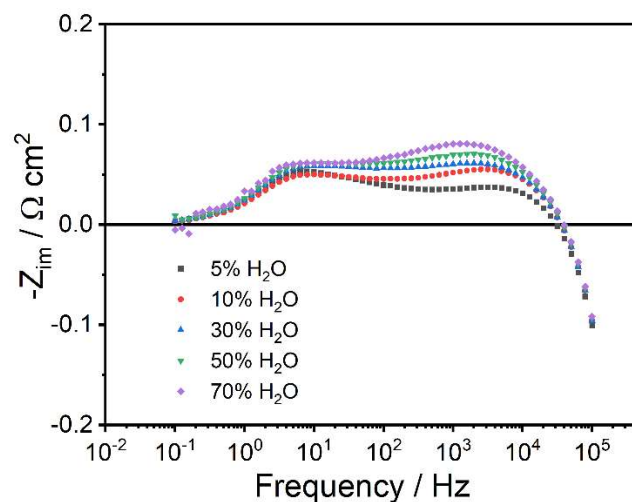


Figure S4. Imaginary impedance spectra of the cell measured with various H₂O concentrations (5–70%) mixed with air at OCV.

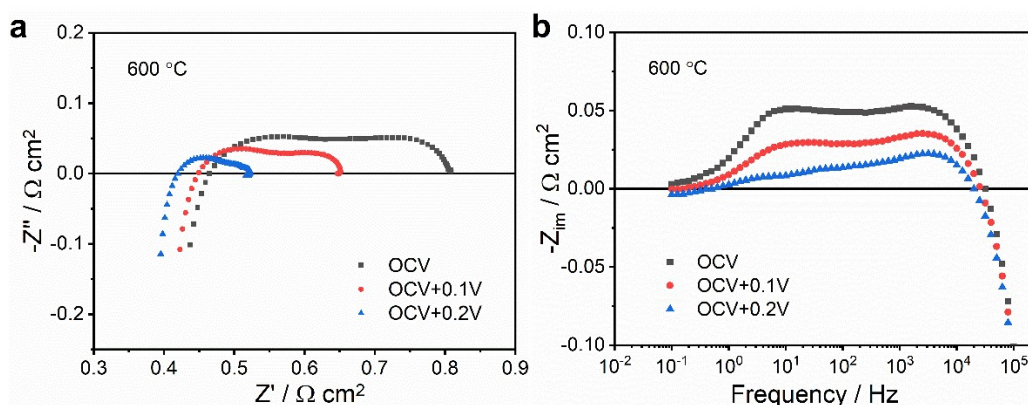


Figure S5. Electrochemical impedance spectra of the PCC cell with BGLC587-BZCY541 oxygen electrode measured at various electrolysis voltages with humidified 20% H₂-80% N₂ and 30% H₂O-70% air supplied to the fuel and oxygen electrode, respectively.

Table S7. Analysis of the impedance spectra at various electrolysis voltages for steam electrolysis at 600 °C.

Voltage	R_t	R_Ω	R_p	$R_{p,r}$	R_i	R_e	t_i	t_e
V	$\Omega \text{ cm}^2$	$\Omega \text{ cm}^2$	$\Omega \text{ cm}^2$	$\Omega \text{ cm}^2$	$\Omega \text{ cm}^2$	$\Omega \text{ cm}^2$		
OCV	0.809	0.464	0.345	0.362	0.473	26.481	0.982	0.018
OCV+0.1	0.650	0.449	0.201	0.228	0.473	8.959	0.950	0.050
OCV+0.2	0.522	0.420	0.102	0.133	0.473	3.768	0.889	0.111

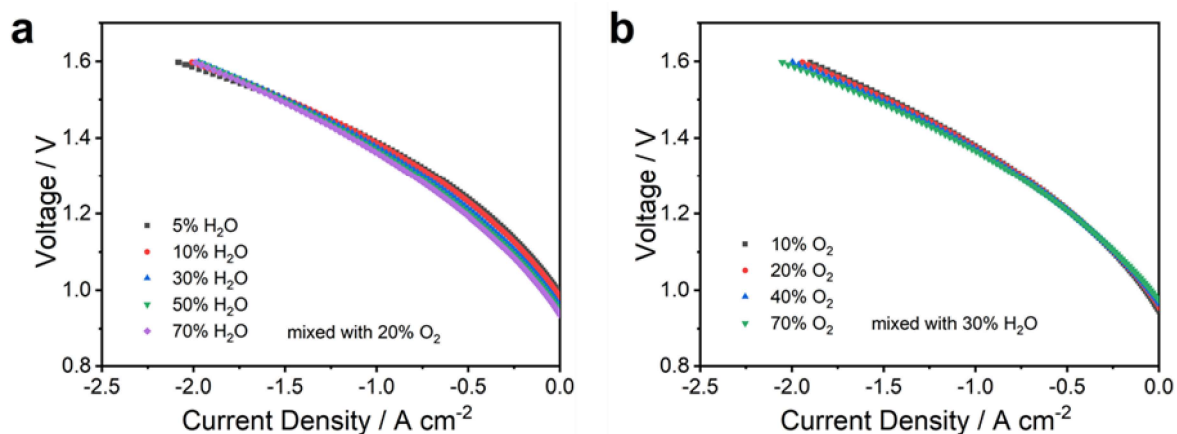


Figure S6. Gaseous atmosphere dependence of I-V curves of BGLC587-BZCY541 oxygen electrode cells at 600 °C. I-V curves as a function of H_2O partial pressure ($p_{\text{H}_2\text{O}}$) (a) and O_2 partial pressure (p_{O_2}) (b). The mixed gas was balanced with N_2 on the oxygen electrode side.

Table S8. Composition of high-performance PCECs and their faradaic efficiency determined by gas analysis in steam electrolysis operation.

Cell configuration: Air electrode Electrolyte fuel electrode	Gas composition		Current density at 1.3 V (A cm ⁻²)	η_{FE} at voltages or current densities	Ref.
	Oxygen electrode	Fuel electrode			
BGLC587-BZCY541 BZCY541 Ni-BZCY541	70%H ₂ O/Air	20%H ₂ /N ₂ (3%H ₂ O)	-0.70 (600 °C)	68% at -0.8 A cm ⁻² 75% at -0.4 A cm ⁻² (600 °C)	This work
BGLC587-BZCY541 BZCY541 Ni-BZCY541	30%H ₂ O/Air	20%H ₂ /N ₂ (3%H ₂ O)	-0.71 (600 °C)	60% at -0.8 A cm ⁻² 70% at -0.4 A cm ⁻² (600 °C)	This work
PBSCF BZCYYb4411 Ni-BZCYYb4411	3%H ₂ O/Air	5%H ₂ /Ar	-1.30 (600 °C)	~48% at -1.3 A cm ⁻² (600 °C)	²⁶
PBCFN BZCYYb1711 Ni-BZCYYb1711	3%H ₂ O/Air	3%H ₂ O/H ₂	-2.15 (650 °C)	~43% at -1.0 A cm ⁻² (650 °C)	¹⁴
PBCC BZCYYb1711 Ni-BZCYYb1711	30%H ₂ O/Air	3%H ₂ O/H ₂	-1.351 (600 °C)	~83% at 1.3 V (600 °C)	¹³
SLF BZCY352 Ni-BZCY352	20%H ₂ O/Air	3%H ₂ O/H ₂	-1.08 (700 °C)	~25% at -0.3 A cm ⁻² (700 °C)	²³
SLF BZCY352 Ni-BZCY352	20%H ₂ O/Air	3%H ₂ O/H ₂	-0.46 (600 °C)	-	²³
PNC BZCYYb4411 Ni-BZCYYb4411	15%H ₂ O/Air	5%H ₂ /Ar	-0.81 (600 °C)	~80% at 1.3 V (600 °C)	²⁷
BCFZY-BZCYYb4411 BZCYYb4411 Ni-BZCYYb4411	10%H ₂ O/Air	H ₂	-	~75% at -0.5 A cm ⁻² (550 °C)	²⁸
BCFZY-BZCYYb1711 BZCYYb1711 Ni-BZCYYb1711	20%H ₂ O/O ₂ -N ₂	Ar	-1.10 (600 °C)	~99% at -1.1 A cm ⁻² (600 °C)	²⁹
BCFZY-BZCYYb1711 BZCYYb1711 Ni-BZCYYb1711	10%H ₂ O/O ₂ -N ₂	Ar	-1.10 (600 °C)	~85% at -1.1 A cm ⁻² (600 °C)	²⁹
BCFZY-BZY20 BZY20 Ni-BZY20	20%H ₂ O/O ₂ -N ₂	Ar	-0.90 (600 °C)	~50% at -0.9 A cm ⁻² (600 °C)	²⁹

PBSCF= PrBa_{0.5}Sr_{0.5}Co_{1.5}Fe_{0.5}O_{5+ δ} ; PBCFN= PrBaCo_{1.6}Fe_{0.2}Nb_{0.2}O_{5+ δ} ; PBCC=PrBa_{0.8}Ca_{0.2}Co₂O_{5+ δ} ; SLF= Sr_{2.8}La_{0.2}Fe₂O_{7- δ}

PNC= PrNi_{0.5}Co_{0.5}O_{3-δ}; BCFZY= BaCo_{0.4}Fe_{0.4}Zr_{0.1}Y_{0.1}O_{3-δ}; BZCYYb4411= BaZr_{0.4}Ce_{0.4}Y_{0.1}Yb_{0.1}O_{3-δ};
BZCYY1711= BaZr_{0.1}Ce_{0.7}Y_{0.1}Yb_{0.1}O_{3-δ}; BZCY352= BaZr_{0.3}Ce_{0.5}Y_{0.2}O_{3-δ}; BZY20= BaZr_{0.8}CeY_{0.2}O_{3-δ}

Note S3.

High-temperature solid oxide electrolyzers based on oxygen ion conductors can reach electrical efficiency of 100% at thermoneutral voltage, that is ca. 1.3 V, which corresponds to practical use cases of the technology for industrial hydrogen production. Table S8 summarizes some of the high-performance fuel electrode supported PCEC in steam electrolysis operation and their faradaic efficiency determined at ~1.3 V. Some of the current density values at 1.3 V listed in Table S8 were estimated based on the polarization curves from the given references. The faradaic efficiency measured at voltages far below 1.3V or at comparatively low current densities (less than 400 A cm⁻²) in literature was excluded in the Table S8, due to the lack of significance for practical usage of the technology. The faradaic efficiency value was comparatively low and demonstrated that more than 50% of the applied current was lost by the electronic leakage. This is detrimental for the energy conversion efficiency. Therefore, it is crucial for the development of high-performance PCEC to achieve high faradaic efficiency values at high current densities of ~1.3 V.

Note S4. DRT analysis

To elucidate the reaction kinetics in the oxygen electrode for steam electrolysis, the distribution of relaxation times (DRT) analysis and equivalent circuit model (ECM) fitting were performed based on the electrochemical impedance of the full cells with BGLC587-BZCY541 oxygen electrodes. The different impedance spectra were recorded with the variation of $p\text{H}_2\text{O}$ and $p\text{O}_2$, accordingly, on the oxygen electrode side. To identify the specific contributions from the relevant processes to the impedance spectra, gas partial pressure variations can help. For example, when EIS measurements are compared where only $p\text{H}_2\text{O}$ or $p\text{O}_2$ were changed, the differences in the spectra should be related to the changes on the oxygen electrode side. Furthermore, the change of R_p with $p\text{H}_2\text{O}$ or $p\text{O}_2$ can give mechanistic insights into the nature of rate-limiting elementary kinetic step. If a single elementary reaction is the rate determining step, the dependence of the separated process in the impedance on $p\text{H}_2\text{O}$ and $p\text{O}_2$ should allow for its assignment to an elementary step based on a comparison with the kinetics formulated by the law of mass action.

Table S9. Electrochemical characteristics of representative PCC cells under OCV condition in steam electrolysis operation with various $p\text{H}_2\text{O}$ and $p\text{O}_2$ on oxygen electrode side.

$p\text{H}_2\text{O}$	$p\text{O}_2$	V_{OC}	V_{E}	R_{t}	R_{Ω}	R_{p}	$R_{\text{p,r}}$	R_{i}	R_{e}	t_{i}	t_{e}
atm	atm	V	V	$\Omega \text{ cm}^2$	$\Omega \text{ cm}^2$	$\Omega \text{ cm}^2$	$\Omega \text{ cm}^2$	$\Omega \text{ cm}^2$	$\Omega \text{ cm}^2$		
0.05	0.2	1.000	1.055	0.701	0.407	0.294	0.320	0.420	13.450	0.970	0.030
0.1	0.2	0.989	1.029	0.707	0.399	0.308	0.327	0.408	18.186	0.978	0.022
0.3	0.2	0.967	0.987	0.722	0.394	0.327	0.338	0.399	35.614	0.989	0.011
0.5	0.2	0.953	0.968	0.736	0.383	0.353	0.362	0.386	47.528	0.992	0.008
0.3	0.1	0.953	0.974	0.801	0.402	0.399	0.412	0.406	37.141	0.989	0.011
0.3	0.2	0.965	0.987	0.728	0.392	0.335	0.347	0.397	32.639	0.988	0.012
0.3	0.4	0.976	1.000	0.668	0.385	0.282	0.293	0.391	27.825	0.986	0.014
0.3	0.7	0.984	1.011	0.626	0.376	0.250	0.261	0.383	23.443	0.984	0.016

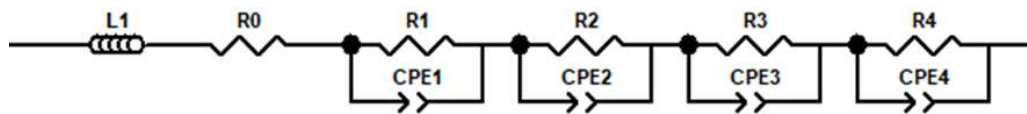


Figure S7. The equivalent circuit model proposed with the fitting on impedance spectra of $p\text{H}_2\text{O}$ and $p\text{O}_2$ variations in oxygen electrode.

Note S5.

The curved lines of the Nyquist plots (Figure 5a and 5b) in the high-frequency region indicate the influence of parasitic inductance in the test rig.³⁰ The typical values of L are 10^{-7} ~ 10^{-6} H. A practical way to eliminate such influences is to use low-inductance cables by twisting the wires between the test rig and measurement device. In our study, due to the fixed configuration of the commercial test rig, twisting the wires is only possible to a limited extent. In order to model the effect from inductance, the introduction of an inductance element to the fitting model is indispensable.

Table S10. Fitting data of the impedance spectra with variation of $p\text{H}_2\text{O}$ (a) and $p\text{O}_2$ (b) at OCV and the temperature of 600 °C.

	H ₂ O dependence / atm ($p\text{O}_2 = 0.20P_0$)				O ₂ dependence / atm ($p\text{H}_2\text{O} = 0.30P_0$)			
	0.05	0.1	0.3	0.5	0.1	0.2	0.4	0.7
R1 / $\Omega \text{ cm}^2$	0.064	0.066	0.067	0.069	0.094	0.086	0.091	0.084
C1 / F cm^{-2}	1.1×10^{-4}	8.9×10^{-5}	9.3×10^{-5}	6.9×10^{-5}	7.9×10^{-5}	7.3×10^{-5}	7.3×10^{-5}	7.2×10^{-5}
R2 / $\Omega \text{ cm}^2$	0.061	0.076	0.100	0.126	0.120	0.100	0.073	0.061
C2 / F cm^{-2}	7.1×10^{-4}	6.2×10^{-4}	5.8×10^{-4}	4.5×10^{-4}	6.3×10^{-4}	6.3×10^{-4}	9.8×10^{-4}	9.5×10^{-4}
R3 / $\Omega \text{ cm}^2$	0.058	0.057	0.058	0.060	0.070	0.059	0.046	0.035
C3 / F cm^{-2}	1.7×10^{-2}	1.6×10^{-2}	1.7×10^{-2}	1.7×10^{-2}	2.1×10^{-2}	2.0×10^{-2}	3.2×10^{-2}	3.0×10^{-2}
R4 / $\Omega \text{ cm}^2$	0.111	0.109	0.103	0.100	0.115	0.090	0.073	0.070
C4 / F cm^{-2}	2.4×10^{-1}	2.3×10^{-1}	2.4×10^{-1}	2.4×10^{-1}	2.4×10^{-1}	2.9×10^{-1}	4.1×10^{-1}	4.5×10^{-1}

Table S11. Polarization resistances of the PCC cells with BGLC587-BZCY541 oxygen electrode at OCV and various $p\text{H}_2\text{O}$ and $p\text{O}_2$ on the oxygen electrode side.

$p\text{H}_2\text{O}$	$p\text{O}_2$	$R_{p,1}$	$R_{p,2}$	$R_{p,3}$	$R_{p,4}$	$R_{p,r,1}$	$R_{p,r,2}$	$R_{p,r,3}$	$R_{p,r,4}$
atm	atm	$\Omega \text{ cm}^2$	$\Omega \text{ cm}^2$	$\Omega \text{ cm}^2$	$\Omega \text{ cm}^2$	$\Omega \text{ cm}^2$	$\Omega \text{ cm}^2$	$\Omega \text{ cm}^2$	$\Omega \text{ cm}^2$
0.05	0.2	0.064	0.061	0.058	0.111	0.068	0.066	0.063	0.123
0.1	0.2	0.066	0.076	0.057	0.109	0.069	0.080	0.061	0.117
0.3	0.2	0.067	0.100	0.058	0.103	0.069	0.103	0.060	0.107
0.5	0.2	0.069	0.126	0.060	0.099	0.070	0.129	0.061	0.102
0.3	0.1	0.094	0.120	0.070	0.115	0.096	0.123	0.073	0.120
0.3	0.2	0.086	0.100	0.059	0.090	0.089	0.103	0.061	0.094
0.3	0.4	0.091	0.073	0.046	0.073	0.094	0.076	0.048	0.076
0.3	0.7	0.084	0.061	0.035	0.070	0.087	0.064	0.036	0.073

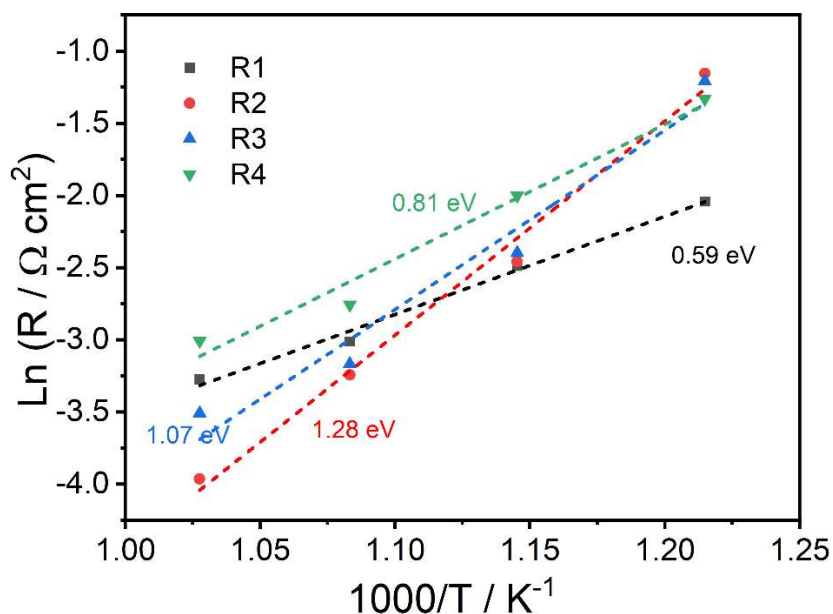


Figure S8. Arrhenius plot of different resistances (R_1 , R_2 , R_3 and R_4) derived from impedance spectra and the corresponding activation energy with (wet) 20% H_2 -80% N_2 on the fuel electrode side and 30% H_2O -70% air on the oxygen electrode side.

Table S12. Reaction models for elementary reaction steps at oxygen electrode for water splitting in proton conducting ceramic cells.

Step	Elementary reactions
Step 1	$H_2O(g) \rightarrow H_2O(ads)$
Step 2	$H_2O(ads) \rightarrow O^{2-}(ads) + 2H^+(surface, electrode)$
Step 3	$H^+(surface, electrode) \rightarrow H^+(interface, electrode)$
Step 4	$H^+(interface, electrode) \rightarrow H^+(electrolyte)$
Step 5	$O^{2-}(ads) \rightarrow O^-(ads) + e^-$
Step 6	$2O^-(ads) \rightarrow O_2^-(ads)$
Step 7	$O_2^-(ads) \rightarrow O_2(ads) + 2e^-$
Step 8	$O_2(ads) \rightarrow O_2(g)$

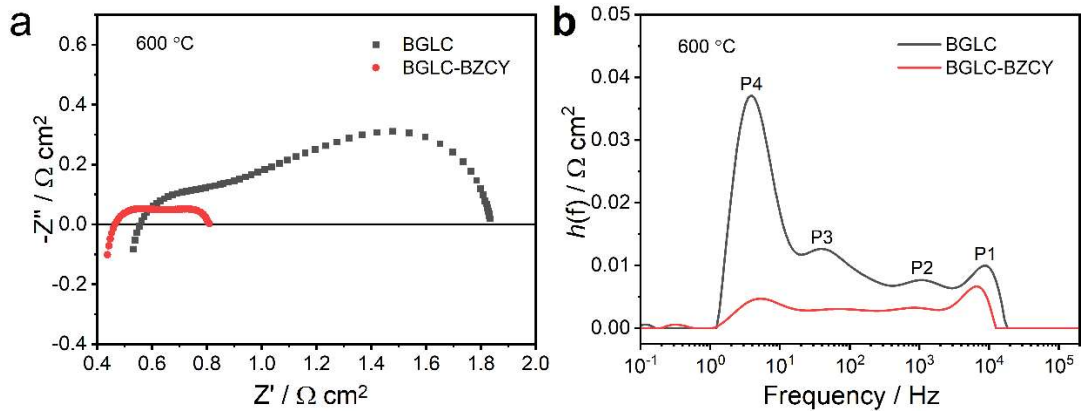


Figure S9. Nyquist impedance plot (a) and DRT deconvolution results (b) of PCCs with BGLC oxygen electrode and BGLC-BZCY composite oxygen electrode at OCV and 600 °C with (wet) 20% H₂-80% N₂ on the fuel electrode side and 30% H₂O-70% air on the oxygen electrode side.

Table S13. Fitting data of the impedance spectra of PCCs with BGLC oxygen electrode and BGLC-BZCY composite oxygen electrode at OCV and 600 °C with (wet) 20% H₂-80% N₂ on the fuel electrode side and 30% H₂O-70% Air on the oxygen electrode side.

Oxygen electrode	R1 Ω cm ²	C1 F cm ⁻²	R2 Ω cm ²	C2 F cm ⁻²	R3 Ω cm ²	C3 F cm ⁻²	R4 Ω cm ²	C4 F cm ⁻²
BGLC	0.168	7.2×10 ⁻⁵	0.248	8.3×10 ⁻⁴	0.440	9.9×10 ⁻²	0.461	1.4×10 ⁻²
BGLC-BZCY	0.080	9.7×10 ⁻⁵	0.082	8.1×10 ⁻⁴	0.087	1.0×10 ⁻²	0.128	1.5×10 ⁻¹

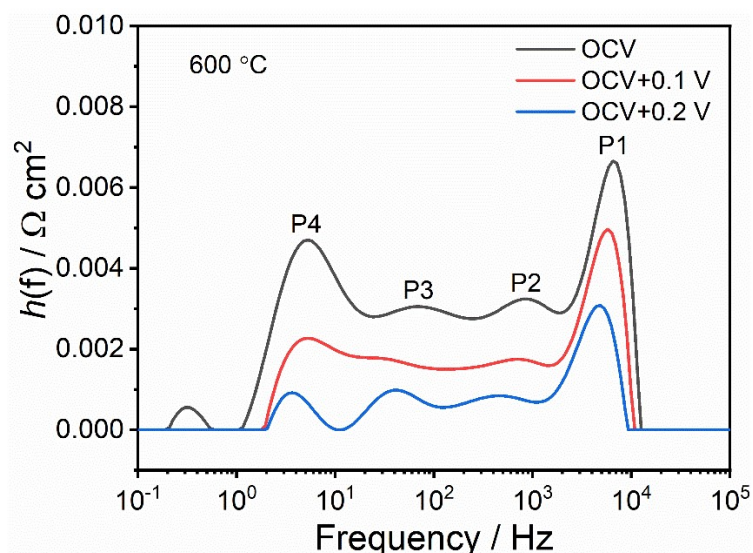


Figure S10. DRT deconvolution results of PCCs with BGLC-BZCY composite oxygen electrode at different voltages (OCV, OCV + 0.1 V and OCV + 0.2 V) and 600 °C with (wet) 20% H₂-80% N₂ on fuel electrode side and 30% H₂O-70% Air on oxygen electrode side.

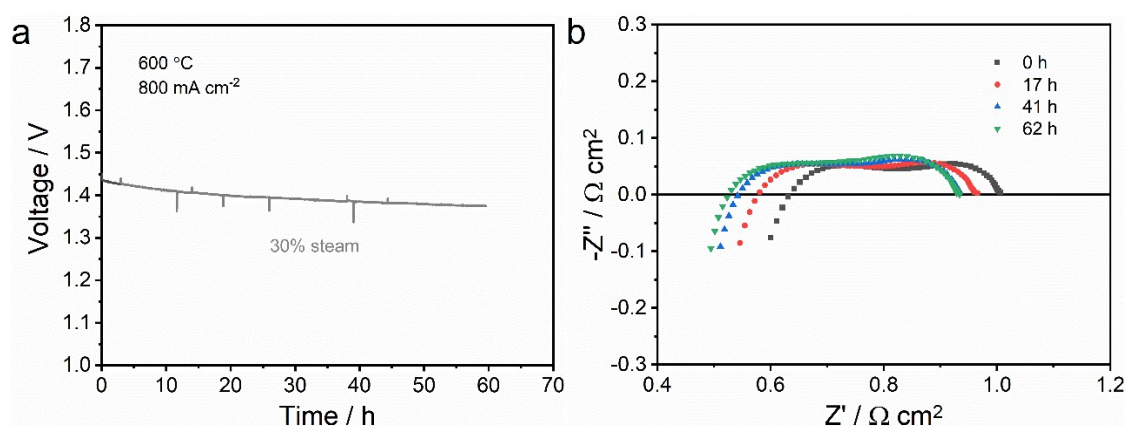


Figure S11. (a) Long-term stability of voltage evolution at 600 °C and a fixed current density of -0.8 A cm^{-2} with 20% H₂ mixed with 80% N₂ in fuel electrode and 30% H₂O mixed air in the oxygen electrode. (b) Electrochemical impedance spectroscopy of the cell before and after 62 h operation.

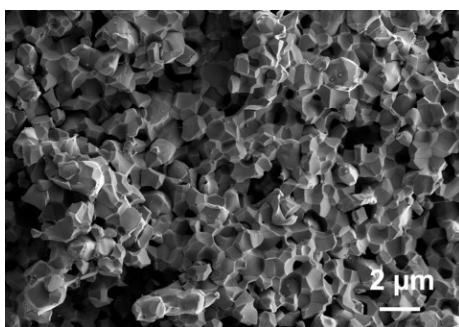


Figure S12. SEM cross-section of the fuel electrode after 366 h operation for steam electrolysis.

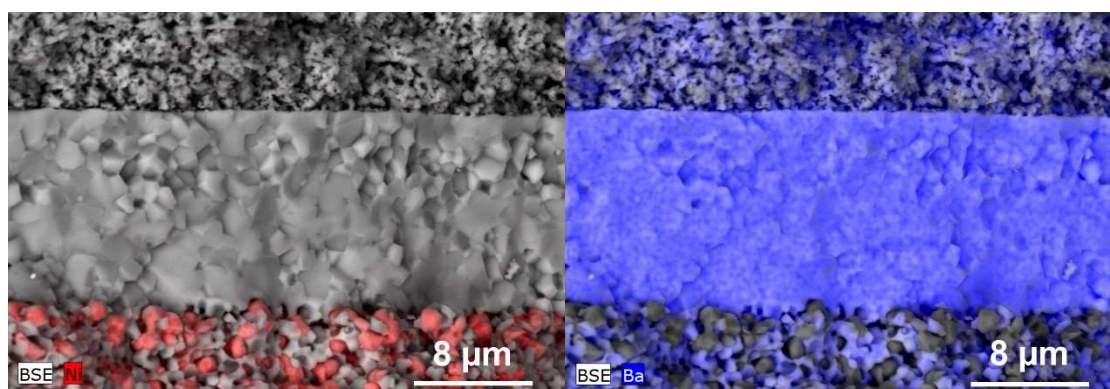


Figure S13. EDX elemental mapping of the cell after 366 h operation for steam electrolysis.

References

1. L. Fan and P.-C. Su, *J. Power Sources*, 2016, **306**, 369-377.
2. A. Zhu, G. Zhang, T. Wan, T. Shi, H. Wang, M. Wu, C. Wang, S. Huang, Y. Guo and H. Yu, *Electrochim. Acta*, 2018, **259**, 559-565.
3. F. Zhao, S. Wang, K. Brinkman and F. Chen, *J. Power Sources*, 2010, **195**, 5468-5473.
4. Y. Guo, Y. Lin, R. Ran and Z. Shao, *J. Power Sources*, 2009, **193**, 400-407.
5. N. Nasani, D. Ramasamy, S. Mikhalev, A. V. Kovalevsky and D. P. Fagg, *J. Power Sources*, 2015, **278**, 582-589.
6. L. Bi, E. Fabbri and E. Traversa, *Electrochem. commun.*, 2012, **16**, 37-40.
7. S. Jeong, T. Kobayashi, K. Kuroda, H. Kwon, C. Zhu, H. Habazaki and Y. Aoki, *RSC adv.*, 2018, **8**, 26309-26317.
8. J. Xiao, W. Sun, Z. Zhu, Z. Tao and W. Liu, *Mater. Lett.*, 2012, **73**, 198-201.
9. H. Lee, S. Lee, T. Lee, S. Park and D. Shin, *Int. J. Hydrog. Energy*, 2017, **42**, 3748-3752.
10. L. Yang, C. Zuo, S. Wang, Z. Cheng and M. Liu, *Adv. Mater.*, 2008, **20**, 3280-3283.
11. M. Liu and h. Hu, *J. Electrochem. Soc.*, 1996, **143**, L109-L112.
12. J. Kim, S. Sengodan, G. Kwon, D. Ding, J. Shin, M. Liu and G. Kim, *ChemSusChem*, 2014, **7**, 2811-2815.
13. Y. Zhou, E. Liu, Y. Chen, Y. Liu, L. Zhang, W. Zhang, Z. Luo, N. Kane, B. Zhao, L. Soule, Y. Niu, Y. Ding, H. Ding, D. Ding and M. Liu, *ACS Energy Lett.*, 2021, **6**, 1511-1520.
14. K. Xu, H. Zhang, Y. Xu, F. He, Y. Zhou, Y. Pan, J. Ma, B. Zhao, W. Yuan, Y. Chen and M. Liu, *Adv. Funct. Mater.*, 2022, **32**, 2110998.

15. H. An, H.-W. Lee, B.-K. Kim, J.-W. Son, K. J. Yoon, H. Kim, D. Shin, H.-I. Ji and J.-H. Lee, *Nat Energy*, 2018, **3**, 870-875.
16. K. Bae, D. Y. Jang, H. J. Choi, D. Kim, J. Hong, B. K. Kim, J. H. Lee, J. W. Son and J. H. Shim, *Nat. Commun.*, 2017, **8**, 14553.
17. K. Bae, D. H. Kim, H. J. Choi, J.-W. Son and J. H. Shim, *Adv. Energy Mater.*, 2018, **8**, 1801315.
18. L. Bi, S. P. Shafi and E. Traversa, *J. Mater. Chem. A*, 2015, **3**, 5815-5819.
19. F. He, D. Song, R. Peng, G. Meng and S. Yang, *J. Power Sources*, 2010, **195**, 3359-3364.
20. L. Lei, Z. Tao, X. Wang, J. P. Lemmon and F. Chen, *J. Mater. Chem. A*, 2017, **5**, 22945-22951.
21. W. Y. Li, B. Guan, L. Ma, S. S. Hu, N. Zhang and X. B. Liu, *J. Mater. Chem. A*, 2018, **6**, 18057-18066.
22. D. Huan, N. Shi, L. Zhang, W. Tan, Y. Xie, W. Wang, C. Xia, R. Peng and Y. Lu, *ACS Appl. Mater. Interfaces*, 2018, **10**, 1761-1770.
23. D. Huan, W. Wang, Y. Xie, N. Shi, Y. Wan, C. Xia, R. Peng and Y. Lu, *J. Mater. Chem. A*, 2018, **6**, 18508-18517.
24. S. Yang, Y. Wen, J. Zhang, Y. Lu, X. Ye and Z. Wen, *Electrochim. Acta*, 2018, **267**, 269-277.
25. W. Tang, H. Ding, W. Bian, W. Wu, W. Li, X. Liu, J. Y. Gomez, C. Y. Regalado Vera, M. Zhou and D. Ding, *J. Mater. Chem. A*, 2020, **8**, 14600-14608.
26. S. Choi, T. C. Davenport and S. M. Haile, *Energy Environ. Sci.*, 2019, **12**, 206-215.
27. H. Ding, W. Wu, C. Jiang, Y. Ding, W. Bian, B. Hu, P. Singh, C. J. Orme, L. Wang, Y. Zhang and D. Ding, *Nat. Commun.*, 2020, **11**, 1907.
28. L. Q. Le, C. Meisel, C. H. Hernandez, J. Huang, Y. Kim, R. O'Hayre and N. P. Sullivan, *J. Power Sources*, 2022, **537**, 231356.
29. C. C. Duan, R. Kee, H. Y. Zhu, N. Sullivan, L. Z. Zhu, L. Z. Bian, D. Jennings and R. O'Hayre, *Nat Energy*, 2019, **4**, 230-240.
30. P. Caliandro, A. Nakajo, S. Diethelm and J. Van herle, *J. Power Sources*, 2019, **436**, 226838.

Appendix B: Supplementary information for Article II

Supporting information

Hydrogen production at intermediate temperatures with proton conducting ceramic cells: Electrocatalytic activity, durability and energy efficiency

Haoyu Zheng^{a,b,*}, Feng Han^a, Noriko Sata^a, and Rémi Costa^{a,*}

^a Institute of Engineering Thermodynamics, German Aerospace Center (DLR), Stuttgart 70569, Germany

^b Institute for Building Energetics, Thermotechnology and Energy Storage (IGTE), University of Stuttgart, Stuttgart 70569, Germany

* Corresponding author.

E-mail address: zhenghaoyu01@gmail.com (H.Y. Zheng), remi.costa@dlr.de (R. Costa)

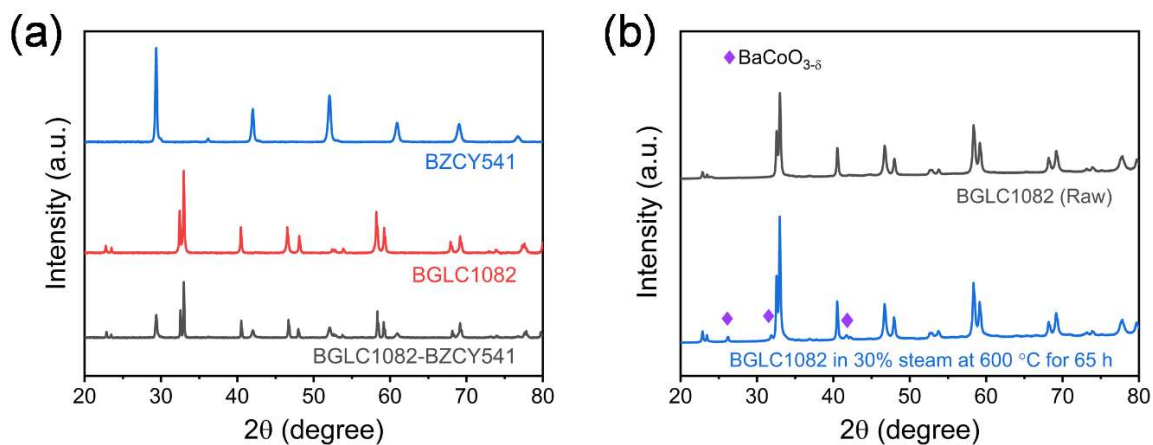


Figure S1. (a) XRD patterns of BZCY541, BGLC1082 and the mixture of BGLC1082-BZCY541 after annealing in air at 1000 °C for 2h. (b) XRD patterns of the BGLC1082 raw power and after exposure in 30% steam/air at 600 °C for 65 h.

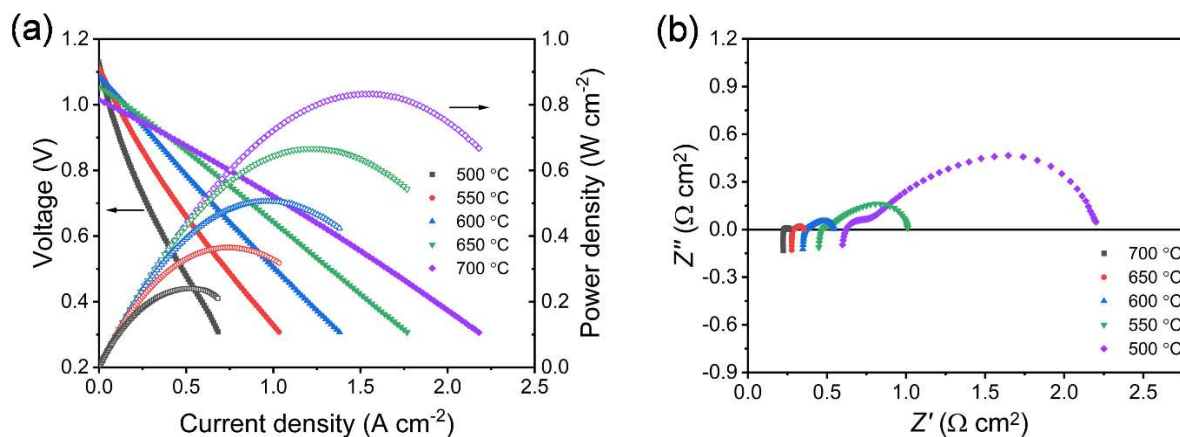


Figure S2. Electrochemical performance of PCCs with BGLC-BZCY positrode in fuel cell mode with wet (~3% H₂O) air supplied to positrode and wet (~3% H₂O) H₂ supplied to negatrode. (a) Polarization curves and the corresponding power density at different temperatures. (b) Electrochemical impedance spectra recorded at OCV.

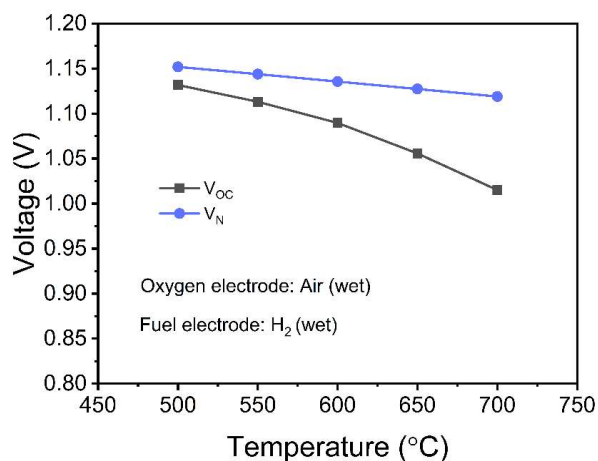


Figure S3. The comparison of measured open circuit voltages and theoretical values of PCCs in fuel cell operation.

Note S1.

As shown in Figure S1, PCCs with BGLC1082-BZCY541 were tested in fuel cell mode at different temperatures. The peak power densities (PPDs) reach 240, 365, 506, 667 and 833 mW cm⁻² at 500, 550, 600, 650 and 700 °C. Electrochemical impedance spectra were recorded at OCV, ohmic resistances are 0.62, 0.47, 0.37, 0.29 and 0.23 Ω cm² at 500, 550, 600,

Appendix B: Supplementary information for Article II

650 and 700 °C. Similarly, the polarization resistances are 1.59, 0.54, 0.18, 0.07 and 0.04 $\Omega \text{ cm}^2$ at the corresponding temperatures. At temperature higher than 550 °C, the cell losses were dominated by the ohmic losses, due to the lower conductance of the electrolyte. The cell performance can be boosted by reducing the electrolyte thickness or by replacing the electrolyte of different composition, such as Ce rich BZCY or of higher Y dopant concentration. Additionally, Figure S2 shows the difference between the measured open circuit voltages and the theoretical values, resulting from the electronic leakage in electrolyte layer.

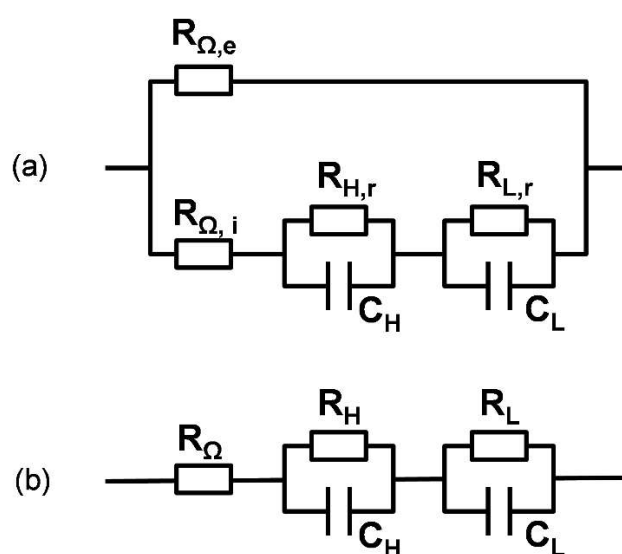


Figure S4. (a) Equivalent circuit model contains parallel electronic resistance representing electronic conduction through electrolyte in PCCs; (b) Equivalent circuit model for SOCs.

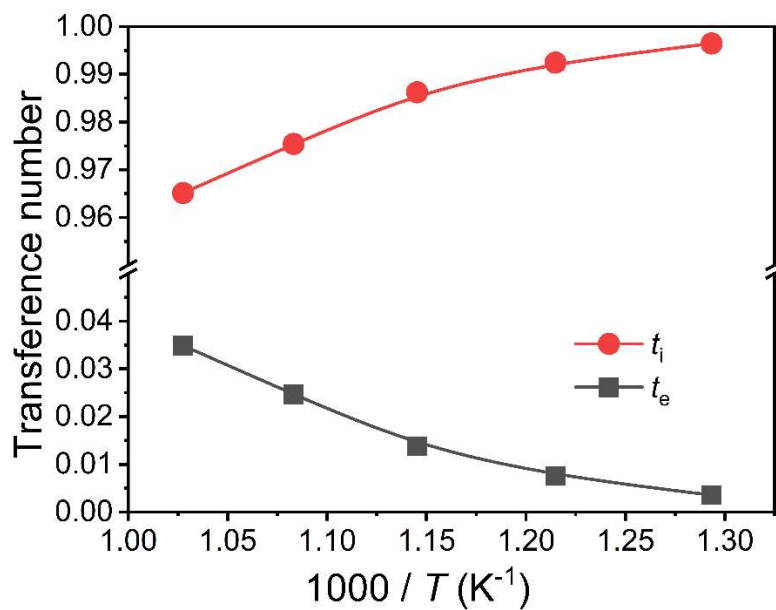


Figure S5. Ionic transference number (t_i) and electronic transference number (t_e) of the PCC as a function of temperature at OCV.

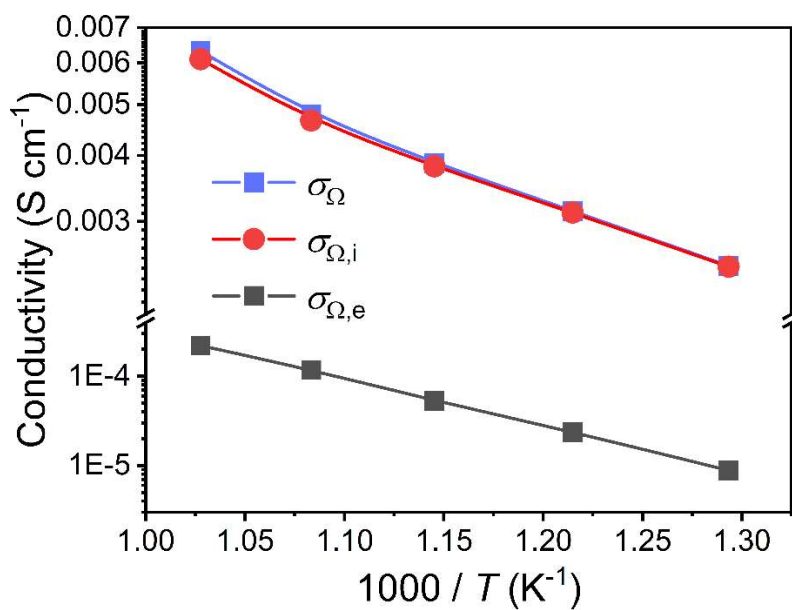


Figure S6. Different conductivities (σ_{Ω} , σ_i and σ_e) for the electrolyte in PCCs.

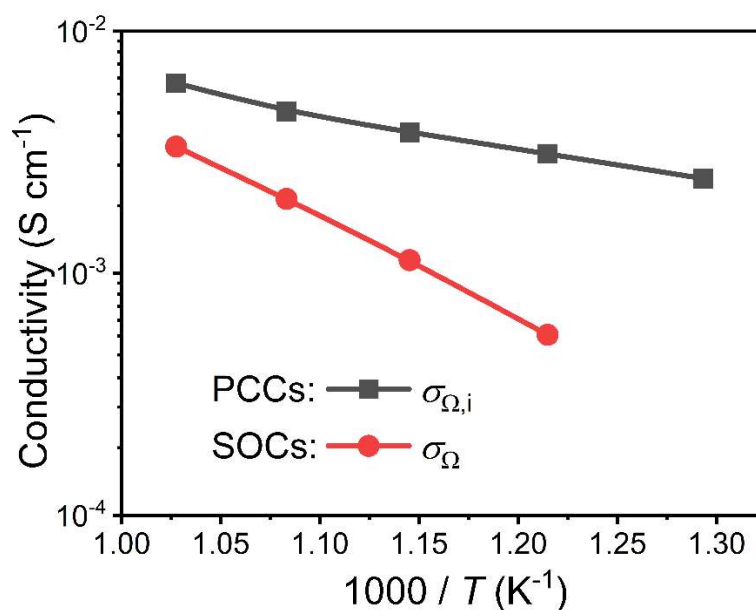


Figure S7. The comparison of ionic conductivity in electrolyte between SOCs and PCCs.

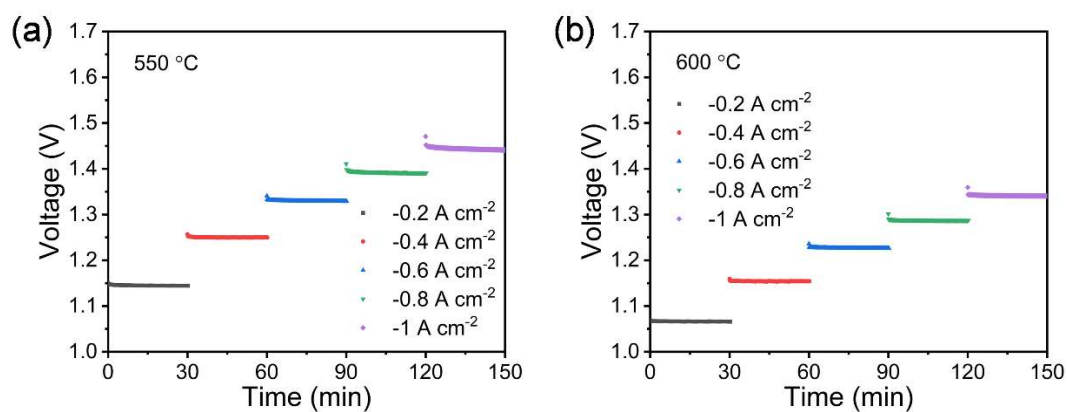


Figure S8. Short-term stability test of the PCC in steam electrolysis operation at 550 °C (a) and 600 °C (b). The cell was operated in galvanostatic mode at different current densities with 30% steam/air supplied to positrode.

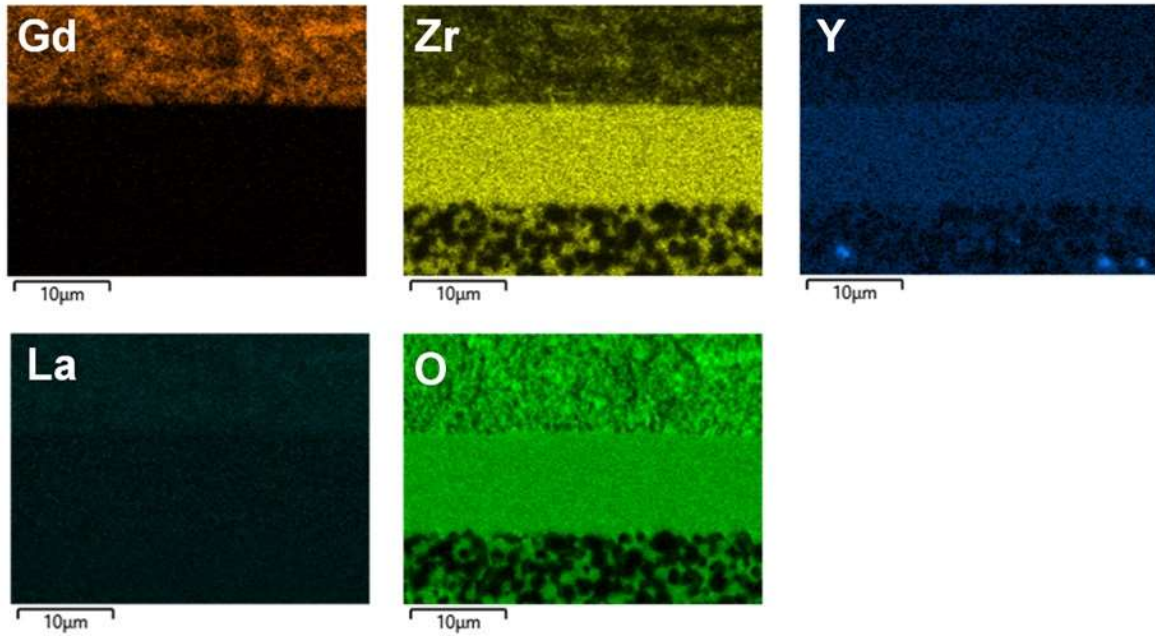


Figure S9. EDX elemental Mapping of the PCC after 1680 h operation in steam electrolysis operation.

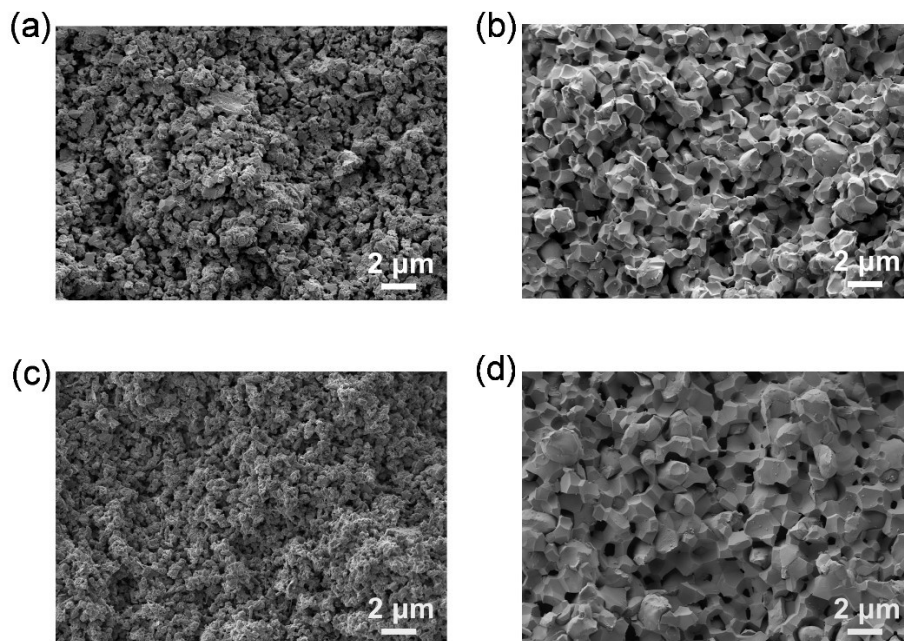


Figure S10. SEM images of the positrode (a), (c) and the negatrode (b), (d) before and after testing of the PCC, respectively.

Appendix B: Supplementary information for Article II

Table S1. Summary of Faradaic efficiency at around thermal neutral voltage (~1.28 V) for steam electrolysis in PCCs.

Cell configuration Positrode Electrolyte Negatrode	Gas composition		Current density (A cm ⁻²)	η_{FE} at voltages/current densities	Ref.
	Positrode	Negatrode			
BGLC1082-BZCY541 BZCY541 NiO-BZCY541	30%H ₂ O/Air	20%H ₂ /N ₂ (~3%H ₂ O)	-0.4 at 1.28V (550 °C) -0.6 at 1.25 V (600 °C) -1.0 at 1.27 V (650 °C) -1.4 at 1.27 V (700 °C)	63% at 1.28V (550 °C) 62% at 1.25 V (600 °C) 61% at 1.27 V (650 °C) 53% at 1.27 V (700 °C)	This work
PNO LCO/BZCYYb1711 Ni-BZCYYb1711	60%H ₂ O/Air	Dry H ₂	-0.98 at 1.3 V (700 °C)	29% at -1.0 A cm ⁻² (700 °C)	[1]
PBCFN BZCYYb1711 Ni-BZCYYb1711	Air (~3%H ₂ O)	H ₂ (~3%H ₂ O)	-2.148 at 1.3 V (650 °C)	~43% at -1.0 A cm ⁻² (650 °C)	[2]
BC1.5MN BZCYYb1711 Ni-BZCYYb1711	30%H ₂ O/Air	H ₂ (~3%H ₂ O)	-1.3 at 1.3 V (600 °C) estimated from I-V curves	~60% at -1.0 A cm ⁻² (600 °C)	[3]
PBSCF BZCYYb4411 Ni-BZCYYb4411	3%H ₂ O/Air	5%H ₂ /Ar	-1.3 at 1.3 V (600 °C)	~48% at -1.3 A cm ⁻² (600 °C)	[4]
PBCC BZCYYb1711 Ni-BZCYYb1711	30%H ₂ O/Air	3%H ₂ O/H ₂	-1.351 at 1.3 V (600 °C)	~83% at 1.3 V (600 °C)	[5]
PNC BZCYYb4411 Ni-BZCYYb4411	15%H ₂ O/Air	5%H ₂ /Ar	-0.81 at 1.3 V (600 °C)	~80% at 1.3 V (600 °C)	[6]
BCFZY-BZCYYb1711 BZCYYb1711 Ni-BZCYYb1711	20%H ₂ O/O ₂ -N ₂	Ar	-1.10 at 1.3 V (600 °C)	~99% at -1.1 A cm ⁻² (600 °C)	[7]
BCFZY-BZCYYb1711 BZCYYb1711 Ni-BZCYYb1711	10%H ₂ O/O ₂ -N ₂	Ar	-1.10 at 1.3 V (600 °C)	~85% at -1.1 A cm ⁻² (600 °C)	[7]
BCFZY-BZY20 BZY20 Ni-BZY20	20%H ₂ O/O ₂ -N ₂	Ar	-0.90 at 1.3 V (600 °C)	~50% at -0.9 A cm ⁻² (600 °C)	[7]

Note: PNO = Pr₂NiO_{4+ δ} , BZCYYb1711 = BaZr_{0.1}Ce_{0.7}Y_{0.1}Yb_{0.1}O_{3- δ} , PBCFN = PrBaCo_{1.6}Fe_{0.2}Nb_{0.2}O_{5+ δ} ,

BC1.5MN = Ba₂Co_{1.5}Mo_{0.25}Nb_{0.25}O_{6- δ} , PBSCF = PrBa_{0.5}Sr_{0.5}Co_{1.5}Fe_{0.5}O_{5+ δ} , BZCYYb4411 = BaZr_{0.4}Ce_{0.4}Y_{0.1}Yb_{0.1}O_{3- δ} ,

PBCC = PrBa_{0.8}Ca_{0.2}Co₂O_{5+ δ} , PNC = PrNi_{0.5}Co_{0.5}O_{3- δ} , BCFZY = BaCo_{0.4}Fe_{0.4}Zr_{0.1}Y_{0.1}O_{3- δ} , BZY20 = BaZr_{0.8}CeY_{0.2}O_{3- δ}

Table S2. Electrochemical characteristics of representative PCCs at OCV in steam electrolysis mode.

T	R _t	R _Ω	R _H	R _L	R _{Ω,i}	R _{Ω,e}	R _{H,r}	R _{L,r}
°C	Ω cm ²	Ω cm ²	Ω cm ²	Ω cm ²	Ω cm ²	Ω cm ²	Ω cm ²	Ω cm ²
500	2.421	0.486	0.63	1.305	0.488	136.652	0.637	1.339
550	1.111	0.382	0.328	0.401	0.385	50.450	0.335	0.416
600	0.641	0.31	0.178	0.153	0.314	22.481	0.184	0.161
650	0.444	0.251	0.112	0.081	0.257	10.201	0.119	0.088
700	0.356	0.19	0.104	0.062	0.197	5.443	0.114	0.070

References:

- [1] W. Li, B. Guan, L. Ma, H. Tian, X. Liu, ACS Appl. Mater. Interfaces 11 (2019) 18323-18330.
- [2] K. Xu, H. Zhang, Y. Xu, F. He, Y. Zhou, Y. Pan, J. Ma, B. Zhao, W. Yuan, Y. Chen, M. Liu, Adv. Funct. Mater. 32 (2022) 2110998.
- [3] F. He, S. Liu, T. Wu, M. Yang, W. Li, G. Yang, F. Zhu, H. Zhang, K. Pei, Y. Chen, W. Zhou, Z. Shao, Adv. Funct. Mater. 32 (2022) 2206756.
- [4] S. Choi, T.C. Davenport, S.M. Haile, Energy Environ. Sci. 12 (2019) 206-215.
- [5] Y. Zhou, E. Liu, Y. Chen, Y. Liu, L. Zhang, W. Zhang, Z. Luo, N. Kane, B. Zhao, L. Soule, Y. Niu, Y. Ding, H. Ding, D. Ding, M. Liu, ACS Energy Lett. 6 (2021) 1511-1520.
- [6] H. Ding, W. Wu, C. Jiang, Y. Ding, W. Bian, B. Hu, P. Singh, C.J. Orme, L. Wang, Y. Zhang, D. Ding, Nat. Commun. 11 (2020) 1907.
- [7] C.C. Duan, R. Kee, H.Y. Zhu, N. Sullivan, L.Z. Zhu, L.Z. Bian, D. Jennings, R. O'Hayre, Nat Energy 4 (2019) 230-240.

Appendix C: Supplementary information for Article III

Supplementary Information

Hydrogen production with a protonic ceramic membrane reactor on porous Fe-Cr alloy

Haoyu Zheng^{1,2}, Noriko Sata¹, Feng Han¹, Amir Masoud Dayaghi³, Fumitada Iguchi⁴, Katherine Develos-Bagarinao⁵, Truls Norby³, Marit Stange⁶, Rémi Costa^{1}*

¹ Institute of Engineering Thermodynamics, Electrochemical Energy Technology, German Aerospace Center (DLR), Pfaffenwaldring 38-40, D-70569 Stuttgart, Germany

² Institute of Building Energetics, Thermotechnology and Energy Storage (IGTE), University of Stuttgart. Pfaffenwaldring 31, D-70569 Stuttgart, Germany

³ Department of Chemistry, Centre for Materials Science and Nanotechnology (SMN), University of Oslo, NO-0315 Oslo, Norway

⁴ Department of Mechanical Engineering, College of Engineering, Nihon University, Koriyama, Fukushima 963-8642, Japan

⁵ Global Zero Emission Research Center, National Institute of Advanced Industrial Science and Technology, Tsukuba, Ibaraki 305-8569, Japan

⁶ SINTEF, Forskningsveien 1, NO-0373 Oslo, Norway

* Corresponding author.

Email: remi.costa@dlr.de

Experimental section

Preparations of the metal supported proton conducting ceramic cells

A 26% - Cr steel alloy (ITM, Plansee GmbH, Austria) with a porosity of about ~38 vol.% was used as the metal substrate.¹ Its robustness provides mechanical stability for the PCCs. The ITM pore size ranges from 10 μm to 30 μm (Figure S2), which is favorable for fuel gas diffusion. On top of the ITM substrate, different functional layers (FLs) with graded pore structure were assembled, aiming to reduce the pore size and the roughness on the surface to enable the fabrication of a thin, homogeneous, and gas-tight electrolyte layer by PLD. The fabricated cell structure and the procedure is schematically illustrated in Figure S1.

The porous $(\text{La}_{0.8}\text{Sr}_{0.2})_{0.95}\text{MnO}_{3-\delta}$ (LSM) diffusion barrier layer and different fuel electrode FLs of NiO-BaZr_{0.7}Ce_{0.2}Y_{0.1}O_{3- δ} (NiO-BZCY721) and NiO-BaZr_{0.5}Ce_{0.4}Y_{0.1}O_{3- δ} (NiO-BZCY541) were produced by tape-casting and co-lamination method on top of the ITM substrate. LSM (Fuelcellmaterials, US) raw powder was mixed in a solvent (mixture of methyl-ethyl-ketone (MEK) and ethanol) by roll-milling for 6 h until a homogeneous suspension was formed. Polyvinyl butyral (PVB, Sigma-Aldrich, Germany) as a binder and polyethylene glycol (PEG, Sigma-Aldrich, Germany) as a dispersant were then added to the suspension and mixed for another 6 h to obtain the corresponding slurry.

Regarding fuel electrode preparation, NiO, BZCY721 and BZCY541 powders purchased from Marion Technologies (France) and were used as received. The NiO-BZCY721 and NiO-BZCY541 fuel electrode slurries were produced in the same way as the LSM slurry preparation, with a weight ratio of NiO to BZCY (for both BZCY721 and BZCY541) of 56 wt%:44 wt%. The obtained slurry was casted with a doctor blade into a green tape with a thickness of 10-20 μm . The green tapes of LSM, NiO-BZCY721 and NiO-BZCY541 were laminated onto the ITM substrate at a uniaxial pressure of 200 bar and then fired at 950 °C with a heating rate of 3 °C min⁻¹ and a dwell time of 30 minutes.

The next step is the manufacture of the thin-film electrolyte on the fuel electrode surface by PLD. The experimental setup of PLD has been described in detail in previous work.² Thin films of BZCY721 electrolyte were prepared using a PLD workstation (SURFACE systems + technology GmbH & Co. KG, Germany, with a COMPex Pro 205, Coherent, KrF excimer laser, wavelength of 248 nm and pulse length of 25 ns). The metal substrate with multi-FLs were

Appendix C: Supplementary information for Article III

mounted in the device chamber. BZCY721 sintered pellets, were used as the PLD target. The pellets were produced by dry pressing BZCY721 powder in a 20 mm diameter die at 1 ton, followed by sintering at 1500 °C for 10 hours. During sintering, the green pellets were covered with the BZCY721 powder to prevent element evaporation.

The distance between target and substrate was adjusted to 6 cm. Prior to deposition, the chamber was evacuated to the base pressure (10^{-6} mbar) and the substrate was heated to 700 °C with a heating rate of 2 °C min⁻¹. The laser power density was set to 1.2 J cm⁻², with a repetition rate of 5 Hz. O₂ partial pressure was 0.006 mbar. After deposition, the cooling step to room temperature was set at 2 °C min⁻¹ in 0.006 mbar O₂.

Platinum (Pt) and Ba_{0.5}Gd_{0.8}La_{0.7}Co₂O_{6-δ}-BaZr_{0.5}Ce_{0.4}Y_{0.1}O_{3-δ} (BGLC-BZCY541, with a weight ratio of 60 wt%:40 wt%) were tested as oxygen electrodes on the MS-PCCs. Pt slurry from Heraeus Electronics (Germany) was used as received. The BGLC-BZCY541 slurry was prepared by mixing BGLC (Marion Technologies, France) and BZCY541 raw powder with the weight ratio of 6:4 in a binder (6 wt% ethyl cellulose in terpineol). Pt or BGLC-BZCY541 slurries were screen-printed onto the BZCY721 electrolyte with an active area of 0.5 cm². After drying at 60 °C in a drying oven, the samples were heated to 700 °C at a ramp rate of 3 °C min⁻¹ and annealed at 700 °C for 2 h. Before testing, an additional Pt layer was brushed onto the surface of BGLC-BZCY541 oxygen electrode as the current collecting layer.

Characterisation techniques

Zeiss ULTRA PLUS scanning electron microscope (SEM, Carl Zeiss AG, Germany) with an X-Flash Detector 5010 (Bruker, Germany) was used for the microstructure investigation of the samples. Surface roughness of each layer in the as-prepared MS-PCCs was investigated using a 3D laser scanning microscope (KEYENCE, VK-X3000 series).

Material phases were analyzed by X-ray diffraction (X ray source: Cu K α). The diffractograms were recorded by D8 ADVANCE (Bruker AXS GmbH, Germany). For the investigation of the 1 μ m-thick electrolyte layer, a grazing incidence X-ray diffraction was recorded.

Dilatometry measurements were conducted using the DIL 402 C dilatometer (Netzsch, Germany) on the NiO-BZCY541 porous membrane prepared by tape-casting (calcined at 1200 °C). The thickness of the membrane was about 270 μ m and the sample was supported on

an Al₂O₃ ceramic sample holder during the measurement. The thermal expansion coefficient (TEC) value was determined in the temperature range of 20 – 1100 °C at a heating rate of 3 °C/min in synthetic air flow. Isothermal dilatometry was performed in a flow of Ar with 5% H₂ to investigate the dimensional change at 450 °C.

Residual stress of the electrolyte layer in the half cell was assessed by XRD parallel-inclination method. It was confirmed that the diffraction intensity of BZCY541 in FL was sufficiently weak at the angles of this assessment and did not influence the diffraction of BZCY coating. Diffraction of (330) lattice planes of the cubic perovskite structure were used for the assessment. In-plane and out-of-plane lattice spacings of the BZCY coating were determined by conventional linear fitting of the $2\theta - \sin^2 \psi$ plot at =90° and 0°, respectively. Residual stress was calculated from $a_{in-plane}$ and a_0 by the following equation.

$$\sigma_{in} = \frac{E_f}{1 - \nu_f} \frac{a_{in-plane} - a_0}{a_0}, \quad (1)$$

where σ_{in} , E_f , ν_f , $a_{in-plane}$, a_0 are residual stress of the coating, Young's modulus and Poisson's ratio of the coating material, in-plane and stress-free lattice parameters, respectively. The elastic properties were determined by an ultrasonic transmission method using ceramic specimens³.

In this study, thermal stress was calculated based on the simple one-dimensional model with multi-layered structure and considered to be residual stress. The model consisted of the component material properties including the volume ratio in cermet, geometrical features, such as thickness and porosity, and elastic and mechano-thermal properties. The in-plane stress condition was considered. Calculations were performed by setting the maximum manufacturing temperature as the stress-free state.

The elemental distribution across the cross-sections was evaluated using a high-resolution secondary ion mass spectrometry (SIMS) equipment (NanoSIMS 50L, Ametek CAMECA) using a Cs⁺ primary ion source operated at a high voltage of 8 kV and beam current of ~30 nA. Specimens were prepared by infiltrating the samples with a high-vacuum-compatible resin and subsequently embedded in a metal holder with a Bi-Sn metal alloy. The surfaces were mechanically polished using diamond slurry and then coated with a thin layer (~5 nm) of evaporated osmium to improve conductivity. The obtained images were processed using

WinImage ver. 4.6 software (Ametek, CAMECA).

Electrochemical measurement

An initial electrochemical testing was performed on the produced cell with Pt oxygen electrode and BGLC-BZCY541 composite oxygen electrodes. All the samples were tested in a test system which contains the ProboStat™ base unit (NORECS, Norway), humidifier (HumiStat, NORECS, Norway) and mass flow controllers (red-y smart series, Vögtlin Instruments GmbH, Switzerland). Pt meshes were used on both side of the full cells for current collection. Each Pt mesh was collected with 2 Pt wires using a 2-point 4-wire setup. A ceramic paste (Ceramabond 552, AREMCO) was used for sealing. After the application of the sealant, it was dried at 90 °C and 260 °C for 2 h at each temperature. A glass paste (GM31107, Schott) was applied on the whole surface of the connection area to ensure sufficient gas-tightness of the sealing. After mounting on the test bench, the cell was heated at 3 °C min⁻¹ up to 700 °C in wet (~3% steam) 20 % H₂ + 80 % N₂ at a flow rate of 50 sccm on fuel electrode side and in 10 % O₂ + 90 % N₂ at a flow rate of 50 sccm on oxygen electrode side. During the measurement, two thermocouples were placed close the cells to monitor the cell temperature. Both MS-PCCs as shown in Figure 3 were tested for ca. 9 days in the test rig between 500 °C and 700 °C, including the reduction of fuel electrode, OCV measurement, impedance and polarization test and the time at 600 °C in idling mode. Polarization curves and electrochemical impedance spectra (EIS) measurements were performed with an electrochemical workstation ZENNIUM XC (Zahner-Elektrik GmbH & Co. KG, Kronach, Germany). Equivalent circuit model fitting was carried out using ZView® (Scribner Associates).

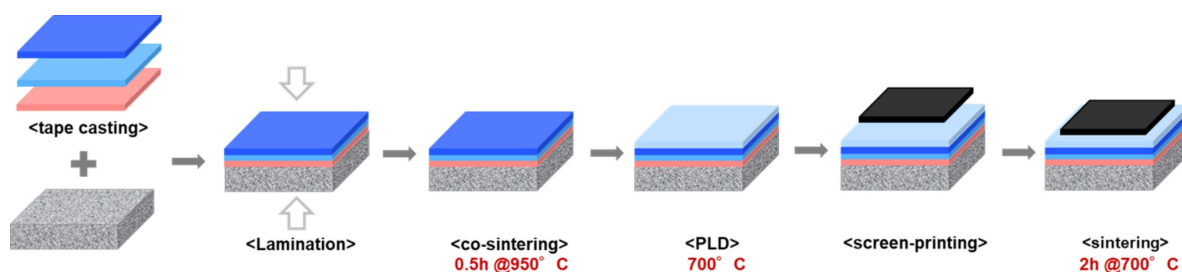


Figure S1. Preparation flow chart of the metal-supported proton conducting ceramic cells.

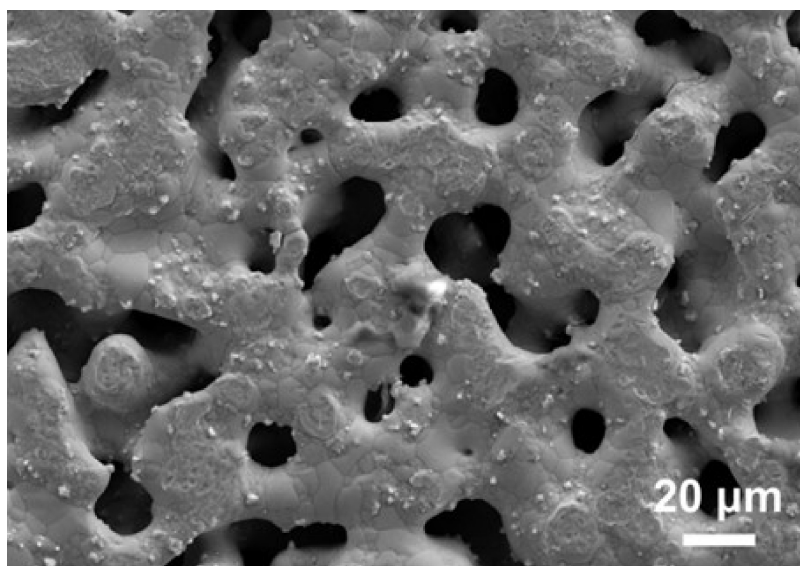


Figure S2. The SEM image of the ITM metal substrate with a porosity about ~ 38 vol%.

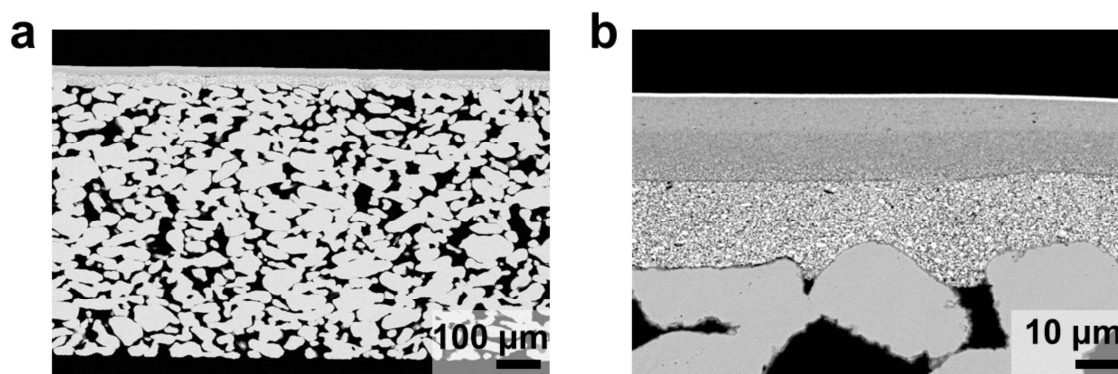


Figure S3. SEM cross-section image of a MS-PCC half-cell with thin-film BZCY721 electrolyte at different magnifications.

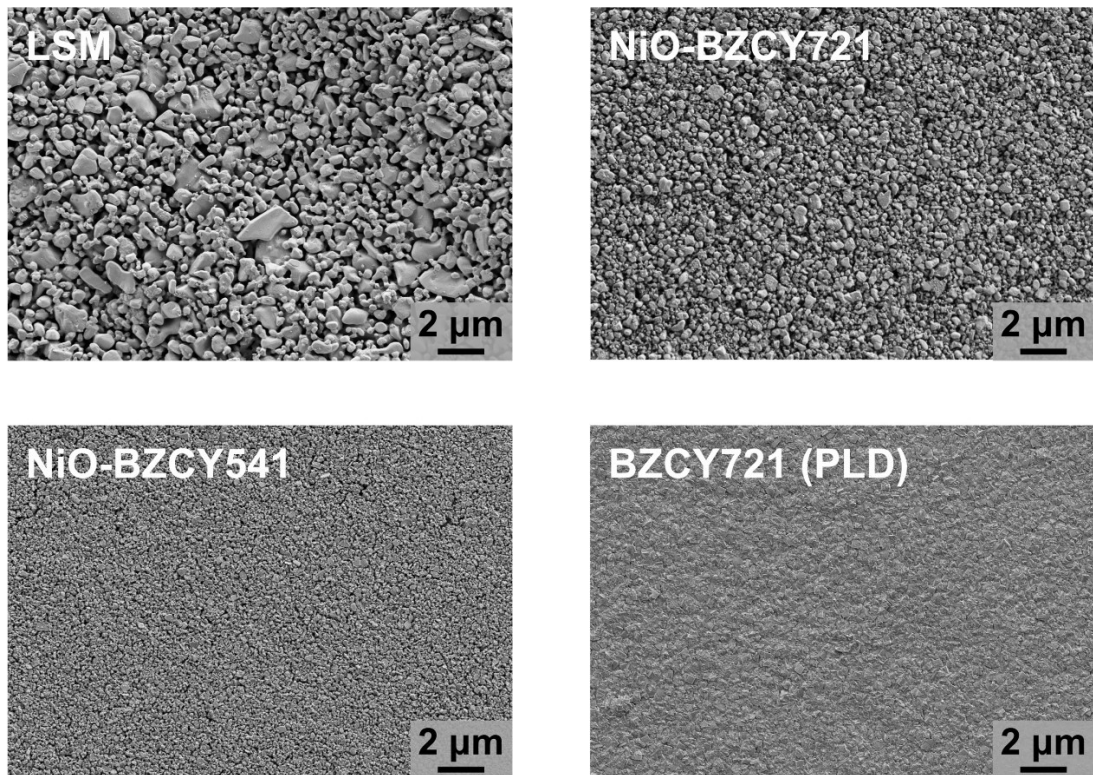


Figure S4. The SEM images of different functional layers at a magnification of 5000x.

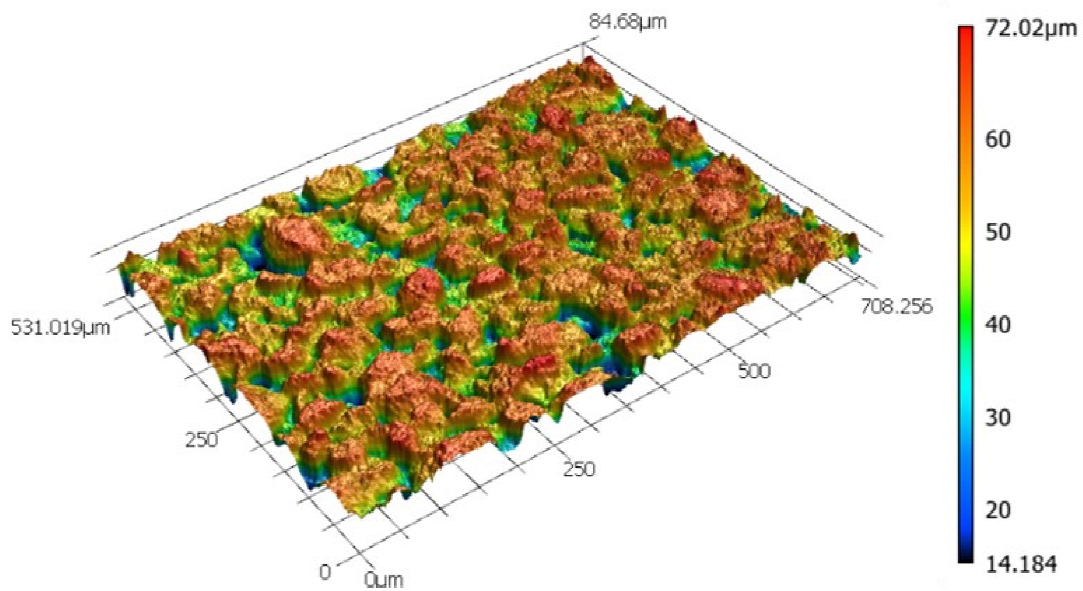


Figure S5. Laser scanning confocal microscopy image of ITM substrate.

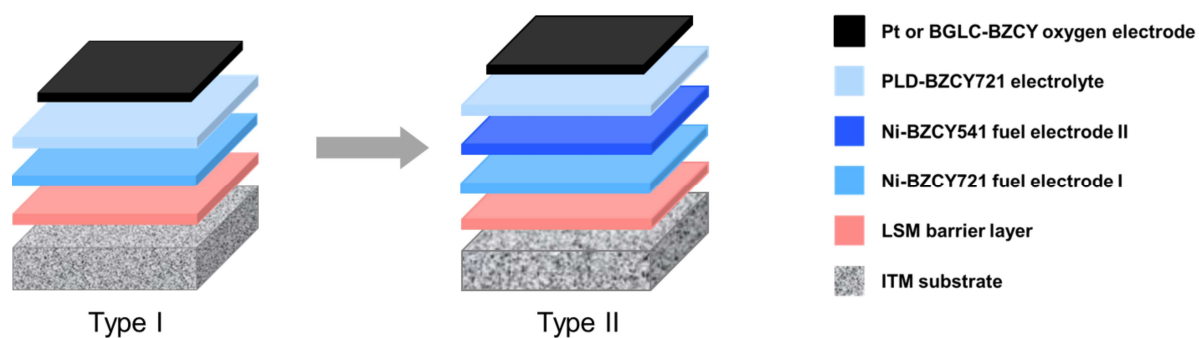


Figure S6. Optimization of processing of the metal-supported protonic ceramic cells.



Figure S7. The MS-PCC (type II) sample photo after PLD process.

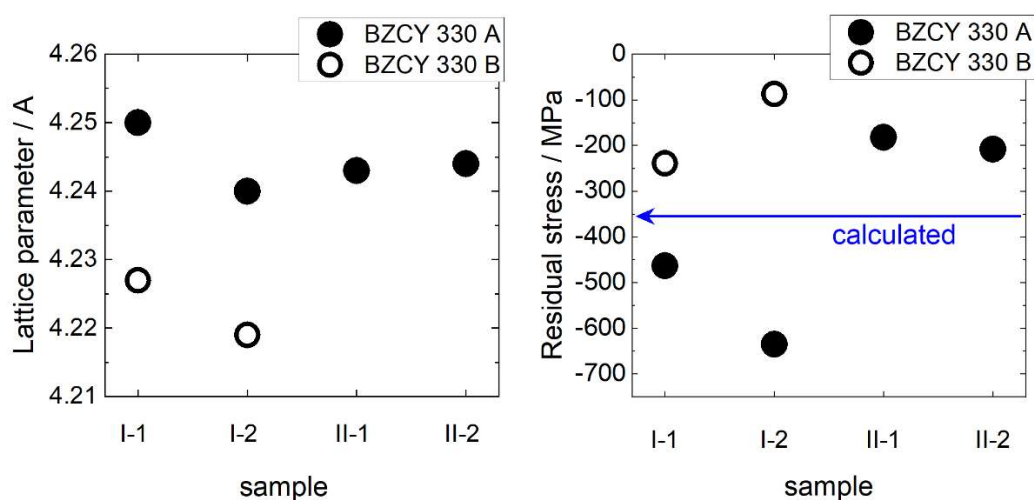


Figure S8. Lattice parameter and residual stress of the PLD coatings in the developed MS-PCC determined by XRD stress assessment.

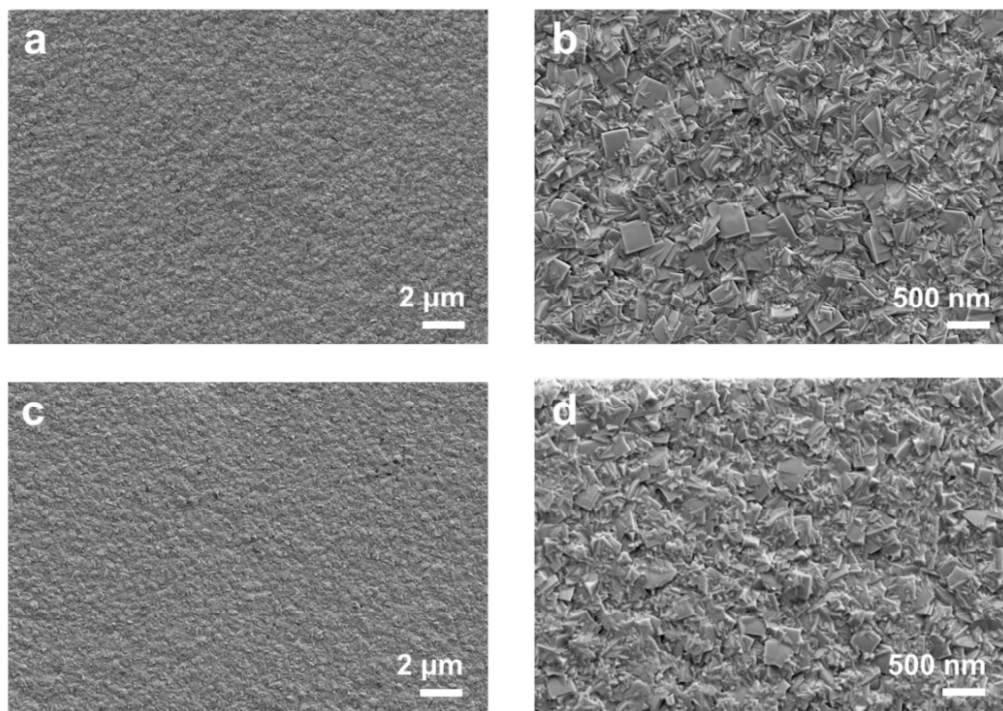


Figure S9. Thermo-mechanical stability of the BZCY721 electrolyte in type II cells. (a) and (b) images of the electrolyte after manufacturing; (c) and (d) after the thermal treatment at 700 °C for 30 h in air.

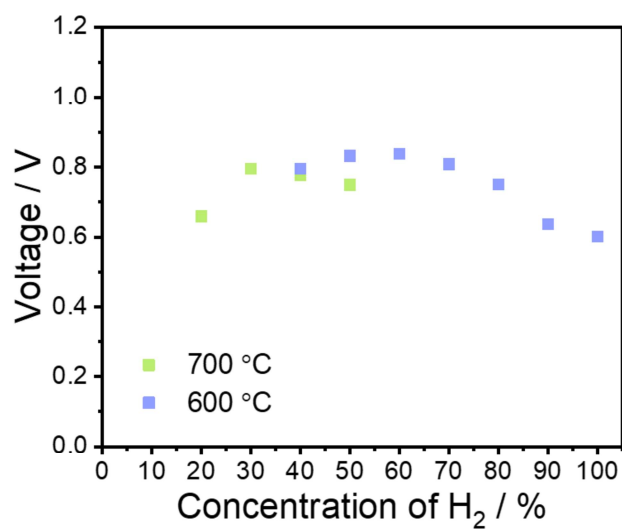


Figure S10. OCV variation of the MS-PCC (Type II) as a function of the H₂ concentration (balanced with N₂) in the feed gas of the negatrode at 600 °C and 700 °C. The positrode was supplied with a mixture of 20% O₂-80% N₂.

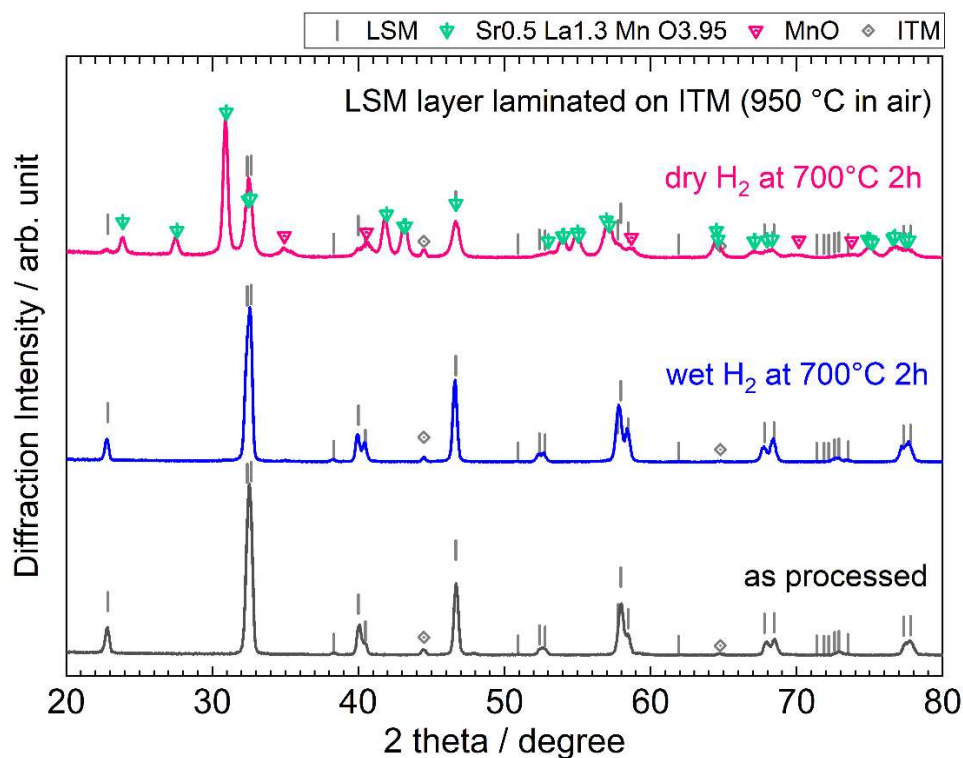


Figure S11. XRD patterns of the LSM layer fabricated on ITM and reduced in dry and wet hydrogen at 700 °C for 2 h.

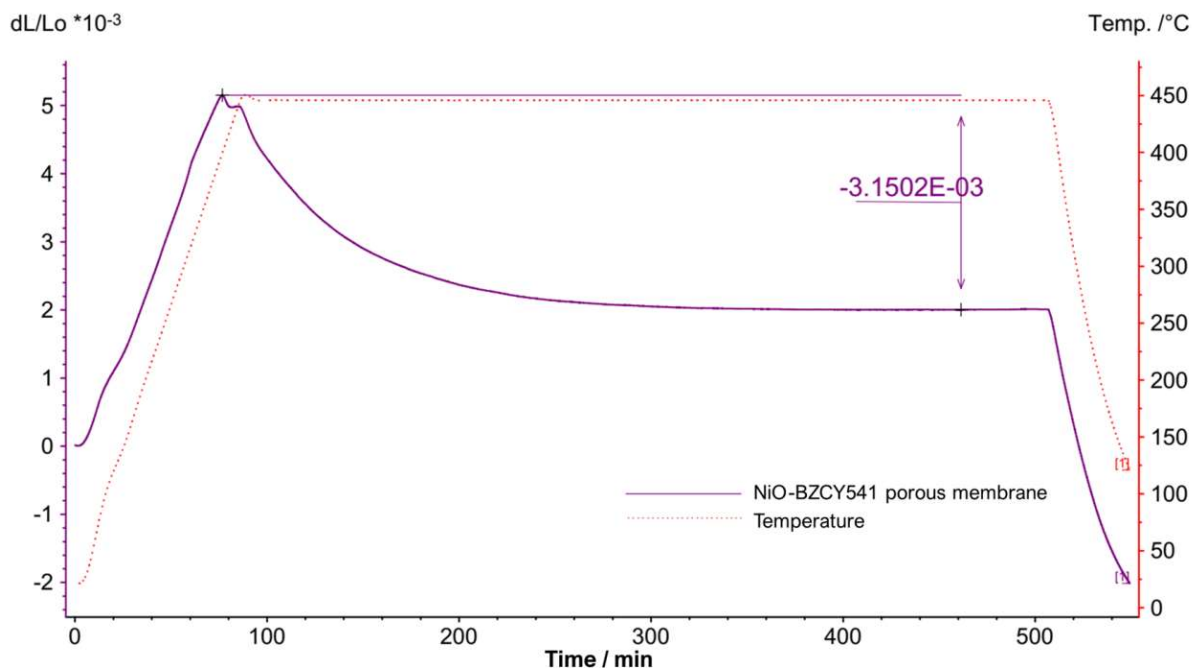


Figure S12. Isothermal dilatometry analysis of the dimensional change of a sintered porous Ni-BZCY membrane at 450 °C in Ar with 5% H₂ atmosphere.

Note S1. Microstructural optimization of fuel electrode functional layer in MS-PCCs.

It is challenging to manufacture ceramic based multi-functional layers on a non-shrinking metal substrate while maintaining its porous structure, an adequate electrocatalytic activity in the electrode, and ensuring a sufficient gas tightness in the electrolyte. Different processing techniques such as, tape-casting, lamination, co-sintering, pulsed laser deposition and screen-printing were investigated to develop the MS-PCC samples, by considering the characteristics of the different cell components. In this concept, the key to a successful MS-PCC production is to achieve an appropriate pore size, porosity, and a smooth surface of the top functional layer, to enable the growth of 1~2 μm thick gas tight electrolyte layers of good crystallinity by the PLD technique.² In the cell type I (Figure S6), the commercial porous stainless-steel sheet with a thickness of $\sim 800 \mu\text{m}$ was used as the substrate. The tape-casted LSM layer with a raw powder particle size of $\sim 1 \mu\text{m}$ and the NiO-BZCY721 fuel electrode functional layer with an average particle size of $\sim 500 \text{ nm}$ were laminated together on the metal substrate. During the lamination step at an applied pressure of 200 bar, the thickness of the metal substrate decreased to $\sim 600 \mu\text{m}$. The assembly of the metal support with the green layers was then sintered at $950 \text{ }^\circ\text{C}$ in air. By contrast, the state-of-the-art metal supported ceramic cells with YSZ electrolyte are usually sintered at temperatures higher than $1200 \text{ }^\circ\text{C}$ and in reducing atmosphere. After sintering, Si migration from the stainless steel to the protonic ceramic that could occur via vapor diffusion during the sintering step and yield the formation of Ba_2SiO_4 could not be evidenced.⁴ This is likely the result of the moderate thermal treatment conditions, the use of the additional LSM barrier layer and the low Si content in the metallic substrate. On the other hand, Cr migration was observed to some extent in the functional layers. However, nearly no Cr was detected in the upper area of the fuel electrode and the electrolyte. In Nano-SIMS analysis, on the other hand, a tiny amount of Cr seems to exist on top of the electrolyte surface. We should note this as a result of the deposition of vaporized Cr phase from the metal surface during the PLD process, while Cr contamination in the electrolyte layer is negligible. It is confirmed that the multi-layer structure and the reduction of the processing temperature can effectively slow down the migration of volatile elements contained in stainless steel.⁵ However, the type I cells with Pt positrode showed relatively low open circuit voltages (OCV) of ca. 0.32 V with 20% H_2 / N_2 on the fuel electrode side and 10 % O_2 / N_2 on the oxygen electrode side at $600 \text{ }^\circ\text{C}$.² Three main reasons or a combination of them can explain a low OCV in the H_2/O_2 concentration cell: i) a faulty sealing, ii) a lack of tightness of the electrolyte due to

pin-holes defects, both yielding a gas cross-over and iii) the presence of electron hole charge carriers in the thin film electrolyte, introduced by oxygen incorporation ($\frac{1}{2} O_2 + V_O^{\bullet\bullet} \rightleftharpoons O_O^x + 2h^{\bullet}$) at the interface of positrode/electrolyte in an oxidizing atmosphere and resulting in a p-type conduction. Even though a contribution from the three is plausible, it is to point out that the cell manufacturing performed in ambient atmosphere (no clean room) yielding a high probability of electrode surface contamination by fine dusts that can result in pin-holes defects after electrolyte deposition. To increase the tightness of the electrolyte further, a second fuel electrode layer of NiO-BZCY541 was added on the top of the assembly, to improve the surface quality of the substrate before the electrolyte deposition by the PLD process (Type II cells in Figure S6). Having a higher sinterability due to the higher Ce content, the smaller particle size of the NiO-BZCY541 yielded a surface with a finer structure and reduced roughness values (Figure 2), as observed on the SEM surface images (Figure S4). After the optimization, values of OCV higher than 0.9 V (Figure 3a) could be obtained confirming the improved quality of the thin-film electrolyte and supporting the hypothesis that pin-holes defects in the thin film electrolyte are the major cause for a low OCV. It is desirable to manufacture the cell in a dust free environment, for instance in a clean room, to minimize the risk of pin-hole formation due to external contamination. The thermo-mechanical stability of the thin-film electrolyte from the type II cells was investigated by annealing in air for 30 h at 700 °C (Figure S9), and the SEM images show no cracks.

Note S2. Two perovskite peaks 330A and B in the sample I-1 and 2 in the stress assessment.

The XRD patterns of the sample I-1 and 2 showed two peaks for the (330) perovskite lattice plane as shown in Figure S8, which was not the case for the sample II-1 and 2. The BZCY electrolyte layers of the sample I-1 and 2 were deposited by PLD in an inappropriate condition. The intensity ratio of those two peaks changed with the inclination angle for both samples, which indicates two layers in the electrolyte coating and the main peak 330A and the subpeak 330B could be of the bottom and the surface layers, respectively. In the PLD system, four sample positions, corresponding to the 4 pre-cut round shape samples visible on Figure S7 are deposited one after another. For samples I-1 and 2, during the PLD process, the laser power density was too high and the laser plume was too large and spread widely to deposit the other positions. In such a condition, the main layer could be grown too fast and another thinner layer might be deposited after the deposition of the main one and may be grown slowly. The fast

Appendix C: Supplementary information for Article III

growth could be the origin of such a high stress of the main layers (330A), which might be the cause of delamination in this case.

References

- (1) Vasechko, V.; Pećanac, G.; Kuhn, B.; Malzbender, J. Mechanical properties of porous ITM alloy. *Int. J. Hydrog. Energy* **2016**, *41* (1), 562-569.
- (2) Zheng, H.; Han, F.; Sata, N.; Riegraf, M.; Dayaghi, A. M.; Norby, T.; Costa, R. Metal supported proton conducting ceramic cell with thin film electrolyte for electrolysis application *ECS Trans.* **2021**, *103* (1), 693-700.
- (3) Hinata, K.; Sata, N.; Costa, R.; Iguchi, F. High Temperature Elastic Modulus of Proton Conducting Ceramics Y-Doped Ba (Zr, Ce) O₃. In *Electrochemical Society Meeting Abstracts prime2020*, 2020; The Electrochemical Society, Inc.: pp 2617-2617.
- (4) Wang, R.; Lau, G. Y.; Ding, D.; Zhu, T.; Tucker, M. C. Approaches for co-sintering metal-supported proton-conducting solid oxide cells with Ba(Zr,Ce,Y,Yb)O_{3-δ} electrolyte. *Int. J. Hydrog. Energy* **2019**, *44* (26), 13768-13776.
- (5) Wang, R. F.; Byrne, C.; Tucker, M. C. Assessment of co-sintering as a fabrication approach for metal-supported proton-conducting solid oxide cells. *Solid State Ionics* **2019**, *332*, 25-33.

Bibliography

- [1] H. Ritchie, P. Rosado and M. Roser. *Energy production and consumption*. 2020. <https://ourworldindata.org/energy-production-consumption>, accessed 2023-08-08.
- [2] B. K. Bose. Global warming: Energy, environmental pollution, and the impact of power electronics. *IEEE Ind. Electron. M.* **2010**, 4 (1), 6-17.
- [3] J. Twidell. *Renewable energy resources*; Routledge, 2021.
- [4] K. T. Møller, T. R. Jensen, E. Akiba and H.-w. Li. Hydrogen - A sustainable energy carrier. *Prog. Nat. Sci-Mater.* **2017**, 27 (1), 34-40.
- [5] A. Sartbaeva, V. L. Kuznetsov, S. A. Wells and P. P. Edwards. Hydrogen nexus in a sustainable energy future. *Energy Environ. Sci.* **2008**, 1 (1), 79-85.
- [6] G. Squadrito, G. Maggio and A. Nicita. The green hydrogen revolution. *Renew. Energ.* **2023**, 216.
- [7] H. Ishaq, I. Dincer and C. Crawford. A review on hydrogen production and utilization: challenges and opportunities. *Int. J. Hydrogen Energ.* **2022**, 47 (62), 26238-26264.
- [8] M. Younas, S. Shafique, A. Hafeez, F. Javed and F. Rehman. An overview of hydrogen production: current status, potential, and challenges. *Fuel* **2022**, 316, 123317.
- [9] F. Dawood, M. Anda and G. M. Shafiullah. Hydrogen production for energy: An overview. *Int. J. Hydrogen Energ.* **2020**, 45 (7), 3847-3869.
- [10] S. Shiva Kumar and H. Lim. An overview of water electrolysis technologies for green hydrogen production. *Energy Rep.* **2022**, 8, 13793-13813.
- [11] S. Y. Kang, J. E. Park, G. Y. Jang, O.-H. Kim, O. J. Kwon, Y.-H. Cho and Y.-E. Sung. High-performance and durable water electrolysis using a highly conductive and stable anion-exchange membrane. *Int. J. Hydrogen Energ.* **2022**, 47 (15), 9115-9126.
- [12] L. Q. Le, C. H. Hernandez, M. H. Rodriguez, L. Zhu, C. Duan, H. Ding, R. P. O'Hayre and N. P. Sullivan. Proton-conducting ceramic fuel cells: Scale up and stack integration. *J. Power Sources* **2021**, 482, 228868.
- [13] S. Megel, C. Dosch, S. Rothe, C. Folgner, N. Trofimenko, A. Rost, M. Kusnezoff, E. Reichelt, M. Jahn and A. Michaelis. Co-electrolysis with CFY-stacks. *ECS trans.* **2017**, 78 (1), 3089-3102.
- [14] K. D. Kreuer. Proton-conducting oxides. *Annu. Rev. Mater. Res.* **2003**, 33 (1), 333-359.
- [15] H. Iwahara. Technological challenges in the application of proton conducting ceramics. *Solid State Ion.* **1995**, 77, 289-298.

Bibliography

- [16] L. Q. Le, C. Meisel, C. H. Hernandez, J. Huang, Y. Kim, R. O'Hayre and N. P. Sullivan. Performance degradation in proton-conducting ceramic fuel cell and electrolyzer stacks. *J. Power Sources* **2022**, 537, 231356.
- [17] F. Forrat, P. Dauge, G. Trevoux, G. Danner and M. Christen. Electrolyte solide à base de AlLaO_3 . Application aux piles à combustible. *C. R. Acad. Sci.* **1964**, 259, 2813-2816.
- [18] S. Stotz and C. Wagner. Die löslichkeit von wasserdampf und wasserstoff in festen oxiden. *Ber. Bunsenges. Phys. Chem.* **1966**, 70 (8), 781-788.
- [19] K. Katahira, Y. Kohchi, T. Shimura and H. Iwahara. Protonic conducting in Zr-substituted BaCeO_3 . *Solid State Ion.* **2000**, 138 (1-2), 91-98.
- [20] L. Lei, J. Zhang, Z. Yuan, J. Liu, M. Ni and F. Chen. Progress report on proton conducting solid oxide electrolysis cells. *Adv. Funct. Mater.* **2019**, 29 (37), 1903805.
- [21] R. Merkle, M. F. Hoedl, G. Raimondi, R. Zohourian and J. Maier. Oxides with mixed protonic and electronic conductivity. *Annu. Rev. Mater. Res.* **2021**, 51 (1), 461-493.
- [22] J. Cao, Y. Ji and Z. Shao. Perovskites for protonic ceramic fuel cells: a review. *Energy Environ. Sci.* **2022**, 15 (6), 2200-2232.
- [23] T. Shimura, Y. Tokiwa and H. Iwahara. Protonic conduction in lanthanum strontium aluminate and lanthanum niobate-based oxides at elevated temperatures. *Solid State Ion.* **2002**, 154, 653-658.
- [24] J. Bielecki, S. F. Parker, D. Ekanayake, S. M. Rahman, L. Börjesson and M. Karlsson. Short-range structure of the brownmillerite-type oxide $\text{Ba}_2\text{In}_2\text{O}_5$ and its hydrated proton-conducting form BaInO_3H . *J. Mater. Chem. A* **2014**, 2 (40), 16915-16924.
- [25] H. Iwahara, T. Esaka, H. Uchida and N. Maeda. Proton conduction in sintered oxides and its application to steam electrolysis for hydrogen production. *Solid State Ion.* **1981**, 3, 359-363.
- [26] H. Iwahara, H. Uchida, a. K. Ono and K. Ogaki. Proton conduction in sintered oxides based on BaCeO_3 . *J. Electrochem. Soc.* **1988**, 135 (2), 529.
- [27] T. Hibino, K. Mizutani, T. Yajima and H. Iwahara. Evaluation of proton conductivity in SrCeO_3 , BaCeO_3 , CaZrO_3 and SrZrO_3 by temperature programmed desorption method. *Solid State Ion.* **1992**, 57 (3-4), 303-306.
- [28] H. Uchida, N. Maeda and H. Iwahara. Relation between proton and hole conduction in SrCeO_3 -based solid electrolytes under water-containing atmospheres at high temperatures. *Solid State Ion.* **1983**, 11 (2), 117-124.
- [29] N. Bonanos, K. Knight and B. Ellis. Perovskite solid electrolytes: structure, transport properties and fuel cell applications. *Solid State Ion.* **1995**, 79, 161-170.
- [30] S. Haile, G. Staneff and K. Ryu. Non-stoichiometry, grain boundary transport and chemical stability of proton conducting perovskites. *J. Mater. Sci.* **2001**, 36, 1149-1160.

- [31] A. Nowick and Y. Du. High-temperature protonic conductors with perovskite-related structures. *Solid State Ion.* **1995**, *77*, 137-146.
- [32] G. Gregori, R. Merkle and J. Maier. Ion conduction and redistribution at grain boundaries in oxide systems. *Prog. Mater. Sci.* **2017**, *89*, 252-305.
- [33] K. Kreuer, E. Schönherr and J. Maier. Proton and oxygen diffusion in BaCeO₃ based compounds: a combined thermal gravimetric analysis and conductivity study. *Solid State Ion.* **1994**, *70*, 278-284.
- [34] C. Duan, J. Huang, N. Sullivan and R. O'Hayre. Proton-conducting oxides for energy conversion and storage. *Appl. Phys. Rev.* **2020**, *7* (1), 011314.
- [35] E. Fabbri, T.-k. Oh, S. Licoccia, E. Traversa and E. D. Wachsman. Mixed protonic/electronic conductor cathodes for intermediate temperature SOFCs based on proton conducting electrolytes. *J. Electrochem. Soc.* **2008**, *156* (1), B38-B45.
- [36] E. Fabbri, D. Pergolesi and E. Traversa. Materials challenges toward proton-conducting oxide fuel cells: a critical review. *Chem. Soc. Rev.* **2010**, *39* (11), 4355-4369.
- [37] E. Vøllestad, H. Zhu and R. J. Kee. Interpretation of defect and gas-phase fluxes through mixed-conducting ceramics using Nernst–Planck–Poisson and integral formulations. *J. Electrochem. Soc.* **2013**, *161* (1), F114-F124.
- [38] E. Vøllestad, R. Strandbakke, M. Tarach, D. Catalan-Martinez, M. L. Fontaine, D. Beeff, D. R. Clark, J. M. Serra and T. Norby. Mixed proton and electron conducting double perovskite anodes for stable and efficient tubular proton ceramic electrolyzers. *Nat. Mater.* **2019**, *18* (7), 752-759.
- [39] H. Shi, C. Su, R. Ran, J. Cao and Z. Shao. Electrolyte materials for intermediate-temperature solid oxide fuel cells. *Prog. Nat. Sci-Mater.* **2020**, *30* (6), 764-774.
- [40] C. W. Tanner and A. V. Virkar. Instability of BaCeO₃ in H₂O-Containing Atmospheres. *J. Electrochem. Soc.* **1996**, *143* (4), 1386-1389.
- [41] N. Zakowsky, S. Williamson and J. T. Irvine. Elaboration of CO₂ tolerance limits of BaCe_{0.9}Y_{0.1}O_{3-δ} electrolytes for fuel cells and other applications. *Solid State Ion.* **2005**, *176* (39-40), 3019-3026.
- [42] S. V. Bhide and A. V. Virkar. Stability of BaCeO₃-based proton conductors in water-containing atmospheres. *J. Electrochem. Soc.* **1999**, *146* (6), 2038-2044.
- [43] H. Matsumoto, Y. Kawasaki, N. Ito, M. Enoki and T. Ishihara. Relation between electrical conductivity and chemical stability of BaCeO₃-based proton conductors with different trivalent dopants. *Electrochem. Solid-State Lett.* **2007**, *10* (4), B77-B80.
- [44] E. Fabbri, A. Depifanio, E. Dibartolomeo, S. Licoccia and E. Traversa. Tailoring the chemical stability of Ba(Ce_{0.8-x}Zr_x)Y_{0.2}O_{3-δ} protonic conductors for intermediate temperature solid oxide fuel cells (IT-SOFCs). *Solid State Ion.* **2008**, *179* (15-16), 558-564.

Bibliography

- [45] K. Kreuer. Aspects of the formation and mobility of protonic charge carriers and the stability of perovskite-type oxides. *Solid State Ion.* **1999**, 125 (1-4), 285-302.
- [46] S. Tao and J. T. S. Irvine. Conductivity studies of dense yttrium-doped BaZrO₃ sintered at 1325 °C. *J. Solid State Chem.* **2007**, 180 (12), 3493-3503.
- [47] Z. Liu, M. Chen, M. Zhou, D. Cao, P. Liu, W. Wang, M. Liu, J. Huang, J. Shao and J. Liu. Multiple effects of iron and nickel additives on the properties of proton conducting yttrium-doped barium cerate-zirconate electrolytes for high-performance solid oxide fuel cells. *ACS Appl. Mater. Interfaces* **2020**, 12 (45), 50433-50445.
- [48] Y. Liu, Y. Guo, R. Ran and Z. Shao. A novel approach for substantially improving the sinterability of BaZr_{0.4}Ce_{0.4}Y_{0.2}O_{3-δ} electrolyte for fuel cells by impregnating the green membrane with zinc nitrate as a sintering aid. *J. Membr. Sci.* **2013**, 437, 189-195.
- [49] S. Tao and J. T. Irvine. A stable, easily sintered proton-conducting oxide electrolyte for moderate-temperature fuel cells and electrolyzers. *Adv. mater.* **2006**, 18 (12), 1581-1584.
- [50] D. Han, S. Uemura, C. Hiraiwa, M. Majima and T. Uda. Detrimental effect of sintering additives on conducting ceramics: Yttrium-doped barium zirconate. *ChemSusChem* **2018**, 11 (23), 4102-4113.
- [51] D. Han, X. Liu, T. S. Bjørheim and T. Uda. Yttrium-doped barium zirconate-cerate solid solution as proton conducting electrolyte: why higher cerium concentration leads to better performance for fuel cells and electrolysis cells. *Adv. Energy Mater.* **2021**, 11 (8), 2003149.
- [52] N. Wang, C. Tang, L. Du, R. Zhu, L. Xing, Z. Song, B. Yuan, L. Zhao, Y. Aoki and S. Ye. Advanced cathode materials for protonic ceramic fuel cells: recent progress and future perspectives. *Adv. Energy Mater.* **2022**, 12 (34), 2201882.
- [53] W. Sun, Z. Zhu, Y. Jiang, Z. Shi, L. Yan and W. Liu. Optimization of BaZr_{0.1}Ce_{0.7}Y_{0.2}O_{3-δ}-based proton-conducting solid oxide fuel cells with a cobalt-free proton-blocking La_{0.7}Sr_{0.3}FeO_{3-δ}-Ce_{0.8}Sm_{0.2}O_{2-δ} composite cathode. *Int. J. Hydrogen Energ.* **2011**, 36 (16), 9956-9966.
- [54] Y. P. Xia, Z. Z. Jin, H. Q. Wang, Z. Gong, H. L. Lv, R. R. Peng, W. Liu and L. Bi. A novel cobalt-free cathode with triple-conduction for proton-conducting solid oxide fuel cells with unprecedented performance. *J. Mater. Chem. A* **2019**, 7 (27), 16136-16148.
- [55] Z. U. D. Babar, M. B. Hanif, J.-T. Gao, C.-J. Li and C.-X. Li. Sintering behavior of BaCe_{0.7}Zr_{0.1}Y_{0.2}O_{3-δ} electrolyte at 1150 °C with the utilization of CuO and Bi₂O₃ as sintering aids and its electrical performance. *Int. J. Hydrogen Energ.* **2021**, 47 (11), 7403-7414.
- [56] M. Zhou, Z. Liu, M. Chen, Z. Zhu, D. Cao and J. Liu. Electrochemical performance and chemical stability of proton-conducting BaZr_{0.8-x}Ce_xY_{0.2}O_{3-δ} electrolytes. *J. Am. Ceram. Soc.* **2022**, 105 (9), 5711-5724.
- [57] P. Sawant, S. Varma, B. N. Wani and S. R. Bharadwaj. Synthesis, stability and conductivity of BaCe_{0.8-x}Zr_xY_{0.2}O_{3-δ} as electrolyte for proton conducting SOFC. *Int. J. Hydrogen Energ.*

2012, 37 (4), 3848-3856.

[58] H. An, H.-W. Lee, B.-K. Kim, J.-W. Son, K. J. Yoon, H. Kim, D. Shin, H.-I. Ji and J.-H. Lee. A 5×5 cm² protonic ceramic fuel cell with a power density of 1.3 W cm⁻² at 600 °C. *Nat Energy* **2018**, 3 (10), 870-875.

[59] L. Yang, S. Wang, K. Blinn, M. Liu, Z. Liu, Z. Cheng and M. Liu. Enhanced sulfur and coking tolerance of a mixed ion conductor for SOFCs: BaZr_{0.1}Ce_{0.7}Y_{0.2-x}Yb_xO_{3-δ}. *Science* **2009**, 326 (5949), 126-129.

[60] C. Duan, J. Tong, M. Shang, S. Nikodemski, M. Sanders, S. Ricote, A. Almansoori and R. O'Hayre. Readily processed protonic ceramic fuel cells with high performance at low temperatures. *Science* **2015**, 349 (6254), 1321-1326.

[61] C. C. Duan, R. Kee, H. Y. Zhu, N. Sullivan, L. Z. Zhu, L. Z. Bian, D. Jennings and R. O'Hayre. Highly efficient reversible protonic ceramic electrochemical cells for power generation and fuel production. *Nat Energy* **2019**, 4 (3), 230-240.

[62] W. Li, B. Guan, L. Ma, H. Tian and X. Liu. Synergistic coupling of proton conductors BaZr_{0.1}Ce_{0.7}Y_{0.1}Yb_{0.1}O_{3-δ} and La₂Ce₂O₇ to create chemical stable, interface active electrolyte for steam electrolysis cells. *ACS Appl. Mater. Interfaces* **2019**, 11 (20), 18323-18330.

[63] S. Choi, C. J. Kucharczyk, Y. Liang, X. Zhang, I. Takeuchi, H.-I. Ji and S. M. Haile. Exceptional power density and stability at intermediate temperatures in protonic ceramic fuel cells. *Nat Energy* **2018**, 3 (3), 202-210.

[64] L. Yang, C. Zuo and M. Liu. High-performance anode-supported solid oxide fuel cells based on Ba(Zr_{0.1}Ce_{0.7}Y_{0.2})O_{3-δ} (BZCY) fabricated by a modified co-pressing process. *J. Power Sources* **2010**, 195 (7), 1845-1848.

[65] B. Hua, N. Yan, M. Li, Y. F. Sun, Y. Q. Zhang, J. Li, T. Etsell, P. Sarkar and J. L. Luo. Anode-engineered protonic ceramic fuel cell with excellent performance and fuel compatibility. *Adv. Mater.* **2016**, 28 (40), 8922-8926.

[66] J. Gao, Y. Meng, T. Hong, S. Kim, S. Lee, K. He and K. S. Brinkman. Rational anode design for protonic ceramic fuel cells by a one-step phase inversion method. *J. Power Sources* **2019**, 418, 162-166.

[67] N. Nasani, D. Ramasamy, I. Antunes, J. Perez and D. P. Fagg. Electrochemical behaviour of Ni-BZO and Ni-BZY cermet anodes for protonic ceramic fuel cells (PCFCs) – A comparative study. *Electrochim. Acta* **2015**, 154, 387-396.

[68] W. G. Coors and A. Manerbino. Characterization of composite cermet with 68wt.% NiO and BaCe_{0.2}Zr_{0.6}Y_{0.2}O_{3-δ}. *J. Membr. Sci.* **2011**, 376 (1-2), 50-55.

[69] B. H. Rainwater, M. Liu and M. Liu. A more efficient anode microstructure for SOFCs based on proton conductors. *Int. J. Hydrogen Energ.* **2012**, 37 (23), 18342-18348.

[70] D. Medvedev. Trends in research and development of protonic ceramic electrolysis cells.

Bibliography

Int. J. Hydrogen Energ. **2019**, *44* (49), 26711-26740.

[71] A. Dubois, S. Ricote and R. J. Braun. Benchmarking the expected stack manufacturing cost of next generation, intermediate-temperature protonic ceramic fuel cells with solid oxide fuel cell technology. *J. Power Sources* **2017**, *369*, 65-77.

[72] Y. Q. Meng, J. Gao, Z. Y. Zhao, J. Amoroso, J. H. Tong and K. S. Brinkman. Review: recent progress in low-temperature proton-conducting ceramics. *J. Mater. Sci.* **2019**, *54* (13), 9291-9312.

[73] Z. Gao, L. V. Mogni, E. C. Miller, J. G. Railsback and S. A. Barnett. A perspective on low-temperature solid oxide fuel cells. *Energy Environ. Sci.* **2016**, *9* (5), 1602-1644.

[74] H. Ding, X. Xue, X. Liu and G. Meng. High performance protonic ceramic membrane fuel cells (PCMFCs) with $\text{Sm}_{0.5}\text{Sr}_{0.5}\text{CoO}_{3-\delta}$ perovskite cathode. *J. Alloys Compd.* **2010**, *494* (1-2), 233-235.

[75] Y.-W. Lai, K.-R. Lee, S.-Y. Yang, C.-J. Tseng, S.-C. Jang, I. Y. Tsao, S.-y. Chen and S.-W. Lee. Production of $\text{La}_{0.6}\text{Sr}_{0.4}\text{Co}_{0.2}\text{Fe}_{0.8}\text{O}_{3-\delta}$ cathode with graded porosity for improving proton-conducting solid oxide fuel cells. *Ceram. Int.* **2019**, *45* (17), 22479-22485.

[76] S. Choi, T. C. Davenport and S. M. Haile. Protonic ceramic electrochemical cells for hydrogen production and electricity generation: exceptional reversibility, stability, and demonstrated faradaic efficiency. *Energy Environ. Sci.* **2019**, *12* (1), 206-215.

[77] J. Kim, S. Sengodan, G. Kwon, D. Ding, J. Shin, M. Liu and G. Kim. Triple-conducting layered perovskites as cathode materials for proton-conducting solid oxide fuel cells. *ChemSusChem* **2014**, *7* (10), 2811-2815.

[78] W. Y. Li, B. Guan, L. Ma, S. S. Hu, N. Zhang and X. B. Liu. High performing triple-conductive $\text{Pr}_2\text{NiO}_{4+\delta}$ anode for proton-conducting steam solid oxide electrolysis cell. *J. Mater. Chem. A* **2018**, *6* (37), 18057-18066.

[79] W. Li, B. Guan, T. Yang, Z. Li, W. Shi, H. Tian, L. Ma, T. L. Kalapos and X. Liu. Layer-structured triple-conducting electrocatalyst for water-splitting in protonic ceramic electrolysis cells: Conductivities vs. activity. *J. Power Sources* **2021**, *495*, 229764.

[80] R. Strandbakke, V. A. Cherepanov, A. Y. Zuev, D. S. Tsvetkov, C. Argirusis, G. Sourkouni, S. Prunte and T. Norby. Gd- and Pr-based double perovskite cobaltites as oxygen electrodes for proton ceramic fuel cells and electrolyser cells. *Solid State Ion.* **2015**, *278*, 120-132.

[81] K. Leonard, J. Druce, V. Thoreton, J. A. Kilner and H. Matsumoto. Exploring mixed proton/electron conducting air electrode materials in protonic electrolysis cell. *Solid State Ion.* **2018**, *319*, 218-222.

[82] R. Strandbakke, E. Vøllestad, S. A. Robinson, M.-L. Fontaine and T. Norby. $\text{Ba}_{0.5}\text{Gd}_{0.8}\text{La}_{0.7}\text{Co}_2\text{O}_{6-\delta}$ infiltrated in porous $\text{BaZr}_{0.7}\text{Ce}_{0.2}\text{Y}_{0.1}\text{O}_3$ backbones as electrode material for proton ceramic electrolytes. *J. Electrochem. Soc.* **2017**, *164* (4), F196-F202.

- [83] A. M. Dayaghi, R. Haugsrud, M. Stange, Y. Larring, R. Strandbakke and T. Norby. Increasing the thermal expansion of proton conducting Y-doped BaZrO₃ by Sr and Ce substitution. *Solid State Ion.* **2021**, 359, 115534.
- [84] L.-W. Tai, M. Nasrallah, H. Anderson, D. Sparlin and S. Sehlin. Structure and electrical properties of La_{1-x}Sr_xCo_{1-y}Fe_yO₃. Part 2. The system La_{1-x}Sr_xCo_{0.2}Fe_{0.8}O₃. *Solid State Ion.* **1995**, 76 (3-4), 273-283.
- [85] H. Zheng, M. Riegraf, N. Sata and R. Costa. A double perovskite oxygen electrode in Zr-rich proton conducting ceramic cells for efficient electricity generation and hydrogen production. *J. Mater. Chem. A* **2023**, 11 (20), 10955-10970.
- [86] Bloom Energy. *Homepage*. <https://www.bloomenergy.com/>, accessed 2023-10-15.
- [87] Sunfire GmbH. *Homepage*. <https://www.sunfire.de/de/>, accessed 2023-10-15.
- [88] Ceres Power. *Homepage*. <https://www.ceres.tech/>, accessed 2023-10-15.
- [89] Elcogen. *Homepage*. <https://elcogen.com/>, accessed 2023-10-15.
- [90] S. H. Morejudo, R. Zanón, S. Escolástico, I. Yuste-Tirados, H. Malerød-Fjeld, P. K. Vestre, W. G. Coors, A. Martínez, T. Norby, J. M. Serra and C. Kjølseth. Direct conversion of methane to aromatics in a catalytic co-ionic membrane reactor. *Science* **2016**, 353 (6299), 563-566.
- [91] D. Clark, H. Malerød-Fjeld, M. Budd, I. Yuste-Tirados, D. Beeaff, S. Aamodt, K. Nguyen, L. Ansaloni, T. Peters and P. K. Vestre. Single-step hydrogen production from NH₃, CH₄, and biogas in stacked proton ceramic reactors. *Science* **2022**, 376 (6591), 390-393.
- [92] M. Zhang, H. Lv, H. Kang, W. Zhou and C. Zhang. A literature review of failure prediction and analysis methods for composite high-pressure hydrogen storage tanks. *Int. J. Hydrogen Energ.* **2019**, 44 (47), 25777-25799.
- [93] M. Marrony. *Proton-conducting ceramics: from fundamentals to applied research*; CRC Press, 2015.
- [94] H. Zheng, F. Han, N. Sata, M. Riegraf, A. M. Dayaghi, T. Norby and R. Costa. Metal Supported Proton Conducting Ceramic Cell with Thin Film Electrolyte for Electrolysis Application. *ECS Trans.* **2021**, 103 (1), 693-700.
- [95] R. O'Hayre. *Fuel cell fundamentals 3rd ed*; wiley, 2016.
- [96] W. Zhang, M. Liu, X. Gu, Y. Shi, Z. Deng and N. Cai. Water electrolysis toward elevated temperature: advances, challenges and frontiers. *Chem. Rev.* **2023**, 123 (11), 7119-7192.
- [97] M. A. Laguna-Bercero. *High temperature electrolysis*; Springer Nature, 2023.
- [98] M. Ni. Modeling of a planar solid oxide fuel cell based on proton-conducting electrolyte. *Int. J. Energ. Res.* **2010**, 34 (12), 1027-1041.

Bibliography

- [99] J. Larminie, A. Dicks and M. S. McDonald. *Fuel cell systems explained*; J. Wiley Chichester, UK, 2003.
- [100] Y. Patcharavorachot, N. P. Brandon, W. Paengjuntuek, S. Assabumrungrat and A. Arpornwichanop. Analysis of planar solid oxide fuel cells based on proton-conducting electrolyte. *Solid State Ion.* **2010**, *181* (35-36), 1568-1576.
- [101] H. Zheng, F. Han, N. Sata, M. Riegraf, A. M. Dayaghi, T. Norby and R. Costa. Metal supported proton conducting ceramic cell with thin film electrolyte for electrolysis application *ECS Trans.* **2021**, *103* (1), 693-700.
- [102] Q.-A. Huang, R. Hui, B. Wang and J. Zhang. A review of AC impedance modeling and validation in SOFC diagnosis. *Electrochim. Acta* **2007**, *52* (28), 8144-8164.
- [103] A. Leonide, Y. Apel and E. Ivers-Tiffée. SOFC modeling and parameter identification by means of impedance spectroscopy. *ECS Trans.* **2009**, *19* (20), 81-109.
- [104] D.-M. Amaya-Dueñas, G. Chen, A. Weidenkaff, N. Sata, F. Han, I. Biswas, R. Costa and K. A. Friedrich. A-site deficient chromite with in situ Ni exsolution as a fuel electrode for solid oxide cells (SOCs). *J. Mater. Chem. A* **2021**, *9* (9), 5685-5701.
- [105] P. Caliandro, A. Nakajo, S. Diethelm and J. Van herle. Model-assisted identification of solid oxide cell elementary processes by electrochemical impedance spectroscopy measurements. *J. Power Sources* **2019**, *436*, 226838.
- [106] J. R. Macdonald and E. Barsoukov. *Impedance spectroscopy: theory, experiment, and applications*; John Wiley & Sons, 2018.
- [107] G. Brug, A. L. van den Eeden, M. Sluyters-Rehbach and J. H. Sluyters. The analysis of electrode impedances complicated by the presence of a constant phase element. *J. electroanal. chem. interf. electrochem.* **1984**, *176* (1-2), 275-295.
- [108] M. Liu and H. Hu. Effect of interfacial resistance on determination of transport properties of mixed-conducting electrolytes. *J. Electrochem. Soc.* **1996**, *143* (6), L109-L112.
- [109] H. Schichlein, A. C. Müller, M. Voigts, A. Krügel and E. Ivers-Tiffée. Deconvolution of electrochemical impedance spectra for the identification of electrode reaction mechanisms in solid oxide fuel cells. *J. Appl. Electrochem.* **2002**, *32*, 875-882.
- [110] E. Ivers-Tiffée and A. Weber. Evaluation of electrochemical impedance spectra by the distribution of relaxation times. *J. Ceram. Soc. Japan* **2017**, *125* (4), 193-201.
- [111] M. Hahn, S. Schindler, L.-C. Triebs and M. A. Danzer. Optimized process parameters for a reproducible distribution of relaxation times analysis of electrochemical systems. *Batteries* **2019**, *5* (2), 43.
- [112] K. Leonard, W. Deibert, M. E. Ivanova, W. A. Meulenber, T. Ishihara and H. Matsumoto. Processing ceramic proton conductor membranes for use in steam electrolysis. *Membranes* **2020**, *10* (11), 339.

- [113] T. Kobayashi, K. Kuroda, S. Jeong, H. Kwon, C. Zhu, H. Habazaki and Y. Aoki. Analysis of the anode reaction of solid oxide electrolyzer cells with $\text{BaZr}_{0.4}\text{Ce}_{0.4}\text{Y}_{0.2}\text{O}_{3-\delta}$ electrolytes and $\text{Sm}_{0.5}\text{Sr}_{0.5}\text{CoO}_{3-\delta}$ anodes. *J. Electrochem. Soc.* **2018**, *165* (5), F342-F349.
- [114] F. He, T. Wu, R. Peng and C. Xia. Cathode reaction models and performance analysis of $\text{Sm}_{0.5}\text{Sr}_{0.5}\text{CoO}_{3-\delta}$ - $\text{BaCe}_{0.8}\text{Sm}_{0.2}\text{O}_{3-\delta}$ composite cathode for solid oxide fuel cells with proton conducting electrolyte. *J. Power Sources* **2009**, *194* (1), 263-268.
- [115] Y. Zhou, E. Liu, Y. Chen, Y. Liu, L. Zhang, W. Zhang, Z. Luo, N. Kane, B. Zhao, L. Soule, Y. Niu, Y. Ding, H. Ding, D. Ding and M. Liu. An active and robust air electrode for reversible protonic ceramic electrochemical cells. *ACS Energy Lett.* **2021**, *6* (4), 1511-1520.
- [116] K. Xu, H. Zhang, Y. Xu, F. He, Y. Zhou, Y. Pan, J. Ma, B. Zhao, W. Yuan, Y. Chen and M. Liu. An efficient steam-induced heterostructured air electrode for protonic ceramic electrochemical cells. *Adv. Funct. Mater.* **2022**, *32* (23), 2110998.
- [117] K. Kousi, C. Tang, I. S. Metcalfe and D. Neagu. Emergence and future of exsolved materials. *Small* **2021**, *17* (21), 2006479.
- [118] R. Strandbakke, D. S. Wragg, M. H. Sorby, M. N. Guzik, A. E. Gunnaes, I. Szpunar, S. L. Wachowski, M. Balaguer, P. A. Carvalho, A. Mielewczyk-Gryn, J. M. Serra and T. Norby. Structural properties of mixed conductor $\text{Ba}_{1-x}\text{Gd}_{1-y}\text{La}_{x+y}\text{Co}_2\text{O}_{6-\delta}$. *Dalton Trans.* **2022**, *51* (48), 18667-18677.
- [119] K. Yang, Y. Wang, Z. Yang, Y. Wang and C. Jin. Degradation of cobalt-free $\text{Ba}_{0.95}\text{La}_{0.05}\text{FeO}_{3-\delta}$ cathode against CO_2 - H_2O and $\text{Ce}_{0.9}\text{Gd}_{0.1}\text{O}_{2-\delta}$ modification. *Int. J. Hydrogen Energ.* **2020**, *45* (58), 34080-34088.
- [120] W. Zhou, R. Ran and Z. Shao. Progress in understanding and development of $\text{Ba}_{0.5}\text{Sr}_{0.5}\text{Co}_{0.8}\text{Fe}_{0.2}\text{O}_{3-\delta}$ -based cathodes for intermediate-temperature solid-oxide fuel cells: A review. *J. Power Sources* **2009**, *192* (2), 231-246.
- [121] S. L. Wachowski, I. Szpunar, M. H. Sørby, A. Mielewczyk-Gryń, M. Balaguer, C. Ghica, M. C. Istrate, M. Gazda, A. E. Gunnæs, J. M. Serra, T. Norby and R. Strandbakke. Structure and water uptake in $\text{BaLnCo}_2\text{O}_{6-\delta}$ (Ln = La, Pr, Nd, Sm, Gd, Tb and Dy). *Acta Mater.* **2020**, *199*, 297-310.
- [122] S. Yamanaka, M. Fujikane, T. Hamaguchi, H. Muta, T. Oyama, T. Matsuda, S.-i. Kobayashi and K. Kurosaki. Thermophysical properties of BaZrO_3 and BaCeO_3 . *J. Alloys Compd.* **2003**, *359* (1-2), 109-113.
- [123] K. Huang, H. Y. Lee and J. B. Goodenough. Sr- and Ni-Doped LaCoO_3 and LaFeO_3 perovskites: new cathode materials for solid-oxide fuel cells. *J. Electrochem. Soc.* **1998**, *145* (9), 3220-3227.
- [124] J. Mougin, S. D. Iorio, A. Chatroux, T. Donnier-Maréchal, G. Palcoux, M. Petitjean and G. Roux. Development of a solid oxide electrolysis stack able to operate at high steam conversion rate and integration into a SOE system. *ECS Trans.* **2017**, *78* (1), 3065-3075.

Bibliography

- [125] U. Mushtaq, S. Welzel, R. K. Sharma, M. C. M. van de Sanden and M. N. Tsampas. Development of electrode-supported proton conducting solid oxide cells and their evaluation as electrochemical hydrogen pumps. *ACS Appl. Mater. Interfaces* **2022**, *14* (34), 38938-38951.
- [126] Q. Wang, T. Luo, Y. Tong, M. Dai, X.-Y. Miao, S. Ricote, Z. Zhan and M. Chen. Large-area protonic ceramic cells for hydrogen purification. *Sep. Purif. Technol.* **2022**, *295*, 121301.
- [127] F. Liu, H. Deng, D. Diercks, P. Kumar, M. H. A. Jabbar, C. Gumecci, Y. Furuya, N. Dale, T. Oku, M. Usuda, P. Kazempoor, L. Fang, D. Chen, B. Liu and C. Duan. Lowering the operating temperature of protonic ceramic electrochemical cells to < 450 °C. *Nat Energy* **2023**, *8*, 1145-1157.
- [128] Y. Matsuzaki, Y. Tachikawa, Y. Baba, K. Sato, G. Kojo, H. Matsuo, J. Otomo, H. Matsumoto, S. Taniguchi and K. Sasaki. Suppression of leakage current in proton-conducting BaZr_{0.8}Y_{0.2}O_{3-δ} electrolyte by forming hole-blocking layer. *J. Electrochem. Soc.* **2020**, *167* (8), 084515.
- [129] IRENA. *Renewable power generation costs in 2022*; International Renewable Energy Agency, Abu Dhabi, 2023.
- [130] M. B. Mogensen, A. Hauch, X. Sun, M. Chen, Y. Tao, S. D. Ebbesen, K. V. Hansen and P. V. Hendriksen. Relation between Ni particle shape change and Ni migration in Ni-YSZ electrodes - a hypothesis. *Fuel Cells* **2017**, *17* (4), 434-441.
- [131] M. B. Mogensen, M. Chen, H. L. Frandsen, C. Graves, A. Hauch, P. V. Hendriksen, T. Jacobsen, S. H. Jensen, T. L. Skaftø and X. Sun. Ni migration in solid oxide cell electrodes: Review and revised hypothesis. *Fuel Cells* **2021**, *21* (5), 415-429.
- [132] W. Deibert, M. E. Ivanova, Y. Huang, R. Merkle, J. Maier and W. A. Meulenbergh. Fabrication of multi-layered structures for proton conducting ceramic cells. *J. Mater. Chem. A* **2021**, *10* (5), 2362-2373.
- [133] E. Stefan, C. Denonville, Y. Larring, M. Stange and R. Haugsrud. Oxidation study of porous metal substrates for metal supported proton ceramic electrolyzer cells. *Corros. Sci.* **2019**, *164*, 108335.
- [134] R. T. Leah, A. Bone, A. Selcuk, D. Corcoran, M. Lankin, Z. Dehaney-Steven, M. Selby and P. Whalen. Development of highly robust, volume-manufacturable metal-supported SOFCs for operation below 600 °C. *ECS Trans.* **2011**, *35* (1), 351-367.
- [135] R. T. Leah, P. A. Bone, A. Selcuk, M. Rahman, A. Clare, M. Lankin, F. Felix, S. Mukerjee and M. A. Selby. Latest results and commercialization of the Ceres Power SteelCell® technology platform *ECS Trans.* **2019**, *91* (1), 51-61.
- [136] R. Leah, A. Bone, P. Hjalmarsson, A. Selcuk, M. Lankin, M. Rahman, F. Felix, J. De Vero, C. Macauley and C. Charbonneau. Commercialization of Ceres SteelCell® technology for power generation and electrolysis. *ECS Trans.* **2023**, *111* (6), 121-131.
- [137] I. A. Amar, R. Lan, C. T. G. Petit and S. Tao. Solid-state electrochemical synthesis of

ammonia: a review. *J. Solid State Electrochem.* **2011**, *15* (9), 1845-1860.